Scanning Lens Phased Array Antennas

Analysis, design and demonstrations at millimeter and submillimeter wavelengths using leaky-wave feeds

Bosma, S.

DOI
10.4233/uuid:ebbce637-e81b-4f1f-b005-834c8f407710

Publication date
2022

Document Version
Final published version

Citation (APA)
Bosma, S. (2022). *Scanning Lens Phased Array Antennas: Analysis, design and demonstrations at millimeter and submillimeter wavelengths using leaky-wave feeds*. [Dissertation (TU Delft), Delft University of Technology]. https://doi.org/10.4233/uuid:ebbce637-e81b-4f1f-b005-834c8f407710

Scanning Lens Phased Array Antennas

Analysis, design and demonstrations at millimeter and submillimeter wavelengths using leaky-wave feeds

Scanning Lens Phased Array Antennas

Analysis, design and demonstrations at millimeter and submillimeter wavelengths using leaky-wave feeds

DISSERTATION

for the purpose of obtaining the degree of doctor
at Delft University of Technology by the authority of the Rector Magnificus prof. dr. ir. T.H.J.J. van der Hagen;
Chair of the Board for Doctorates

to be defended publicly on Wednesday the 18th of January, 2023 at 12:30 o'clock
by

Sjoerd BOSMA
Master of Science in Electrical Engineering, Delft University of Technology, The Netherlands
born in Camperdown, Australia.

This dissertation has been approved by the promotors.

Composition of the doctoral committee:

Rector Magnificus,	Chairman
Prof. dr. ir. N. Llombart Juan,	Delft University of Technology, *promotor*
Dr. M. Alonso-delPino,	Delft University of Technology, *copromotor*
Independent members:	
Prof. dr. ing. A. Neto,	Delft University of Technology
Dr. M. Albani,	Università degli Studi di Siena
Prof. dr. A. Yarovoy,	Delft University of Technology
Dr. E. Saenz,	European Space Agency
Dr. G. Carluccio,	NXP Semiconductors
Reserve member:	
Prof. dr. ir. J.J.A. Baselmans,	Delft University of Technology

The work presented in this dissertation was performed in a collaboration between Delft University of Technology and the Jet Propulsion Laboratory, National Aeronautics and Space Administration, California, United States of America. The work was financed by the Starting Grant LAA-THz-CC 639749 from the European Research Council.

Keywords	Lens antennas, leaky waves, near field, antenna arrays, beam steering.
Cover	Microscope image of the broadband lossless matching layer presented in Chapter 7 taken by dr. Juan Bueno.
Printed by	Gildeprint B.V.

ISBN 978-94-6384-392-8

An electronic version of this dissertation is available at: https://repository.tudelft.nl.

Supra et ultra

Preface

The work presented in this thesis was performed between September 2017 and February 2022 at the Delft University of Technology (TU Delft), The Netherlands, funded by a Starting Grant from the European Research Council (ERC) LAA-THz-CC (639749). A part of the work was carried out in collaboration with, and at, the Jet Propulsion Laboratory (JPL), California Institute of Technology, California, United States of America, under a contract with the National Aeronautics and Space Administration (NASA).

Summary

Millimeter- and submillimeter wave applications, such as point-to-point wireless communications in beyond-5G scenarios, long-range automotive radars and astronomy and astrophysics science cases from space require antennas with high-gain beams that are steerable. At lower (microwave) frequencies, fully sampled phased arrays with thousands of elements have been demonstrated for this purpose. However, above roughly 100 GHz, integrated-circuit technology faces major bottlenecks in terms of size, power efficiency, thermal management and technological immaturity. Consequently, only integrated phased arrays with very few elements have been reported in the literature above 100 GHz. To still achieve the gain and enable beam scanning, mechanically actuated reflectors are now typically employed. However, such solutions are bulky, power-hungry and do not allow rapid beam steering.

To overcome these limitations, we propose, analyze, design, fabricate and demonstrate a new antenna architecture in this thesis: the scanning lens phased array. The scanning lens phased array is a compact, low-power and very sparse array of integrated lens antennas that we demonstrate with scanning capabilities up to 25 degrees around broadside. A hybrid electro-mechanical approach to beam steering is employed: the array factor is scanned electronically and the element patterns are steered mechanically. The grating lobes that arise in the array factor due to the array's sparsity are suppressed by the high directivity of the lens elements. This results in a clean, high-gain beam towards the desired scan angle.

Our analysis finds that the grating lobes can only be suppressed when the lens elements are illuminated with sufficiently high aperture efficiency. We have therefore studied and exploited the properties of resonant leaky-wave lens antenna feeds that achieve such high aperture efficiency. The analysis of resonant leaky-wave feeds was extended, with respect to previous work, to include lenses that are in the near field of the feed. As such, we were able to analyze lenses with a diameter as small as two free-space wavelengths. We found that the poles associated to the propagating leaky-wave modes can be used to derive closed-form expressions that describe the required lens antenna geometry. We have used this analysis to demonstrate several single-element lens antenna prototypes. At 180 GHz, an improved leaky-wave feed for plastic lenses was demonstrated that includes a circular waveguide and corrugations in the ground plane. We have also demonstrated, at 550 GHz, a wideband leaky-wave feed that supports the propagation of multiple leaky-wave modes to feed a silicon lens. To overcome the high reflections that occur for silicon lenses at the lens-air interface, we have pro-

posed and demonstrated a broadband and lossless matching layer suitable for shallow lens arrays.

We have then used the lens antennas as the elements of a scanning lens phased array. At 100 GHz, we demonstrated high-gain (>30 dBi) continuous beam steering up to 20 degrees with a 4x1 lens array prototype of plastic lenses with a diameter of six free-space wavelengths. Mechanical phase shifting is achieved with a fast, high-precision piezo-electric motor. Electronic phase shifting of each element is achieved with four channels, each consisting of a low-frequency IQ-mixer and a frequency multiplier. An over-the-air setup was used to calibrate and measure this array.

We also demonstrate a coherent seven-element silicon lens array at 550 GHz. To feed the elements from a single source, we have developed a novel quasi-optical power distribution architecture. In this transmit array architecture, a single, large lens is used to distribute power to the seven elements. Since the array elements are fed in phase, we were able to demonstrate discrete-angle beam steering towards the grating lobe angles by mechanically actuating the lens array. The high-gain beam from the lens array (>30 dBi) is thus mechanically steerable to 25 degrees from broadside.

Although we have demonstrated several improved feeds and the first scanning lens phased arrays, we have also identified several lines for future research. In the last Chapter, these opportunities are listed based on broad categorizations of lens and lens array analysis, technology development and possible application cases.

Samenvatting

Toepassingen van millimeter- en submillimeter golflengtes, waaronder draadloze punt-tot-punt communicatie voor de komende 6G implementaties, langeafstandsradars in auto's en wetenschappelijke experimenten in de astronomie en astrofysika vanuit de ruimte vereisen antennes met een smalle, stuurbare stralingsbundel. Op lagere frequenties (mikrogolven), zijn volledig bezette gestuurde arrays met duizenden elementen gemeengoed. Echter, boven de circa 100 GHz ontstaan er bottlenecks in het ontwikkelen van geintegreerde circuits door de afmetingen, vermogensefficientie, hitteafvoer en technologische onvolwassenheid. Om deze redenen zijn er slechts geintegreerde arrays met een zeer beperkt aantal elementen gepubliceerd in de wetenschappelijke literatuur. Om toch nog de vereiste smalle, stuurbare stralingsbundel te verkrijgen wordt veelal een mechanisch verplaatsbare schotel gebruikt. Echter, oplossingen als deze zijn vrij lijvig, vereisen veel vermogen en zijn niet snel te sturen.

Om deze beperkingen op te heffen, stellen we in dit proefschrift een nieuwe antenne architectuur voor die we ontwerpen, implementeren en valideren: de gestuurde lens array. De gestuurde lens array is een compacte array van geintegreerde lens antennes waarvan de elementen ver uit elkaar staan en die weinig vermogen gebruikt en toch tot 25 graden gestuurd kan worden. Een hybride elektro-mechanische benadering is de sleutel tot bundelsturing: de array factor wordt elektronisch gericht en de lens element stralingspatronen worden mechanisch gericht. De grating lobes die optreden door de roosterafstand worden onderdrukt door de smalle bundel die wordt uitgestuurd door de lens elementen. Dit heeft een mooie dunne stralingsbundel in de gewenste richting tot gevolg.

Uit onze analyse blijkt dat de grating lobes alleen kunnen worden onderdrukt wanneer de lenzen belicht worden met een hoge diafragma-efficientie. Daarom hebben we de eigenschappen van resonerende lekgolfantennes bestudeerd en uitgebuit die zulke hoge diafragma-efficientie tot gevolg hebben. De bestaande analyse van resonerende lekgolfantennes is uitgebreid om ook lenzen die in het nabije veld van de bron zijn te bestuderen. Hierdoor zijn we in staat geweest om lenzen met een doorsnede van slechts twee golflengtes te bestuderen. Uit ons onderzoek blijkt dat de polen behorend bij de voortplantende lekgolven gebruikt kunnen worden om, in gesloten vorm, uitdrukkingen af te leiden die de vorm van de lens volledig beschrijven. De resultaten van deze analyse zijn gebruikt om diverse lens antenne prototypes te maken. Op 180 GHz hebben we een verbeterde lekgolfantenne ontwikkeld die gebruik maakt van cirkelvormige uitsparingen in een geaard vlak en die voor plastic lenzen werkt. We

hebben ook, op 550 GHz, een breedbandige lekgolfantenne ontwikkeld die de voortplanting van vijf lekgolven mogelijk maakt en die voor silicium lenzen werkt. Om de ongewenste reflecties die bij de silicium-lucht overgang optreden te verminderen hebben we een nieuw soort antireflectiecoating ontwikkeld die geschikt is voor ondiepe lens arrays.

We hebben daarna zulke lens elementen gebruikt als de elementen in gestuurde lens arrays. Op 100 GHz hebben we een antenne met een hoge versterkingsfactor (>30 dBi) en continue bundelsturing tot 20 graden ontwikkeld. De array bestaat uit 4 plastic lenzen op een rij die elk een doorsnede van zes golflengtes hebben. De mechanische bundelsturing wordt door een snelle en zeer nauwkeurige piezo-elektrische motor gedaan. Elektronische bundelsturing van de lens elementen wordt bereikt door vier kanalen die elk bestaan uit een IQ-mixer op lage frequenties en een frequentievermenigvuldiger. We gebruiken een nieuw-ontwikkelde opstelling in de vrije ruimte om deze lens array elementen te calibreren en door te meten.

We tonen ook de werking van een silicium lens array met zeven lens elementen op 550 GHz aan. Om de elementen aan te sturen uit een enkele bron hebben we een nieuwe quasi-optische vermogensverdeler ontwikkeld. In deze doorstuur-array opstelling wordt een enkele, grote lens gebruikt om het vermogen te verdelen over de zeven elementen. Doordat de array elementen op deze manier in-fase aangestuurd worden kunnen we discrete-hoek bundelsturing aantonen naar de grating lobes door mechanische verplaatsing van de lens array. Een smalle bundel met hoge versterkingsfactor (>30 dBi) kan zo mechanisch gestuurd worden tot wel 25 graden.

Hoewel we de werking van verschillende verbeterde antennes en gestuurde lens arrays hebben aangetoond hebben we ook diverse nieuwe onderzoeksrichten op het oog. In het laatste hoofdstuk worden deze mogelijkheden benoemd.

Contents

Appendices

Introduction

Chapter 1
Introduction

Millimeter- and submillimeter-wave phased arrays have attracted significant research interest in the past decade [1]–[3] due to their applicability in a wide range of subjects, such as wireless communication [4]–[7], automotive radar [8], [9], security scanners [10], non-destructive testing [11], [12], biology [13] and applications in space such as astronomy [14], [15] and Earth [16], [17] and planetary science [18]. In Section 1.1, an overview of recent developments in arrays for some of these applications are highlighted. We will see that, in general, the higher the frequency, the lower the number of array elements that are integrated due to power efficiency and thermal limitations or routing difficulties.

In order to overcome this limitation, sparse phased arrays have been studied extensively to achieve beam steering of a high-gain beam using a relatively small number of elements. In Section 1.2, an overview of sparse array technology and techniques is given.

In this thesis, a new antenna architecture, consisting of a sparse array of actuated lenses, is introduced. The scientific contributions that have resulted from this work are given in Section 1.3 and an outline of the rest of the thesis is presented in Section 1.4.

1.1 Applications and Technology

Wireless Communication

Increasing demand for high-throughput wireless links is driving communication technology towards higher frequencies, where more bandwidth is available [4]–[7]. Scenarios where such links are indispensable include fixed wireless access [7], backhaul links (outdoors [5], [19] and indoors [7]) or simultaneously serving tens of thousands of users (such as a crowded stadium) [20]. For these use cases, an antenna gain of 30-50 dBi is required [5].

At 28 GHz, where spectrum has been allocated for 5G New Radio [21], a wide range of phased arrays have been demonstrated, ranging from arrays with only a few elements [22] to extremely large phased arrays with up to 4096 elements [1]. In the allocated 40 GHz band [23], integrated arrays have been demonstrated with 64 elements [24] and in architectures scalable to exceed 500 elements [25]. At 60 GHz, 256-element arrays have been demonstrated [26]. In the past decade, W-band (75-

Parts of this Chapter have been published in **[J1]**.

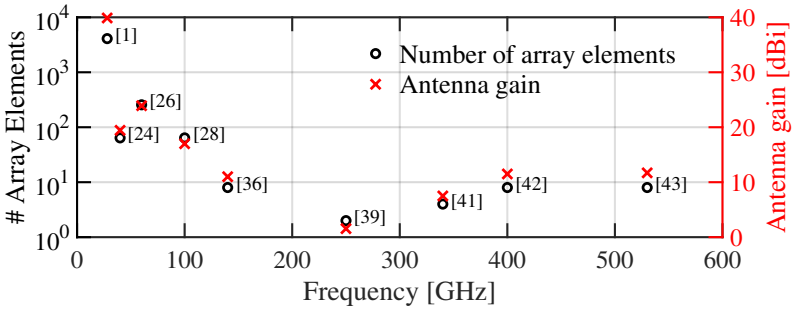

Fig. 1.1: Number of array elements in integrated phased array antennas for communications and their antenna gain.

110 GHz) integrated phased arrays have received considerable attention [27]–[30] to enable wireless communication. To reach distances of 10 km, the array should contain in the order of one thousand elements [31]. Several smaller arrays with 16 elements have been demonstrated [27], [30] but scalable architectures with 64 elements have also been demonstrated [28], [32].

Above 100 GHz, where the Federal Communications Commission in the United States has recently opened several-gigahertz-wide frequency bands [33], multiple phased array demonstrations have been reported. Around 140 GHz, a fully-integrated transceiver was demonstrated in [34], a transceiver front-end module was demonstrated in [35] and an eight-element phased array array was presented in [36]. A transceiver chip was coupled to an integrated dielectric lens in [37] at 130 GHz. Above 200 GHz, phased arrays for communications have not been demonstrated. However, progress is made with integrated technology. For example, several sources [38], [39] have been integrated on a chip around 250 GHz. At 340 GHz, a heterodyne receiver front-end was shown in [40] for imaging applications and a 2×2 phased array was demonstrated in [41]. A 400 GHz 1×8 phased array was demonstrated in [42] and a 1×4 phased array at 530 GHz in [43].

The number of elements in integrated phased array antennas for communication applications is summarized in Fig. 1.1 as a function of the frequency. The gain of these integrated antenna arrays, also shown in Fig. 1.1, especially above 100 GHz is not enough to fulfil the requirements for the communications applications outlined above.

Automotive and Imaging Radars

Efforts to improve vehicle safety and comfort have resulted in widespread availability of automatic emergency braking, adaptive cruise control, lane-assist systems and parking assistance systems in modern cars and trucks. Such sensors often rely on radar technology. In particular, the frequency bands around 24 GHz [44] and 77 GHz [8] have been widely exploited. Recently, the development of (semi-)autonomous vehicles

has resulted in the development of more complex and higher-frequency automotive instruments for 3D mapping or object detection and classification [9].

To increase the angular resolution in automotive radar, one approach has been the use of integrated arrays using multiple-input multiple-output (MIMO) technology [45]. In such architectures, a small array of N antennas transmit orthogonal sequences and, by using a small array of M receivers, a virtual antenna array of size $N \times M$ is synthesized. For example, MIMO frequency-modulated continuous wave (FMCW) radars at 77 GHz for automotive applications were demonstrated with four elements in [46] and with eight elements in [47]. Alternatively, the angular resolution can be increased by using a dielectric focusing lens [48].

To increase the range resolution of FMCW radars, larger bandwidths are required. To meet this demand, integrated radars are being developed at higher frequencies where there is more available spectrum. For example, in [49], a 94 GHz FMCW phased array radar transceiver was demonstrated. This array achieved 20 dBm equivalent isotropic radiated power (EIRP) with four transmit and four receive antennas-in-package. A sidelobe level (SLL) of 5 dB was achieved at scan angles of 20°. A MIMO radar at 94 GHz with four transmit and four receive channels was demonstrated in [50]. Above 100 GHz, several fully integrated imaging radar arrays have been demonstrated such as a MIMO radar at 145 GHz [51], a single-input single-output (SISO) radar at 170 GHz [52] and a SISO radar at 220 GHz [53].

At submillimeter waves, focal plane arrays of receivers under a mechanically actuated reflector are used for (real-time) imaging [10], [54]–[56]. At 350 GHz, a single-transceiver imaging radar system was developed for standoff concealed weapon detection, capable of imaging at 10 meters in 10-20 seconds [54]. A next-generation airport security screening system with 10 Hz frame rate was developed with 16 transceivers at 350 GHz in [55]. A submillimeter-wave radar was developed at 680 GHz with a 40 $\times$ 40 cm field of view at 5-9 meters [10]. An 800 GHz system with one transmitter and 32 receivers was demonstrated in [56] at an object plane distance of 4 meters.

Submillimeter-Wave Technology in Space

Astronomical observations of planets [15], comets [57], [58], the Moon [59], the cosmic microwave background [60] and the interstellar medium [14] along with remote sensing of the Earth's atmosphere [16], [61], [62] have been driving forces behind the development of ultra-sensitive terahertz technology in the last decades [63].

Although many important scientific and engineering milestones have been achieved, practical limitations of size, weight, power and technological readiness have prevented integrating more than a few array elements on space-based instruments at submillimeter wavelengths [14]. Furthermore, the extreme sensitivity required by these instruments can not be achieved with integrated technology. Therefore, small focal plane ar-

rays of receivers coupled to quasi-optical systems have been used in space applications to achieve the required sensitivity and gain. The latest technological developments are starting to enable the integration of more elements on next-generation terahertz spacecraft. For example, the most recent room-temperature frequency-multiplied sources are able to pump Schottky diode-based mixers up to 2-3 terahertz [64], [65].

One application for such multi-pixel instruments is cometary mapping: the Microwave Instrument on the Rosetta Orbiter (MIRO) [58] contained two heterodyne receivers (at 190 GHz and 562 GHz) that probed Comet 67P/Churyumov-Gerasimenko. The outgassing rates from the nucleus of the comet could be determined using MIRO but mapping of the comet was impossible before it rotated significantly, due to the single-pixel design. To allow mapping of comets, a dual-band 16-pixel instrument, COMETS, is being developed at the Jet Propulsion Laboratory [66]. Details on the development of the lens antennas for this instrument are given in Appendix C.

A new enabling technology is the advent of CubeSats: satellites with a mass below 10 kg that cost in the order of several tens of millions of dollars (compared to billions of dollars!) with five-year mission duration [67]. The Venus Atmospheric Sounder with Terahertz (VAST) has been proposed [68] as a submillimeter-wave spectrometer on a small satellite. A recent sub-orbital flight demonstration with a 183 GHz CMOS-InP receiver and 570 GHz CMOS and GaAs Schottky mixer has demonstrated limb-sounding of the atmosphere in a size that is compatible with the CubeSat limitations [69]. Given the limited available space on CubeSats, reflectors are too bulky to integrate. Therefore, new, compact approaches to wide-angle beam steering are required.

1.2 Sparse Phased Arrays

The applications outlined in Section 1.1 require high-gain beams that can be scanned over a certain field of view in a wide bandwidth. Below 100 GHz, significant maturity in integrated technology exists to create large, fully-sampled phased arrays. Above 100 GHz, only small arrays with low-to-moderate gains have been demonstrated. This observation has two causes: on the one hand (integrated-circuit) technology becomes less efficient at higher frequencies (the well-known “terahertz gap”), such that further integration reaches bottlenecks in terms of power, temperature or packaging. On the other hand, applications which have traditionally been drivers of terahertz technology, such as astronomy, demand the most sensitive instruments (e.g. SIS-, HEB- or Schottky-based). For these systems, either the local oscillator (LO) multiplication chain’s size is larger than the radio frequency (RF) wavelength [70], [71], or it suffers high losses in the LO distribution network [71].

Therefore, at submillimeter-waves the only realistic scanning antenna architecture for high-gain beams has been the use of quasi-optical systems (reflectors) combined with bulky mechanical scanners [55], [61], [62]. In order to achieve more compact

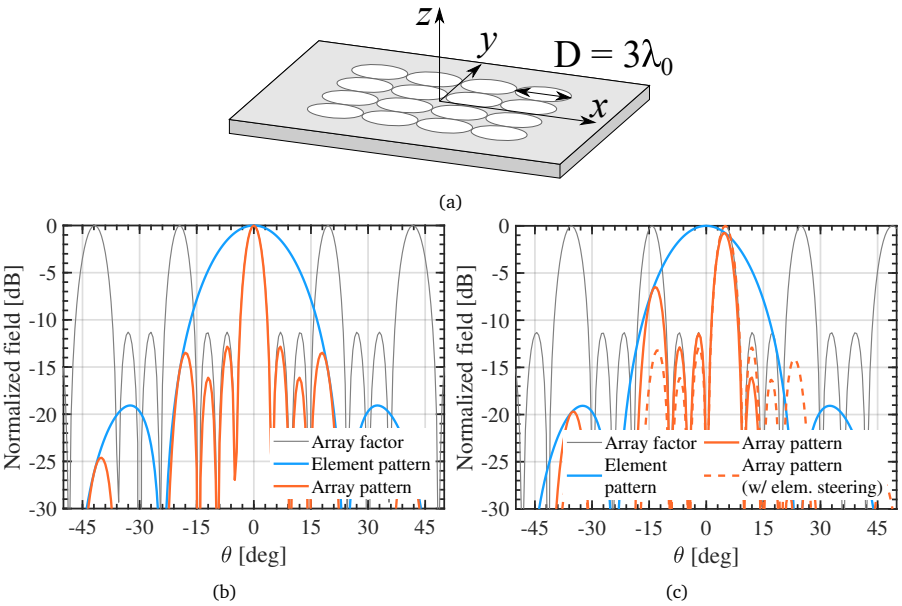

Fig. 1.2: An example of a limited-scan array configuration: A 4×4 phased array of circular, uniform current distributions in a semi-infinite ground plane (a) geometry and radiation patterns scanning to (b) broadside and (c) $5°$. The dashed line shows the array pattern when the element pattern is also steered towards $5°$.

systems, it is necessary to develop integrated beam steering antenna architectures. The challenge in developing such architectures are the requirements for typical space applications: large steering angles ($\pm 25°$) from large apertures (i.e., a directivity larger than 40 dBi) and wide bandwidths (larger than 10%).

An alternative to reflector systems consists of increasing the spacing between array elements: sparse phased arrays. These arrays allow scanning over limited angular ranges, as long as the grating lobes are properly attenuated by the element pattern [72]. Therefore, antenna array elements larger than typical patches or dipoles are required. As an example, we can consider a phased array of 4×4 circular uniform current distributions with a diameter of $D = 3\lambda_0$ and period $p = D$ in a ground plane, schematically shown in Fig. 1.2a. For broadside operation, the grating lobes in the array factor are clear and shown in Fig. 1.2b. The grating lobes are suppressed by the directive element pattern and the array pattern has sidelobe levels around -13 dB. When scanning to a small angle of $5°$ (Fig. 1.2c), the grating lobe appearing around $\theta = -15°$ is not suppressed well by the element pattern, resulting in a sidelobe level of the array pattern of around -6 dB. Furthermore, the scan loss is associated with the roll-off of the element pattern. In Fig. 1.2c it can be seen to be around 1 dB for $5°$ scanning. These are a fundamental limitations of limited-scan arrays which are caused by the inability to scan the element pattern. Nevertheless, such arrays are able

to produce high-gain beams with a reduced number of elements and are useful in applications that require only small-angle scanning.

Limited-scan arrays have been shown in the microwave regime by using leaky-wave (LW) feeds [73], [74] and subarray techniques [75], [76]. However, both the bandwidth (<5%) and the beam steering angles ($< 5^\circ$) are small or they suffer from high distribution network losses. At microwave frequencies, the use of phased lens arrays with large spacing has been proposed for astrophysical applications [77]. Small lens phased arrays with limited scanning ranges have also been developed in microwaves [78]–[80]. Specifically, it was anticipated in [80] that, in order to extend the otherwise very limited scanning capabilities, one would need to mechanically or electronically manoeuvre feed elements. More recently, the communications industry has also started to move in that direction; more patents are being published utilizing array of lenses with specific applications for communications in the Ka band [81]–[84].

In this thesis, we extend the scanning capabilities of lens phased arrays by introducing a mechanical shift of the feed relative to the lens. This results in the scanning of the element pattern, thereby eliminating the fundamental limitation of limited-scan arrays and enabling a wide scanning lens phased array. For the example of a 4×4 array of circular current distributions, if the element pattern would be able to scan along with the array factor, the improvement in SLL and scan loss can be appreciated in Fig. 1.2c (dashed line).

1.3 Scientific Contributions in this Thesis

The work described in this thesis has resulted in eight journal papers (two still in preparation) and 24 conference contributions. These contributions are listed on Page 193. The main scientific contributions in this thesis are listed below, categorized as Theory **[T]**, Antenna Design **[A]** or Demonstration of Lens Arrays **[D]**.

Theory

[T1] The Scanning Lens Phased Array antenna architecture is introduced: a wideband, scalable, hybrid electro-mechanical, very sparse phased array of lens antennas that can achieve beam steering of a highly directive beam (>30 dBi) over a field of view of $\pm 25^\circ$. Based on a study of this lens array architecture, the requirements of the constituting lens antenna elements are derived and the performance of such arrays is given.

[T2] To enable the analysis of electrically small dielectric lens antennas, which could be the elements in a lens phased array, we have applied the Fourier Optics methodology in reception to lens antennas that are an order of magnitude smaller than before ($\approx 2\lambda_0$).

[T3] Such small lenses can be illuminated efficiently with resonant leaky-wave antennas. However, for such small lenses, the surface of the lens will be in the near

field of the feed. We therefore show that the near field of leaky-wave resonant antennas radiating into a dense medium can be locally represented as a spherical wave in a certain solid angle around broadside when an accurate definition of the phase center is used. The near field in this solid angle can be efficiently evaluated via the integration of the spectral Green's function along the Steepest Descent Path (SDP). This approach is also valid for lens antennas with very low dielectric permittivity. From the propagating leaky-wave modes in the structure, we derive closed-form expressions for the elliptical lens shape that is efficiently illuminated by such feeds.

Antenna Design

[A1] We have developed a wider-bandwidth, more efficient resonant leaky-wave lens feed with annular corrugations in the ground plane. The corrugations significantly reduce the impact of the spurious TM_0 leaky-wave mode in all planes over a wide bandwidth while reducing assembly complexity compared to previous methods. The lens antenna achieves an aperture efficiency higher than 80% over a bandwidth of 2:1. A 3 cm diameter lens antenna with such a feed is designed at 110-220 GHz and demonstrated in the WR-5 band (140-220 GHz).

[A2] We have developed a wideband, leaky-wave lens feed that uses multiple modes to radiate a "top hat" (i.e., uniform) pattern into a silicon lens. A leaky-wave analysis of this multi-mode structure is presented and a submillimeter-wave lens antenna prototype ($D = 9.2\lambda_0$) with this feed has been demonstrated at 550 GHz.

[A3] We have developed a wideband matching layer for shallow silicon lens arrays at terahertz frequencies. The matching layer consist of frusta (truncated pyramids) that provide a smooth transition between the silicon lens and free space. The performance of this matching layer is evaluated around 500 GHz and compared to a conventional quarter-wavelength parylene-C matching layer.

[A4] We have developed a dual-band leaky-wave lens feed that operates at 210-240 and 500-580 GHz simultaneously. The lens was designed to be used in a focal-plane array under a reflector and achieves equal and overlapping beams at both frequencies for cometary mapping applications.

Demonstration of Lens Arrays

[D1] The first demonstration of high-gain dynamic beam steering with a scanning lens phased array is presented. We have developed a 4-element linear array of lens antennas ($D = 6\lambda_0$) at WR-10 (75-110 GHz) fed by the leaky-wave feed with corrugated ground plane (**[A1]**). We have designed an electronic phase-shifting mechanism that is able to accurately control the phase of each antenna at WR-10. We have designed a measurement setup and over-the-air calibration method

which we have used to characterize the performance of the array. This antenna achieves a gain of >30 dBi with scan angles up to $\pm 20^\circ$ and low grating lobe levels.

[D2] We have demonstrated a seven-element coherent lens array at submillimeter waves (450-650 GHz). The lenses are excited in-phase from a single source by using a novel quasi-optical transmit-array power distribution architecture.

1.4 Outline of this Thesis

This thesis consists of 11 chapters, divided in three parts, and three appendices. In Part I, a very sparse lens phased array architecture, the Scanning Lens Phased Array, is introduced and general design guidelines are derived. Furthermore, the methodology used throughout this thesis for the analysis of lenses in reception is introduced. The last chapter of Part I concerns the analysis of (very) small lenses which are in the near field of the leaky-wave feed.

In Part II, two leaky-wave feeds that have been developed in the framework of this thesis are discussed in detail. Furthermore, a wideband matching layer for shallow silicon lens arrays is presented. In Chapter 5, a novel, wideband (2:1) approach to suppressing the TM_0 mode in resonant leaky-wave antennas using annular corrugations in the ground plane is introduced, analyzed and validated with a 180 GHz prototype. In Chapter 6, a leaky-wave feed supporting the propagation of five leaky-wave modes is presented. Such a feed achieves high aperture efficiency illumination (>80%) of a silicon lens over a wide bandwidth (>35%). A demonstration of this feed is presented at 550 GHz. In Chapter 7, a broadband, lossless matching layer for shallow silicon lens arrays at terahertz frequencies is presented, consisting of frusta (truncated pyramids) that provide a smooth transition between the silicon lens and free space. The performance of this matching layer is evaluated at 500 GHz and compared to a conventional quarter-wavelength parylene-C matching layer.

In Part III, two of the feeds introduced in Part II are used as array elements to demonstrate the scanning lens phased array concept that was developed in Part I. A four-element linear array at millimeter waves (75-110 GHz) is demonstrated in Chapter 8. The design, fabrication, calibration and measurement process are described in detail. A seven-element coherent lens array at submillimeter waves (450-650 GHz) is demonstrated in Chapter 9. The lenses are excited in-phase from a single source by using a quasi-optical transmit-array power distribution architecture that is proposed, simulated and measured. The analysis methodology in reception, along with details on fabrication, assembly measurements and results are presented for this prototype.

Conclusions of this thesis are drawn in Chapter 10 regarding the analysis, design and demonstration of lens phased arrays. Future research avenues are discussed in Chapter 11.

The appendix to this thesis presents some miscellaneous results that were not published in the literature before. In Appendix A, the space- and leaky-wave field contributions of leaky-wave antennas are given, which is an extension to the result in Chapter 4. In Appendix B, some closed-form integrals that are useful for the analysis of antennas fed by a double-slot iris are presented. In Appendix C, a submillimeter-wave dual-band leaky-wave lens feed is introduced covering 210-240 GHz and 500-580 GHz simultaneously. The lens is designed to be used in a focal-plane array under a reflector to achieve equal and overlapping on-sky beams for cometary mapping. Simulated results of the performance are presented for a single lens element along with the fabrication status.

Part I
Analysis and Design of Lens Phased Arrays

Chapter 2
Scanning Lens Phased Array

In this Chapter, we describe a hybrid electromechanical scanning lens antenna array architecture suitable for the steering of highly directive beams at submillimeter wavelengths with a field of view (FoV) of $\pm 25^{\circ}$. The concept relies on the combination of electronic phase shifting of a sparse array with a mechanical translation of a lens array. The use of a sparse phased array significantly simplifies the RF front-end (number of active components, routing, thermal problems), while the translation of a lens array steers the element patterns to angles off-broadside, reducing the impact of grating lobes over a wide FoV. The mechanical translation required for the lens array is also significantly reduced compared to a single large lens, leading to faster and low-power mechanical implementation. We demonstrate that the scanning lens phased array must be fed with high aperture aperture efficiency in order to reduce the impact of the grating lobes. Such feeds are investigated in Part II.

2.1 Introduction

With the support of the European Union under the ERC starting under Grant LAA-THz-CC (639749) granted in 2015, we proposed the use of coherent lens arrays integrated with LW antennas and mechanical piezoelectric motors to solve the array integration problem at submillimeter wavelengths [85]. This dynamic beam steering architecture combines low mechanical complexity (reduced mass with respect to translating a single lens) with a greatly reduced number of phase shifters. The geometry of the proposed array based on a LW feed is shown in Fig. 2.1. The array is composed of a sparse array of active RF array elements distributed over the whole array aperture coupled to a layer of actuated lenses (one per array element). The single layer of lenses can be translated mechanically relative to the ground plane, using an implementation similar to [86], to achieve element pattern scanning, while the active RF phase shifters cause array factor (AF) scanning. The grating lobes resulting from the array's sparsity are attenuated by the directive element patterns of the lenses.

2.2 Design Guidelines

In this section, we describe the main design parameters that impact the performance of the proposed scanning lens-phased array architecture: the electronic shifting affecting the array factor, the mechanical phase shifting impacting the element pattern and the

Parts of this Chapter have been published in **[J1]**.

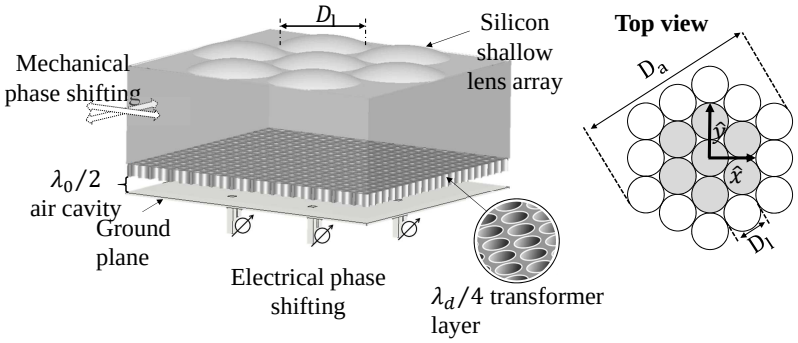

Fig. 2.1: Geometry of the proposed scanning lens-phased array that uses a combination of mechanical phase shifting of a silicon lens array and electronic phase shifting in the feeds. The lens array is fed by a multi-mode LW fed that uses a synthesized quarter-wavelength transformer on top of a resonant air cavity. The inset shows the lens array layout with a circular aperture of D_a and 19 lenses of diameter D_l. The prototype array consists of seven elements (shaded).

requirements this gives for the field radiated by the lens feed.

To describe these guidelines, we consider a circular array aperture of diameter $D_a = 100\lambda_0$, which can theoretically provide up to 50 dBi of directivity, a number that is in line with future needs of security [55] and planetary applications with Cubesats or SmallSats [68]. The considered aperture is filled with a hexagonal arrangement of 19 circular lenses as shown in the inset of Fig. 2.1. In Section 2.3, the hexagonal array lattice is compared to other lattices. We consider silicon ($\varepsilon_r = 11.9$) lenses with a diameter $D_l = 20\lambda_0$, which is a reasonable size for the aforementioned applications.

2.2.1 Electronic Phase Shifting: Array Factor

A phase shift is applied to each array element, which leads to an array factor (AF) that is associated with the periodicity of the array and with this, the beam can be steered electronically. The number of active elements is reduced by a factor $(2D_l/\lambda_0)^2$ compared to a fully sampled array. It is well known that if the periodicity of the array is larger than $\lambda_0/2$, grating lobes can appear at angles θ_g^n. The electronic phase shift enables the steering of the array factor (AF). Since the AF has multiple beams due to the grating lobes, it is only necessary to scan the AF in the angular region from broadside until the first grating lobe θ_g^1. This is because the mechanical translation of the lens allows the array to scan to larger angles than θ_g^1 by steering the element pattern toward the different grating lobes θ_g^n.

As will be shown in Section 2.3, grating lobes appear in the array factor of the considered hexagonal lattice at angles $\theta_g^n = \arcsin\left(n2\lambda_0/(D_l\sqrt{3})\right)$ in the $\phi = 0°$ plane, which is approximately every $3.3°$, see Fig. 2.2a. Therefore, the overall electronic phase shift required to scan the main beam of the lens phased array to any angle θ_s is

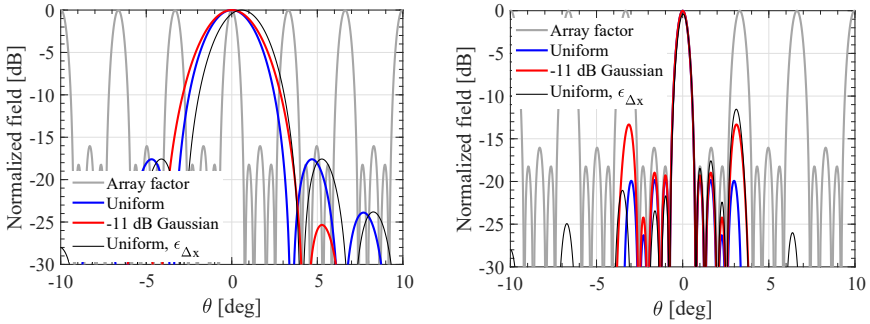

Fig. 2.2: (a) Broadside array factor and element patterns of the 19-element hexagonal array shown in the inset of Fig. 2.1 with $D_l = 20\lambda_0$ and uniform amplitude (blue) or -11 dB Gaussian taper (red) apertures. The impact of the mechanical tolerance $\epsilon_{\Delta x} = 58\mu m$ and $N_{RF} = 5$ is shown in black for a uniform aperture; (b) Array pattern for the same cases as in (a).

limited to

$$\psi_s(\theta_g^1) = \sin(\theta_g^1)k_0(D_a - D_l) = 4\pi(N_{RF} - 1)/\sqrt{3} \approx 9.2\pi \tag{2.1}$$

with $N_{RF} = D_a/D_l$. By contrast, a fully sampled array of the same size requires a phase shift of $2\pi D_a \sin(30°)/\lambda_0 = 100\pi$. Thus, the lens array reduces the required phase shift by a factor of more than 10.

2.2.2 Mechanical Phase Shifting: Element Pattern

The number of lens element pattern beams that are steered towards θ_s is given by:

$$N_l = \frac{\theta_s}{\Delta\theta_e} \tag{2.2}$$

where $\Delta\theta_e = \lambda_0/D_l$ is the beamwidth of the element pattern. For a single free-standing lens with the same size as the lens array, the number of beams scanned are $N_l^f = \theta_s/\Delta\theta_a$ with $\theta_a = \lambda_0/D_a$, an increase by a factor N_{RF}.

The required mechanical translation of an integrated lens scanning N_l beams is:

$$\Delta x = N_l \lambda_d f_\# \tag{2.3}$$

where λ_d is the wavelength in the lens medium and $f_\#$ is the lens' focal length to diameter ratio. This is a reduction by a factor $N_{RF}\sqrt{\varepsilon_r}$ compared to a free-standing lens of the same diameter and $f_\#$.

The tolerance of the mechanical position $\epsilon_{\Delta x}$ is dictated by the full array's angular

beam width $\Delta\theta_a = \lambda_0/D_a$. This can be expressed as follows:

$$\epsilon_{\Delta x} = \frac{\Delta\theta_a}{\Delta\theta_e}\lambda_d f_\# = \frac{\lambda_d f_\#}{N_{RF}} \tag{2.4}$$

The beam steering capability of the phased lens array is dictated by the scan performance of the single element. To limit the spillover loss inside the lens while being translated, we impose that $|\Delta x| \leq D_l/4$. From Eqs. (2.2) and (2.3), the scan angle is then limited to:

$$\theta_s \leq \frac{\sqrt{\varepsilon_r}}{4f_\#} \tag{2.5}$$

Based on the considerations in Eqs. (2.2), (2.3) and (2.5), the lens array will have better lens steering performance, a lower profile and a significant reduction in mechanical displacement (a factor $N_{RF}\sqrt{\varepsilon_r}$) compared to a free-standing lens. However, the tolerance on the mechanical displacement becomes a factor $N_{RF}\sqrt{\varepsilon_r}$ stricter.

For the considered example, we need to scan $N_l = 8.7$ beams to achieve $\theta_s = 25°$ and the $f_\#$ should be lower than 2 to limit the spill-over losses. In this case, the required displacement to reach this is $\Delta x \leq 5\lambda_0$. The effect of the tolerance of the mechanical position $\epsilon_{\Delta x} \approx 0.1\lambda_0$ is illustrated in Fig. 2.2 for our example array. Fig. 2.2a shows the element pattern for broadside scanning $(\theta_s = 0°)$ and a black line for a lens displaced by $\epsilon_{\Delta x}$. The resulting array pattern is shown in Fig. 2.2a for both cases. Note that the pattern of the displaced lens array still points to broadside, but with a slightly lower directivity, in this case it is reduced by around 0.4 dB. Note that N_{RF} will impact the directivity loss due to $\epsilon_{\Delta x}$: the larger N_{RF}, the smaller the loss in directivity. Moreover, as shown in Fig. 2.2a, the side lobes are strongly impacted by the shift, increasing from -20 dB to -12 dB.

For submillimeter wavelength applications, the maximum translation Δx required for such lens arrays can be in the order of few millimeters. It is therefore possible to implement this using piezoelectric motors such as in [86]. The accuracy of the position of such motors are in the nanometers, much smaller than $\epsilon_{\Delta x}$.

2.2.3 Requirements on the Lens Feed

In Fig. 2.2a, the element radiation pattern from a uniform circular aperture of diameter $D_l = 20\lambda_0$ is superimposed on the 19 elements hexagonal array factor. It is evident that the highest resulting grating lobe of the combined pattern is around -19 dB, see Fig. 2.2b. The level of this first grating lobe is related to the width of the main beam of the element pattern. Therefore, this level will be the lowest when the array element has a uniform aperture illumination.

A comparison of the patterns resulting from an array illuminated with uniform circular apertures and with Gaussian apertures of -11 dB edge taper is shown in Figs. 2.2a

and 2.2b. For the Gaussian case, the main beam of the element pattern is wider and the grating lobes of the combined pattern increase to -12 dB, which may still be acceptable for many applications. For instance, the use of synthetic apertures via interferometry leads to grating lobe levels of -6.6 dB [16]. However, what it is evident from this figure is that the grating lobe level of the array pattern improves with the uniformity of the array elements. Therefore, lens feeds with very high aperture efficiency are needed to achieve low grating lobe levels. Such lens feeds are discussed in Part II.

2.3 Array Lattice

The choice of array lattice is primarily dictated by the shape of the available array area, A_a. The N array elements are considered circular here, which is the shape of a truncated lens, with diameter D_l and area $A_l = \pi(D_l/2)^2$. We define the lattice efficiency η_L as

$$\eta_L = \frac{NA_l}{A_a} \tag{2.6}$$

The lattice efficiency is an important figure of merit, because it limits the aperture efficiency (and thus gain) of a lens array in a given area. Note that the lattice efficiency is limited by the chosen circular element shape. For free-form lens shapes, the $\eta_L = 1$ is possible. For this analysis, we consider rectangular, triangular and hexagonal sampling of the array area.

2.3.1 Rectangular lattice

For a rectangular array area that is sampled by a uniform rectangular lattice (see Fig. 2.3a), the lattice efficiency follows from Eq. (2.6): $\eta_L = \pi/4 \approx 0.785$ independently of the number of elements. Note that rectangular lattices do not exist when N is prime, except the trivial $1 \times N$ array. The efficiency of the rectangular lattice is shown in Fig. 2.4, with the squares indicating the special case of a square lattice.

The grating lobes that arise in a sparse rectangular array [87, p. 85] occur at

$$U_g^{(n)} = U_{sc} + \frac{n\lambda_0}{D_l}, V_g^{(m)} = V_{sc} + \frac{m\lambda_0}{D_l} \tag{2.7}$$

in the $\{U, V\}$-plane and $U_{sc} = \sin(\theta_{sc})\cos(\phi_{sc})$, $V_{sc} = \sin(\theta_{sc})\sin(\phi_{sc})$ referring to the scan angle. Grating lobes thus appear in a regular rectangular lattice in the $\{U, V\}$-plane spaced λ_0/D_l apart. As an example, the array factor of a 4×4 array scanned to broadside with $D_l = 3\lambda_0$ is shown in Fig. 2.3d.

2.3.2 Triangular lattice

A triangular lattice arrangement [88], [89] is shown in Fig. 2.3b. In general, there are N_x rows and N_y columns where each column is alternated between being aligned with the first column or offset by $D_l/2$. The rows are compressed by a factor $\sqrt{3}/2$.

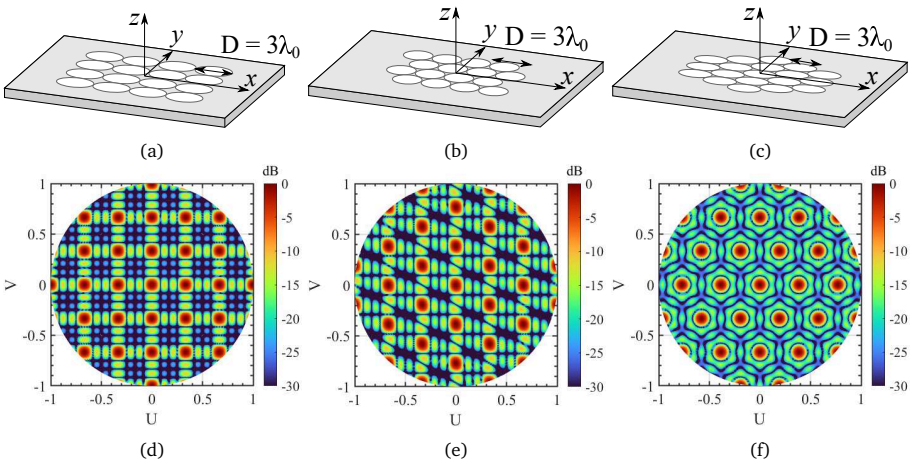

Fig. 2.3: (a) Square, (b) triangular and (c) hexagonal lattice sampling and corresponding array factors in (d), (e) and (f).

The rectangle containing the array has area

$$A_a = D_l^2 \left(N_x + \frac{1}{2} \right) \left(1 + (N_y - 1) \left(\frac{1}{2} + \frac{\sqrt{3}}{4} \right) \right). \tag{2.8}$$

The lattice efficiency is shown in Fig. 2.4 and $\eta_L \to 0.8418$ when $N \to \infty$. The efficiency exceeds that of the rectangular lattice when $N \geq 64$.

The grating lobes in a triangular lattice also appear in a triangular lattice in the $\{U, V\}$-plane, as illustrated in Fig. 2.3e for an array with $N_x = 4$, $N_y = 4$ and $D_l = 3\lambda_0$. The first grating lobe is at a distance $|\theta_g - \theta_{sc}| = \arcsin(2\lambda/(\sqrt{3}D_l))$. Thus, the first grating lobes are further away than in a rectangular lattice, due to the closer spacing of the elements, but there are more of them (six for the triangular lattice versus four for the rectangular lattice).

2.3.3 Hexagonal lattice

The hexagonal lattice, shown in Fig. 2.3c, is characterized by a central element surrounded by N_r rings of elements such that the array fits in a regular hexagon. The total number of elements is given by $N = 1 + 3N_r(N_r + 1)$, thus the number of elements in such an array is restricted to $N = \{1, 7, 19, 36...\}$. The circle that circumscribes the hexagonal tiles has a radius $R = D_l(N_r + 1/2)$ and the lattice efficiency, shown in Fig. 2.4, is:

$$\eta_L = \frac{N}{4\left(N_r + \frac{1}{2}\right)^2} \tag{2.9}$$

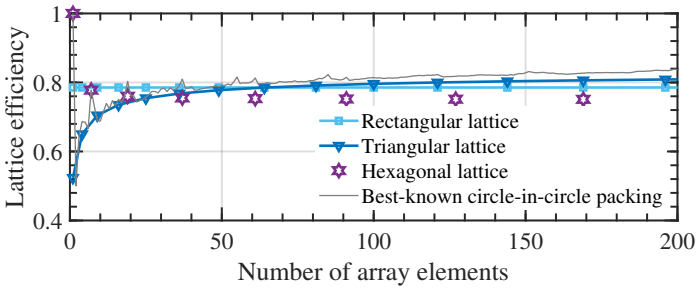

Fig. 2.4: Lattice efficiency for the geometries shown in Fig. 2.3.

An analysis of the grating lobes of such lattices was given in [90] and a closed-form expression of the array factor in [91]. Grating lobes appear in a hexagonal lattice in the $\{U, V\}$-plane, although a 90° rotation of this lattice relative to the array lattice appears. The grating lobes are spaced at $2\lambda_0/(\sqrt{3}D_l)$ in the $\{U, V\}$-plane, as with the triangular lattice. This is expected, since the density of elements is the same. The grating lobes of a 19-element array with period $p = D_l = 3\lambda_0$ are shown in Fig. 2.3f.

Optimal sampling of a circle by N circular apertures is an open mathematical problem with proven solutions only for several N. The current best-known packing strategies and associated lattice efficiency are given in [92]. For completeness, the lattice efficiency of these solutions is also included in Fig. 2.4. [1]

Overall, a lattice efficiency close to 80% can be achieved for any desired number of array elements. Therefore, the main considerations when choosing the lattice are the number of elements and the shape of the desired aperture. For small-to-moderate arrays ($N < 50$), a rectangular (square) lattice is almost always the most efficient, with the resulting aperture being rectangular (square). For large arrays ($N \geq 50$), the best-known circle-in-circle packing solution leads to the highest lattice efficiency and a circular array aperture. However, the resulting array positions in the lattice are generally not very symmetric and may therefore be more complex in terms of phasing. The triangular lattice is nearly as efficient for such large arrays and supports a square aperture for a limited number of N.

[1] Notably, the most efficienct 19-element packing is *not* given by the intuitive hexagonal lattice.

Chapter 3
Lens Analysis Methodology and Definitions

In this Chapter, we describe the Fourier Optics (FO) methodology for the analysis of dielectric lenses in reception that is used throughout this thesis to simulate the performance of lens antennas. Most of the analysis methodology described here was presented before in [93, Ch. 2] and successfully applied in, among others, [20], [94], [95]. A free software tool that implements the FO procedure was described in [96].

Since the FO methodology has been applied throughout this thesis to obtain the performance of lens antennas, we present this method here. Specifically, we present the analysis of a single lens antenna in reception and the analysis for two lenses facing each other. In Chapter 9, the method is extended to the analysis of a single lens facing an array of lenses.

3.1 Single Lens Antenna Analysis in Reception

In the FO approach, the power received by an antenna under plane-wave illumination is calculated. Although the method can be applied to any antenna, the application in this thesis is the elliptical lens antenna, schematically shown in Fig. 3.1a: a dielectric lens is fed by a leaky-wave waveguide feed. The lower focus of the lens coincides with the phase center of the lens feed, which is below the ground plane for the leaky-wave feeds considered in this thesis (for details on this, see Chapter 4). The lens is illuminated by a plane wave $\vec{E}_{pw}$ propagating along $\hat{k}_{pw}$ and we would like to calculate the power received by a load Z_L^{Rx} connected to the single-moded waveguide terminals AA'.

This problem can be analyzed in reception by using the equivalent Thévenin circuit of Fig. 3.1b. The antenna impedance is Z_A and the load impedance is Z_L^{Rx} is connected at the terminals AA'. The voltage in this equivalent circuit, $V_{oc}(\hat{k}_{pw})$, is the open-circuit voltage at AA' induced by the incident plane wave. The received power, P_{Rx}, is given by the real power in the load:

$$P_{Rx}(\hat{k}_{pw}) = \frac{1}{2}\left|\frac{V_{oc}(\hat{k}_{pw})}{Z_A^{Rx}+Z_L^{Rx}}\right|^2 \cdot \mathrm{Re}\{Z_L^{Rx}\} \tag{3.1}$$

By identifying the term $\eta_m = 4R_L^{Rx}R_A/|Z_A+Z_L^{Rx}|^2$ as the impedance matching efficiency, the received power under impedance-matched conditions can be separated

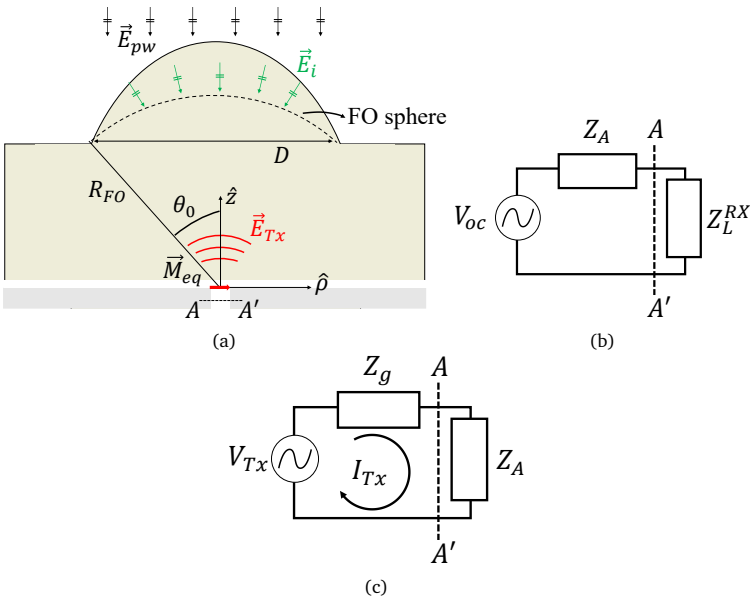

Fig. 3.1: (a) Geometry used for the analysis of the single lens antenna in reception. Equivalent Thévenin circuits of (b) the lens antenna in reception and (c) in transmission.

from this efficiency as follows:

$$P_{Rx}(\hat{k}_{pw}) = \frac{\left|V_{oc}(\hat{k}_{pw})\right|^2}{8R_A^{Rx}}\eta_m. \tag{3.2}$$

An equivalent Thévenin circuit of the same antenna operating in transmission is given in Fig. 3.1c. A voltage generator V_{Tx} provides a current I_{Tx} through the generator impedance Z_g and antenna impedance Z_A. Thus, the radiated power is $P_{Tx} = |I_Tx|^2 R_A/2$. By re-arranging $R_A = 2P_{Tx}/|I_Tx|^2$ and substituting into Eq. (3.2), we obtain:

$$P_{Rx}(\hat{k}_{pw}) = \frac{\left|V_{oc}(\hat{k}_{pw})I_{Tx}\right|^2}{16P_{Tx}}\eta_m. \tag{3.3}$$

The term $V_{oc}I_{Tx}$ can be calculated as the reaction integral between the surface currents $\{\vec{J}_i, \vec{M}_i\}$ induced by the incident field $\{\vec{E}_i, \vec{H}_i\}$ and the field radiated by the antenna in transmission, $\{\vec{E}_{Tx}, \vec{H}_{Tx}\}$, over a closed surface S surrounding the antenna:

$$V_{oc}(\hat{k}_{pw})I_{Tx} = \iint_S \left(\vec{H}_{Tx}\cdot\vec{M}_i(\hat{k}_{pw}) - \vec{E}_{Tx}\cdot\vec{J}_i(\hat{k}_{pw})\right)\mathrm{d}A \tag{3.4}$$

Equations (3.2) and (3.4) can be used to calculate the received power of any an-

tenna. However, for the specific case of the elliptical lens antenna, Eq. (3.4) can be simplified. Specifically, we choose the surface $S = S_{FO}$ as a sphere centered at the phase center of the feed to ensure that its surface normal satisfies $\hat{n}_S = \hat{k}_{Tx}$. The induced equivalent currents are $\vec{M}_i = -\hat{n}_S \times \vec{E}_i$ and $\vec{J}_i = \hat{n}_S \times \vec{H}_i$. The integral is then:

$$V_{oc}(\hat{k}_{pw}) I_{Tx} = \iint\limits_{S_{FO}} \left(\frac{1}{\zeta} \vec{E}_{Tx} \cdot \vec{E}_i(\hat{k}_{pw}) - \zeta \vec{H}_{Tx} \cdot \vec{H}_i(\hat{k}_{pw}) \right) \mathrm{d}A \tag{3.5}$$

If the propagation direction of the incident field on S_{FO} can then be approximated as $\hat{k}_i \approx -\hat{n}_S$ for a generic $\hat{k}_{pw}$, then $\zeta \vec{H}_{Tx} \cdot \vec{H}_i \approx -\vec{E}_{Tx} \cdot \vec{E}_i / \zeta$ and Eq. (3.5) becomes:

$$V_{oc}(\hat{k}_{pw}) I_{Tx} = \frac{2}{\zeta} \iint\limits_{S_{FO}} \vec{E}_{Tx} \cdot \vec{E}_i(\hat{k}_{pw}) \, \mathrm{d}A \tag{3.6}$$

which is the integral given in [20].

The field radiated by the transmitting antenna, $\vec{E}_{Tx}$, must be calculated over S_{FO}. When the radius R_{FO} of this sphere is large, the far-field of the feed can be considered. However, for small lenses, the near field of $\vec{E}_{Tx}$ must be considered. This near field can be calculated with the spectral Green's function, as in Chapter 4, or by using (commercial) full-wave solvers.

The radiation pattern of a lens can be calculated by varying $\hat{k}_{pw}$ and the aperture efficiency of the lens is defined as the maximum ratio of received power to the power in the plane wave incident on the lens area:

$$\eta_{ap} = \max \left\{ \frac{P_{Rx}(\hat{k}_{pw})}{P_{pw}} \right\} \tag{3.7}$$

where $P_{pw} = A_l \left| \vec{E}_{pw} \right|^2 / (2\zeta_0)$ is the power incident on the lens with projected area A_l.

Scanned beams from a lens are achieved by displacing the feed laterally, away from the focus, over a distance $\Delta\rho$. The radiation patterns and aperture efficiency are calculated in the same manner as the aligned case. Note, however, that the FO sphere is no longer centered above the feed. As such, the field $\vec{E}_{Tx}$ should be calculated over a surface that is not spherical when seen from the phase center.

3.2 Lens-to-lens Coupling Analysis in Reception

Next, we calculate the power received by a lens antenna when it is illuminated by another lens antenna as illustrated in Fig. 3.2. In this case, the bottom lens B is con-

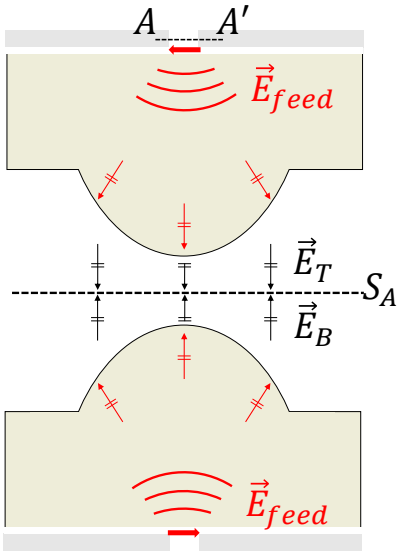

Fig. 3.2: Geometry used for the analysis of the lens-to-lens coupling between two lens antennas.

sidered as the transmitter and the top lens T as the receiver. Although the same equations Eqs. (3.3) and (3.5) hold, it is useful to move the reaction surface S to the shared aperture of the lenses $S = S_A$ since $\hat{n}_S = \hat{k}_B = -\hat{k}_T$ for center-fed elliptical lenses and Eq. (3.6) can be used:

$$V_{oc}(\hat{k}_{pw}) I_{Tx} = \frac{2}{\zeta_0} \iint_{S_A} \vec{E}_T \cdot \vec{E}_B \, \mathrm{d}A \tag{3.8}$$

The fields $\vec{E}_T$ and $\vec{E}_B$ are calculated as the geometrical-optics propagation of the fields transmitted by the feeds inside the lens feed onto S_A.

In this case of two lenses facing each other, we define the coupling efficiency as the ratio of received power to transmitted power:

$$\eta_C = \frac{P_{Rx}}{P_{Tx}} \tag{3.9}$$

Note that P_{Tx} is the power radiated by the bottom feed into a semi-infinite medium.

Chapter 4
Near-Field Spherical Wave Formation in Resonant Leaky Wave Antennas

In this Chapter, we show that the near field of leaky-wave resonant antennas radiating into a dense medium can be locally represented as a spherical wave in a certain solid angle around broadside using an accurate definition of the phase center. The near-field in this solid angle can be efficiently evaluated via the integration of the spectral Green's function along the Steepest Descent Path (SDP). Beyond this solid angle, defined as the shadow boundary angle, a residual contribution due to the leaky-wave pole must also be added to fully describe the near field. It is found that this shadow boundary angle can be used to define the phase center and geometry of a truncated lens that couples well to leaky-wave antennas, even in electrically small-to-medium sized lenses and low-contrast cases. To demonstrate the applicability of the proposed study, we combine the SDP field calculation with a Fourier Optics methodology to evaluate the aperture efficiency and radiation patterns of small-to-medium sized lenses in reception. A truncated silicon lens with a diameter of only 4 free-space wavelengths is presented with almost 80% aperture efficiency. Excellent agreement with full-wave simulations is achieved, which demonstrates the accuracy of the proposed design and analysis methodology.

4.1 Introduction

Leaky-wave resonant antennas (LWA), also called Fabry-Pérot antennas, have been widely studied in the literature to increase the directivity from a small source by using a planar stratification consisting of a dielectric [97] or metallic [98] superstrate. Multiple demonstrations of these antennas have been shown at various frequencies up to the submillimeter wave spectral region [99]–[103]. A fundamental trade-off between the directivity and bandwidth of these antennas exists, which depends on the level of reflection between the cavity and superstrate [104], [105]. In the literature, shielded cavities [106] and the addition of lenses [20], [107] or phase correcting geometries [108], [109] have been proposed to increase the directivity of these classic geometries without compromising the bandwidth.

At mm- and sub-mm waves frequencies, when scanning to limited angles is required, there is an interest of developing sparse arrays to reduce the integration complexity

Parts of this Chapter have been published in **[J3]**.

[94], [110]–[112]. Leaky-wave antennas with overlapped feeds have been proposed for improving the performances of sparse arrays [73], [104], [113], [114] where sparse arrays with periodicities in the order of a free-space wavelength (λ_0), bandwidths smaller than 10% and scanning angles of at most 10° have been demonstrated. Larger periodicities will only come at the cost of even smaller bandwidths in such geometries. For example, sparse leaky-wave phased arrays with a period of $2\lambda_0$ will have less than 5% bandwidth as shown in [114]. In [94], [111], the use of leaky wave antennas with dielectric lenses was proposed to enable sparse arrays with large periodicity $(> 2\lambda_0)$, wide bandwidth (35%) and larger scanning angles up to $\pm 25^\circ$. One of the difficulties that arises in the design of such small size lenses or phase correcting structures in combination with resonant leaky wave feeds is the efficient evaluation of the leaky-wave near-field [94].

Most of the works in the literature on leaky-wave or Fabry-Pérot antennas consider only the far-field radiation patterns of the feed [20], [97], [104], [105], [115] and often make approximations on the solutions of the potentials in stratified media [97], [115]. For lenses that are small-to-medium in diameter (i.e., smaller than $\approx 15\lambda_0$, where λ_0 is the free-space wavelength) fed by leaky-wave feeds, as in the lens phased array application [94], [111], the lens surface is in the near field of the feed. The design of such lenses has previously been approached as a parametric optimization by combining Physical Optics with full-wave simulations [116] or full-wave simulations with optimization algorithms [107] for other phase correcting geometries.

Here, we describe a way to design such lenses without the need for time-consuming full-wave simulations. To achieve this, we derive the shape of the lenses directly from the propagation constants of the leaky-wave modes. For that purpose, we use a spectral-domain method to efficiently and accurately compute the near-field radiation patterns which, additionally, brings the needed physical insight. The spectral analysis decomposes the near field of these antennas into the summation of a branch contribution or space wave, that can be evaluated by an integration over the Steepest Descent Path (SDP) when a proper phase center is introduced, and multiple leaky-wave modal fields, associated with poles that are captured in the deformation into the SDP [117, p. 468].

The asymptotic decomposition of the near field in leaky-wave antennas was previously investigated in a different configuration, based on a single-mode leaky-wave slot antenna [118], where the phase center is stable and coincident with the feeding point of the antenna. It has also been applied to a very high contrast resonant leaky-wave antenna in [119] (equivalent to an air cavity with an infinite medium of $\varepsilon_r = 100$) as well as to other resonant leaky-wave antennas [120]–[122]. For a resonant LWA, the phase center is not coincident with the feeding point [123]. Moreover, in these later works no explicit link has been made between the space-wave near-field evaluation

and the phase center of the LWAs. Here, we will extend this analysis to the understanding of the formation of a clean spherical wave in the near field by making this link, also for low contrast cases, where the leaky wave poles lie far away from the real axis.

We show that the near field in resonant LW antennas is well modelled by a spherical wave in a solid angle Ω_{SB} around broadside emanating from the phase center located far below the ground plane. We find that, also for points close to the source, the space-wave contribution to the total field can be calculated by integration over the SDP when the reference system is chosen to coincide with the phase center of the antenna, located at Δz. Both the solid angle, Ω_{SB}, of the spherical-wave representation and the phase center can be defined with the knowledge of the shadow boundary angle defined by the SDP deformation angle.

The spectral analysis gives the physical insight in the formation of the local spherical wave and leads to the derivation of an analytical geometry of an ideal lens, with high aperture efficiency, which is defined using only the propagation constants of the main leaky-wave poles. Moreover, the SDP integration can then be efficiently combined with a Fourier Optics (FO) approach to calculate the aperture efficiency and radiation patterns of the lens-coupled leaky-wave antenna in reception [20], [96]. The combined method is computationally very fast and shows excellent agreement with full-wave lens simulations, removing the need for time-consuming parametric analyses as in [107], [116].

The rest of this chapter is structured as follows. Section 4.2 describes the geometry under consideration and introduces the near-field spectral approach. In Section 4.3, the near field is decomposed into the sum of an SDP contribution and (multiple) LW contributions. In Section 4.4, the phase center of LWAs is discussed, which brings physical insight into the decomposition of Section 4.3. In Section 4.5, we show that the near field can be considered a local spherical wave in the solid angle Ω_{SB} around broadside. The near field spherical wave representation is combined with an FO approach in reception in Section 4.6 to evaluate the lens efficiency and radiation patterns of electrically small lenses. Conclusions are drawn in Section 4.7.

4.2 Problem Statement

The physical phenomenon exploited in a standard resonant LWA is the excitation of a pair of nearly-degenerate TM_1 / TE_1 leaky-wave modes inside a resonant dielectric cavity [97], such as air, placed between a ground plane and a partially reflecting surface. These modes propagate radially by means of multiple reflections along the cavity, leaking at the same time energy into the infinite air medium. This effect increases the antenna's effective area and thus its directivity. In [103], it was shown that an enhancement in the bandwidth $\times$ directivity performance of a reso-

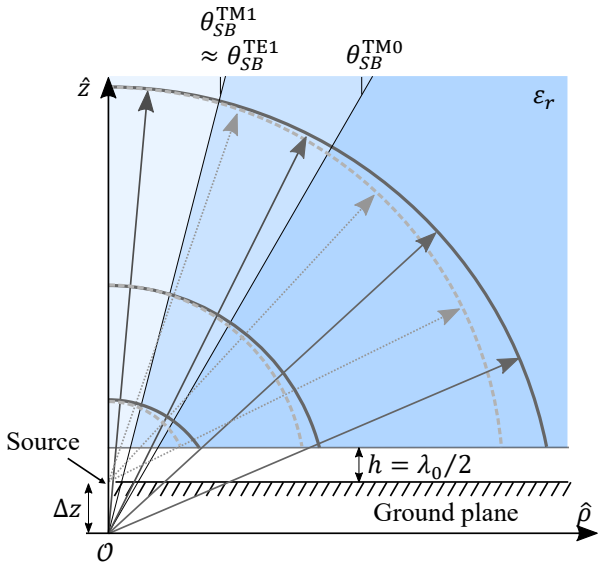

Fig. 4.1: Cross-section of the geometry considered in this contribution with a semi-infinite dielectric separated from a ground plane (containing the source) by a $h = \lambda_0/2$ air cavity. The origin of the reference system is Δz below the source. The shaded blue regions are separated by the shadow boundary associated with the leaky-wave modes. The solid and dashed semi-circles and associated arrows are centered at O and the source, respectively.

nant LWA can be achieved by using a resonant air cavity below a semi-infinite dense medium (the lens), as displayed in Fig. 4.1. When comparing the radiation of a LWA into a semi-infinite medium with a dense permittivity ε_r to a standard LWA with a partially-reflecting surface radiating into free space, both antennas present the same propagation constants and therefore same effective area, A_e. However, the LWA radiating into a dense medium achieves a ε_r-times higher directivity since the directivity is $4\pi A_e \varepsilon_r / \lambda_0^2$, where λ_0 is the wavelength at the center frequency f_0. One of the implications of this enhanced directivity is that the far-field region will be at a much further distance.

To illustrate this effect, we analyze the near field of the geometry shown in Fig. 4.1, consisting of a source located in an infinitely-extended ground plane and a lossless semi-infinite dielectric medium with relative permittivity $\varepsilon_r = 11.9$ (silicon) separated by a $h = \lambda_0/2$ air cavity. The origin of the reference system is taken at a distance Δz below the ground plane, since it is known that these kind of leaky wave antennas have the phase center below the ground plane [123]. The electric field at observation point $\vec{r}(\rho, \phi, z)$, located in the semi-infinite silicon, can be evaluated by resorting to a spectral Green's function representation [124]. The electric field radiated in the infinite medium by a magnetic current source located in the ground plane and, without

loss of generality, oriented along $\hat{y}$ can be expressed as:

$$\vec{e}(\vec{r}) = \frac{1}{4\pi^2}\int_0^{\infty}\int_0^{2\pi} \tilde{G}^{em}(k_\rho,\alpha)M(k_\rho,\alpha)\hat{y} \cdot e^{-jk_\rho\rho\cos(\alpha-\phi)}e^{-jk_z z}k_\rho \,\mathrm{d}\alpha\,\mathrm{d}k_\rho \tag{4.1}$$

with $\tilde{G}^{em}(k_\rho,\alpha)$ being the dyadic spectral Green's function for stratified media that gives the electric field at the top of the air cavity due to a magnetic current source, $k_z = (k_d^2 - k_\rho^2)^{1/2}$ with $k_d = k_0\sqrt{\varepsilon_r}$ the wavenumber in the infinite medium and $M(k_\rho,\alpha)$ the Fourier transform of the equivalent magnetic current of the source along $\hat{y}$. The cylindrical spectral coordinates are given from the Cartesian spectral coordinates by the transformation $k_x = k_\rho\cos\alpha$ and $k_y = k_\rho\sin\alpha$ and the cylindrical spatial coordinates are given by the transformation $x = \rho\cos\phi$, $y = \rho\sin\phi$, respectively. The spectral Green's function can be expressed as a function of the forward voltage $V^+_{\text{TM/TE}}$ solution in the infinite medium at the air-dielectric interface of the corresponding transmission line problem as follows [124]

$$\tilde{G}^{em}(k_\rho,\alpha) = V^+_{\text{TE}}\hat{\alpha}\hat{k}_\rho - V^+_{\text{TM}}\hat{k}_\rho\hat{\alpha} + \frac{k_\rho}{k_z}V^+_{\text{TM}}\hat{z}\hat{\alpha} \tag{4.2}$$

where $\hat{k}_\rho = \frac{k_x\hat{x}+k_y\hat{y}}{k_\rho}$ and $\hat{\alpha} = \frac{k_x\hat{y}-k_y\hat{x}}{k_\rho}$. To make the dependence of the phase center explicit, one can consider the spectrum of the electric field assuming the origin of the reference system centered at the ground plane wherein the source is located, $V^+_{\text{TM/TE}}(k_\rho,\Delta z=0)$, and construct the following auxiliary functions:

$$\tilde{V}^+_{\text{TM/TE}}(k_\rho,\Delta z) = V^+_{\text{TM/TE}}(k_\rho,\Delta z=0)e^{-jk_z\Delta z} \tag{4.3}$$

so that integrand in Eq. (4.1) now contains $\tilde{G}^{em}(k_\rho,\alpha)e^{-jk_z z'}$ where $z' = z + \Delta z$.

For an elementary source, the α-integral can be closed analytically into Hankel functions of the second kind with order n, $H_n^{(2)}$, such that only the k_ρ-integrals remain [117]–[119]. For a distributed source, similar steps can be taken for observation points far from the source when the spectral current $M(k_\rho,\alpha)$ can be assumed to be slowly-varying in α compared to $\tilde{G}^{em}$ and can therefore be evaluated in the α-saddle point, i.e., $M(k_\rho,\phi)$. The complete $\vec{e}(\vec{r})$ and $\vec{h}(\vec{r})$ expressions, given in Appendix A, are then of the form:

$$\int_{-\infty}^{\infty} V^+_{\text{TM/TE}}H_n^{(2)}(k_\rho\rho)M(k_\rho,\phi)e^{-jk_z z}k_\rho\,\mathrm{d}k_\rho \tag{4.4a}$$

$$\text{with } n = \{0,2\} \text{ or}$$

$$\int_{-\infty}^{\infty} I^+_{\text{TM/TE}}H_1^{(2)}(k_\rho\rho)M(k_\rho,\phi)e^{-jk_z z}k_\rho^2\,\mathrm{d}k_\rho \tag{4.4b}$$

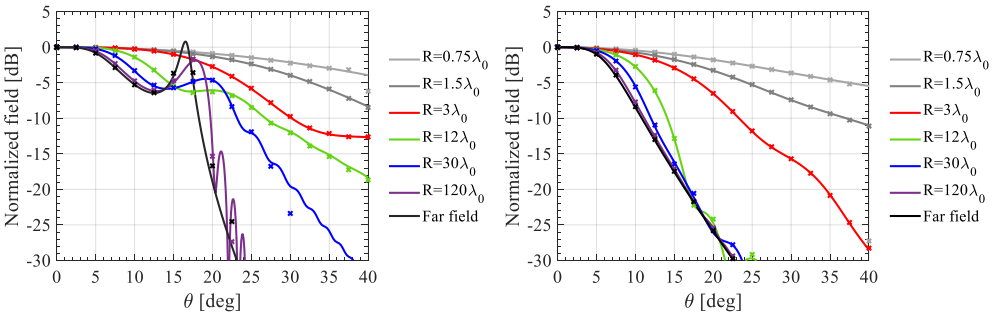

Fig. 4.2: Electric fields in the E-plane ($\hat{\theta}$-component, left) and H-plane ($\hat{\phi}$-component, right) radiated by a $\hat{y}$-oriented elementary magnetic current source evaluated over a spherical region with radius R from the source (i.e., $\Delta z = 0$). Solid lines: Eqs. (4.4a) and (4.4b), crosses: CST.

When the observation point is in the far field of the LWA, an asymptotic evaluation in both saddle points for $k_\rho = k_d \sin\theta$ and $\alpha = \phi$ can be done arriving to the following expression:

$$\vec{e}(\vec{r}_\infty) \approx jk_d \left(-\hat{\theta}\, V_{\text{TM}}^{+} \cos\phi + \hat{\phi}\, V_{\text{TE}}^{+} \cos\theta \sin\phi \right) M(k_\rho, \alpha) \frac{e^{-jkr}}{4\pi r} \tag{4.5}$$

As a first example let us consider an elementary magnetic current source with the reference system located in the source as most cases in the literature [119], [120]. The $\hat{\theta}$-component of the electric field in the E-plane radiated by this source into the semi-infinite (silicon) medium is shown in Fig. 4.2. The electric field has been calculated using Eq. (4.1) over several spherical cuts in the E-plane with radii R between $0.75\lambda_0$ and $120\lambda_0$ centered at the origin (the spheres are shown as dashed lines in Fig. 4.1). For reference, the far field approximation of Eq. (4.5) is also shown. We can observe that the shape of the near fields shown in Fig. 4.2 is strongly dependent on R and converges to the far field only at very large distances from the source. This is due to the TM_0 modal field, that dominates the field in the angular region close to the complex pole location even for very large R. Furthermore, the radiation patterns are asymmetric in ϕ, since the TM_0 mode does not radiate in the H-plane. Therefore, in order to efficiently feed electrically small silicon lenses, it is clear that the TM_0 mode must be suppressed, for example by using a double-slot iris [20], [103], [125], [126] or dipole source configurations [95]. To illustrate the accuracy of Eq. (4.1), the obtained fields are compared to those obtained from the time-domain solver of CST [127], a commercial full-wave solver. Open boundary conditions were applied to an elementary source or a double-slot iris radiating into a semi-infinite structure made of the considered dielectric materials.

The fields radiated into the same stratification as above but now for the double-

slot iris source with the same dimensions as in [103] are shown in Fig. 4.3a, taking again the coordinate reference system located at the center of the double slot. The inset of Fig. 4.3a shows the geometry of the double-slot iris and the dimensions are given as $\alpha_i = 100°$, $\rho_i = 0.55\lambda_0$ and $w_i = 0.15\lambda_0$ [103]. The near field is calculated over the same spherical regions as for the elementary source in Fig. 4.2, again using Eq. (4.1) (solid lines) and full-wave simulations (crosses) to validate the fields. The small discrepancy at the closest distances comes from the approximation of the spectral current $M(k_\rho, \alpha) \approx M(k_\rho, \phi)$. At distances smaller than λ_0 from the double-slot source, the approximation on the α-integral is not accurate anymore. The use of a double slot source leads to much faster convergence of the near field to the far field compared to the elementary source due to the suppression of the TM_0 mode.

It is well known that the phase center in leaky-wave resonant antennas lies below the ground plane in the far field. In [123], the following approximate formula for the phase center, dependent only on the normalized attenuation constant of the leaky-wave pole $\hat{\alpha}_{LWi}$, was given:

$$\frac{\Delta z_i}{\lambda_0} \approx -\frac{1}{2\pi\hat{\alpha}_{LWi}^2\sqrt{\varepsilon_r}} \tag{4.6}$$

where $\hat{\alpha}_{LWi} = \mathrm{Im}\{k_\rho^{LWi}/k_d\}$ and the term $\sqrt{\varepsilon_r}$ appears in the denominator in case of a LW radiating into a dense medium, .

We can now plot the near fields of the same source considered in Fig. 4.3a, but evaluated at spheres centered at this approximated phase center, which is $\Delta z = -5.6\lambda_0$ for a silicon semi-infinite medium (the spheres are shown as solid lines in Fig. 4.1). Shown in Fig. 4.3b, we can see that the amplitude converges even faster to the far-field approximation indicating that the field may be considered, also very close to the source, as a spherical wave but with a more accurate phase center evaluation. In [123], other phase minimization formulas were also considered to improve the accuracy of Eq. (4.6), however these were not closed-form and were given as a function of a generic solid angle.

To properly understand the properties of the field radiated by this kind of LWA close to the source, we will employ a spectral analysis that decomposes the total field in terms of a space wave, calculated by integration over the Steepest Descent Path (SDP) from the phase center, and multiple leaky-wave modal fields, associated with poles that are captured by the SDP path deformation [117, p. 468] in the next section.

4.3 Spectral Field Decomposition of the Near Field in Resonant Leaky-Wave Antennas

In this section, we apply a spectral-domain field decomposition to the near field radiated by resonant leaky-wave antennas into a semi-infinite medium. This near field is

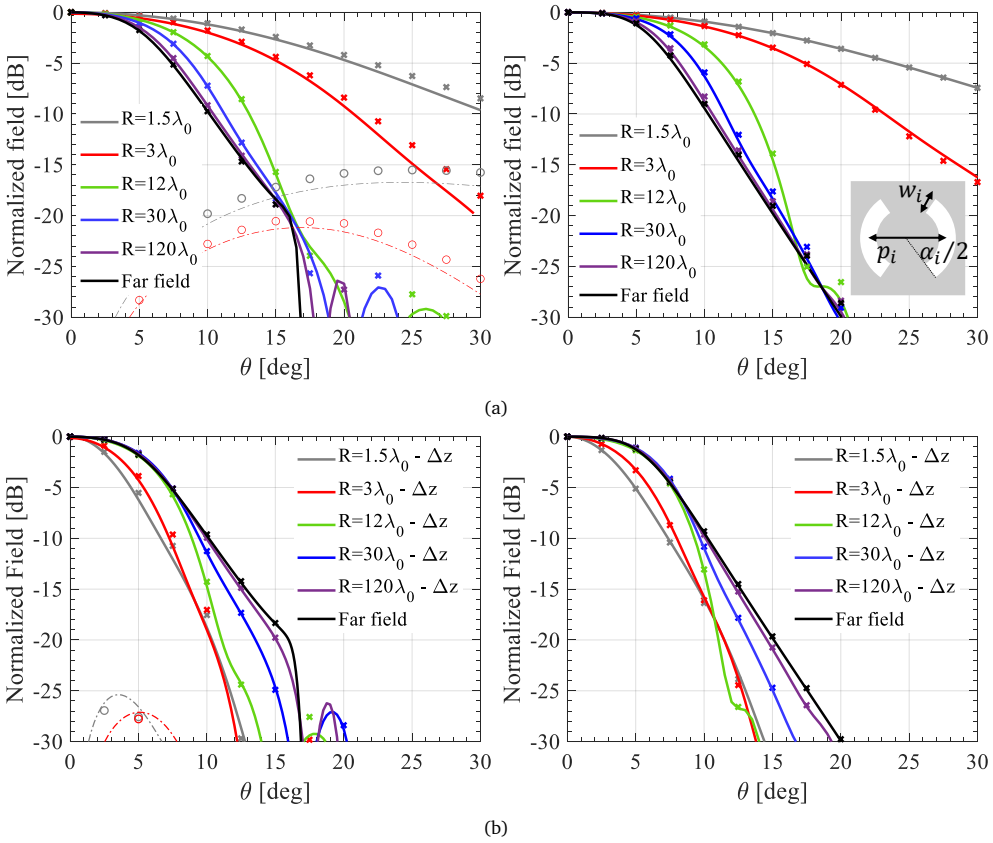

Fig. 4.3: Electric fields radiated by the double-slot iris of [103], evaluated over a spherical region with several radii calculated using Eqs. (4.4a) and (4.4b): (a) E-plane ($\hat{\theta}$-component, left) and H-plane ($\hat{\phi}$-component, right) amplitude seen from the slots ($\Delta z = 0$) and (b) E-plane ($\hat{\theta}$-component, left) and H-plane ($\hat{\phi}$-component, right) amplitude seen from the phase center according to [123] ($\Delta z = -5.6\lambda_0$). Dashes: $\hat{r}$-component, crosses and circles: CST.

expressed as the summation of (multiple) leaky-wave modal fields plus a space wave contribution. This later one can be evaluated with an integration path over the branch point close-by the source as in [121] or using the Steepest Descent Path (SDP) for larger distances [117, p. 467]. Here, in contrast to [119] and [121], we apply this SDP directly for the near-field evaluation in resonant LWAs, provided that the reference system is located in the phase center and that the near field is evaluated at a distance from the source such that the asymptotic decomposition holds (i.e., the observation point is outside the region that includes the phase center and source points).

In order to evaluate the SDP field contribution, a change of spectral variables $k_\rho = k_d \sin\beta$, $k_z = k_d \cos\beta$ suggests using a spherical coordinate system for the observation point $\vec{r}(\theta, \phi, R)$ in Eqs. (4.4a) and (4.4b) with origin in the antenna phase center, Δz.

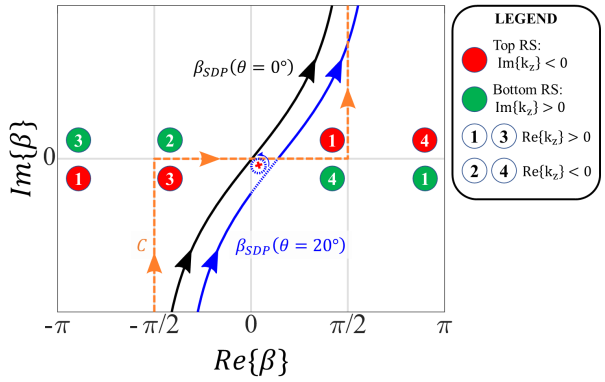

Fig. 4.4: Steepest Descent Paths β_{SDP} in the complex β-plane for observation points $\theta = 0°$ and $\theta = 20°$. The choice of Riemann sheet for the β_{SDP}-integral is indicated in the legend.

The resulting integrals are then of the form:

$$\int_C V^+_{\text{TM/TE}} H_n^{(2)}(k_d\rho\sin\beta) M(k_d\sin\beta,\phi)\cdot e^{-jk_d z\cos\beta} k_d^2 \sin\beta\cos\beta\,\mathrm{d}\beta \tag{4.7a}$$

with $n = \{0, 2\}$ or

$$\int_C I^+_{\text{TM/TE}} H_1^{(2)}(k_d\rho\sin\beta) M(k_d\sin\beta,\phi)\cdot e^{-jk_d z\cos\beta} k_d^3 \sin^2\beta\cos\beta\,\mathrm{d}\beta \tag{4.7b}$$

with the integration path C shown in the complex β-plane in Fig. 4.4. The odd and even numbered regions indicate $\mathrm{Re}\{k_z\} > 0$ and $\mathrm{Re}\{k_z\} < 0$ and the red and green regions indicate the top and bottom Riemann sheets (i.e., $\mathrm{Im}\{k_z\} < 0$ and $\mathrm{Im}\{k_z\} > 0$), respectively [117, p. 463].

When the original path C is deformed and no singularities are crossed, the total field $\vec{e}(\vec{r})$ is given by the integration over the deformed path. When the deformation leaves a pole between the original and the new path, the residue contribution corresponding to the pole encountered must be summed to the new path integral to obtain the total field.

It can be shown using the method in [118] that for large observation distances, i.e., where the large-argument approximation of the Hankel functions [117, p. 467] is valid, the parameterization of the SDP in Eqs. (4.7a) and (4.7b) is achieved with a change of variable $\beta \to \tau$ with $\tau \in [-\infty, \infty]$ and τ given by inverting:

$$\beta_{SDP} = \theta + 2\arcsin\left(\frac{\tau e^{j\frac{\pi}{4}}}{\sqrt{2}}\right) \tag{4.8}$$

Accordingly, this contribution, when evaluated asymptotically will give rise to a dom-

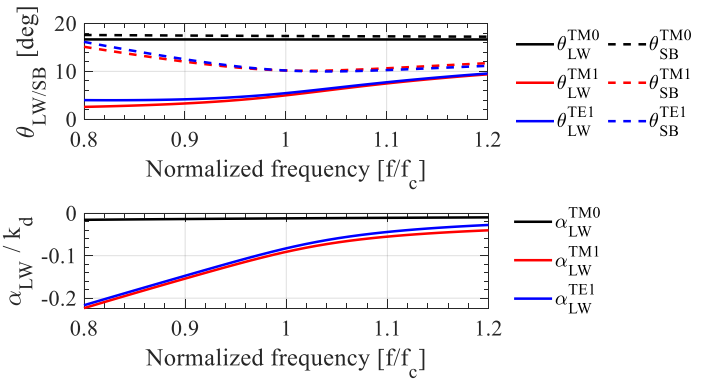

Fig. 4.5: Leaky-wave poles $k_{\rho,LW}^{TM/TE} = k_d[\sin(\theta_{LW}^{TM/TE}) + j\alpha_{LW}^{TM/TE}]$ that propagate in the stratification of Fig. 4.1 with semi-infinite dielectric permittivity $\varepsilon_r = 11.9$ (silicon). The shadow boundary angle (Eq. (4.9)) is also shown.

inant spherical wave emerging from the phase center. From Fig. 4.4, one can note that the path of the SDP includes portions in the bottom Riemann sheet, and thus the poles encountered are leaky-wave poles and we call the residue contribution of these poles the leaky-wave modal field $\vec{e}_{LW}(\vec{r})$.

The leaky-wave poles $k_{\rho,LW}^{TM/TE}$ arise from the denominator of $V_{\text{TM/TE}}^{+}$ in Eq. (4.1). They may be found by solving the appropriate dispersion equation (or by using approximated analytical expressions [128]). They are conveniently represented as $k_{\rho,LW}^{TM/TE} = k_d(\sin\theta_{LW}^{TM/TE} + j\alpha_{LW}^{TM/TE})$ in which $\theta_{LW}^{TM/TE}$ is the leaky-wave pointing angle and $\alpha_{LW}^{TM/TE}$ is the leakage rate [97] of the TM or TE pole. The stratification of Fig. 4.1 supports three leaky-wave modes: TM_0, TM_1 and TE_1, with their propagation constants shown in Fig. 4.5 as a function of frequency.

The SDP crosses a TM or TE leaky-wave pole when $\theta \geq \theta_{SB}^{TM/TE}$, i.e., when the observation point lies below the corresponding shadow boundary, see Fig. 4.1. The shadow boundary angle is a function of the pole's complex propagation constant as follows [117, p. 468][118]:

$$\theta_{SB}^{TM/TE} = \text{Re}\{\beta_{LW}^{TM/TE}\} + \arccos\left(\text{sech}\left(\text{Im}\{\beta_{LW}^{TM/TE}\}\right)\right) \tag{4.9}$$

in which $\beta_{LW}^{TM/TE} = \arcsin\left(k_\rho/k_d\right)$. This shadow boundary angle is also shown as a function of frequency in Fig. 4.5 for each of the leaky wave poles present. It is clear that $\theta_{SB}^{TM/TE}$ is not close to the corresponding $\theta_{LW}^{TM/TE}$, except for the TM_0 mode which does not enhance the broadside directivity of the antenna, as explained in Section 4.2.

If multiple leaky-wave poles are crossed, the total field is given by adding the modal

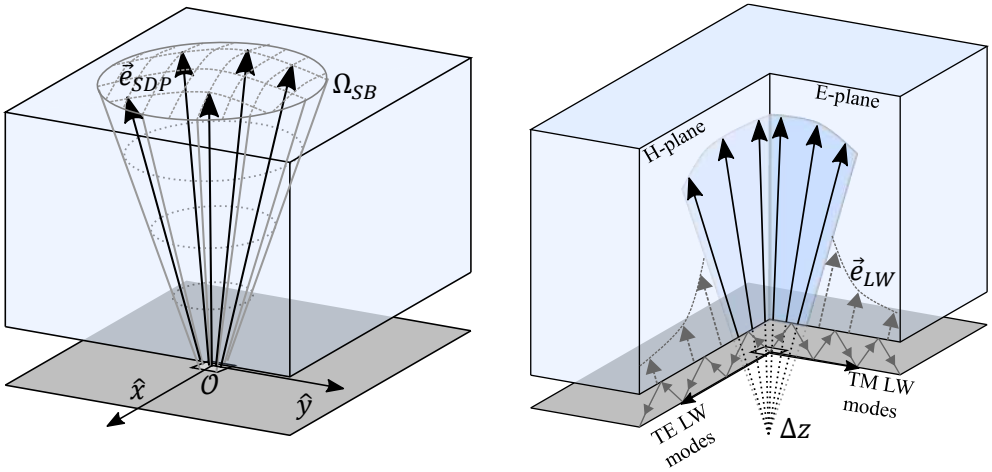

Fig. 4.6: Three-dimensional view of the considered LWA. In the spherical cone region Ω_{SB} as seen from the phase center at Δz below the ground plane, the total field is given by $\vec{e}_{SDP}$ (solid arrows, left). Outside this cone, the LW modal field $\vec{e}_{LW}$ (dotted arrows, right) must be added to the SDP contribution to obtain the total field.

fields associated with each crossed pole to the contribution from the SDP:

$$\vec{e}(\vec{r}) = \vec{e}_{SDP}(\vec{r}) + \sum_{i=1}^{m} \vec{e}_{LW}^{TM/TE}(\vec{r})\Big|_{\theta \geq \theta_{SB}^{TM/TE}} \tag{4.10}$$

as long as the observation point is outside the elliptical transition region [118] and the LW poles are not close together. Expressions for $\vec{e}_{LW}^{TM/TE}(\vec{r})$ may be found in Appendix A. The LW modal field is a cylindrical wave that propagates in the $\theta_{LW}^{TM/TE}$-direction (Fig. 4.5) in the infinite medium. Therefore, this field decomposition indicates that the total field could only be represented by a spherical wave until the shadow boundary when $\vec{e}_{SDP}$ dominates. The field representation of Eq. (4.10) in terms of an SDP contribution and LW modal field contribution is shown in Fig. 4.6. The origin of this spherical wave will be at the phase center of the antenna, Δz, which will be evaluated in the next section.

4.4 Phase Center Evaluation

The phase center in the considered LWAs can be defined for the near field, similar to the far field, as the apparent origin of radiation such that the phase of the integrals in Eqs. (4.4a) and (4.4b) is minimized over a certain solid angle. Based on the understanding that the near field could only be a spherical wave when $\theta < \theta_{SB}$ (see Section 4.3), the solid angle over which to minimize this can be given as $\Omega_{SB}(\theta, \phi)$ such that $\theta \in [0, \theta_{SB}]$ and $\phi \in [0, 2\pi]$, instead of a generic angle as in [123]. Since

the considered LW antennas are nearly rotationally symmetric (with similar TE_1 / TM_1 modes), the location of the phase center will be along the z-axis. The phase in Eqs. (4.4a) and (4.4b) is dominated by the phase of the transmission-line voltage solutions, $V^{+}_{\mathrm{TM/TE}}$. In [123], an approximated expression of this phase is given using only the LW propagation constant.

To find the most appropriate value Δz that guarantees the path deformations in Fig. 4.4 correspond to the SDP, one can consider a non-uniform asymptotic evaluation of the integral in Eqs. (4.4a) and (4.4b). The integral can be deformed into an SDP and recognized as a spherical wave, if the kernel, now Eq. (4.3), separated from the exponential oscillating phase associated with the observation point is slowly varying. Expressing $k_\rho = k_d \sin\beta$, the normalized phase of $\tilde{V}^{+}_{\mathrm{TM/TE}}(k_\rho, \Delta z)$ can be expressed as function of β as [123]:

$$\tilde{\Psi}(\beta, \Delta z) = \arctan\left(\sin^2\beta/(2\alpha_{LW}^2)\right) - k_d \Delta z \cos\beta \tag{4.11}$$

In Fig. 4.7, $\tilde{\Psi}(\beta, \Delta z)$ is shown for a silicon medium and $\Delta z = 0$ together with the phase of $e^{jk_z \Delta z}$ when $\Delta z = -3.2\lambda_0$. It can be seen from the figure that the two phases are very similar until the shadow boundary angle θ_{SB}. Therefore, we can evaluate the phase center $\Delta z^{TM/TE}$ associated with the TM and TE poles by imposing that the two functions are equal at the shadow boundary for each of the poles:

$$\Psi(\theta_{SB}^{TM/TE}, \Delta z = 0) = k_{z,SB}^{TM/TE} \Delta z^{TM/TE} \tag{4.12}$$

where $k_{\rho,SB}^{TM/TE} = k_d \sin\theta_{SB}^{TM/TE}$. Solving this equation, a good evaluation of the phase center per pole can be given by:

$$\frac{\Delta z^{TM/TE}}{\lambda_0} = -\frac{\arctan\left(\sin^2\theta_{SB}^{TM/TE}/(2(\alpha_{LW}^{TM/TE})^2)\right)}{\sqrt{\varepsilon_r}2\pi(1-\cos\theta_{SB}^{TM/TE})} \tag{4.13}$$

in which a negative $\Delta z^{TM/TE}$ refers to a phase center position below the ground plane. In general, the TM pole will give the E-plane phase center and the TE pole will give the H-plane phase center. For high dielectric contrast cases, $k_{\rho,LW}^{TM} \approx k_{\rho,LW}^{TE}$ [123] leads to nearly overlapping E- and H-plane phase centers at Δz. For example, the phase center of the silicon LWA described previously is $\Delta z = -3.2\lambda_0$ when the TE and TM solutions are averaged. The validity of this equation is shown in Fig. 4.7 (right) where the E-plane phase radiated by the LWA fed by a double-slot iris is indeed nearly constant for $\theta < \theta_{SB}$ when the reference system is taken to coincide with the phase center given by Eq. (4.13).

With the phase center definition of Eq. (4.13), a uniform asymptotic expansion of the

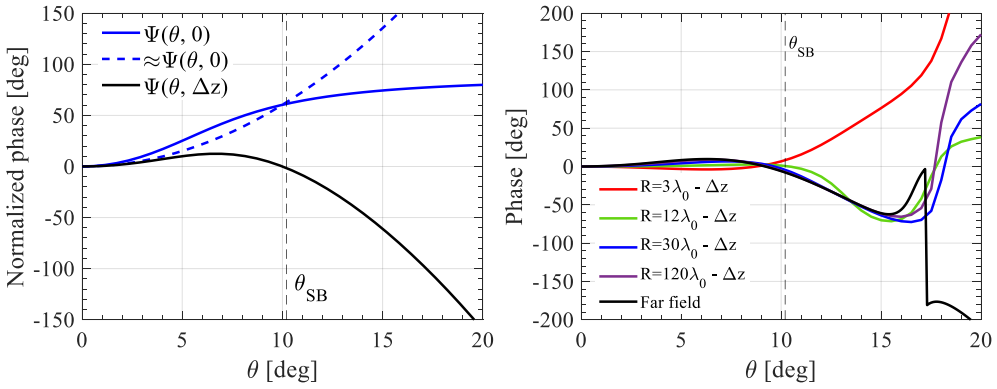

Fig. 4.7: Phase $\Psi(\theta, \Delta z = 0)$ of Eq. (4.3) along with its approximation (blue). The corrected phase for the phase center of Eq. (4.13) $\Psi(\theta, \Delta z = -3.2\lambda_0)$ is also shown (black). The shadow boundary angle is indicated. The phase of the E-plane near field radiated by the LWA with a double-slot iris, evaluated at different radii from the phase center $\Delta z = -3.2\lambda_0$ is shown on the right.

integral in Eqs. (4.4a) and (4.4b) over the SDP can be derived using the approach in [118]. Such a uniform asymptotic expansion results in a contribution from a Fresnel-type transition function in an elliptical region around the phase center. The equality of the phase of the space wave and the leaky-wave modal fields, which have spherical and cylindrical spreading, respectively, at the shadow boundary imposed by the phase center definition in Eq. (4.13), leads to the smallest possible dimension of the elliptical transition region.

4.5 Spherical Wave Near-Field Representation for Resonant LWAs

In this section, the formation of a spherical wave in a certain solid angle around broadside in the near field of resonant LWAs is investigated based on the previous spectral field decomposition. In Section 4.5.1 the analysis is performed for high-permittivity (silicon) lenses and in Section 4.5.2 the analysis is performed for low-permittivity (plastic) lenses. In Section 4.6 the leaky-wave poles, shadow boundary angle and phase center are presented as a function of the permittivity of the infinite medium $(2 \leq \varepsilon_r \leq 12)$.

4.5.1 High Dielectric Contrast: Silicon Lenses

The fields of the double-slot iris-fed LWA are calculated using Eq. (4.10) over spheres centered at the phase center, as defined by Eq. (4.13) with the aim of understanding the behavior of the field amplitude, polarization and propagation direction. The radius of the spheres is chosen between $1.5\lambda_0 - \Delta z$ and $120\lambda_0 - \Delta z$ so that the spheres have coincident observation points at broadside with those of Fig. 4.3b. The resulting E-plane and H-plane near fields are shown in Fig. 4.8a. The near field, when evaluated from the phase center, is almost independent of the distance from the source in the

region $\theta < \theta_{SB}$. In Fig. 4.8b we show the field decomposition into the space wave evaluated via the SDP and the leaky wave terms. The influence of the TM_1 and TE_1 leaky-wave modal fields is observed when $\theta > \theta_{SB}$, at which point the field level is already below -10 dB. The radial field component diminishes very rapidly with R and is already below -25 dB at $R = 1.5\lambda_0 - \Delta z$.

Since the phase over the SDP is nearly constant, the space-wave evaluation can be approximated using a non-uniform asymptotic expansion of the SDP integral which corresponds to the far field given in Eq. (4.5):

$$\vec{e}_{SDP}(\vec{r})\big|_{\theta<\theta_{SB}} \approx \vec{e}(\vec{r}_\infty, \Delta z)\big|_{\theta<\theta_{SB}} \tag{4.14}$$

where it is highlighted that this applies only with a proper phase center definition. The far-field is also shown in Fig. 4.8a. This non-uniform asymptotic evaluation can be considered sufficiently accurate to describe the SDP field until θ_{SB} because the field level at the shadow boundary is already very low (i.e., about -10 dB in Fig. 4.8a). This is due to the fact that the geometry considered in the present chapter supports two $\pm k_{\rho,LW}$ leaky waves which cumulatively provide a maximum at broadside, and a decreasing total field already for observation points close to the shadow boundaries. For other configurations where the shadow boundary would correspond to higher field levels, a uniform asymptotic evaluation as in [118] would be needed to maintain useful accuracy. The phase in Fig. 4.7 varies by less than 10° in the region $\theta < \theta_{SB}$ for any R and thus the near field can be considered a spherical wave. Since this angle also corresponds to the -10 dB point of the radiation pattern, the lens' subtended solid angle, seen from the phase center can be approximated by Ω_{SB}. This solid angle in Eq. (4.9) and phase center in Eq. (4.13), which are only a function of the propagation constant of the LW mode, fully define the shape of the lens needed to enhance the directivity in this kind of antennas as shown in the next section.

To illustrate that the field close to the LW source can be well represented by a spherical wave, a 2-D cut of the real part of the electric field in the E-plane is shown in Fig. 4.9a (left) which has been obtained from a full-wave simulation. It is clear from this figure that there is a spherical wavefront in the semi-infinite medium, even very close to the air-dielectric interface. Next, the direction of time-averaged power density has been calculated from the Poynting vector $\vec{S} = Re\{\vec{e} \times \vec{h}^*\}/2$ in the E-plane seen from the phase center. This direction is shown in Fig. 4.9b (left) and is compared to the geometrical radial vector. Indeed, when the near field is evaluated from the phase center, the Poynting vector is almost along $\vec{r}$, which confirms that the near field may be considered a local spherical wave in the region $\theta < \theta_{SB}$ and that it will couple well to an elliptical lens, even for electrically small lenses.

We can also evaluate the fraction of power in the space wave by integrating the

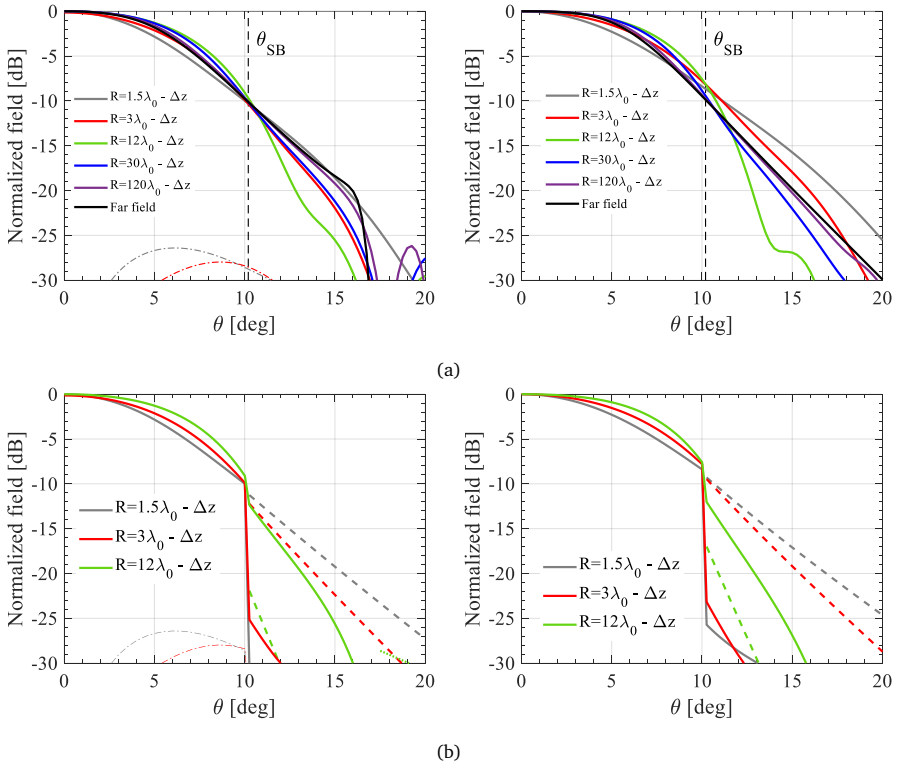

Fig. 4.8: (a) Electric fields in the E-plane ($\hat{\theta}$-component and $\hat{r}$-component, left) and H-plane ($\hat{\phi}$-component, right) radiated by the double-slot iris of [103], evaluated over a spherical region with several radii taken from $\Delta z = -3.2\lambda_0$ i.e., below the ground plane. The shadow boundary angle of Eq. (4.9) is indicated. (b) The decomposition of these fields into the SDP contribution (solid lines) and LW modal fields (dashes: main modes, dots: TM_0 mode).

Poynting vector over the solid angle Ω_{SB}:

$$P_{rad}(R) = \frac{1}{2}\iint_{\Omega_{SB}} Re\{\vec{e}\times\vec{h}^*\}\cdot\hat{r}R^2\,\mathrm{d}\Omega \tag{4.15}$$

The ratio of this power to the total radiated power by the LWA, i.e., $P_{rad}(R)/P_{tot}$, will correspond to the spillover efficiency of the truncated lens. In Fig. 4.10, this spillover efficiency is shown as a function of the lens diameter $D = 2R\sin\theta_{SB}$. From this result, we can see that the spillover efficiency is higher than 85% for lenses larger than $D = 2\lambda_0$. Thus, depending on the specific requirements, silicon lenses as small as $D_l = 2.5\lambda_0$ can be used. When the double-slot iris is omitted, and thus the TM_0 mode is present, the lens size must be significantly larger in order to achieve the same efficiency.

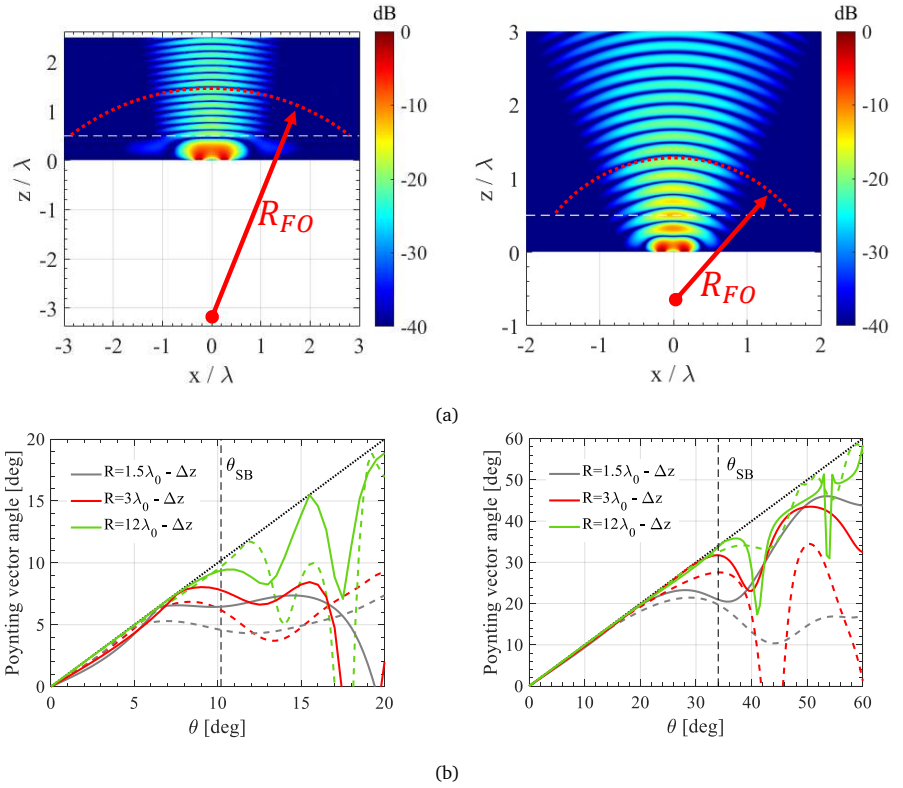

Fig. 4.9: (a) 2-D E-plane cut of the field radiated by the double-slot iris source into a silicon (left) and plastic (right) semi-infinite medium. (b) Poynting vector angle (solid: E-plane, dashes: H-plane) for the fields above them. The black dotted line indicates the geometrical angle seen from the phase center.

4.5.2 Low Dielectric Contrast: Plastic Lenses

The use of low-permittivity lenses, which have LW poles that are much further from the real axis has recently been proposed to achieve a very wide bandwidth of 40% [20]. The stratification is the same as considered before (see Fig. 4.1), except the semi-infinite silicon is replaced with HDPE ($\varepsilon_r = 2.5$, considered lossless here), a low-cost plastic commonly used in mm-wave applications. The proposed lens feed is a waveguide-fed double-slot iris, similar to [20], with dimensions $\alpha_i = 120°$, $\rho_i = 0.6\lambda_0$ and $w_i = 0.2\lambda_0$, designed to suppress the TM_0 mode. The leaky-wave propagation constants are shown in Fig. 4.11 as a function of frequency, along with the resulting shadow boundary angle. Note again that θ_{SB} is very far from θ_{LW} for the main TM_1 / TE_1 modes and that they are nearly equal for both modes. Since the main LW poles are not as close together as in the silicon case, the phase center $\Delta z = -0.64\lambda_0$ has been calculated by averaging Eq. (4.13).

The field radiated by this source into the semi-infinite medium, $\vec{e}$, has been calcu-

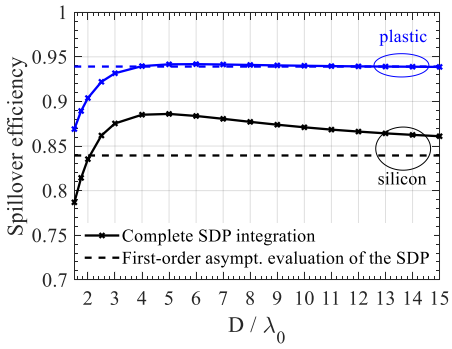

Fig. 4.10: Spillover efficiency as a function of the lens diameter.

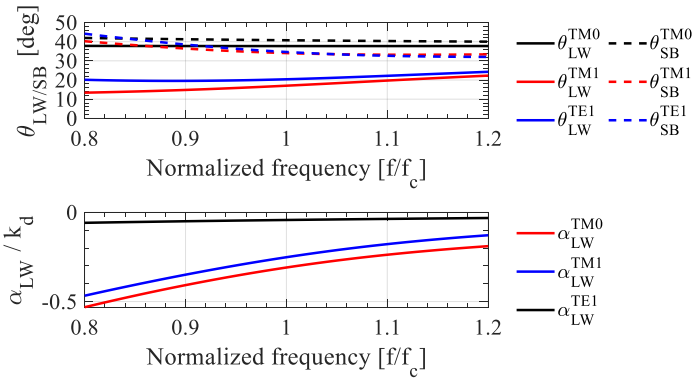

Fig. 4.11: Leaky-wave poles $k_{\rho,LW}^{TM/TE} = k_d[\sin(\theta_{LW}^{TM/TE}) + j\alpha_{LW}^{TM/TE}]$ that propagate in the stratification of Fig. 4.1 with semi-infinite dielectric permittivity $\varepsilon_r = 2.5$ (plastic). The shadow boundary angle of Eq. (4.9) is also shown.

lated using Eq. (4.10) over several spherical cuts in the E-plane with radii R between $1.5\lambda_0 - \Delta z$ and $12\lambda_0 - \Delta z$, centered at the phase center. For reference, the far field is also shown. The result is shown in Fig. 4.12a (solid lines). The field is again not strongly dependent on R. In Fig. 4.12b the field is decomposed into the contributions from $\vec{e}_{SDP}$ (solid lines) and $\vec{e}_{LW}$ (dashes and dots), which sum to $\vec{e}$ (Fig. 4.12a). The discontinuity in $\vec{e}_{SDP}$ is due to the SDP crossing the LW pole.

To illustrate that the near field can be considered a local spherical wave, a 2-D cut of the near field is shown in the E-plane in Fig. 4.9b (right). Furthermore, the angle between the time-averaged Poynting vector $\vec{S}$ and the radial direction, seen from the phase center, is shown in Fig. 4.9b (right). It is clear that the field can be considered a local spherical wave for $\theta < \theta_{SB}$ even for observation points close to the source. Thus, the approach can be used for stratifications that are less resonant than in Section 4.5.1 and much less resonant than previously described in the literature [119].

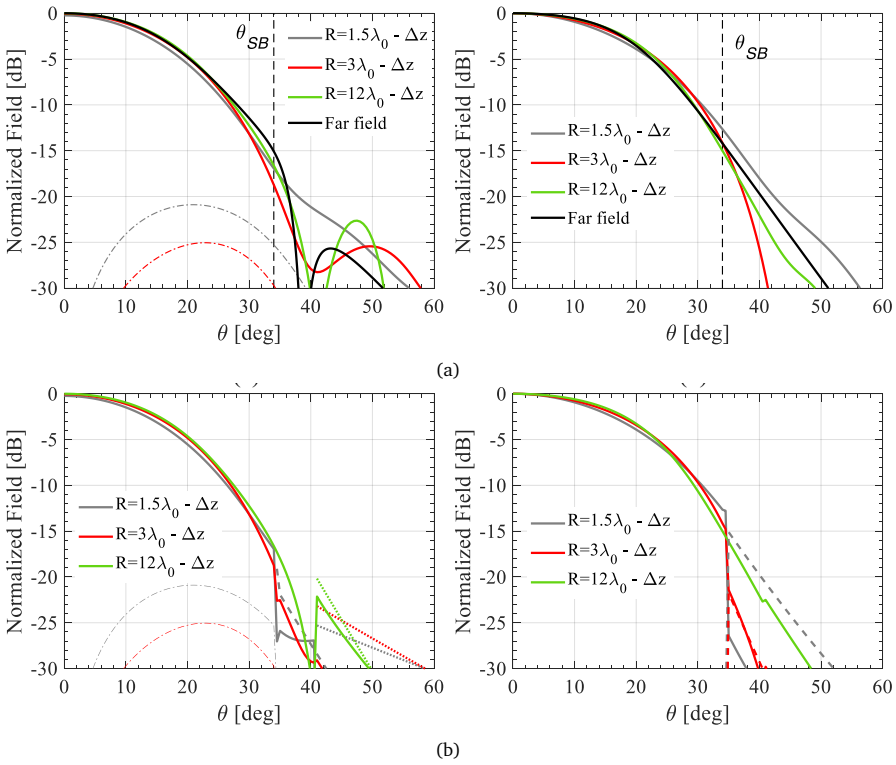

Fig. 4.12: (a) Electric fields in the E-plane ($\hat{\theta}$-component and $\hat{r}$-component, left) and H-plane ($\hat{\phi}$-component, right) radiated by the double-slot iris of [20], evaluated over a spherical region with several radii taken from $\Delta z = -0.64\lambda_0$ i.e., below the ground plane. The shadow boundary angle of Eq. (4.9) is indicated. (b) The decomposition of these fields into the SDP contribution (solid lines) and LW modal fields (dashes: main modes, dots: TM_0 mode).

4.6 Application To Small Elliptical Lenses

In this section, the geometry of the elliptical lens fed by the resonant leaky-wave feed with a double-slot iris is given analytically, based on the SDP field decomposition, for arbitrary lens permittivity. The formulas provided can be used to design the lens geometry even in the near field with high aperture efficiency. We apply an FO methodology in reception [20], [96] to calculate the aperture efficiency and the radiation patterns of a small silicon lens, which are verified using full-wave simulations. The aperture efficiency is then calculated as a function of the lens diameter D_l.

4.6.1 Spherical-Wave Parameters for Arbitrary Dielectric Contrast

To define the geometry of an elliptical lens antenna, we must know θ_{SB} and Δz for the desired lens permittivity. Therefore, we present here the LW poles as a function of the permittivity of the semi-infinite dielectric medium, ε_r. These are then used to

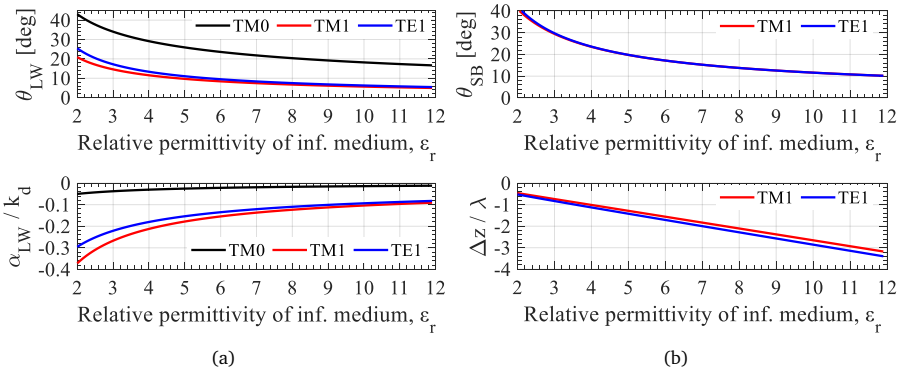

Fig. 4.13: (a) Leaky-wave pointing angles θ_{LWi} and normalized attenuation constants $\hat{\alpha}_{LWi}$ at the central frequency and (b) shadow boundary angle θ_{SB} and phase center Δz corresponding to the main modes as a function of the permittivity of the infinite medium.

derive θ_{SB} and Δz as a function of ε_r.

The leaky-wave pointing angle θ_{LW} and normalized leakage rate $\hat{\alpha}_{LW} = \alpha_{LW}/k_d$ are shown in Fig. 4.13a as a function of the relative permittivity of the semi-infinite medium. The LW angle decreases and the leakage is slower as the permittivity increases, which is in line with the results for the classical Fabry-Pérot antenna geometry [97], [128].

The shadow boundary angle θ_{SB} and phase center location for the main TM_1 and TE_1 modes, calculated using Eq. (4.9) and Eq. (4.13) are shown in Fig. 4.13b as a function of the relative permittivity of the semi-infinite medium. The shadow boundary angles are almost equal for both modes and decrease with an increasing ε_r. The phase center is further below the ground plane as ε_r increases. Together, the shadow boundary angle and phase center location fully define the elliptical lens geometry to which the LWA couples well, as will be demonstrated next.

4.6.2 Elliptical Lens Geometry

The analytical elliptical lens geometry (see Fig. 4.14) that provides high aperture efficiency is as follows. The lower focus of the ellipsoid, F_2, coincides with the phase center Δz of the feed given by Eq. (4.13) and the lens is truncated at an angle θ_{SB}, given by Eq. (4.9), seen from this focus since the shadow boundary angle corresponds roughly to the -10 dB field taper angle. The values for Δz and θ_{SB} can be found in Fig. 4.13b. The distance from F_2 (i.e., the phase center) to the rim of the lens is $R_{FO} = D_l/(2\sin\theta_{SB})$. The sphere centered at F_2 with radius R_{FO} is the FO sphere. The semi-major axis of the ellipsoid is given by:

$$a = R_{FO}\frac{1 - e\cos\theta_{SB}}{1 - e^2} \tag{4.16}$$

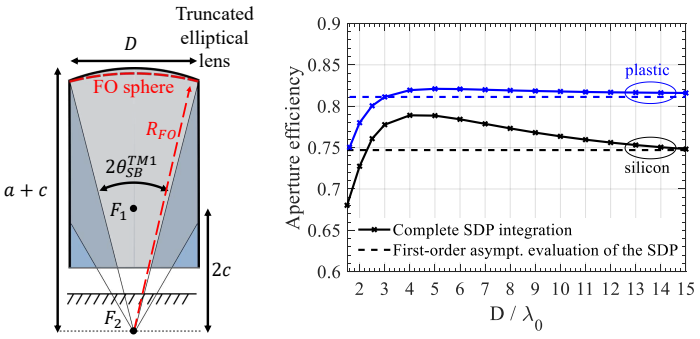

Fig. 4.14: (a) Cross-section of an elliptical lens fed by the stratification of Fig. 4.1 with the foci and dimensions of the ellipse and lens. (b) Aperture efficiency of the analytical lens geometry of (a) based on the leaky modes as a function of the lens diameter.

and the inter-focal distance is given by $c = a + e$, where $e = 1/\sqrt{\varepsilon_r}$ is the eccentricity of the lens.

4.6.3 Lens Analysis in Reception

To calculate the aperture efficiency of the lens, we use the FO method in reception [96], which we briefly summarize here. In the FO approach, a plane wave incident on the lens in the $\hat{k}_i = -\vec{z}$-direction is propagated into the lens and onto the FO sphere (S_{FO} with normal $\hat{n} = -\hat{r}$ pointing inward) using geometrical optics (GO). The equivalent electric and magnetic currents on the FO sphere $\vec{J}^{eq}_{S_{FO}} = \hat{n} \times \vec{h}^{GO}_i$ and $\vec{M}^{eq}_{S_{FO}} = -\hat{n} \times \vec{e}^{GO}_i$, are then correlated with the SDP contribution to the near field of the leaky-wave feed, $\vec{e}_{SDP}(\vec{r})$, $\vec{h}_{SDP}(\vec{r})$ as follows:

$$P_L(\hat{k}_i) = \frac{R_{FO}^4}{16 P_{tot}} \cdot \left| \iint_{\Omega_{SB}} \left(\vec{h}_{SDP} \cdot \vec{M}^{GO}_{S_{FO}}(\hat{k}_i) - \vec{e}_{SDP} \cdot \vec{J}^{GO}_{S_{FO}}(\hat{k}_i) \right) \mathrm{d}\Omega \right|^2 \tag{4.17}$$

and the aperture efficiency is given as $\eta_{ap} = P_L / P_{PW}$, where $P_{PW} = |E_{PW}|^2 \pi D_l^2 / (8\zeta_0)$ and $|E_{PW}|$ is the amplitude of the incident plane wave. Since we know from the previous section that the field can be modelled by a local spherical wave until the lens angle, the magnetic field is given by $\vec{h}_{SDP}(\vec{r}) = \vec{r} \times \vec{e}_{SDP}(\vec{r})/\zeta_d$ and we can simplify the correlation integral in Eq. (4.17) to $2/\zeta_d \iint_{\Omega_{SB}} \vec{e}_{SDP} \cdot \vec{e}^{GO}_{S_{FO}}(\vec{k}_i)\, \mathrm{d}\Omega$, which is the integral given in [20]. However, we emphasize that this approximation is only valid when the lower focus F_2 coincides with the phase center of the feed. The main novelty here is that the FO sphere is in the near field of the LW feed where only the SDP field contribution is needed to evaluate the radiation properties of the lens-coupled LWA. Combining the FO approach with this spectral field decomposition is computationally very fast.

4.6.4 Leaky-Wave Antenna Performance

The aperture efficiency of silicon lenses has been calculated for lens diameters between $D = 1.5\lambda_0$ and $D = 15\lambda_0$ with a truncation angle θ_{SB} and phase center Δz given by Eqs. (4.9) and (4.13), respectively. The rest of the lens dimensions are derived as described above. The lenses are fed by the double-slot iris of [103] and have a quarter-wave anti-reflection coating with a permittivity of $\varepsilon_{AR} = 3.45$ on top. The resulting aperture efficiency is shown in Fig. 4.14. The highest aperture efficiency is obtained when $D = 4\lambda_0$ and is almost 80%. For comparison, the field over the FO sphere has also been calculated using the far-field approximation of Eq. (4.14), which is the first term in the asymptotic evaluation of the SDP integral. It can be seen that the aperture efficiency of the proposed lens geometry varies less than 5% as a function of the diameter with respect to the numerical evaluation of the SDP integral.

The bandwidth achieved by such silicon LW lens antennas is in the order of 15% [103]. A larger bandwidth, around 40%, can be achieved by using a lower permittivity lens [20]. The aperture efficiency of a plastic ($\varepsilon_r = 2.5$) lens at the central frequency is shown in Fig. 4.14, where the elliptical lens' geometry has been obtained from the phase center and shadow boundary angle as described as above. The aperture efficiency of a LW-fed plastic lens is above 80% when the lens diameter is larger than $2.5\lambda_0$. The plastic lens achieves a higher aperture efficiency than the silicon lens because there is a better matching of the leaky-wave feed far field to the incident GO field [20].

Depending on the source and lens diameter, a fine tuning of the lens parameters could lead to a slight increase of aperture efficiency. However, compared to the full-wave approach for the optimization of the phase correcting structure that have been presented in the literature [107], the fine tuning of the lens parameters here could also be achieved by using the SDP and FO approach, significantly decreasing the required optimization time.

The radiation patterns of the $D_l = 4\lambda_0$ silicon lens fed by the LW feed have been calculated using the same FO method in the near field described above, by varying $\hat{k}_i$ as explained in [94]. The radiation patterns of this lens are shown in Fig. 4.15, along with a full-wave simulation of the lens. The match between the patterns obtained with the FO methodology (black) and CST results (red) is excellent, especially in the main beam. The side-lobe level differs at most by 1 dB. The directivity of this lens antenna is 21 dBi. The performance of this single lens indicates we can efficiently feed lenses with a diameter as small as $4\lambda_0$, which is very relevant for communication [83], [94], [95] and space [106], [111] arrays that are not fully sampled. Moreover, the achieved performances of a lens design based only on the complex propagation constant provides higher aperture efficiency than other numerically optimized phase correcting structures or shielded cavity based LWAs [106]–[109].

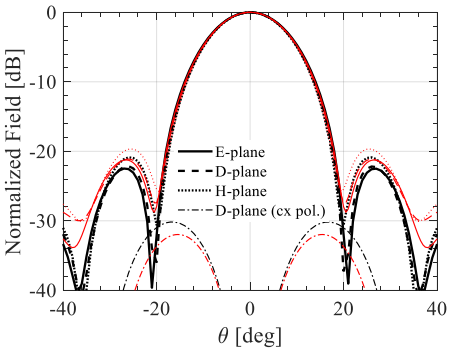

Fig. 4.15: Radiation pattern from a silicon lens with diameter of $D_l = 4\lambda_0$ fed by the LW stratification of Fig. 4.1 and double-slot iris from [103]. Black: SDP-FO method, red: full-wave simulations.

4.7 Conclusion

In this chapter, we have shown that the near field of leaky-wave resonant antennas radiating into a semi-infinite dielectric medium can be locally represented as a spherical wave in a certain solid angle around broadside from the phase center far below the ground plane. The near field in this solid angle can be efficiently evaluated via the integration of the spectral Green's function along the Steepest Descent Path (SDP), even very close to the LW cavity. Beyond this solid angle, defined as the shadow boundary angle, a contribution due to the leaky-wave pole must also be considered to fully describe the near field. It is shown that the LW complex propagation constants and the shadow boundary angle can be used to define the properties of the spherical wave formation accurately even in low contrast LW cases. Therefore, the physical insight gained in this analysis can be extended to other resonant LWAs made with different kind of stratifications such as FSS based cases.

To demonstrate the applicability of the proposed study, we apply the understanding of the near-field spherical wave formation to the design and analysis of small-to-medium sized lenses. It is shown that the LW complex propagation constants can be used to define a truncated lens geometry that couples well to the leaky-wave antennas and achieves a high aperture efficiency for any diameter. Moreover, we have combined the SDP calculation with an FO methodology in reception to efficiently calculate the aperture efficiency and radiation patterns of such lenses. A truncated silicon lens design with a diameter of only 4 free-space wavelengths is presented. This achieves almost 80% aperture efficiency. Excellent agreement with full-wave simulations is achieved, which demonstrates the accuracy of the SDP-FO methodology.

Part II
Leaky-Wave Lens Antennas

Chapter 5
Wideband Leaky-Wave Feed with Annular Corrugations in the Ground Plane

In this Chapter, we present a resonant leaky-wave lens antenna, fed by a circular waveguide with annular corrugations in the ground plane. The proposed leaky-wave feed reduces the impact of the spurious TM_0 leaky-wave mode in all planes over a wide bandwidth while reducing assembly complexity compared to previous methods. The proposed leaky-wave antenna has an aperture efficiency above 80%, a return loss below -15 dB, and a cross-polarization level below -20 dB in a bandwidth from 110-220 GHz (2:1). We have fabricated and measured a WR-5 band (140-220 GHz) antenna prototype with a lens diameter of 3 cm that achieves excellent agreement between measurement and simulation in terms of return loss, directivity and gain.

5.1 Introduction

Dielectric lens antennas fed by resonant leaky-wave (LW) feeds have been demonstrated at millimeter and submillimeter wavelengths, achieving high aperture efficiency and low losses [20], [94], [103], [111] for communication and sensing applications. Due to their high directivity and aperture efficiency, they have been proposed as lens elements in scanning lens phased arrays [94], [111] and fly's eye arrays [20].

Resonant LW feeds consist of a half-wavelength resonant air cavity between a ground plane and a semi-infinite dielectric material with relative permittivity ε_r (i.e., the dielectric lens). This resonant Fabry-Pérot like cavity supports the propagation of the main TM_1 / TE_1 leaky-wave modes that contribute to a directive beam around broadside in the semi-infinite dielectric [20], [97], [103]. Additionally, a spurious, nearly frequency-independent TM_0 LW mode, which propagates in the cavity and results in high cross-polarization, can reduce the aperture efficiency of the lens antenna. Therefore, the TM_0 mode is generally suppressed by the lens feed. Examples are a waveguide-fed double-slot iris [20], [103], a slot-fed dipole in PCB technology [94] and a dipole centered in the air cavity [95].

Although these LW feeds illuminate the lens with high aperture efficiency, the cross-polarization level of these antennas remains high when operated over a broad bandwidth due to poor TM_0 mode suppression. Furthermore, the development of double-slot irises is complex at (sub-)THz frequencies due to the need of a thin membrane

Parts of this Chapter have been published in **[J4]**.

[20], [103]. A recent overview of the state of the art in integrated lens antennas was given in [20].

Metallic corrugations, by contrast, can be fabricated with the same process as the waveguide itself. It is well known that quarter-wavelength corrugations can be used in parallel-plate waveguides (PPW) to attenuate the TEM mode [129]–[131]. They are also used as mode filter in horn antennas [132]. Corrugated ground planes with waveguides have been used to generate a single LW mode around broadside [133], [134] with a non-rotationally symmetric beam and in shielded Fabry-Pérot cavity antennas to enhance the aperture efficiency [106]. However, those geometries have not explored the possibility of using the corrugations to reduce the impact of the TM_0 LW mode in resonant LW lens antennas.

In this Chapter, we propose a resonant leaky-wave lens antenna feed (see Fig. 5.1) that greatly reduces the impact of the TM_0 mode in all planes over a wide bandwidth. At high frequencies, the TM_0 is suppressed due to the electrical size of a circular waveguide. At low frequencies, annular corrugations in the ground plane increase the attenuation constant of the TM_0 LW mode, similar to a TEM PPW mode enhancing the rotational symmetry and cross-polarization of the feed pattern. We present the optimization of the proposed feed to illuminate a plastic ($\varepsilon_r = 2.3$) lens with high aperture efficiency covering the WR-6 and WR-5 waveguide bands (110-220 GHz in total). The obtained performance is better than state-of-the-art plastic lens antennas [20] while reducing assembly complexity. We have manufactured and measured a WR-5 (140-220 GHz) prototype to corroborate these results.

5.2 Corrugated Leaky-Wave Antenna

The proposed LW lens antenna geometry is shown in Figs. 5.1a and 5.1b. It consists of a $\lambda_0/2$ air cavity with a low permittivity ($\varepsilon_r = 2.3$) elliptical dielectric lens to achieve wide bandwidth, as in [20]. The feeding structure is modified with respect to [20]. An open-ended circular waveguide, without a double-slot iris, is proposed here in combination with annular corrugations in the ground plane surrounding the waveguide. The low air-dielectric contrast ensures good impedance matching of waveguide over a wide bandwidth. A large circular waveguide can achieve better suppression of the TM_0 LW mode in all azimuthal directions compared to a square waveguide. However, a large diameter of such circular waveguide will lead to a significant frequency variation of the primary field (i.e., field radiated into the semi-infinite dielectric medium). Consequently, poor lens aperture efficiency over a large bandwidth will be achieved. Therefore, we have added annular corrugations in the ground plane that reduce the impact of the TM_0 LW mode close to the cut-off frequency of the waveguide, and therefore enlarge the antenna's overall bandwidth.

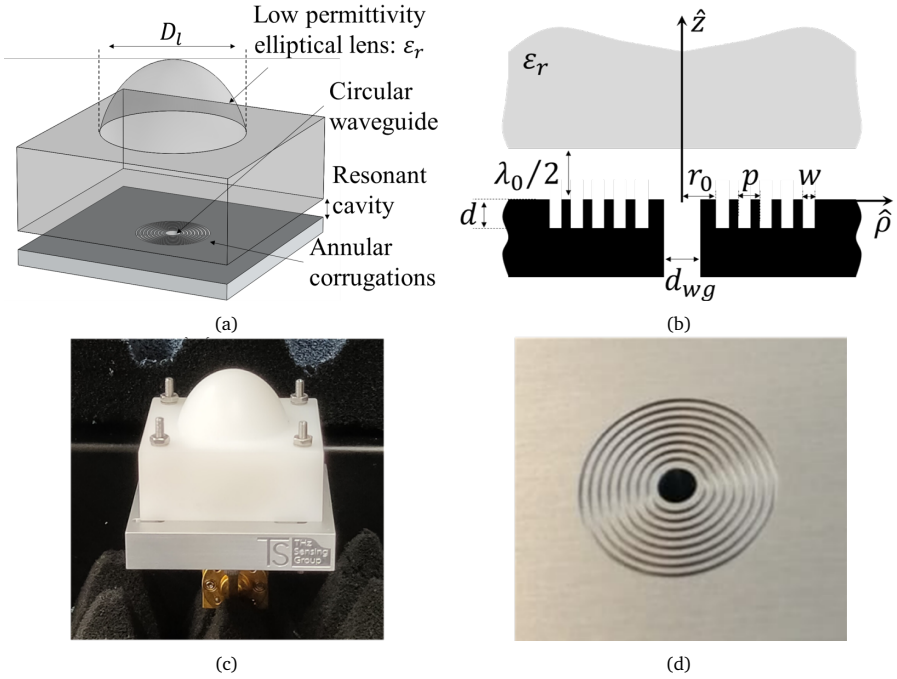

Fig. 5.1: (a) Geometry of the proposed LW lens antenna. (b) Dimensions of the feed stratification consisting of a circular waveguide, corrugated ground plane, air cavity and semi-infinite medium. Photographs of (c) the assembled prototype and of (d) the circular waveguide and annular corrugations.

5.2.1 Geometry Optimization for 2:1 Bandwidth

The proposed LW feed geometry is optimized as explained in this section for operation in a 2:1 bandwidth (110-220 GHz). First, the circular waveguide diameter is chosen to be the smallest possible to achieve a good impedance match starting at 110 GHz while exciting only the fundamental mode. A diameter $d_{wg} = 0.95\lambda_0$ leads to a cut-off frequency of 102 GHz, giving a good compromise between the excitation of higher-order modes at high frequencies and the impedance match at low frequencies. The achieved reflection coefficient (S_{11}) is below -15 dB over the entire bandwidth of interest, see Fig. 5.2a. For reference, the achieved impedance matching bandwidth with a double-slot iris feed as in [20] is also given.

Second, we maximize the aperture efficiency of a truncated elliptical dielectric lens with a diameter of 3 cm ($16.5\lambda_0, \lambda_0$ being defined at 165 GHz) over the entire 110-220 GHz bandwidth to find the optimal corrugation dimensions. The performance of this lens antenna is evaluated using the analysis procedure described in [20]: First, the primary fields are obtained in the entire bandwidth by a full-wave simulation for a specific feed structure. Second, the aperture efficiency of the lens is calculated in

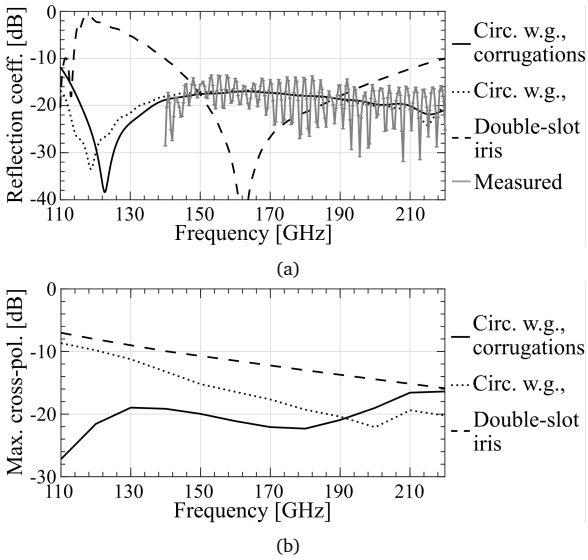

Fig. 5.2: (a) Simulated reflection coefficient and (b) cross-polarization in the primary field of the three compared LW feeds: double-slot iris, circular waveguide and circular waveguide with corrugated ground plane. The measured reflection coefficient of the prototype in Fig. 5.1c is shown in (a).

reception using the Fourier Optics (FO) approach [96], optimizing for the phase center Δz and θ_0. This procedure is iterated as a function of the depth (d), width (w), periodicity (p) and distance from the waveguide (r_0) of the corrugations as indicated in Fig. 5.1a.

Starting from the dimensions in [130]: $d = p = \lambda_0/4$, $w = \lambda_0/10$, we found the optimized dimensions to be $d = 0.33\lambda_0$, $p = 0.23\lambda_0$, $w = 0.11\lambda_0$, $r_0 = 0.69\lambda_0$. We found that geometries with 8 corrugations are sufficient to enhance the aperture efficiency at the low frequencies. The lens geometry that maximizes the aperture efficiency is found as having $\Delta z = -0.66\lambda_0$ with a truncation angle of $\theta_0 = 36.5^\circ$ seen from the phase center. The optimized phased center and lens truncation angle are in line with the theoretical ones in Fig. 4.13b based on the LW propagation constants of the TM_1 and TE_1 modes.

The aperture efficiency as a function of the frequency for the optimized lens antenna with a corrugated LW feed is shown in Fig. 5.3a. The aperture efficiency is above 80% over the entire bandwidth, which is significantly higher than the same antenna without corrugations and the double-slot iris feed, especially at the low frequencies. The figure indicates that the circular waveguide feed without corrugations performs similar to the double-iris in the WR-5 band (with a significant reduction in the fabrication and assembly complexity). If an extended bandwidth is targeted (WR-5 and WR-6), the corrugated LW feed is the best performing solution. The achieved reflection coefficient

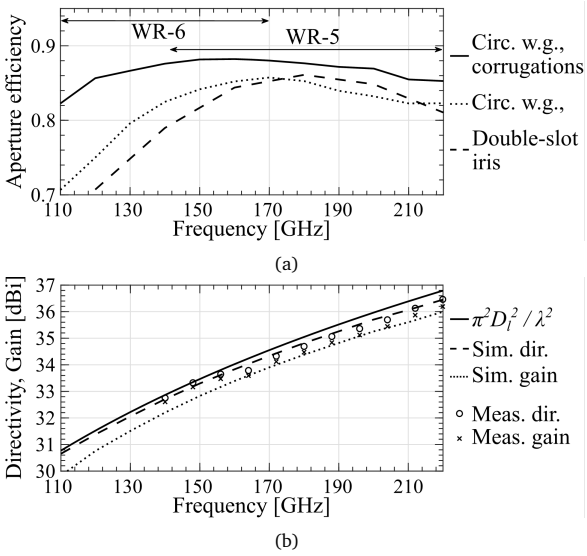

Fig. 5.3: (a) Simulated aperture efficiency for the same feeds as in Fig. 5.2. (b) Simulated and measured directivity and gain of the corrugated LW feed. The circles and crosses in (b) correspond to measured directivity and gain, respectively.

with this corrugated feed is in line with the one without the corrugations as shown in Fig. 5.2a.

5.2.2 Radiation Patterns in the Semi-Infinite Dielectric Medium

To better understand the enhancement of the aperture efficiency achieved due to the corrugations, it is useful to compare the primary fields at 110 GHz with or without corrugations shown in Fig. 5.4a. The primary patterns of the corrugated waveguide are significantly more rotationally symmetric and have lower cross-polarization. The cross-polarization level is reduced from -8 dB to -27 dB when the corrugations are added. The cross-polarization in the primary fields over the entire bandwidth is reported in Fig. 5.2b for the three considered LW feeds. At the high end of the bandwidth, the cross polarization of the circular waveguide with and without corrugations is comparable. Indeed, the suppression of the TM_0 LW mode is achieved at the higher part of the band thanks to the large size of the circular waveguide - its Fourier Transform has a null approximately in the same direction as the TM_0 LW mode - and not the corrugations.

The aperture efficiency can be calculated as a field match between the field on a sphere centered at the lens focus propagated via Geometrical Optics (GO) from an incident plane wave on the lens, i.e., the GO field, and the feed primary pattern [96]. The highest aperture efficiency is achieved when these fields are a conjugate match. The frequency-independent GO field was given in [20] and is also shown in Fig. 5.4

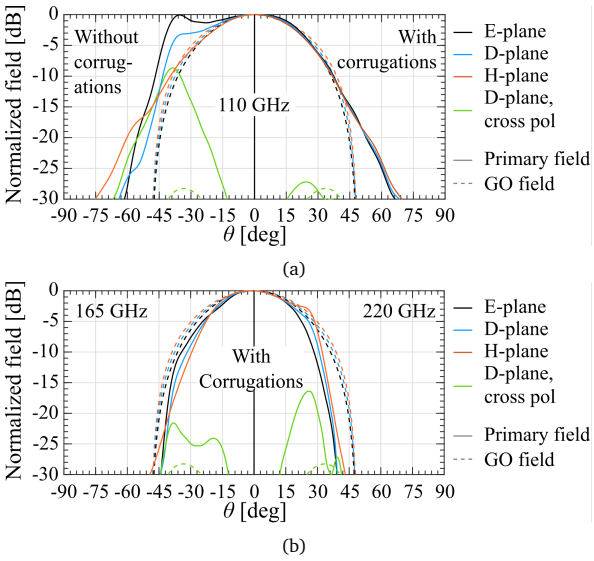

Fig. 5.4: Comparison between the primary and GO fields. (a) Fields at 110 GHz of the LW feed without (left) or with (right) corrugations. (b) Fields of the LW feed with corrugations at 165 GHz (left) and 220 GHz (right).

(dashed lines) for comparison. It is clear from Fig. 5.4a that the field match to the GO field is much better at the low frequency band if the corrugations are used. The primary patterns of the corrugated LW feed at 165 GHz and 220 GHz are shown in Fig. 5.4b. A good match between the incident GO field and the primary patterns is observed leading to an aperture efficiency higher than 80% over the entire bandwidth.

5.2.3 TM_0 Mode Suppression

To understand the effect that the corrugations have on the TM_0 LW poles, we analyzed the fields in the resonant cavity using full-wave simulations with a large number of corrugations, i.e., 20. Radially close to the waveguide ($\rho \leq \lambda_0$, see Fig. 5.1b), the field is given by the sum of the space wave contribution and the TM_1 / TE_1 LW modal fields [135]. For larger ρ, the TM_0 modal field is dominant. Since the TM_0 modal field is mostly polarized along $\hat{z}$ [111], we can study the effect of the corrugations by analyzing the $\hat{z}$-component of the electric field in the middle of the resonant cavity (i.e., at $z = h/2$) as a function of ρ. We show $|E_z|\sqrt{\rho}$ in the D-plane in Fig. 5.5 to remove the cylindrical spreading of the LW modal fields. The figure compares the LW feed with and without the corrugations at beginning, middle and end of the bandwidth. The results show that the $|E_z|\sqrt{\rho}$ level at the end of the corrugated section is lower when the corrugations are present. The highest attenuation is achieved at low frequencies.

It is well known that periodic structures do not fully suppress a mode, but do impact its attenuation constant [131]. Since the modal field is proportional to $e^{-j\beta_{TM0}\rho}$

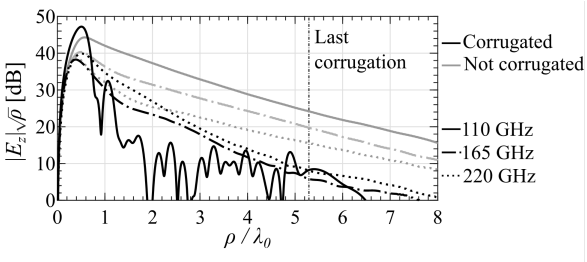

Fig. 5.5: Electric field along $\hat{z}$ at $z = h/2$ as function of the radial direction in the D-plane for the LW feed with or without corrugations at three frequencies.

$\cdot\, e^{-\alpha_{TM0}\rho}/\sqrt{\rho}$ [131], the TM_0 phase and attenuation constants, β_{TM0} and α_{TM0}, respectively, can be calculated from the simulated E_z. At the central frequency and no corrugations, it is found that $\beta_{TM0}/k_d = 0.6$ and $\alpha_{TM0}/k_d = 0.045$, in line with the analytical result from the dispersion equation [20]. The attenuation constant corresponds to -3.7 dB/λ_0. For the corrugated ground plane, $\alpha_{TM0}/k_d = 0.086$ has been found, which corresponds to -7.1 dB/λ_0. Therefore, the corrugations decrease the impact of the TM_0 mode even in the middle of the bandwidth.

5.2.4 Lens Antenna Radiation Performance

We calculated the radiation patterns of the lens antenna fed by the proposed corrugated LW feed (secondary patterns) using the FO approach in reception [96]. The secondary patterns are shown in Figs. 5.6a and 5.6b at 140 and 220 GHz, respectively. The patterns are highly symmetric around broadside and achieve a sidelobe level of between -20 dB to -17 dB in the bandwidth, which is very close to the sidelobe level of a uniform circular current distribution of 3 cm in diameter. The simulated cross polarization of the secondary patterns is below -25 dB across the full bandwidth.

The simulated directivity and gain of the lens antenna are shown in Fig. 5.3b as a function of the frequency. The directivity and gain have been calculated using full-wave simulations of the lens antenna in CST. For the gain, the dielectric losses in the plastic (below 0.5 dB) and ohmic losses in the aluminum ground plane (below 0.05 dB) are taken into account. The maximum directivity that can be achieved by a 3 cm diameter lens is shown for reference, which is at most 0.2 dB higher than the simulated directivity. The simulated gain is around 0.8 dB below the maximum achievable directivity in the full bandwidth.

5.3 Validation with WR-5 Antenna Prototype

We have fabricated and measured two identical G-band (WR-5, 140-220 GHz) prototypes to validate the simulated performance. The fabricated antennas, shown in Fig. 5.1c, consist of an HDPE lens with a diameter of 3 cm and a 1 cm thick aluminum

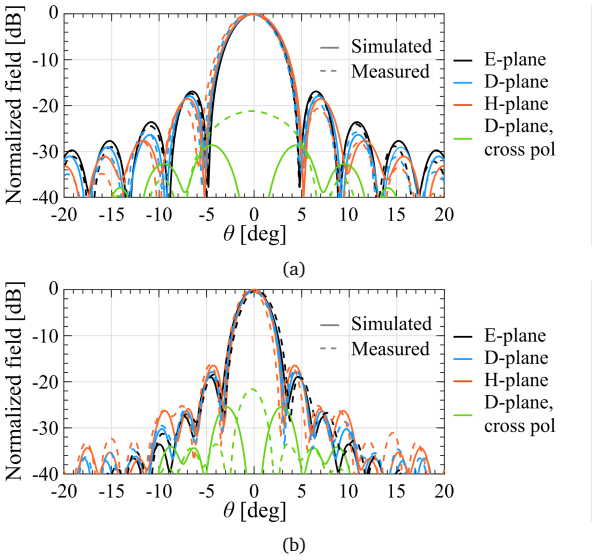

Fig. 5.6: Simulated (solid) and measured (dashed) radiation patterns at (a) 140 GHz and (b) 220 GHz.

split block with a WR-5 flange on the bottom that is tapered to a circular waveguide. A CNC milling process was used for the fabrication of the lens and the split block; the corrugations were milled into the ground plane after assembling the split block, see Fig. 5.1d.

The measured reflection coefficient of the antenna prototype is shown in Fig. 5.2a. An excellent agreement is achieved with the simulated value: below -15 dB in the entire bandwidth. The antenna prototype was measured on a planar near-field antenna measurement setup using a PNA with WR-5 frequency extenders. A WR-5 waveguide probe was used to sample the field at 4 cm above the lens surface. The far-field radiation patterns were calculated from the 2D near-field scans using standard near-to-far field conversion. The obtained radiation patterns are shown in Figs. 5.6a and 5.6b at 140 GHz and 220 GHz with excellent agreement to full-wave simulations. The increase in measured cross-polarization is due to limited fabrication tolerances in the waveguide split-block transition which causes the excitation of the orthogonal mode in the circular waveguide. As a result, the measured cross-polarized patterns have a similar shape to the co-polarized patterns. The measured directivity is compared to the simulated values in Fig. 5.3b, giving a very good agreement between measurement and simulation in the entire WR-5 band. The machining tolerance achieved in corrugations was less than 20 μm and was found not to have a significant effect on the performance.

The procedure in [20] has been followed to measure the gain. Two lenses were

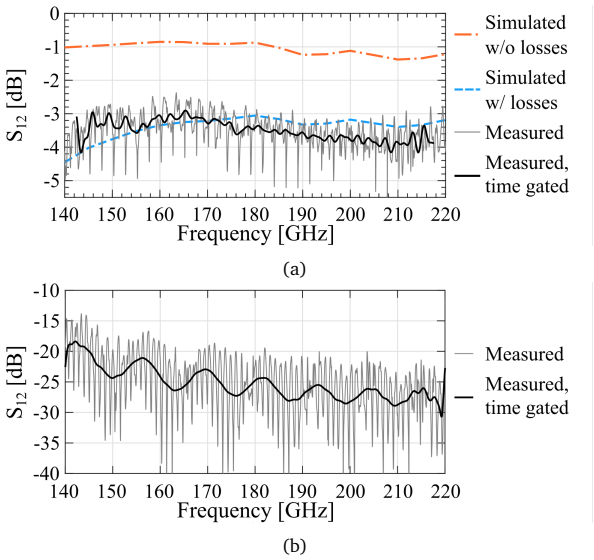

Fig. 5.7: Simulated and measured near-field coupling between two lenses that are (a) co- and (b) cross-polarized.

placed facing each other at a distance of 1.5 cm, and the S_{12} was measured. The result is shown in Fig. 5.7a in gray. The raw measurements oscillate ± 1 dB around the time-gated value (black), a significant improvement with respect to the 8 dB in [20], which we attribute to the higher aperture efficiency achieved. For comparison to the simulations, the S_{12} has been time-gated after the first received pulse as in [20]. The simulation results in a lens-to-lens coupling of around -1 dB in the entire WR-5 band, i.e., around 90% efficiency per lens. The losses in the waveguide are lower than 1.6 dB ($\sigma = 3.6 \cdot 10^5$ S/m) and the losses in the plastic lens are below 0.3 dB ($\tan\delta = 3.3 \cdot 10^{-4}$). When the losses are combined with the semi-analytical simulation, the lens-to-lens coupling is around -3.5 dB, which is in excellent agreement with the measured value. The measured antenna gain, shown in Fig. 5.3b, is calculated from the measured directivity and takes into account the dielectric loss in the lens. The gain is in excellent agreement with simulations.

The cross-polarization coupling was measured using the same procedure, but with one antenna rotated 90° around the z-axis. The simulated coupling between orthogonal antennas is zero owing to the null at broadside in the simulated cross-polarized pattern. However, due to the limited fabrication accuracy in the waveguide split block, the measured coupling is between -20 dB and -30 dB as shown in Fig. 5.7b, which is in line with the measured cross-polarization level at broadside (Fig. 5.6).

5.4 Conclusion

We have presented a resonant leaky-wave antenna feed for plastic lenses that includes annular corrugations in the ground plane around a circular waveguide. These corrugations in combination with the circular waveguide significantly reduce the impact of the spurious TM_0 mode in a wide bandwidth and all azimuthal planes. The corrugations extend the achieved bandwidth of the circular waveguide feed to lower frequencies to cover both the WR-5 and WR-6 bands, leading to a total bandwidth of 2:1. A lens illuminated by such LW feed is shown to have cross-polarization level below -20 dB, an aperture efficiency above 80% and an S_{11} below -15 dB over the entire bandwidth. We fabricated and measured a WR-5 band prototype which shows excellent agreement with the anticipated results.

Chapter 6
Multimode Leaky-Wave Waveguide Feed

In this chapter, we present the beam-shaping capabilities of LW feeds radiating into dense media when an artificially synthesized quarter-wavelength layer is added between a resonant air cavity and a dense semi-infinite medium. The complete LW feed geometry consists of a waveguide opening into a ground plane in the presence of $\lambda_0/2$ air cavity and a dielectric transformer slab of thickness $\lambda_0/4\sqrt{\varepsilon_m}$ below a semi-infinite medium, as shown in Fig. 6.1a. The relative permittivity ε_m is used to tune the propagation properties of LWs present in the cavity. In the following section, we analyze the LW modes and compare them to the ones in the standard stratification shown in Fig. 6.1b [103], which lacks the transformer layer. We have found that the inclusion of the quarter-wavelength transformer enables high lens aperture efficiency (>80%) by exciting multiple LW modes. The use of multiple modes to illuminate quasi-optical systems was first demonstrated in [105] over a 10% bandwidth. Here, the achieved bandwidth is above 35%. Moreover, no double-slot iris is needed to match the input impedance of the structure to a waveguide which significantly simplifies the fabrication and assembly complexity of the feed at (sub)-THz frequencies.

6.1 Introduction

6.1.1 LW Mode Analysis

In the standard stratification with a half wavelength cavity below a semi-infinite dense medium [see Fig. 6.1b], there is a pair of nearly degenerate TM_1 / TE_1 LW modes that radiate close to broadside, plus a TM_0 mode radiating toward the critical angle [103]. This TM_0 mode is usually suppressed with a double slot iris in order to efficiently illuminate a lens [103]. In Fig. 6.2a, the propagation constants $k_\rho = k_0\sqrt{\varepsilon_m}(\sin\theta_{LW} + j\alpha_{LW})$, with LW pointing angle θ_{LW} and attenuation α_{LW}, of the three modes in a silicon infinite medium are shown as a function of frequency. The TM_1/ TE_1 pair points toward $\theta_{LW} \approx 5^\circ$ and a frequency-independent TM_0 mode points toward $\theta_{LW} \approx 18^\circ$. When the transformer layer is introduced, the propagation properties of these modes as well as the number of modes change. For instance, Fig. 6.2b shows the propagation constants of the LW modes as a function of frequency when $\varepsilon_m = 2.5$. It can be observed that there are three TM modes and two TE modes for this geometry.

Parts of this Chapter have been published in **[J1]**.

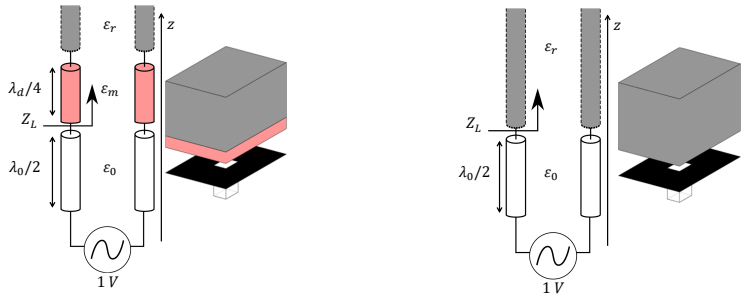

Fig. 6.1: Stratification and equivalent transmission line model of (a) the proposed LW antenna in this work and (b) the standard LW antenna in [103].

To understand the topology of the different LW modes present in the stratification, it is useful to evaluate the ρ-component of the modal field inside the stratification as follows [119]:

$$e_\rho\ (\vec{r}) = \frac{-jk_{\rho i}\cos\phi}{2}\mathrm{Res}\left(V_{\text{TM}}\left(k_{\rho i}, z\right)\right) H_0^{(2)}\left(k_{\rho i}\rho\right)$$

where $\mathrm{Res}\left(V_{\text{TM}}(k_{\rho i}, z)\right)$ is the residue of the TM voltage solution of the transmission line in Fig. 6.1 evaluated at pole location $k_{\rho i}$ (see Fig. 6.2), and $H_0^{(2)}$ is the zeroth-order Hankel function of the second kind. The modal fields e_ρ corresponding to the TM modes in the standard stratification are shown in Fig. 6.3a as a function of z. The profile of the modes inside the cavity is similar to the modes that propagate in a parallel-plate waveguide (PPW) with a plate separation of $h_0 = \lambda/2$ [136]. For instance, the TM_1 / TE_1 modal field resembles a $\sin(\pi z/h_0)$-like shape.

When the transformer has a relative permittivity $\varepsilon_m > 5$ and thickness $\lambda_0/4\sqrt{\varepsilon_m}$, the poles and resulting modal fields are very similar to the results from [103]. The presence of the quarter-wave transformer makes Z_L larger than the impedance of the infinite medium, which is the opposite effect to a standard LW radiating into free-space [97]. The LW angle and attenuation constant are larger because the impedance contrast between Z_L and Z_0 is reduced. For example, the modal fields are shown in Fig. 6.3a (thin lines) for $\varepsilon_m = 8$. The associated propagation constant at the resonant frequency is shown in Fig. 6.4.

When the relative permittivity of the transformer layer is small $1 < \varepsilon_m < 3$, the reflection at the top of the cavity is very small and therefore the structure is comparable to a PPW with a plate separation of $3\lambda_0/4$. However, in contrast to the PPW, the TM_2 / TE_2 modes are not in cutoff because there is no PEC boundary condition at $z = 3\lambda_0/4$.

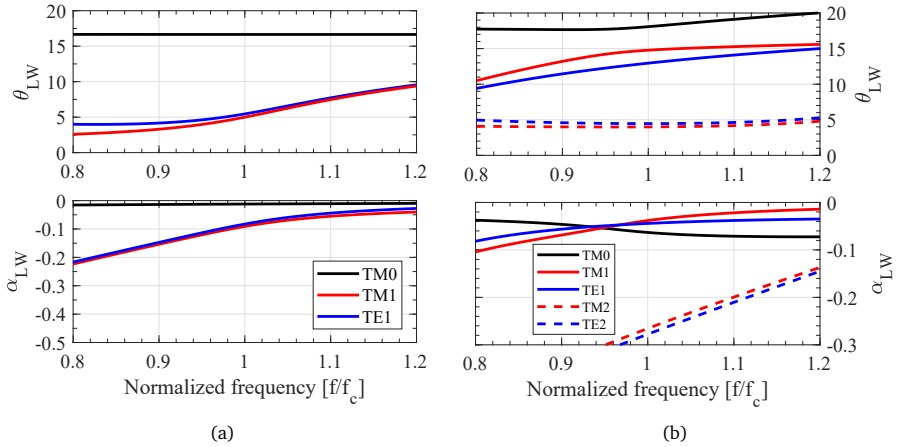

Fig. 6.2: Frequency dispersion diagram of the LW modes, radiating into an infinite silicon medium, in the presence of a $\lambda_0/2$ air cavity (a) without and (b) with a $\varepsilon_m = 2.5$ transformer.

Therefore, five modes propagate in this configuration. The frequency behavior of the five poles is shown in Fig. 6.2b for $\varepsilon_m = 2.5$. The TM_0 mode is similar to the TM_0 mode in Fig. 6.2a. The attenuation α^1_{LW} of TM_1 / TE_1 poles is lower and their pointing angle $\theta^1_{LW} \approx 15°$ is larger than without transformer. The TM_2 / TE_2 modes attenuate quickly and have a pointing angle $\theta^1_{LW} \approx 5°$. The modal field components e_ρ along z corresponding to this stratification are shown in Fig. 6.3b. The TM_0 and TM_1 field profiles are similar to the fields shown in Fig. 6.3a. It is clear that the TM_2 mode shows a $\sin(2\pi z/(h_0+h_1))$-shape, which is similar to the profile of the TM_2 mode in a PPW.

A complete overview of the five LW modes that propagate in the stratification at f_c is shown in Fig. 6.4 as a function of ε_m. The regions $\varepsilon_m < 3$ and $\varepsilon_m > 5$ in which the LW modes resemble PPW modes are indicated in the figure with $h_0 = 3\lambda_0/4$ and $h_0 = \lambda_0/2$, respectively. In the region $3 \leq \varepsilon_m \leq 5$, the TM poles switch roles which corresponds to the region, where $Z_L \approx 120\pi$. For example, the TM_0 pole for $\varepsilon_m < 3$ is associated with the TM_2 mode for $\varepsilon_m > 5$. Therefore, a transition region $3 \leq \varepsilon_m \leq 5$ is required so that the numbering of the modes and the associated field profile are consistent with both those in a PPW [136] and the stratification without transformer [103].

The far field radiated into the semi-infinite dielectric is evaluated using the spectral Green's function (SGF) approach [105]. To identify the contribution of each of these modes in the far field, the total voltage solution in the transmission line of Fig. 6.1a

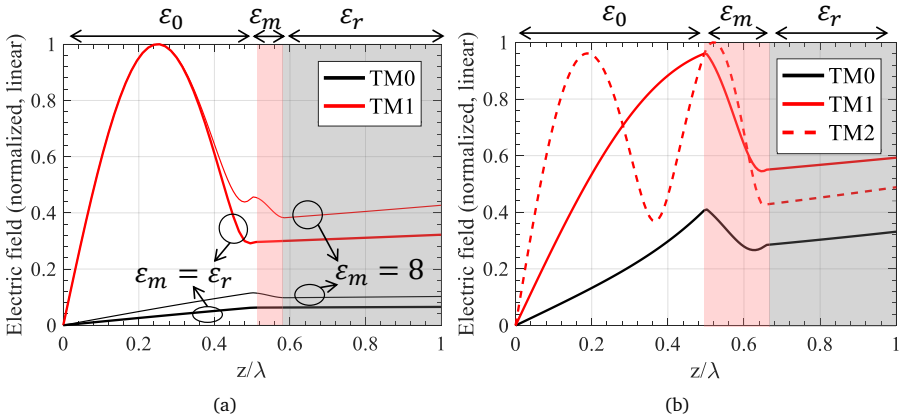

Fig. 6.3: TM modal fields (ρ-component) at the central frequency along z in the stratifications of (a) Fig. 6.1a with $\varepsilon_m = 8$ (thin lines) and of Fig. 6.1b (thick lines) and of (b) Fig. 6.1a with $\varepsilon_m = 2.5$.

can be approximated around each LW pole $k_{\rho i}$ as follows [97], [105]:

$$V_{\text{TM/TE}}(k_\rho)\big|_{k_\rho \approx k_{\rho i}} = \frac{2k_{\rho i}}{k_\rho^2 - k_{\rho i}^2}\text{Res}\left(V_{\text{TM/TE}}(k_{\rho i})\right) \tag{6.1}$$

Fig. 6.5 shows the far-field contribution due to each LW pole, using Eq. (6.1), for $\varepsilon_m = 2.5$ and a square waveguide of size $0.68\lambda_0$ (the colors correspond to the poles in Fig. 6.2). In the H-plane [see Fig. 6.5a], the contributions are due to TE modes, whereas the E-plane contributions [see Fig. 6.5b] are due to TM modes. The sum of the LW pole contributions (dashed gray) is a good approximation of the far field radiation pattern calculated with the non-approximated voltage solution (solid gray). The radiation pattern resembles a "top-hat" pattern: it is nearly uniform in the region $\theta \leq 15°$ and then rapidly decays. This beam shape can be attributed to the presence of multiple LW modes that together illuminate the region nearly uniformly and results in a high aperture efficiency when it is coupled to a lens with $f_\# = 1.8$.

6.1.2 Optimal Transformer Permittivity

The optimal transformer permittivity was found by evaluating the aperture efficiency of a silicon elliptical lens fed by a number of different stratifications with $1 < \varepsilon_m < 11.9$. Note that $f_\#$ of the lens is different for each ε_m.

The aperture efficiency of the lens antenna was calculated in reception using a Fourier Optics (FO) approach [137] and assuming a lens with a quarter-wavelength of perfect anti-reflective coating at $f_c = 550$ GHz. The optimization consisted of finding out the optimal phase center, lens $f_\#$ and iris geometry similar to what it was done in [20]. With this approach, we have calculated the aperture efficiency in the frequency

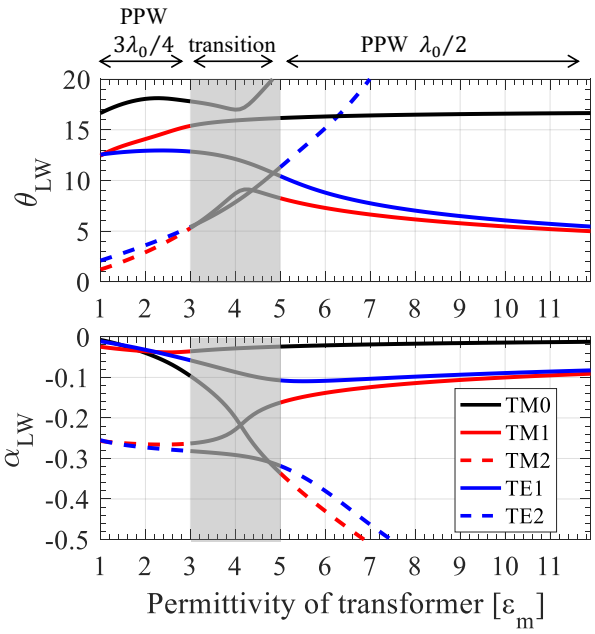

Fig. 6.4: LW poles present in the stratification of Fig. 6.1a at the central frequency for different choices of dielectric permittivity of the transformer layer, ε_m between 1 and 11.9.

range 400–750 GHz of different transformer relative permittivities ε_m to determine its optimal value.

The results of the aperture efficiency optimization are shown, for several values of ε_m, in Fig. 6.6. The aperture efficiency bandwidth, defined as the bandwidth in which the aperture efficiency is larger than 80%, is larger for any choice of transformer permittivity than for the standard case. Furthermore, a lower transformer permittivity corresponds to a lower lens $f_\#$, which is consistent with the pointing angles of the main modes in Fig. 6.4. The optimal value for the transformer relative permittivity is found to be $\varepsilon_m = 2.5$, which couples to a $f_\# = 1.8$ lens with an aperture efficiency bandwidth of 35%.

It was found that when $\varepsilon_m > 5$, it is necessary to suppress the TM_0 mode since only the TM_1 / TE_1 modes will be exploited for the pattern shaping, for example, by using a double-slot iris [103]. When $\varepsilon_m \leq 5$, all the modes are used to synthesize the top-hat pattern as in Fig. 6.5 and the structure can be fed directly by an open-ended waveguide. Specifically, using an open-ended square waveguide of size $0.68\lambda_0$ leads to a decrease of only 2% in aperture efficiency, as shown in Fig. 6.6, while significantly simplifying the fabrication and assembly complexity.

The optimized LW lens antenna has a truncation angle of $15.5°$ and a phase center of

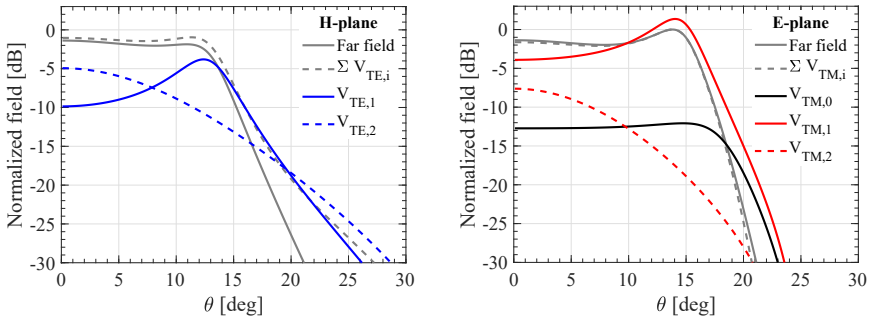

Fig. 6.5: Far-field radiation pattern in (a) the H-plane and (b) E-plane decomposed into the contributions from each LW pole (see Fig. 6.2b), calculated using Eq. (6.1) for the stratification in Fig. 6.1a with $\varepsilon_m = 2.5$ at the central frequency. The structure is fed by a square waveguide of size $0.68\lambda_0$.

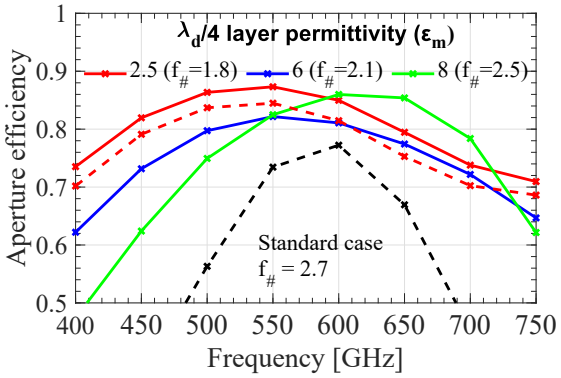

Fig. 6.6: Lens aperture efficiency as a function of frequency when fed by the multimode LW feed in Fig. 6.1a for different values of ε_m. The $f_\#$ of the lens varies for each permittivity. A double-slot iris has been used for the results shown in solid lines, while the red dashed line has been simulated with an open-ended square waveguide of $0.68\lambda_0$.

1.44 mm below the ground plane. An overview of the single lens geometrical parameters is given in Fig. 6.7a. The far-field radiation patterns (i.e., the primary patterns) into the silicon lens are shown in Fig. 6.7b.

The input impedance of the waveguide in the presence of the proposed stratification has been calculated as in [105] using:

$$\frac{1}{Z_{\text{in}}} = \frac{1}{4\pi^2} \int_{-\infty}^{\infty} \int_{-\infty}^{\infty} \left| M_x(k_x, k_y) \right|^2 G_{xx}^{hm}(k_x, k_y, z = 0)\, \mathrm{d}k_x\, \mathrm{d}k_y \tag{6.2}$$

where G_{xx}^{hm} is the SGF of the structure in Fig. 6.1a and M_x is the spectral current associated with the TE_{10} waveguide mode. This result is validated with the impedance

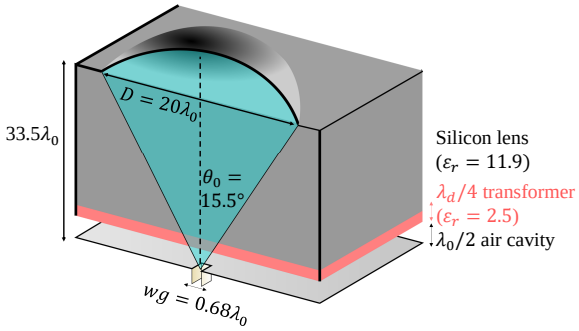

(a)

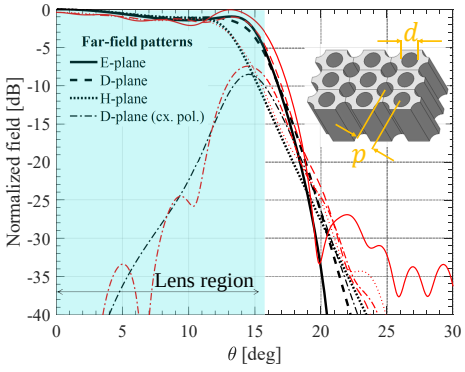

(b)

Fig. 6.7: (a) Cross section of a single elliptical lens array element fed with the optimized LW feed and its geometrical parameters. (b) Far-field radiation patterns into an infinite silicon medium by the lens feed shown in (a). Fields calculated using the SGF in black, full-wave results in red are done with the perforated silicon layer shown in the inset, where periodicity $p = 79\mu$m and hole diameter $d = 73\mu$m.

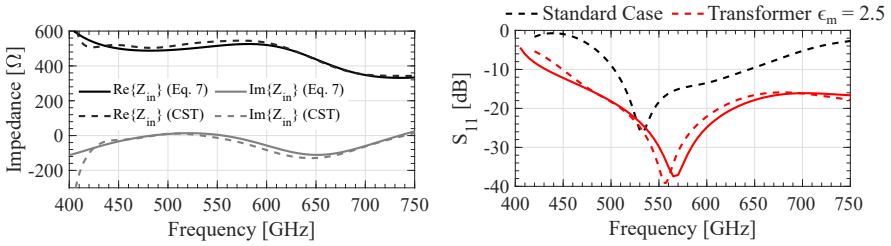

Fig. 6.8: (a) Waveguide impedance from full-wave simulations (dashed) compared to Eq. (6.2) (solid) and (b) the associated reflection coefficient of the optimized lens antenna with transformer layer compared to the standard case [103].

obtained from CST in Fig. 6.8a. The agreement between the result of Eq. (6.2) and the full-wave simulation is excellent. Furthermore, Z_{in} is not strongly frequency dependent and can be matched without a double-slot iris.

The simulated reflection coefficient is shown in Fig. 6.8b, calculated using Eq. (6.2) and compared to the full-wave approach. The reflection coefficient is below -10 dB for frequencies higher than 450 GHz. The impedance bandwidth is significantly larger than the standard structure without a transformer layer fed by a double-slot iris [103]. The bandwidth of the antenna is not limited by the impedance matching bandwidth but by the frequency dispersion of the radiation patterns.

6.2 Lens Phased Array Performances

In this section, we investigate the performance of the scanning lens-phased array based on the proposed multimode LW feed. The considered array topology is the same as discussed in Chapter 2, consisting of 19 lenses of diameter $D_l = 20\lambda_0$ in a hexagonal grid. Each lens is fed by the waveguide-fed LW stratification discussed in Section 6.1 and is covered by a quarter-wavelength AR coating. The waveguide's E-plane is parallel to $\hat{x}$, according to the reference system shown in the inset of Fig. 2.1. The lens and array geometry are shown in Fig. 6.7a and the inset of Fig. 2.1, respectively.

6.2.1 Single Lens Element Performance

The broadside and steering properties of a single lens element at 550 GHz have been analyzed using the FO approach described in [137]. In this model, the effect of multiple reflections at the lens surface or spillover at the lens edge is not taken into account; instead, they are included as a loss in the gain. However, because of the AR coating of the lens, multiple reflections are low, and due to the proposed multimode LW feed, the spillover is low as well.

The broadside patterns radiated by a single lens element with the proposed LW feed (i.e., the secondary patterns) are shown in Figs. 6.9a and 6.9b. The pattern displays

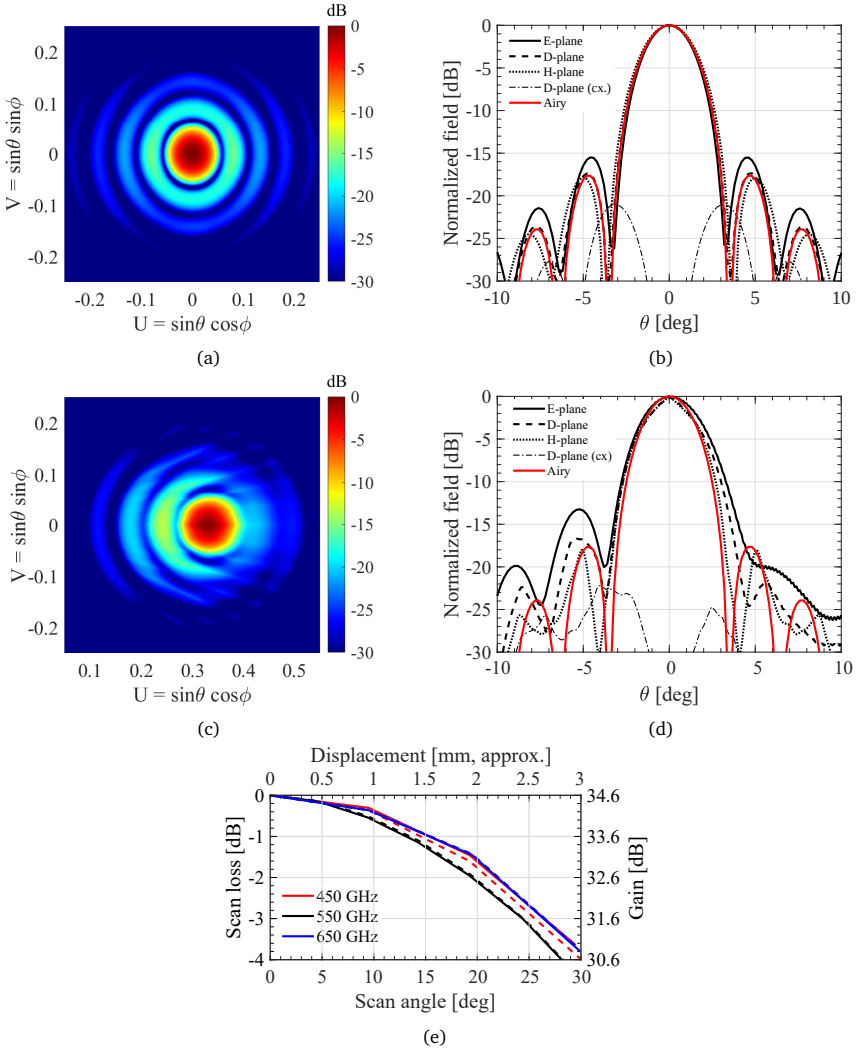

Fig. 6.9: Radiation pattern of a single lens for (a) and (b) broadside and (c) and (d) scanned to 20° at 550 GHz. The scan loss and gain of the lens element pattern is shown in (e) as a function of scan angle and approximate displacement.

good symmetry at broadside. The side-lobes are slightly lower in the H-plane due to the taper of the primary pattern in this plane [see Fig. 6.7b]. Furthermore, the pattern strongly resembles an airy pattern radiated by a $20\lambda_0$ uniform circular current distribution (shown in red). A directivity of 35.7 dBi in the array element pattern is achieved with an aperture efficiency of 85%.

Next, the lens is displaced 2 mm relative to the feed along the E-plane. This results in a scan angle in the secondary pattern of 19.2°. The scanned secondary radiation pattern is shown in Fig. 6.9c in UV-coordinates. Fig. 6.9d shows the radiation pattern, where the beam has been rotated toward its maximum to show the three main planes. The radiation pattern in the H-plane is almost the same as the broadside pattern. In the E-plane, the side-lobes become 2 dB higher and the main beam is broadened. The directivity of the steerable array element pattern toward 19.2° is 34.6 dBi with an aperture efficiency of 54%. The scan loss (i.e., the gain relative to broadside) of the single lens is shown in Fig. 6.9e. The lens can be scanned up to 25° (2.5 mm lens displacement) in both the E- and H-planes with a loss below 3 dB. It can also be seen in the same figure that the achieved scan loss is stable over the entire 35% bandwidth.

6.2.2 Lens Phased Array Performance

In order to evaluate the steering properties of the 19-element lens phased array, we multiply the obtained single lens patterns with the corresponding array factor. Since the array periodicity is very large, no mutual coupling effects will be present in this case. For broadside, all the array elements are fed in phase; for the scanned cases the lenses are fed progressively.

For broadside, Figs. 6.10a and 6.10b, the grating lobe level is -17 dB with a gain of 48.2 dB. When scanning to 19.2°, shown in Figs. 6.10c and 6.10d, the highest grating lobe is in the E-plane and is -13.2 dB. The grating lobe level is higher than the broadside case due to the lower aperture efficiency of the scanned lens, but still acceptable for many applications. The gain when scanning the array toward 19.2° is 46.7 dB. The E-plane radiation pattern is shown in Fig. 6.10e for scan angles up to 30°.

6.3 LW Lens Antenna Prototype at 550 GHz

A prototype at 550 GHz has been developed to validate the radiation properties of the LW feed and demonstrate the dynamic steering capabilities of the proposed lens antenna. The prototype, shown in Fig. 6.11, consists of a silicon lens array where the central element is fed by the proposed LW feed. The overall array geometry is a scaled version of the one shown in Section 6.1, in order to fit the array in the metal fixture developed in [86]. The number of elements has been reduced to 7, marked in gray in the inset of Fig. 2.1 and the lens diameter is around $10\lambda_0$ instead of $20\lambda_0$. As a consequence of the smaller diameter, the lens surface lies in the near field of the feed. For this specific diameter of $10\lambda_0$, we have optimized the lens subtended angle θ_0, as in

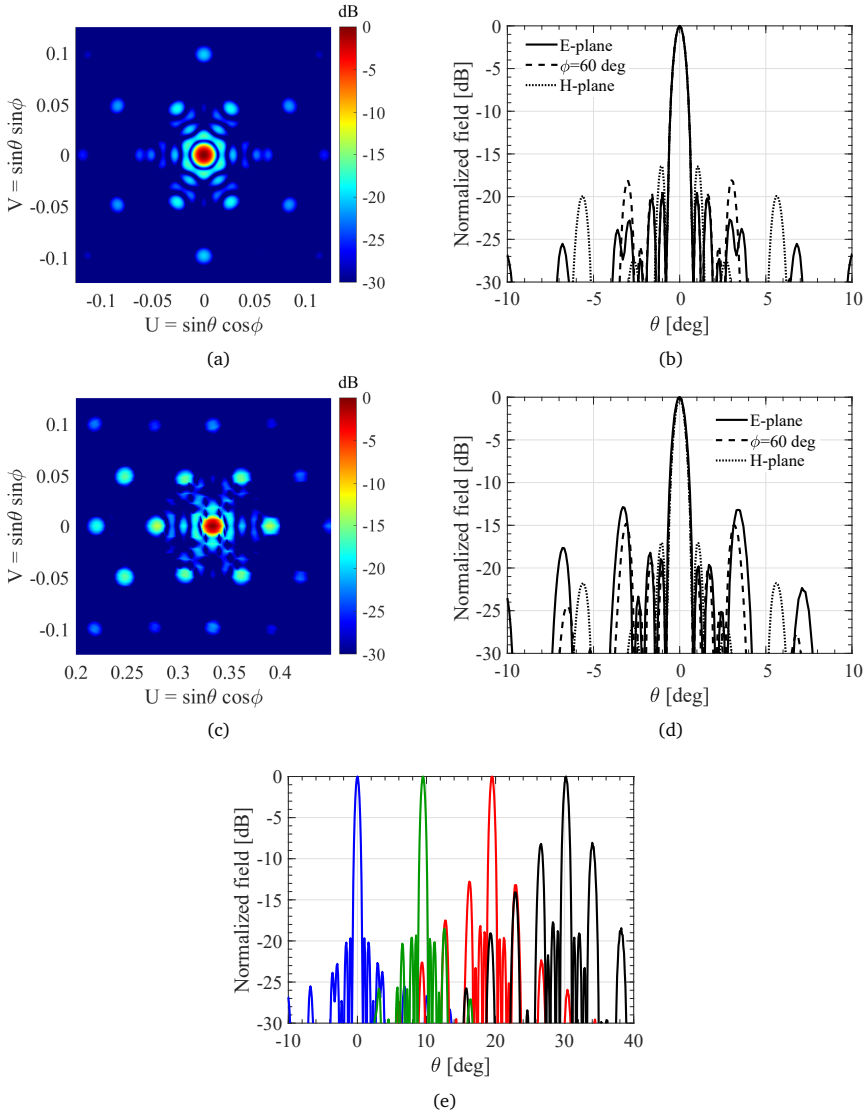

Fig. 6.10: Radiation pattern of a 19-element lens array at 550 GHz for (a) and (b) broadside and (c) and (d) scanned to 20°. The E-plane radiation pattern is shown in (e) for scanning up to 30°.

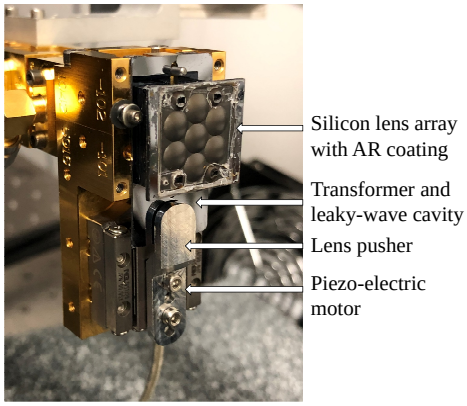

Fig. 6.11: Photograph of the prototype at 550 GHz that validates the embedded element pattern of the lens-phased array using an integrated piezoelectric motor to perform the mechanical scanning of the array element pattern. The height of the complete stack of wafers, including the LW cavity wafer, transformer wafer, stacked silicon wafers, and lens array wafer is 7.1 mm measured from the ground plane. The elliptical lenses subtend an angle of 17.3° from the focus which is 1.2 mm below the ground plane.

[116], in order to achieve the maximum aperture efficiency. The resulting optimized $\theta_0 = 17.3^\circ$ or equivalently, $f_\# = 1.6$.

The lenses, the transformer, and air cavity are synthesized in silicon wafers. This stack of wafers sits on a metal fixture, where a receiver array could be potentially integrated. In this case, the metal block consists of a straight waveguide that transforms the standard WR1.5 waveguide into a square waveguide of 362 $\times$ 362 μm as in [86]. The piezoelectric actuator sits on the side of this metal fixture and translates the stack of wafers in one axis. The translation displacement achieved by the prototype is $\pm$1.25 mm, i.e., a scan angle of around $\pm 24^\circ$, and it is executed by a piezoelectric actuator motor as in [86]. A lens pusher fixture translates the silicon stack across the LW feed using alignment metal pins as rails that support the movement of the lens.

6.3.1 Silicon Lens Array Wafer Stack

The silicon lens array consists of seven elliptical lenses of aperture $D_l = 5.13$ mm $(9.4\lambda_0)$ and height of 548 μm synthesized in a hexagonal configuration in order to provide a tight array spacing with high aperture efficiency. The array of lenses has been fabricated from a 1-mm high-resistivity silicon wafer using laser micromachining and was then coated with a Parylene anti-reflection coating. The lens array is shown in Fig. 6.12.

A few other high-resistivity silicon wafers, i.e., 5 wafers of 1 mm thick and 4 wafers of 300 μm, were stacked to create the required thickness of the array. These wafers have been processed using a DRIE process developed in [138]. The alignment of these

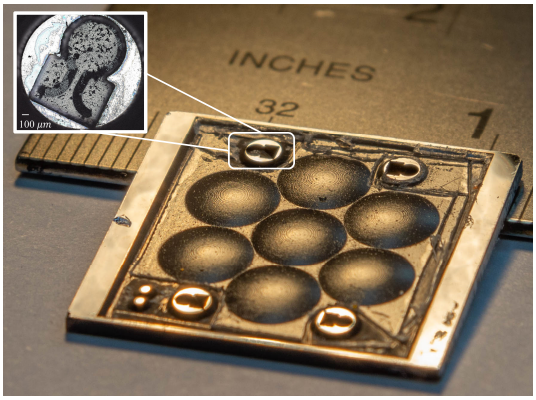

Fig. 6.12: Photograph of lens array wafer fabricated using laser micromachining. Inset photograph of the silicon pensile alignment pin on its pocket, defining the alignment between the lens wafer and the bottom silicon wafer.

wafers was performed using a silicon pin technique used in [139]. A silicon pin of 1 mm, shown in the inset of Fig. 6.12, was used in the alignment of the lens array wafer with the silicon stack. This increment in size facilitates the fabrication of the socket in the lens array with the laser without compromising the alignment. Unfortunately, the alignment of these two layers could not be measured accurately but was estimated to be better than 20 μm.

6.3.2 Transformer Layer and LW Cavity

The transformer layer has been synthesized by creating an artificial dielectric from a high-resistivity silicon wafer. The artificial dielectric targeted a relative permittivity of $\varepsilon_m = 2.5$ and it was synthesized with circular perforations [140] of 73 μm diameter to a depth of 88 μm in a regular triangular lattice of period 79 μm.

The validation of this artificial dielectric synthesis is shown in Fig. 6.7b, where radiation patterns of the LW feed using a homogeneous dielectric layer are compared with a full-wave simulation of the perforated layer in silicon. The figure shows the good agreement between the radiation patterns and confirms the little impact that the anisotropy of synthesized dielectric has, thanks to the highly directive LW patterns. Note that the spurious radiation in the E-plane for angles larger than 20° is associated with the finite size of the structure in the full wave simulation.

A photograph of the perforated silicon layer and its dimensions is shown in Fig. 6.13. A good agreement between the fabricated and designed dimensions has been achieved using the silicon micromachining process based on DRIE [138].

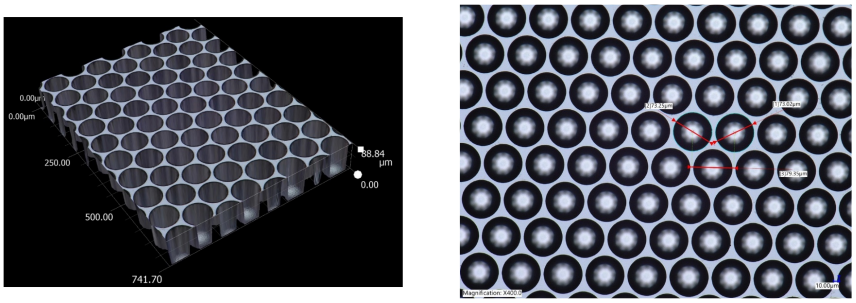

(a) (b)

Fig. 6.13: (a) 3-D and (b) top view of the fabricated artificial dielectric taken under the microscope.

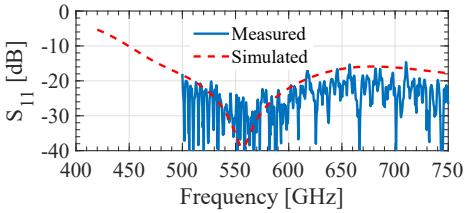

Fig. 6.14: Measured and simulated reflection coefficient of the embedded lens antenna array prototype measured in the WR-1.5 frequency band and plotted against full wave simulations.

6.4 Measurements

First, the reflection coefficient of the antenna was measured using a PNA-X and a calibrated WR-1.5 frequency extender. Its comparison with full-wave simulation is shown in Fig. 6.14. Note that the level of the measured reflection coefficient lies below the simulation due to the losses of the metal block fixture which are around 2.8 dB, as explained in [86]. But overall, the general shape of the reflection coefficient agrees well with the simulated performance of the antenna. The compression of the spring was calibrated by moving the lens back and forth with the piezo while verifying that the reflection coefficient did not have significant changes. All in all, the measured reflection coefficient is below -20 dB in a bandwidth of more than 50%, which is higher than the bandwidth of the aperture efficiency for this antenna.

The embedded element pattern prototype was validated using a far-field setup similar to the one used in [86]. The prototype was connected to an ad-hoc Schottky based transmitter that is fed by one of the synthesizers of the PNA-X to be able to fit in two rotational stages. To receive the signals, we used one of the WR1.5 PNA-X extenders as receiver and a standard gain horn. This ad hoc far-field setup limits the measurement band from 525 to 575 GHz, constrained by the available bandwidth of the transmitter

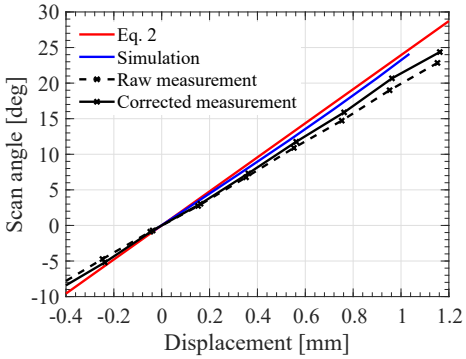

Fig. 6.15: Scan angle as a function of the displacement of the lens antenna array of the measured radiation patterns. The red line represents the scan angle obtained from displacing the feed of a quasi-optical system of an $f_{\#} = 1.6$.

and the scanning range was limited to $40°$ in azimuth and $45°$ in elevation.

6.4.1 Embedded Element Patterns

The lens array was translated with the piezoelectric motor with steps of 0.2 mm along $\hat{y}$, according to the reference system shown in Fig. 2.1. At each step, the radiation pattern of the AUT was measured. A small correction in the reference system of the radiation patterns was applied to these measurements since center of rotation of the scanner was a centimeter below the phase center of the lens array prototype. The effect of this correction is very small and it is shown in Fig. 6.15, where the scan angle versus displacement is compared for the corrected and the raw set of measurements. The figure also shows a good agreement between the measurements and the simulations using the aforementioned FO analysis. The solid red line shows the scan angle with the displacement for an optical system of $f_{\#} = 1.6$ using the geometrical expression from Eq. (2.3). A good agreement of the measurements and simulations with this red solid line shows low $f_{\#}$ of this multimode LW feed compared with the standard case.

Fig. 6.16 shows the measured radiation patterns for the central frequency at three different scan angles in the H plane, broadside, $10°$ and $20°$, which correspond to a lens array displacement of 0, 0.5, and 1 mm. Note that the three measurements, and the rest of the scanned angles, present a small tilt of $3.5°$ in the E-plane, that corresponds to a misalignment in $\hat{x}$ of 150 μm between the lens array with the feed. It is suspected that this is misalignment comes from a combination of errors and tolerances: the alignment tolerance given by the metal pins and the silicon wafer, the position accuracy between the pin pockets used in the lens wafer with respect to the actual lens array, and last, a cumulative error between the front and back alignment of the silicon pin pockets on the bulk silicon wafers employed. Nevertheless, this small

tilt has barely any impact on the aperture efficiency of the antenna and it could potentially be removed with another piezoelectric motor that would allow the scanning of the array in $\hat{x}$. Note that this tilt has been taken into account in the simulation shown. Figs. 6.16b, 6.16d and 6.16f shows E-, H-, and D-plane cuts normalized to 0° of the 2-D measured radiation pattern and the FO simulations. A very good agreement between the two is shown, especially for the broadside case. The medium and large angle displacement presents slightly higher discrepancy on the side-lobe level, due to the higher spillover/reflection power presented in these cases, which is not taken into account in the FO simulation. Moreover, the relative permittivity of the quarter-wavelength Parylene antireflection coating ($\varepsilon_r = 2.62$) used for this lens array prototype deviates from the ideal relative permittivity ($\varepsilon_r = 3.45$) for a silicon lens. As presented in [86], the effects of a non-ideal AR layer affect the side-lobes more while scanning. Nevertheless, the main beam and position of the nulls of the side-lobes are very close to the simulated results.

The gain loss as a function of the scan angle and relative to the broadside case is shown in Fig. 6.17, for the center frequency of 550 GHz and the extremes of the measured frequency band, 525 and 575 GHz. The loss is measured by taking the peak power received on each scanned position and comparing it to the gain drop evaluated using the FO simulations. Simulations and measurements differ at most 0.5 dB for the three points in the band, which we consider a very good agreement considering the limitation on the measurement setup, power fluctuations, and the effect of the multiple reflections in the lens array.

Unfortunately, the absolute gain could not be measured across the frequency due to a power fluctuation between the calibration and the actual gain measurement in this ad hoc measurement setup. However, considering that the fabrication techniques and materials employed for this effort are analogous to the ones presented [86], we can expect that the actual gain will be close to the simulated single lens gain of 28.2 dB[1].

6.4.2 Array Patterns

In order to estimate the performance of the array, we calculated the array radiation pattern by multiplying the measured radiation patterns of the embedded lens antenna by the array factor. The array factor is composed of the seven lenses in the hexagonal pattern, as shown in gray in Fig. 2.1.

Fig. 6.18 shows the array patterns of the broadside case, 10° and 20° of scan angle. The 2-D array patterns show the multiple grating lobes from the array factor but as a result of the multiplication with the element pattern, they remain below -9 dB even for the largest scan angle, in the 60° plane. The E, H-, and 60° planes of the radiation pattern normalized to 0° are shown for these scan angles and plotted against the array

[1] Indeed, we can see later in Fig. 7.6c that the gain of this antenna matches well with the expected value.

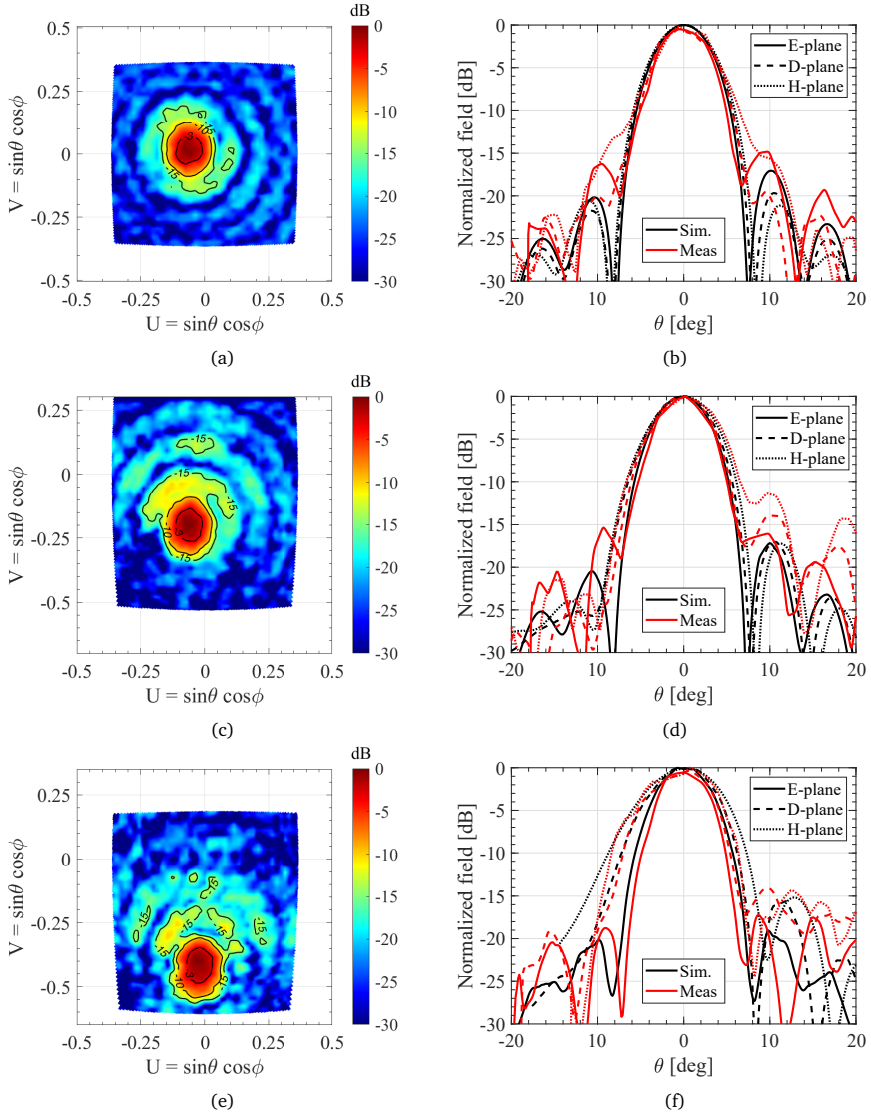

Fig. 6.16: Measured 2-D radiation pattern of the embedded lens antenna at 550 GHz for (a) broadside, (c) 10° scan angle and (e) 19.2° scan angle. E/H/D-Plane cuts of the measured and simulated pattern at the aforementioned scanned positions in (b), (d), (f).

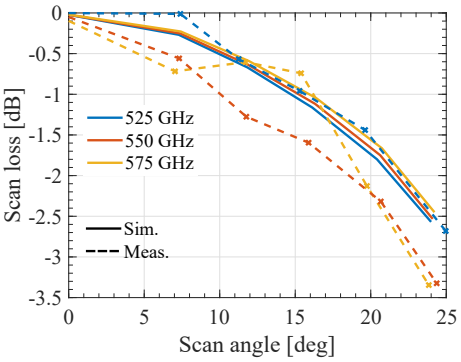

Fig. 6.17: Measured (dashed lines) and simulated (solid lines) gain scan loss in the H-plane normalized to the broadside case as a function of the scan angle for 525, 550, and 575 GHz.

pattern using the FO simulation. The maximum grating lobe level for broadside, $10°$ and $19.2°$ scan angle is -12, -11, and -9 dB, values that are considerably lower than other sparse arrays [72]. The results obtained with this prototype show higher grating lobes than those reported in Fig. 6.10 due to the limited lens diameter, which leads to a near field illumination of the lens.

Fig. 6.19 shows the directivity of the array patterns for the lowest, central, and highest measured frequency, as a function of the scan angle. The simulated directivity is calculated by integrating the array pattern in the measured solid angle. The expected deviation due to this truncation is less than 0.25 dB. The agreement between the simulations and measurements is within 1 dB in the worst cases. The fluctuations in the measured directivity are due to the measurement setup, the use of a Parylene matching layer instead of an ideal one which increases the impact on the multiple reflections in the directivity, especially when scanning and the feed spill over while scanning. Note that the FO simulations of the directivity do not consider the multiple reflections inside the array.

Overall, the experimental results follow the predictions obtained from the simulations, which demonstrate the operability and performance of the new proposed LW lens feed, as well as the dynamical steering of the element pattern up to around $25°$ applicable in future implementations of active lens-phased arrays at these high frequencies.

6.5 Conclusion

We have derived the requirements of the lens antenna feed in order to control the level of the grating lobes over wide angles. For this purpose, we have proposed a multimode LW feed that is able to achieve an aperture efficiency greater than 80% over a bandwidth of 35% and a scan loss lower than 3 dB up to $25°$. This LW feed uses

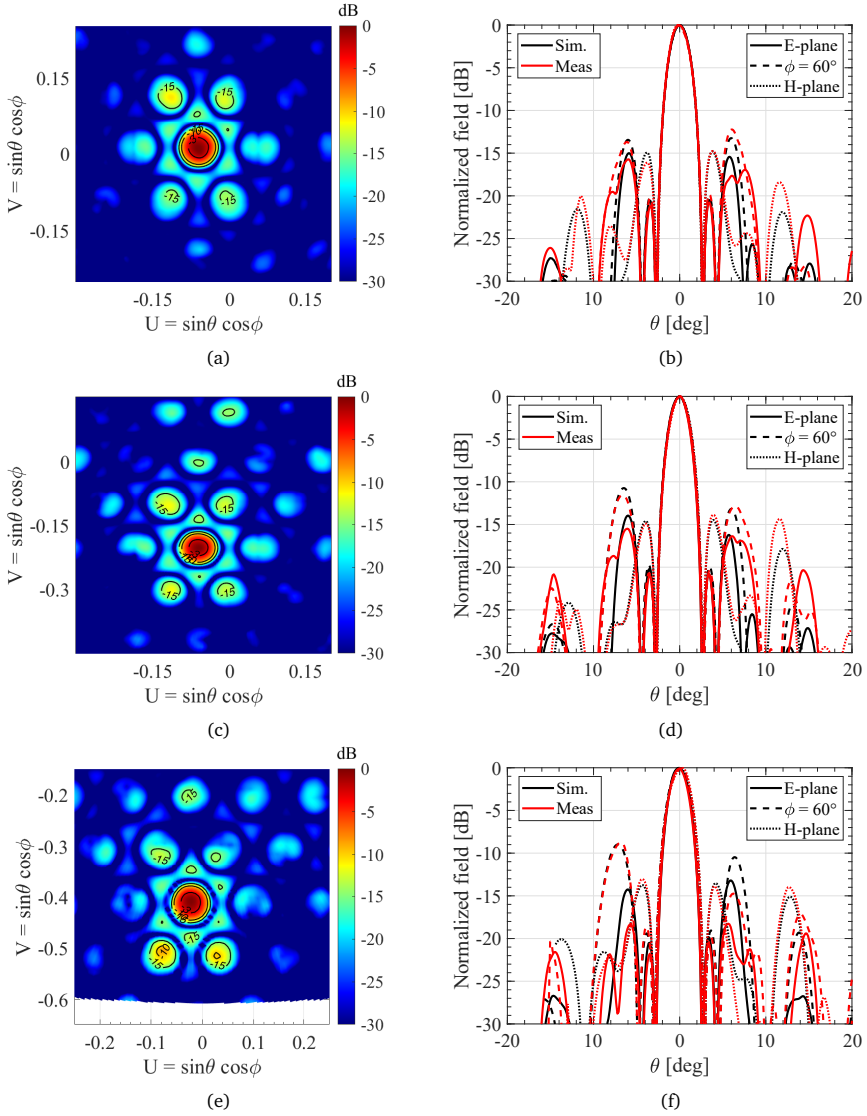

Fig. 6.18: Measured 2-D radiation pattern of the array at 550 GHz for (a) broadside, (c) 10° scan angle and (e) 19.2° scan angle in the H plane. E/H/D-Plane cuts of the measured and simulated pattern at the aforementioned scanned positions in (b), (d), (f).

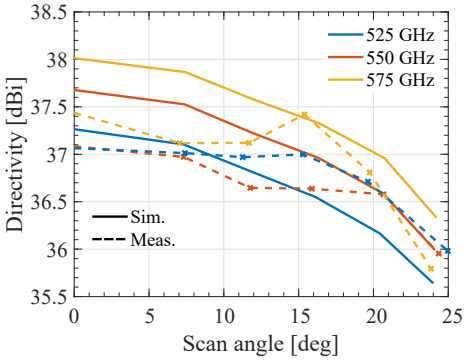

Fig. 6.19: Directivity as a function of the scan angle for the 7 element array for 525, 550, and 575 GHz.

a transformer layer to generate multiple modes which help to produce a top hat pattern with a suitable $f_{\#}$ for scanning. Additionally, this layer ensures impedance matching of the feed without a double slot iris, which simplifies the fabrication process.

A prototype of an embedded lens antenna has been built at 550 GHz, integrated with a piezoelectric motor. We measured the radiation and scanning performance of the embedded pattern and combined these results with the array factor to obtain the array pattern of the phased array. We found excellent agreement between the measurement and simulated performance, validating the capability of this antenna architecture for future implementations of scanning lens phased arrays.

Chapter 7
Broadband Lossless Matching Layer for Lens Arrays at THz Frequencies

We present the design, fabrication and characterization of a broadband lossless matching layer for shallow silicon lens arrays. The proposed matching layer is based on silicon frusta (truncated pyramids) on top of the lens array fabricated by means of laser ablation. This matching layer is advantageous over quarter-wavelength dielectric matching layers since it covers over an octave of bandwidth in nearly lossless silicon using the same fabrication process as the lens array. We compare the performance of this matching layer with the commonly-used parylene-C matching layer at the center of the targeted band (500 GHz). We measure a 1.6 dB higher transmission of the proposed silicon frusta matching compared to the parylene-C matching layer.

7.1 Introduction

Silicon is widely used for submillimeter-wave integrated lens antennas [86], [103], [141]. However, the high permittivity of silicon ($\varepsilon_r^{Si} = 11.9$) results in high reflection at the lens-air interface. These reflections negatively impact the sidelobes [86], [142] decrease the gain [142] and have a strong impact on the input impedance [143].

Numerous anti-reflection coatings (AR coatings, also known as matching layers) have been developed to limit these reflections [144]–[146]. Single-layer thin-films of parylene-C ($\varepsilon_r = 2.62$) [144], SUEX ($\varepsilon_r = 2.86$) [145] and Cirlex ($\varepsilon_r = 3.37$) [146] were successfully used as quarter-wavelength impedance transformers, since their relative permittivity is close to that of an ideal quarter-wavelength transformer $\sqrt{\varepsilon_r^{Si}} = 3.45$. Multiple dielectric matching layers were used in [142], [147] to increase the transmission bandwidth.

However, the coating materials themselves may incur additional dielectric losses, which may not be negligible at submillimeter wavelengths, and the deposition of the thin films is costly. Furthermore, the adhesion of the matching layers to the silicon lens can be difficult, especially for cryogenically cooled lenses.

Periodic sub-wavelength structures imprinted in a dense material (silicon) have also been widely used as matching layers [148]–[156]. Several fabrication techniques, such as deep-reactive ion etching [148]–[150], dicing techniques [151]–[154] and laser ablation [155], [156] have been proposed and used at THz frequencies.

Parts of this Chapter have been published in **[J6]**.

Deep-reactive ion etching (DRIE) was used in [148]–[150] to create an anti-reflective coating on flat silicon wafers but has, to our best knowledge, never been demonstrated on a curved surface (i.e., silicon lens), which might not be straightforward.

A dicing saw technique was used in [151]–[154] to create impedance transformers on both flat silicon surfaces and silicon lenses. Reflection and/or transmission measurements were performed at frequencies up to 300 GHz but the authors conclude that this technique is not scalable to higher frequencies.

The laser ablation technique has two main advantages over a dicing saw method: i) the smallest achievable dimension is set by the laser (1-2 μm) whereas the dicing blade width is 20-100 μm; ii) the laser spot can be tuned, allowing a smooth taper of the frusta walls in comparison to the fixed width of available dicing saws. The combination of these two advantages allows a broader frequency transmittance coverage reaching frequencies up to a few THz, which is not possible with the dicing saw fabrication.

In fact, laser ablation has been used to create continuous impedance transformers on a flat silicon wafer [155] and on alumina lenses [156]. The authors reported the transmittance and/or reflectance of periodic sub-wavelength structures at frequencies up to 700 GHz. However, a direct comparison between the radiation performance - where the beam pattern, directivity and gain are measured - of a quarter-wavelength AR coating and a continuous impedance-transforming matching layer in an integrated silicon lens antenna architecture has not been presented before at these high frequencies.

Another potential advantage of laser ablation is that, since the lens and the matching layer are made of the same material, the anti-reflective coating will not suffer from thermal stress when cryogenically cooled. Similar structures made on alumina have been succesfully tested cryogenically [156], and there is no reason why the frusta matching layer presented in this chapter could not be used as a broadband matching layer for cryogenically cooled lens arrays.

In this Chapter, we compare the performance of the silicon multimode leaky-wave lens antenna that was demonstrated in Chapter 6 with a quarter-wavelength AR coating to a continuous impedance-transforming matching layer. We have fabricated and measured two otherwise identical silicon lens antennas (see Fig. 7.1) with different matching layers: a quarter-wavelength AR coating of parylene-C and a periodic structure consisting of flat-topped square pyramids (frusta) in silicon. We measure an improved gain of 1.4-2.0 dB at 450-500 GHz using the frusta matching layer compared to the parylene-C AR coating.

7.2 Lens Matching Layer Design

We compare the simulated performance of two matching layers on the silicon lens antenna described in [111] (Chapter 6) in the operational bandwidth of this antenna

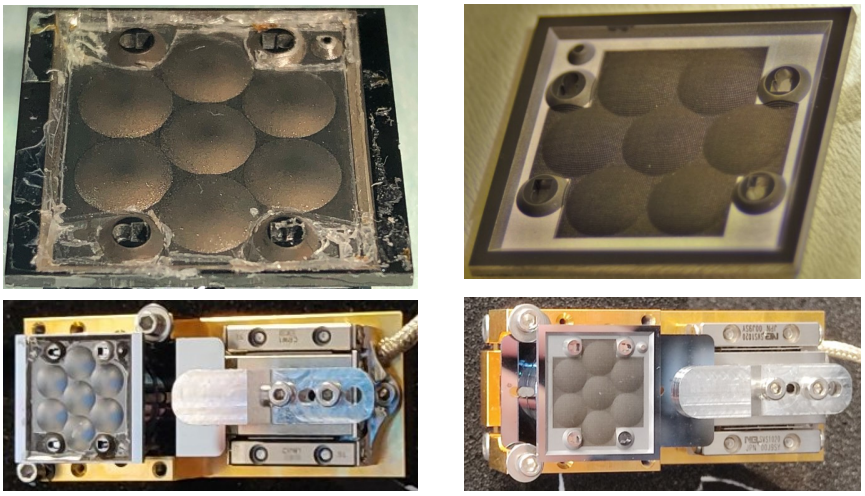

(a) (b)

Fig. 7.1: Photographs of the silicon lens arrays. (a) Parylene-C (top) and assembled antenna (bottom). (b) Frusta matching layer (top) and assembled antenna (bottom).

of 450-650 GHz: a quarter-wavelength (94 μm) layer of parylene-C and a periodic arrangement of sub-wavelength flat-topped square pyramids (frusta) in silicon.

The frusta are fabricated using laser ablation, which is performed by Veld Laser Innovations B.V.[1]. Laser ablation is the process in which material from a surface is removed by a pulsed laser beam. The material, in the case of this lens array silicon, is locally heated by the absorbed laser energy and evaporates or sublimates. The laser pulses are very short, of the order of a few tens of picoseconds, causing only minimal material damage during processing due to the ultra short light-matter interaction making it suitable for micro-fabrication.

Due to the small dimensions of the pyramids, this micro-fabrication technique has two constraints that need to be considered for the design: i) it is not possible to carve straight walls in the silicon. The minimum angle that can be obtained for these specific pyramid dimensions is 13 degrees. This is not a problem since we want a broadband matching layer and the tapered walls increase the bandwidth; ii) it is very difficult to reliably end the pyramids in a sharp point at the top for the entire lens array. We therefore decided to truncate the top of the pyramids and make frusta instead.

Considering these constraints, we therefore design the pyramids, as indicated in the inset of Fig. 7.2. These dimensions are given in [157] for a higher frequency design (2 THz) and have been scaled to 500 GHz to meet our frequency band. The design values can be found in Table 7.I.

[1] www.veldlaser.nl

Table 7.I: Frusta dimensions and laser parameters as indicated in Fig. 7.2.

Frusta dimensions		
Dimension	Designed	Fabricated
d [μm]	40	32±5
p [μm]	108	109±5
h [μm]	127	149±10
α [°]	15	14±2
Laser fabrication parameters		
Average power	7 W	
Spot size	25 μm	
Pulse duration	<12 ps	
Repetition rate	200 kHz	

The transmission at the interface between the silicon lens and free space is simulated for a frustum unit cell for broadside incidence using CST from 200-900 GHz. The reflection coefficient at broadside is an accurate approximation for such very shallow lens arrays. A full-wave periodic structure simulation is performed for the frusta structure; for the parylene-C matching layer, an equivalent transmission line was used assuming lossless parylene-C. The simulated transmission is given in Fig. 7.2 and is better than -0.3 dB for both structures in the center of the band but the parylene-C matching layer decays for lower and higher frequencies whereas the frusta matching layer stays fairly constant for the full bandwidth. The radiation patterns are simulated using the Fourier Optics methodology [96], which was also used in [111], assuming a quarter-wavelength matching layer with $\varepsilon_r = 2.62$. The simulated radiation patterns are shown in Fig. 7.5b.

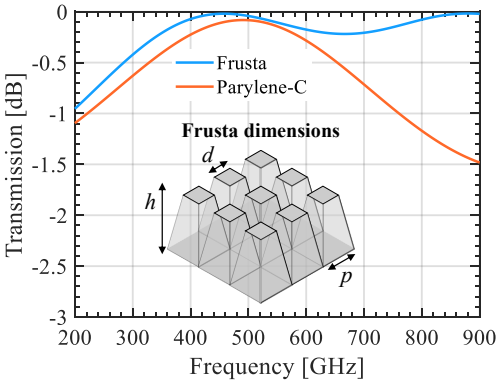

Fig. 7.2: Simulated transmission of both the parylene-C and the periodic matching layer. The figure's inset shows a sketch of the simulated periodic frusta used as the matching layer.

7.3 Fabrication and Characterization of the Periodic Frusta Matching Layer

The lens array with frusta matching layer is fabricated in two steps. These two fabrication steps are performed in the same laser setup but with two different settings. First, the entire lens array is manufactured thicker than the nominal lens. This extra thickness corresponds exactly to the height of the frusta. The lens array geometry is made using an imported 3-D file. Second, this extra thickness is locally removed to form the frusta. For this step, a 2-D file containing the grid from which the excess material will be removed from the lenses is loaded into the laser ablating setup. Dedicated optics move the focus of the laser along the shape of the lens and the frusta are carved by passing the laser several times over the lens surface to obtain the correct depth. The parameters used by the laser for the fabrication of the frusta are shown in Table 7.I. Conformal carving is not possible at this point using our current setup since it can only move along three axes (x-, y- and z-axes) and the laser cannot follow the lens profile. This limits the application of the ablation fabrication technique to shallow lenses (i.e., lenses in which only the top part of the lens is illuminated). To apply this technique to more curved lenses, two routes could be investigated: i) the current laser setup could be modified and the number of axes could be increased to five (x-, y-, z-, θ- and ψ-axes) so the laser can follow the lens profile; ii) a new frusta design that takes the angle of incidence along the profile of the lens surface into consideration. This new design would have to vertically adjust the length of the frusta (h) to ensure high transmission for off-broadside angles.

After fabrication, the shape of the frusta is measured in 3-D using a confocal microscope (Fig. 7.3a). The 3D image can be sliced and used to measure the profile of the frusta, and therefore obtain their period, dimension of the top flat part and height, as shown in Fig. 7.3b. The shape of the frusta is measured at three different locations on the array (left, middle and right) along two perpendicular planes. The dimension of each frustum along these cuts is recorded and its average valued is given in Table 7.I, together with the fabrication accuracy and designed values. The small difference between the designed and fabricated frusta moves the center of the frequency band slightly (about 10%) but the design is so broadband that this shift does not affect the overall performance of the frusta matching layer. Furthermore, the accuracy in the fabrication process of the frusta matching layer is similar to the accuracy of the parylene-C thickness during its deposition process (5 to 20% thickness variation depending on the location of the lens array in the deposition chamber).

7.4 Antenna Assembly and Measurement Setup

The lens arrays with the two different matching layers are integrated and measured one-by-one in a lens antenna fed by a high-efficiency leaky-wave feed described in

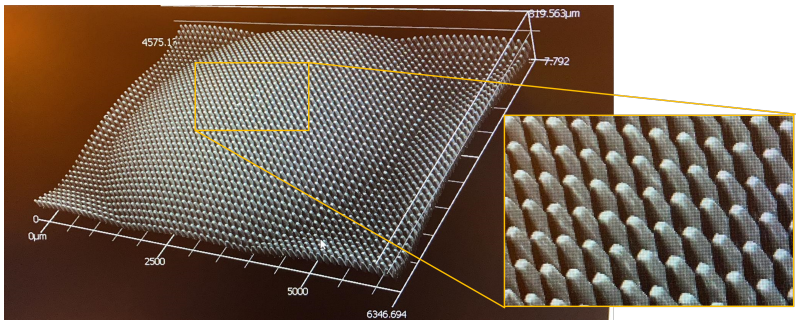

(a)

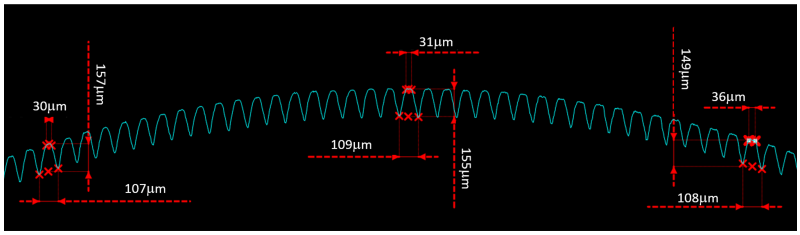

(b)

Fig. 7.3: (a) 3D image of a lens and zoomed view of the frusta taken with a confocal microscope and (b) measurement of the frusta dimensions using the cross-section along the center of the lens array.

[111]. Although seven lenses are fabricated in each array, only the central element is excited. The antenna assembly is extensively explained in [111], and consists of a gold-plated waveguide split block with a WR-1.5 waveguide flange on the bottom and a waveguide transition to a square (362 μm) aperture at the top. Next, two silicon wafers are placed on the block containing the leaky-wave cavity and transformer layer. The height of the lens is achieved with a solid cylindrical block of silicon placed on top of the wafers. Finally, either the lens array with the parylene-C or with the pyramid structures are placed on this silicon block. A piezo-electric motor is used to align the lens array with the feed as in [111]. A sketch of the assembled antenna is shown in Fig. 7.4a and a photograph of the assembled antenna with the two different lens arrays is shown in Figs. 7.1a and 7.1b.

We measure the antenna at 450-500 GHz using a VNA and two WR-2.2 frequency extenders. The antenna under test is in a fixed position and the receiving antenna is placed in a 3-axis CNC stage, and they are both facing each other. The 2-D antenna patterns are measured in an angle of 30 degrees around broadside in the far field at a distance of 10 cm. The patterns are measured using an open-ended waveguide flange with eccosorb material surrounding the waveguide aperture on the flange, similar to [158]. The absorber on the flange greatly reduces the measured oscillations due to the presence of the waveguide flange and can be interchanged with a horn antenna,

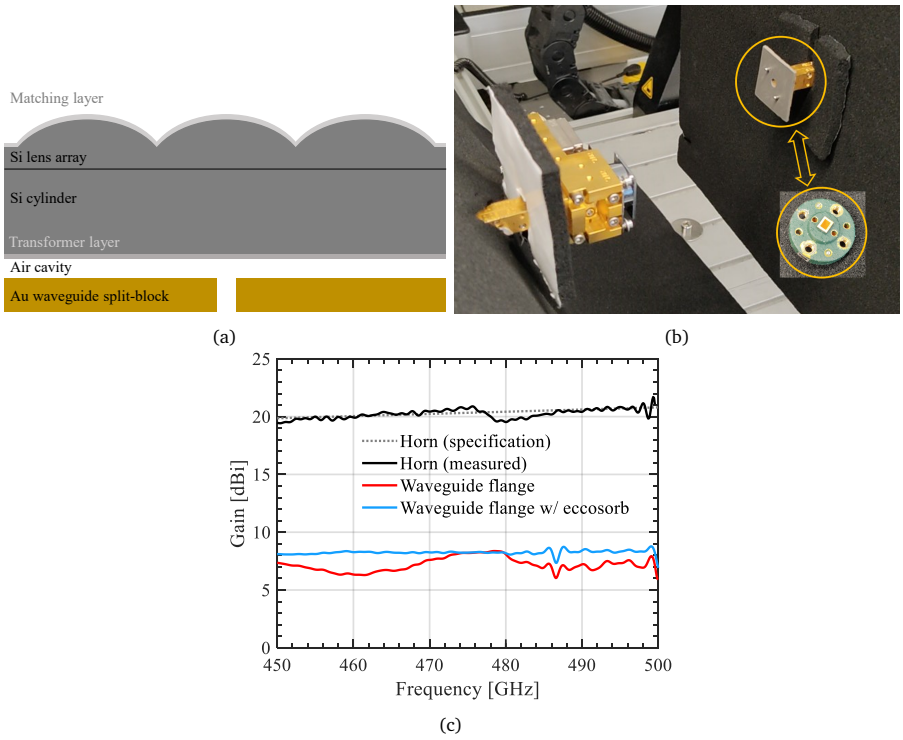

Fig. 7.4: (a) Schematic of the antenna assembly. (b) Measurement setup. Either an open-ended waveguide flange with eccosorb around it (for pattern measurements) or a horn antenna (for gain measurements) are used on the second extender, as indicated by the arrow. (c) Measured gain of the waveguide flange with and without the eccosorb and the measured and specified gain of the horn antenna.

as shown in Fig. 7.4b. The gain of the flange is measured with and without the absorber and is shown in Fig. 7.4c. The gain of the waveguide with the absorber is much less oscillatory. We use the horn antenna, with a gain of around 20 dB, to measure the gain of the antennas under test in the far field. The gain of this horn is separately measured to be in good agreement with the specified gain from the manufacturer (Flann Microwave), also shown in Fig. 7.4c. We later use this measured gain to characterized the gain of the antennas under test.

7.5 Measurements and Results

We compare the simulated and measured reflection coefficient (S_{11}) of both antennas in Fig. 7.5a. The antenna is well-matched above 425 GHz, the agreement with simulations is good, and the reflections in the S_{11} are not noticeably different for the two prototypes. The measured and simulated reflection coefficient do not match below 425 GHz because the leaky lens antenna that we use for the characterization of the frusta matching layer has a bandwidth between 450 and 650 GHz, and the cut-off

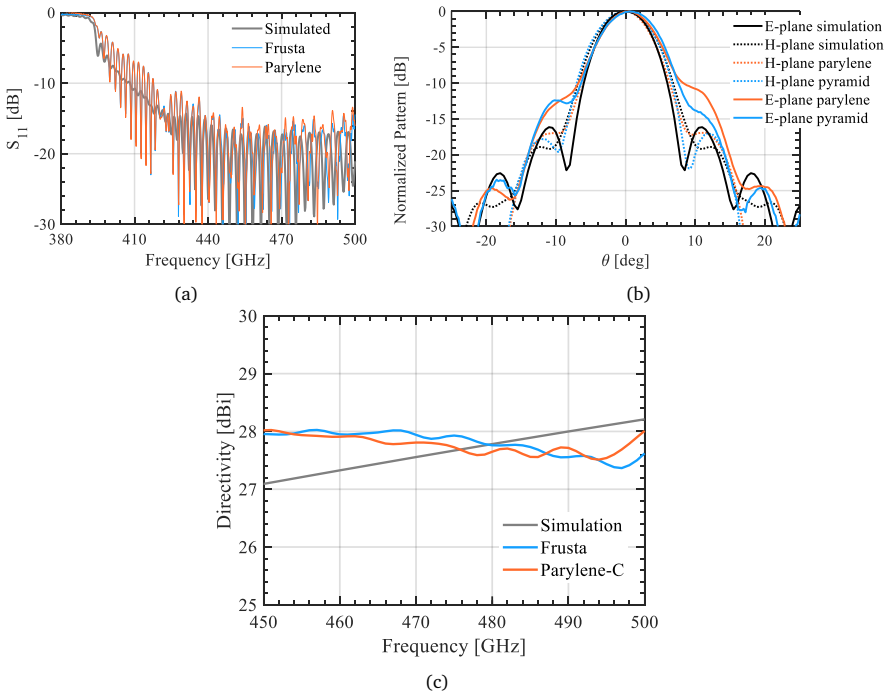

Fig. 7.5: (a) Simulated and measured S_{11} of both leaky-wave lens antennas. (b) Simulated and measured beam patterns at 480 GHz. (c) Simulated and measured directivity of both antennas.

frequency of the waveguide is around 400 GHz. The measured radiation patterns are compared to the simulated patterns at 480 GHz in Fig. 7.5b. The measurements are in reasonable agreement with the simulated patterns. The measured patterns from the parylene-C and frusta matching layer are very similar, indicating similar directivity. Indeed, the measured directivity, which is obtained by integrating the 2-D measured patterns and shown in Fig. 7.5c, is nearly the same for both prototypes and is also in agreement with the simulated directivity. The array coupling or cross-polarization have not been measured but, although it cannot be directly extracted from the directivity measurements, the fact that the parylene-C and frusta directivities are nearly identical suggests that both matching layers are performing similarly in terms of array coupling and cross-polarization. Moreover, the fabricated frusta layer is symmetric, having same response for TE/TM polarization. Therefore, we expect not to see any impact on the cross-polarization.

We use Friis' equation to simulate the coupling between the antenna and horn (S_{21}) at broadside at a distance of 10 cm. To remove the effect of multiple reflecting waves in the measurement setup, we apply a time gate to the measured S_{21} that filters out these reflections after the first received time-domain pulse. The simulated S_{21} takes into

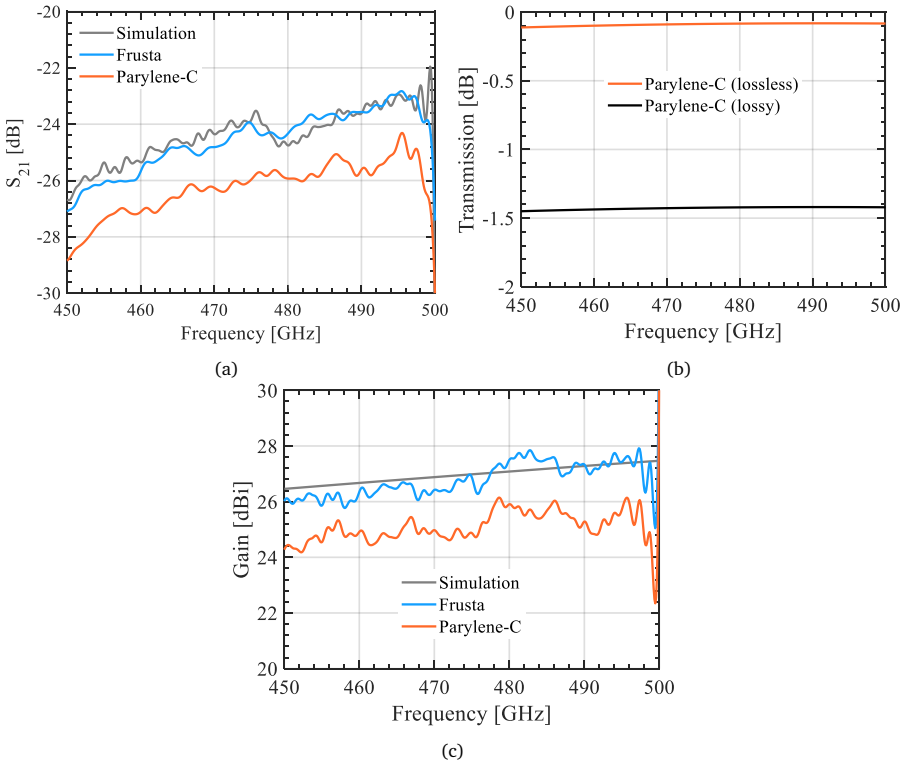

Fig. 7.6: (a) Simulated and measured S_{12} of the antenna with both matching layers. (b) Simulated loss of the parylene-C matching layer when ohmic loss is included. (c) Simulated and measured gain of the antenna with both matching layers. Note that the gain difference between the pyramids matching layer and the parylene-C matching layer is explained by the ohmic loss of the parylene-C.

account the loss in the gold-plated split block ($\sigma = 3.5 \times 10^6$ S/m) and the simulated gain. As shown in Fig. 7.6a, the simulated coupling is between -27 dB and -23 dB at 450-500 GHz. The measured coupling is in very good agreement for the frusta matching layer but 1.6dB lower for the parylene-C matching layer. This difference can be explained by the dielectric loss present in the parylene-C (Fig. 7.6b), where we use an absorption coefficient of 35 cm^{-1} [144], [159], [160]. The measured gain is evaluated from the measured S_{21} (Fig. 7.6a) and the measured horn gain (Fig. 7.4c) removing the loss in the waveguide block. The comparison between the simulated and measured gain is shown in Fig. 7.6c, and is above 26 dBi for the frusta matching layer and above 24 dBi for the parylene-C matching layer.

7.6 Discussion

The fabricated lens arrays are the same, except for the matching layer on top. The measured results in Fig. 7.6c show that the gain of the periodic frusta matching layer

is higher than for the parylene-C matching layer, suggesting a better performance as an AR coating of the periodic frusta structure. This difference in performance is not due to a difference in impedance match or directivity, as demonstrated in Fig. 7.4c. Both matching layers perform similarly in term of S_{11}, and we thus associate the gain difference to the dielectric loss in the parylene-C. In fact, an absorption coefficient of 35 cm^{-1} explains the difference in gain, as demonstrated in Fig. 7.6b. Although the reported values for absorption coefficient vary largely in the literature, our modeled absorption coefficient lies within the reported values. For example, an absorption coefficient of 27 cm^{-1} is reported in [159] at frequencies between 1 and 3 THz for parylene-C whereas and the reported value above 6 THz was 75 cm^{-1} in [160] for parylene-N. These values are in line with the value that we assume in our analysis although lower values have also been found: 2 cm^{-1} and 16 cm^{-1} at 450 GHz and 2.8 THz, respectively [144]. Although different types of parylene with lower dielectric loss than the parylene-C are available [161] (measured at low RF frequencies), the frusta matching layer has significant advantages as it operates over more than an octave bandwidth and it is fabricated using the same process as the lens array itself.

7.7 Conclusion

We compare the performance at submillimeter wavelengths of two different matching layers on the same silicon leaky-wave lens antenna arrays. The fabricated antennas are the same with the exception for the matching layer. The first is a quarter-wavelength parylene-C anti-reflecting coating and the second a continuous impedance-transforming matching layer which is realized by periodic sub-wavelength frusta features laser-ablated directly on the lens surface. We describe the laser machining process to manufacture the frusta suitable for silicon lens arrays. We characterize both antennas in terms of reflection coefficient, radiation patterns (directivity) and gain and compare these results to high-frequency simulations. The measured performance from both antennas is the same except for the measured gain. The measured gain of the frusta matching layer is in very good agreement with simulations and is around 1.6 dB higher than for the parylene-C matching layer, which is explained by the dielectric loss in the parylene-C. Furthermore, the frusta matching layer has significant advantages as it operates over more than an octave bandwidth and it is fabricated using the same process as the lens array itself.

Part III
Demonstration of Scanning Lens Phased Arrays

Chapter 8
First Demonstration of Dynamic Beam Steering with a Scanning Lens Phased Array

We report on the first demonstration of dynamic beam steering with a scanning lens phased array. A scanning lens phased array relies on a combination of mechanical and electrical phase shifting to dynamically steer a highly-directive beam beyond the grating-lobe free region using a sparse array. These concepts have been demonstrated separately in the past, but we present here the first demonstration of the concept with active mechanical and electrical phase shifting combined. For this purpose, we developed a sparse 4x1 scanning lens phased array at W-band (75-110 GHz) that is capable of beam steering a directive (>30 dBi) beam towards $\pm 20^{\circ}$ with low grating lobe levels. The design of the lens array and leaky-wave feeding structure is also detailed. This feed illuminates the lenses with high aperture efficiency over a wide bandwidth, which is required in the scanning lens phased array architecture. An ad-hoc measurement setup has been developed using IQ-phase shifters around 15 GHz in combination with x6 multiplication chains to reach the W-band. The entire active array is calibrated over the air. Resulting measurements show excellent agreement with the anticipated performance.

8.1 Introduction

Millimeter- and submillimeter-wave scanning arrays will play a major role in communication and sensing scenarios in future 6G networks and automotive applications [6], [31]. Antennas for such applications should achieve very high gains (>30 dBi) and include dynamic scanning capabilities [5], [94]. Fully sampled phased arrays at or above 100 GHz, such as [27], [30], [36], [39], [43], [162], are capable of wide-angle beam scanning but have low gain due to the limited number of array elements. Increasing the number of elements in such arrays is difficult due to thermal and integration constraints.

To overcome these limitations, we have recently proposed a scanning lens phased array concept in [111] (and in this thesis) that achieves a high-gain, steerable beam using a very sparse array of only a few electrically large lens antenna elements. The geometry of the scanning lens phased array is indicated in Fig. 8.1a. The grating lobes resulting from the sparsity of the array are suppressed by the directive beams from the

Parts of this Chapter have been published in **[J5]**.

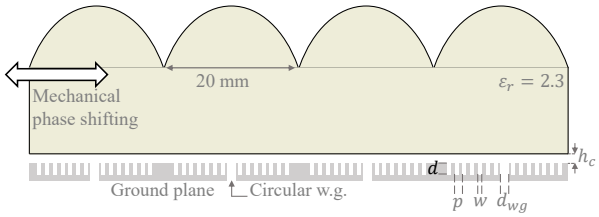

(a)

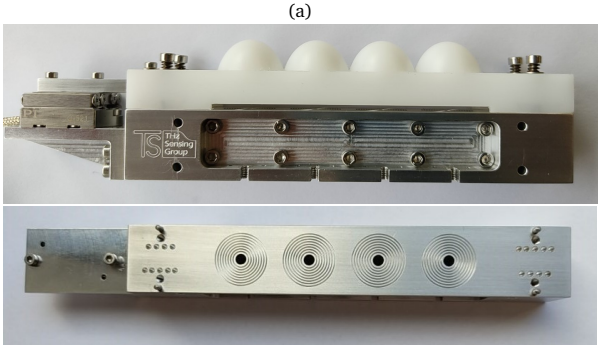

(b)

Fig. 8.1: (a) Geometry of the 4x1 W-band scanning lens phased array. The ground plane contains periodic annular corrugations. (b) Photographs of the assembled prototype (top) including the piezo-motor and of the corrugated ground plane (bottom).

lens elements. To achieve this suppression, high aperture efficiency lens antennas are required as the array elements [111].

Beam steering beyond the grating-lobe-free region from this sparse lens array is achieved by mechanically displacing the lens array relative to their feeds and, simultaneously, applying a relative electronic phase shift between the array elements. The mechanical displacement causes the element pattern of the lenses to be steered towards the desired angle, while the electronic phase shifts steer the array factor. The steering of the element pattern enables achieving low grating lobe levels when scanning beyond the grating-lobe-free region, in contrast to limited scan arrays [72], [73], [75], [76], [113]. The required mechanical displacement for such lens arrays can be achieved by using a piezo-electric motor, as demonstrated in [86], [111]. Static phase shifting of these kinds of arrays has been demonstrated at 10 GHz [163] and 30 GHz in [94] by using corporate feeding networks. In [84], the contributions of each lens antenna at 38 GHz were measured independently and subsequently delayed by the required phase shift in postprocessing before being summed. Thus, the combination of mechanical displacement and active electronic phase shifting to realize dynamic steering has not yet been demonstrated.

In this chapter, we demonstrate a 4x1 W-band (75-110 GHz) scanning lens phased array prototype using the combination of a piezo-electric motor and an electronic

phase steering architecture based on low frequency IQ-mixers and multipliers [164]. The design, simulated performance and fabrication of the lens array prototype is described in Section 8.2. The embedded lens elements are characterized in Section 8.3. We present the active array demonstration setup in Section 8.4, the over-the-air calibration setup in Section 8.5 and the demonstration of the active array in Section 8.6. Conclusions are drawn in Section 8.7.

8.2 Lens Array Prototype at W-band

We have designed a 4x1 lens phased array with a periodicity of 20 mm ($6\lambda_0$) at W-band (λ_0 being the free-space wavelength at 90 GHz), which achieves a gain larger than 30 dBi. The design, simulated performance and fabrication of the array prototype are detailed in this section.

8.2.1 Single Lens Antenna Performance

In order to control the level of the grating lobes, the single lens antenna must be illuminated with high aperture efficiency as explained in Chapter 2. To achieve this high efficiency over a wide bandwidth, we use the leaky-wave lens feed proposed in Chapter 5 and shown in Fig. 8.1a. This feed consists of a circular waveguide with a diameter of $d_{wg} = 3.18$ mm in a ground plane with annular corrugations, a half-wavelength air cavity and a high-density polyethylene (HDPE) elliptical lens with $\varepsilon_r = 2.3$. The air cavity with height $h_c = \lambda_0/2$ supports three leaky-wave modes of which only the main $\mathrm{TE}_1/\mathrm{TM}_1$ modes contribute to broadside radiation [103]. The spurious TM_0 mode is suppressed over a 2:1 bandwidth by the annular corrugations, as demonstrated in Chapter 5. The dimensions of the corrugations and the diameter of the circular waveguide in this design are also scaled from that design to the W-band and have a periodicity of $p = 0.75$ mm, a width of $w = 0.35$ mm and a depth of $d = 1.1$ mm. The lens geometry is then derived in closed form based on the leaky-wave propagation constants using the procedure in Chapter 4. We evaluated the aperture efficiency of this lens antenna using the Fourier Optics (FO) methodology in reception [96] and found an aperture efficiency above 84% over the entire WR-10 band, in line with the results from [135]. Note that the FO methodology considers the effect of multiple reflections at the lens interface as a loss.

The performance of the single element was then evaluated in terms of its reflection coefficient and radiation patterns in the W-band. These results, along with all results presented from here onwards, are obtained by using full-wave simulations in CST which do include the effects of multiple reflections. The simulated reflection coefficient (S_{11}) is shown in Fig. 8.2a (black) and is below -15 dB in the entire bandwidth. The simulated broadside radiation pattern of one of the central embedded elements at 90 GHz is shown in Fig. 8.2b (black). The pattern is nearly rotationally symmetric with sidelobe levels between -17 dB to -20 dB, which is close to the sidelobe level

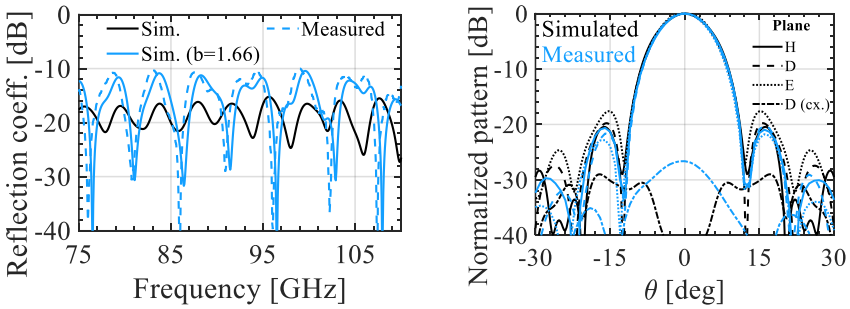

Fig. 8.2: (a) Reflection coefficient of a single lens element as simulated (solid) and measured (dashed). Note that due to a fabrication error, a waveguide with $b = 1.66$ mm was fabricated. (b) Single lens element radiation pattern simulated (black) and measured (blue) at 90 GHz.

radiated by a uniform circular current distribution, similar to [165]. Thus, the single element is directive enough to achieve a good suppression of the grating lobes in the array factor.

8.2.2 Lens Array Performance

We have designed an E-plane linear array, consisting of 4 single lens antenna elements as described in Section 8.2.1 and shown schematically in Fig. 8.1a. The period of the array is equal to the lens diameter ($6\lambda_0$), which results in the array factor shown in gray in Fig. 8.3a with grating lobes appearing approximately every 10° in the E-plane. To demonstrate the suppression of the grating lobes, the far-field pattern radiated by the array can be approximated by multiplying the embedded element pattern of Fig. 8.2b by the array factor. As shown in Fig. 8.3a, the grating lobes are indeed suppressed by the directive single element pattern (black) which results in the array patterns (red). The approximated array pattern obtained in this way is shown in the three main planes in Fig. 8.3b. The resulting array pattern has a sidelobe level below -12 dB (this level can be reduced if the array is designed with a 2-D hexagonal grid [30]). Due to the one-dimensionality of the array, the H-plane patterns are equal to the single-element patterns with a maximum sidelobe level of -20 dB. The simulated cross-polarization level of this array is below -40 dB.

To include all the effects of multiple reflections and the effects of the edge elements in the array, we have performed full-wave simulations of the complete array. The broadside pattern is obtained by in-phase excitation of all elements when the lens array is centered over the elements. For scanned beams, a combination of mechanical displacement of the lens array relative to the feed and progressive phase shifting of each element is applied. For example, the mechanical shift required to scan towards $\theta_{sc} = 10^\circ$ is 2.4 mm and the progressive phase shift is 375°. The simulated array

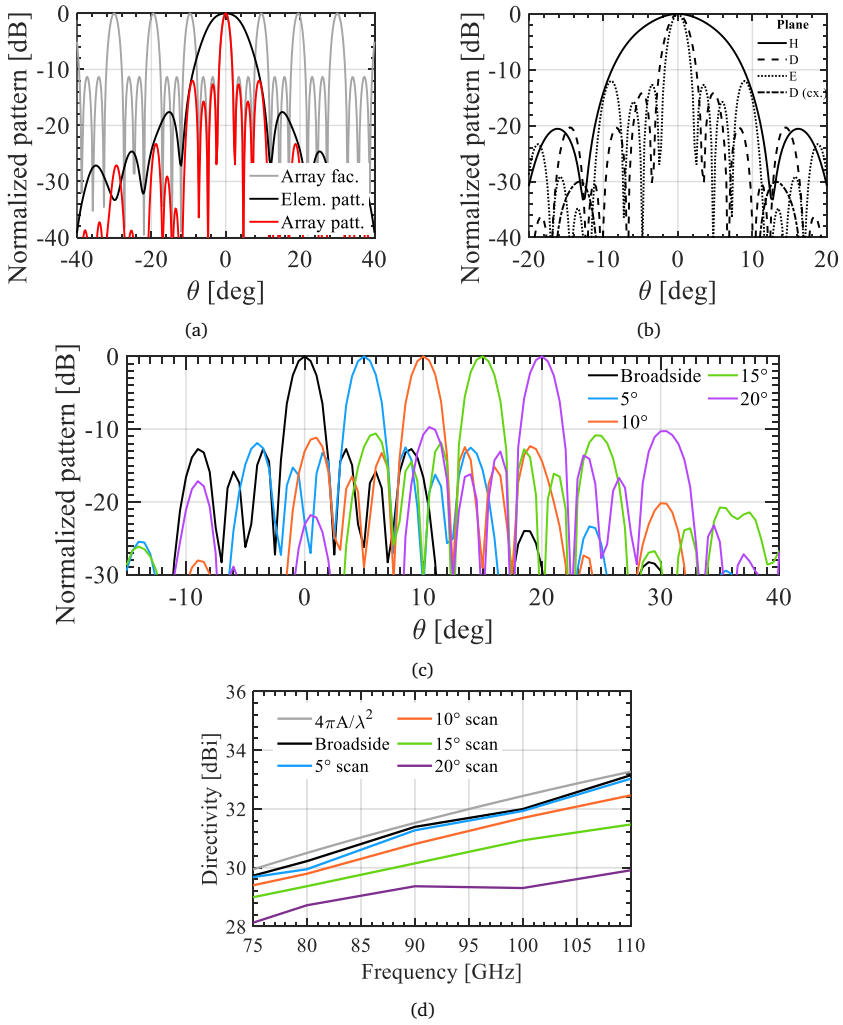

Fig. 8.3: (a) Simulated array factor, single element pattern and resulting array pattern in the E-plane. (b) Simulated array patterns in the main planes. (c) Simulated E-plane radiation patterns for scanning from broadside up to 20°. All patterns are presented at 90 GHz. (d) Simulated directivity of the 4x1 array in the W-band when scanning towards θ_{sc}. The maximum theoretical directivity from an aperture with the array's size is shown for comparison.

patterns are shown in Fig. 8.3c at 90 GHz for several scan angles up to 20°. Due to the mechanical displacement, the illumination efficiency of the lens decreases and the sidelobe level of the array pattern increases. Still, the sidelobes are around -10 dB for scan angles up to 20°, which is acceptable for many applications.

The simulated directivity of the complete array is shown as a function of frequency in Fig. 8.3d. The achieved directivity is very close to the maximum theoretical directivity of an antenna of such physical dimensions, A, considered to be four times the area of a single lens. For scan angles up to 15°, the directivity remains within 1.7 dB of the broadside value in the entire W-band. The scan loss of the array is determined by the scan loss of the single element [111].

8.2.3 Prototype Fabrication

The designed linear 4x1 array has been fabricated at W-band as shown in Fig. 8.1b. The dimensions of the lenses and the corrugations in the ground plane correspond to the simulated dimensions in Section 8.2.1 and are indicated in Fig. 8.1a. The lens array has been milled from a block of HDPE. The annular corrugations and waveguide array are milled in an aluminum split block. The same fabrication process as Chapter 5 was used with comparable fabrication tolerance. Since the design is very wideband, the achieved tolerance does not noticeably impact the performance of the antenna. A photograph of these structures is shown in the inset of Fig. 8.1b. The circular waveguides in the top of the ground plane taper to WR-10 waveguide connectors in the bottom of the block.

The circular waveguide is tapered to the WR-10 rectangular waveguide using a linear transition of 17 mm. A piezo-electric motor is connected to the plastic lens array for accurate mechanical displacement of the lens array with respect to the metal block [86], [111]. The speed of the piezo-electric motor is 6 mm/s, resulting in a scan speed of 25 $^\circ$/s in the current prototype.

8.3 Embedded Element Characterization

In this Section, we present the measured performance of the individual lens elements in the array in terms of S_{11}, radiation patterns and mutual coupling.

The reflection coefficient of each array element, measured with a VNA and a WR-10 frequency extender, is shown in Fig. 8.2a. Due to a fabrication error, the b-dimension (i.e., the short side of the rectangular waveguide) in the bottom of the split block increased from $b = 1.26$ mm to $b = 1.66$ mm. The maximum measured S_{11} increases from -15 dB for nominal dimensions to -10 dB for the fabricated dimensions. This result closely matches the simulated S_{11} with the incorrect waveguide dimensions. Since the circular waveguide at the top of the block has the correct dimensions, the radiation patterns are not affected.

The far-field radiation patterns from each individual array element were calculated from a near-field planar scan measured with a probe 2 cm above the lens. The array element and probe were both connected to a VNA by WR-10 frequency extenders. The measured single-element pattern from one of the lenses is shown in Fig. 8.2b at 90 GHz. The measured patterns are in good agreement with the simulations. However, the cross-polarization is higher at broadside which is attributed to the limited tolerance in the fabrication of the waveguide transition, which was also observed in Chapter 5. In Figs. 8.4a and 8.4b, the pattern measurements are shown in the E-plane and H-plane, respectively, for all four individual lens elements at 90 GHz. The measured embedded element patterns are very similar to each other, indicating good manufacturing consistency of the lens array.

The scanned patterns of the embedded element were measured by displacing the lens array relative to the feed with the piezo-electric motor. The simulated and measured E-plane radiation patterns are shown in Fig. 8.4c for scan angles up to $\theta_{sc} = 20°$ and show good agreement. The mechanical displacement of the piezo-electric motor required to scan the beam is shown in Fig. 8.4d and is 0.24 mm/°.

Due to the large period of the array, the mutual coupling between each element is expected to be low. The mutual coupling between each element is simulated to be -45 dB at broadside, which is in good agreement with the measured value as shown in Fig. 8.4f. When the lens array is mechanically displaced, the mutual coupling increases. The maximum measured mutual coupling is below -30 dB for the largest mechanical displacement, see Fig. 8.4f.

8.4 Active Array Demonstration Setup

In order to make a demonstration of the dynamic beam steering capabilities of a scanning lens phased array, we developed a setup to achieve electronic control in amplitude and phase of four W-band signals, and a setup to calibrate these signals over-the-air.

8.4.1 Electronic Amplitude and Phase Control Setup

To simultaneously control the amplitude and phase of the four-element array in the W-band, we use an IQ-steering technique similar to the one described in [164] at Ka-band. A schematic overview of this IQ-steering technique is shown in Fig. 8.5a. A continuous-wave f_{in} = 12.5-18.3 GHz signal is generated and distributed to four IQ-mixers that individually control the amplitude and phase of their output signal at f_{in}. The output of these IQ-mixers is fed into 4 frequency extenders that multiply the frequency of the signal by a factor of 6, to end up in the W-band (f_{out} = 75-110 GHz). Since the IQ-mixers can apply a phase shift of $\phi_{in} = [0, 2\pi]$ to the signal at f_{in}, the resulting phase shift to the multiplied signal is $\phi_{out} = [0, 12\pi]$. We thus have four independently controllable channels.

We have implemented the amplitude and phase control architecture of Fig. 8.5a

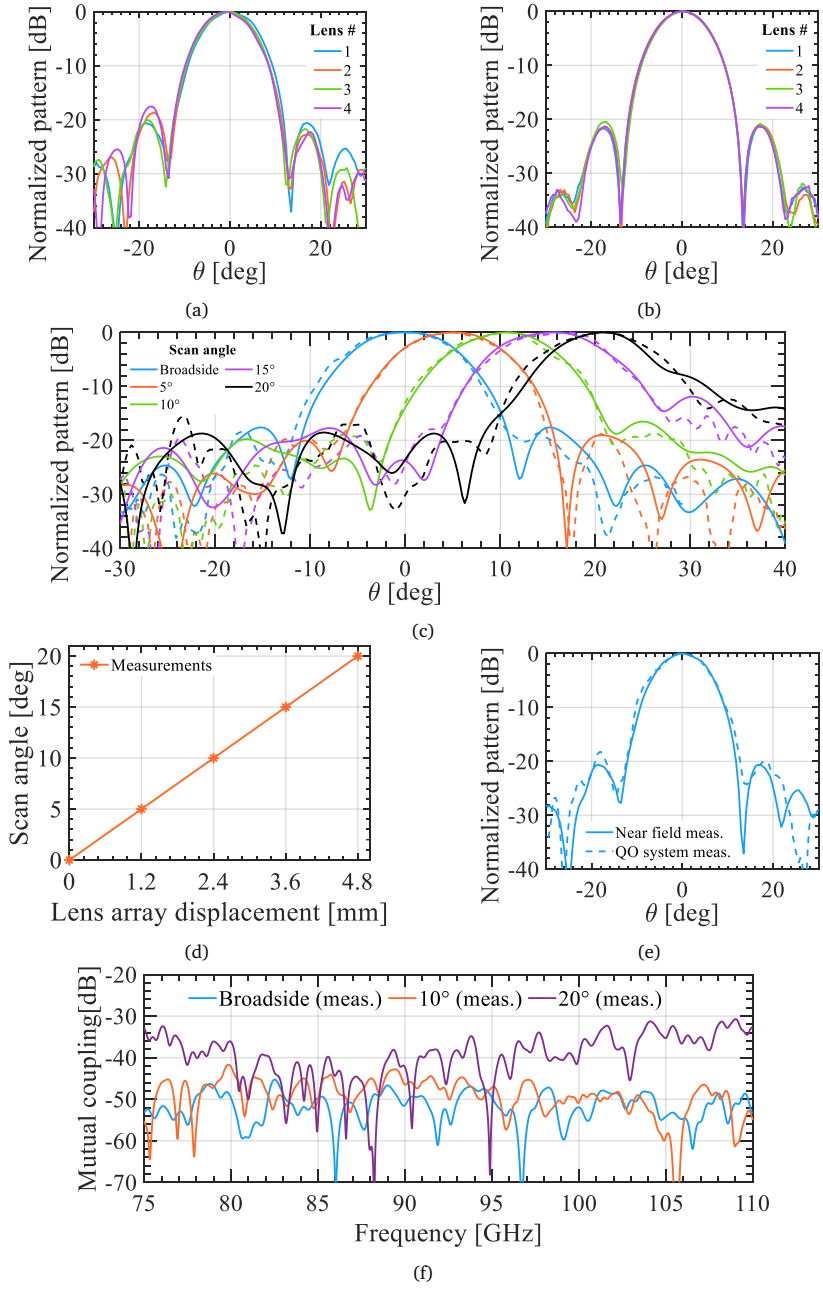

Fig. 8.4: Measured single-element radiation pattern at 90 GHz of lens elements 1-4 in the (a) E-plane and (b) H-plane and (c) the E-plane when scanning. (d) The required displacement of the lens array with respect to the feed. (e) E-plane pattern measurement: comparison of the near field measurement result and QO measurement result. (f) Measured mutual coupling between two adjacent lenses in the array for several scan positions of the array.

with a signal generator, a four-way Wilkinson power divider, four IQ-mixers, four power amplifiers and four frequency extenders, pictured in Fig. 8.5b (the signal generator and frequency extenders are not shown). Each IQ-mixer is controlled by two high-resolution digital-to-analog converters: $V_I^{(i)}$ and $V_Q^{(i)}$ with the superscripts (i) referring to the channels $i = 1...4$ in Fig. 8.5a. The voltages V_I, V_Q provide the bias level of the in-phase and quadrature-phase mixer to control the output signals that are summed at the output of the mixer. In this way, the output signal of each IQ-mixer realizes a Cartesian vector modulator by varying the real and imaginary part of the high-frequency signal. In our implementation, the DC voltages are supplied by 12-bit DACs that allow us to control amplitude and phase in steps of 7 millidegrees and 0.1 μW at f_{in}. By implementing the phase shifters at f_{in} instead of at f_{out} we are not limited by the performance of W-band phase shifters and we can use commercial components available in our lab to demonstrate the active array. The implementation of the phase shifters represents a significant improvement over earlier lens array demonstrations [84], [94], [163].

The measured output power and phase at 15 GHz, before the frequency extenders, are shown in Figs. 8.5c and 8.5d, respectively. The control of the amplitude will allow us to adjust the input power of each extender in order to achieve the same power level at the output of each frequency extender. The measured output power and relative output phase that corresponds to the -9 dBm contour in Figs. 8.5c and 8.5d is shown in Fig. 8.5e. Indeed, power and phase control are achieved. The IQ-mixers were then connected to the frequency extenders, which were in turn connected to the lens antenna array.

8.4.2 Over-the-air Active Array Measurement Setup

The far-field distance of the active antenna array (several meters) is larger than our laboratory facilities can accommodate. We have therefore developed a quasi-optical system that will be used to calibrate and measure the active array at a reasonable distance in the lab. The quasi-optical system consists of a focusing lens in front of the array with a focal distance of $F = 200$ mm. In the region around the focus of this lens, called the spot in the rest of the thesis, the field distribution is related to the far field pattern by $\rho = F \tan\theta$, where ρ indicates the lateral distance from lens focus, and θ is the far-field radiation angle [166], [167]. Since the field radiated by each array element is coherently summed in the spot, this setup can be used for over-the-air calibration of the channels relative to each other. Furthermore, we can obtain the far-field patterns of the array from a small, planar displacement of the receiver around the spot. The -3 dB spot size is approximately 7.2 mm at 90 GHz and by measuring a $\pm$170 mm displacement we can approximately measure the far-field patterns up to $\pm 40^\circ$.

To measure the patterns in the spot, only the amplitude must be measured, similar

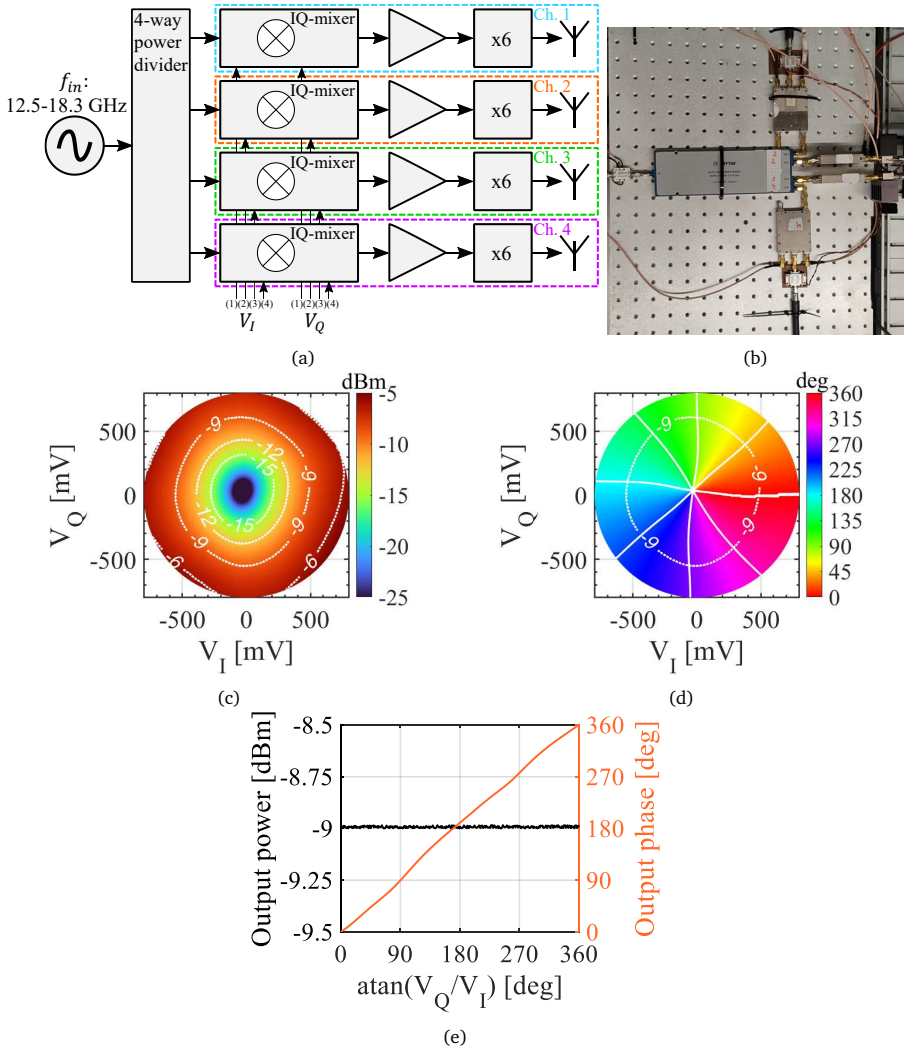

Fig. 8.5: (a) Schematic of the IQ-steering technique used to control the amplitude and phase fed to the array's elements. (b) Photograph of the implemented IQ-steering electronics. The extenders and antennas are shown in Fig. 8.6. Measured (c) Power and (d) Relative phase of the IQ-mixer in channel 1 at 15 GHz. Solid lines are constant-phase contours. The -9 dBm power contour is indicated and the measured amplitude and phase on this contour are shown in (e).

to a far-field measurement setup. We therefore used a WR-10 waveguide probe connected to a commercial down-converting mixer as a receiver, which was connected to a spectrum analyzer for readout of the signals. This receiver provides us with fast measurements of relative power to perform radiation pattern measurements. The measurements with this receiver were later calibrated against absolute power measurements using a power meter, detailed in Section 8.5.2.

A schematic overview of this measurement setup is shown in Fig. 8.6a and photographs of the setup are provided in Figs. 8.6b and 8.6c. The amplitude and phase of the array inputs are controlled as described in Section 8.4.1. The focusing lens is a polytetrafluoroethylene (PTFE, $\varepsilon_r = 2$) hyperbolic lens placed directly above the antenna array and held in place using a 3-D printed fixture. The receiver is positioned in the spot of the focusing lens and can be moved around it using a 3-axis CNC stage.

To validate the accuracy of the quasi-optical measurement setup, we have compared the measured E-plane pattern of a single active element using this setup to the earlier near-field measurements. Indeed, as shown in Fig. 8.4e, there is a good agreement between the two measurement techniques. With this setup we achieve a dynamic range of at least 50 dB. After calibrating the array as described in Section 8.5, the same setup is used to measure the active array patterns.

8.5 Over-the-air Active Array Calibration

In this section, we describe the calibration procedure necessary for the active array demonstration, that will be presented in Section 8.6.

8.5.1 IQ-mixer Calibration at W-band

The broadside calibration at W-band was performed by positioning the receiver at the focus of the lens and measuring the received power using the spectrum analyzer.

Each lens element of the array was measured independently at 90 GHz as a function of the IQ-mixer voltages $V_I^{(i)}$, $V_Q^{(i)}$ that control the amplitude and phase fed to the lens. For example, the calibrated measured power at 90 GHz is shown in Figs. 8.7a and 8.7b for channels 1 and 2, respectively. Due to hardware differences, the received power varies per channel. The greatest common received power for all individual channels, around -31 dBm, was set as the contour in the $V_I^{(i)}$, $V_Q^{(i)}$-plane over which each channel operates. A few such constant-power contours are illustrated in Fig. 8.7a and Fig. 8.7b.

To demonstrate quasi-optical power combining in the spot, only the first array element is turned on and the power in the spot is measured while the phase angle $\phi_{in}^{(1)} = \arctan\left(V_Q^{(1)}/V_I^{(1)}\right)$ is swept from 0° to 360° over the contour of constant power. The calibrated measured power is shown in Fig. 8.7c, where we see that indeed -31 dBm is measured independent of $\phi_{in}^{(1)}$. The first array element is then fixed at $\phi_{in}^{(1)} = 0^\circ$ and the second array element is turned on. We then measure the received

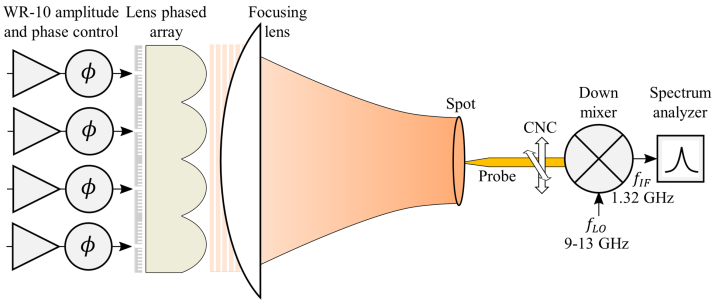

(a)

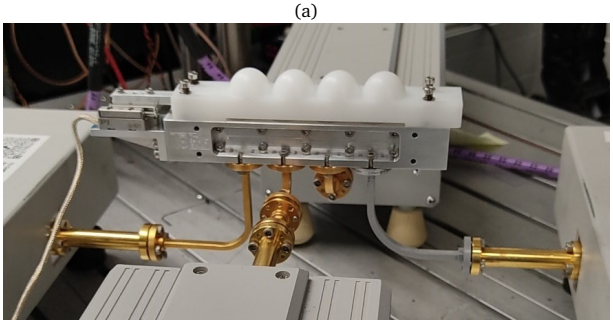

(b)

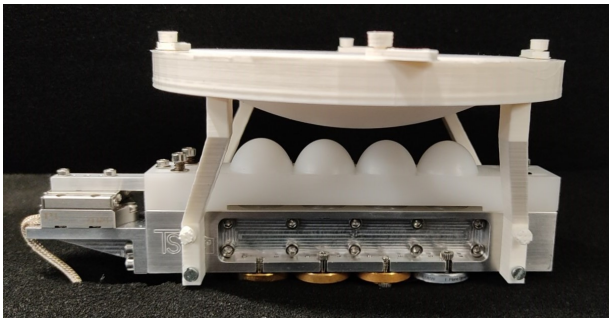

(c)

Fig. 8.6: (a) Schematic of the quasi-optical antenna measurement setup. (b) Frequency extenders connected to the prototype. (c) The PTFE focusing lens is placed above the array.

power, i.e., the combined power of channels 1 and 2, as a function of the phase angle $\phi_{in}^{(2)} = [0°, 360°]$ over its contour of equal power. A clear interference pattern with 6 constructive (destructive) peaks (valleys) can be observed in the measured power in Fig. 8.7c, which is consistent with the phase shifting after the frequency extenders achieving a range of $[0, 12\pi]$.

For the channels $i = \{3, 4\}$, the preceding steps are repeated: channels $1...i-1$ are fixed at a point of maximum constructive interference. Channel i is turned on and $\phi_{in}^{(i)}$ in is swept over a contour of constant power. The measured power is shown

in Fig. 8.7c, in which the characteristic peaks and valleys are indeed observed. The maximum received power with four active lens elements is 12 dB above the received power of a single antenna element, as expected from the increased antenna gain and transmit power. Maximum destructive interference with four active channels is 6 dB below the maximum constructive interference, which is expected since channels $1-3$ are fed in phase and only the fourth channel is out of phase.

The calibration procedure for scanned beams is the same as the procedure outlined above, except for the position of the piezo-electric motor and the position of the receiver. The piezo-electric motor was displaced by 0.24 mm/° of desired scan angle (see Section 8.3). The receiver was positioned at the scanned focus of the focusing lens which is displaced $\Delta\rho = F\tan\theta_{sc}$ relative to the broadside spot of the focusing lens.

The calibration procedure described above was performed for 78 GHz, 90 GHz and 102 GHz for scan angles up to $\theta_{sc} = 20°$ in steps of $\Delta\theta_{sc} = 5°$. For example, the received power with 1-4 active channels as a function of $\phi_{in}^{(i)}$ for $\theta_{sc} = 20°$ at 102 GHz is shown in Fig. 8.7d where we can also observe the 12 dB gain in received power of the active array relative to a single active element. This calibration procedure provides us with the values for the IQ-mixer voltages $V_I^{(i)}$, $V_Q^{(i)}$ that correspond to the progressive phase shifts required to steer the beam towards the desired scan angle θ_{sc}.

8.5.2 Absolute Power Calibration

After calibration, we measured the power in the spot radiated by the active array using a standard gain horn and a W-band power meter. The measured power was used to calibrate the relative power measurements performed with the spectrum analyzer. The measured power in the spot with both setups is reported in Table 8.I as P_{spot}^{SA} (spectrum analyzer) and P_{spot}^{PM} (power meter), respectively. Finally, the input power to the array, P_{in}^{PM}, was measured by summing the power measured at the output of the frequency extenders with a power meter. This power is also reported in Table 8.I.

Table 8.I: Measured power in the over-the-air measurement setup

Frequency [GHz]	P_{spot}^{SA} [dBm] at f_{IF}	P_{spot}^{PM} [dBm] at f_{out}	P_{in}^{PM} [dBm] at f_{out}
78	-44.4	-16.7	0.6
90	-45.2	-18.6	-2.9
102	-57.0	-21.2	-6.0

8.6 Active Array Demonstration

The active 4x1 scanning lens phased array performance was measured using the setup and calibration procedure described in Sections 8.4 and 8.5.

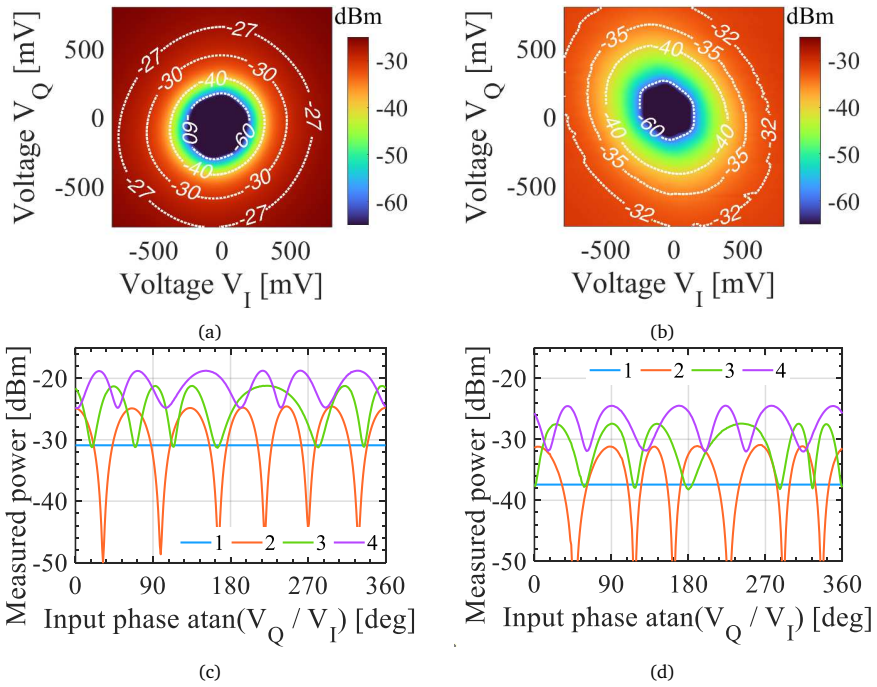

Fig. 8.7: Received power at 90 GHz for (a) Channel 1 and (b) Channel 2 in the focus of the focusing lens as a function of the IQ-voltages. Received power with 1–4 active channels as a function of ϕ_{in} at (c) 90 GHz, broadside and (d) 102 GHz, 20° scan.

The measured broadside E-plane radiation patterns of the active array are shown in Figs. 8.8a to 8.8c at 78 GHz, 90 GHz and 102 GHz, respectively. The radiation patterns show excellent agreement with full-wave array simulations of the far field patterns for all frequencies. The maximum sidelobe level is around −12 dB in the E-plane and around -20 dB in the H-plane.

The measured scanned E-plane radiation patterns are shown in Figs. 8.8a to 8.8c at 78 GHz, 90 GHz and 102 GHz, respectively. The scanned patterns also show very good agreement with the expected patterns from the simulations, with maximum sidelobe level increasing to around -10 dB for $\theta_{sc} = 15°$.

The array's antenna gain is obtained by applying Friis' equation, which can still be applied in the focused spot as explained in [167]. The transmit power is P_{in}^{PM}, the received power is P_{spot}^{PM} as reported in Section 8.5.2 and Table 8.I. The gain of the horn is 10.8 dBi at 90 GHz. The dielectric and reflection loss due to the PTFE focusing lens is estimated at 0.36 dB ($\tan\delta = 4 \cdot 10^4$ [168]). The measured antenna gain is shown in Fig. 8.8d for 78-102 GHz. For broadside, the measured gain is 31.2 dBi at 90 GHz. The simulated gain in Fig. 8.8d takes into account the estimated dielectric loss in the lens array of 0.07 dB ($\tan\delta = 3.3 \cdot 10^4$ [168]) and the ohmic loss in the

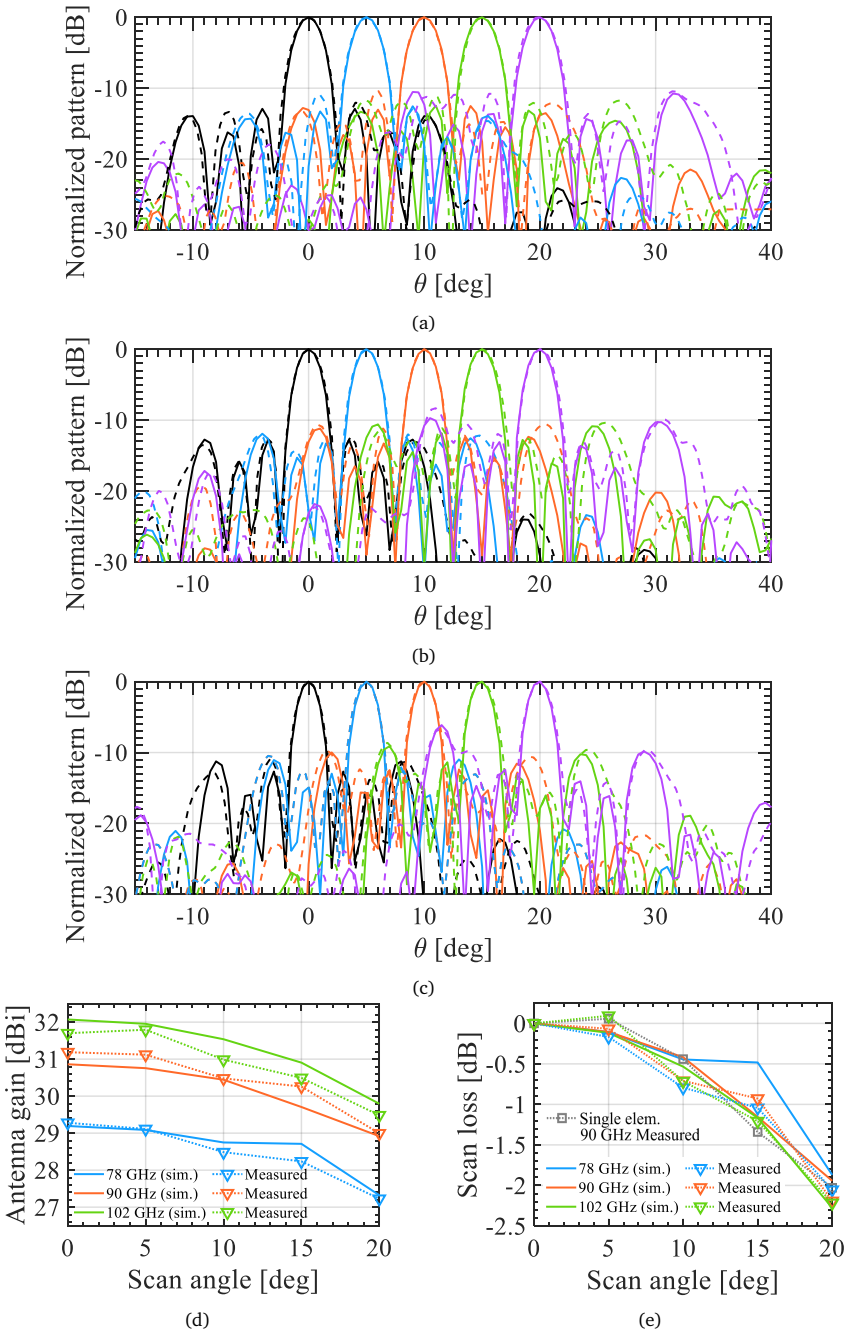

Fig. 8.8: (a)-(c) 4x1 active array E-plane radiation patterns at 78-102 GHz. The achieved (d) Antenna gain and (e) Scan loss of the active array. Solid lines are simulations, dashes are measurements.

waveguide block between 0.5-0.75 dB ($\sigma = 3.6 \cdot 10^5$ S/m [165]).

The measured scan loss is determined as the difference in received power in a scanned position relative to broadside, taking the pattern of the receiving probe in consideration, and is shown in Fig. 8.8e. The measured scan loss is in good agreement with the simulated scan loss and is between -2 dB and -2.2 dB for $\theta_{sc} = 20^\circ$ in the W-band, depending on the frequency. The measured scan loss of a single element is also shown in Fig. 8.8e, demonstrating that the scan loss is indeed defined by the scanning ability of the single element as anticipated in [111]. Consequently, the scan loss of the array and grating lobe levels can be improved by using lens elements with better scanning performance. The antenna gain as a function of scan angle, shown in Fig. 8.8d, is in good agreement with simulations.

Although other works at lower frequencies, such as [84], [163], have demonstrated beam scanning to larger angles, i.e., $\theta_{sc} = 30^\circ$, the gain reported in those works was much lower: below 20 dBi for roughly the same number of array elements. This is due to the smaller diameter of the single lenses: $D_l \approx 2.5\lambda_0$ in [84], [163] versus $D_l = 6\lambda_0$ in this work. Consequently, the maximum number of beams scanned $N = \theta_{sc} D_l / \lambda_0$ is $N \approx 1.3$ in [84], [163] and $N = 2.1$ in this work. Scanning $N = 1.3$ beams ($\theta_{sc} = 12.5^\circ$) using our antenna results in a scan loss of around 0.9 dB, which is lower than the 1.6 dB and 2.5 dB scan loss reported in [84], [163], respectively, for the same N. Additionally, the pattern quality and aperture efficiency in [84], [163] are not as high as reported here. For example, in [163] the aperture efficiency is below 40% while we achieve around 84%. In [84] the sidelobe level is around -6 dB for $N = 1$ while we remain below -10 dB for $N = 2$. Finally, the measured bandwidth of our antenna is more than 25%, while the bandwidths in [84], [163] are 11% and 8.5%, respectively.

8.7 Conclusion

We have reported on the simulation, fabrication and measurement of a sparse 4x1 scanning lens phased array with a periodicity of $6\lambda_0$ operating over the entire W-band (75-110 GHz). The array is capable of continuous and dynamic beam steering of a high-gain (>30 dBi) beam towards $\pm 20^\circ$ with low grating lobe levels around -10 dB. The array achieves low grating lobe level thanks to the use of a leaky wave feed in combination with HDPE lenses to reach high aperture efficiency illumination of the lens that is required in the scanning lens phased array architecture.

The active scanning lens phased array relies on a combination of electrical and mechanical phase shifting to steer the beams. To achieve electrical phase shifting, we developed and measured a W-band setup that uses IQ-mixers at low frequencies to achieve $[0, 2\pi]$ phase shift before x6 multiplication, resulting in $[0, 12\pi]$ phase control at W-band. Mechanical phase shifting was implemented with a high-precision piezo-

electric motor. The proposed dynamic beam steering concept can be extended to two dimensions using 2-D piezo-electric motors. This will enable translating the lens array in the xy-plane, achieving the steering of the element pattern in two dimensions.

An over-the-air active array calibration method was presented and implemented. Measurements of this W-band 4x1 array prototype show excellent agreement with simulations in terms of radiation patterns, gain and scan performance, demonstrating the potential of the proposed scanning lens phased array concept.

Chapter 9
A 7-Element Coherent Transmit Lens Array at 500 GHz

In this Chapter, we demonstrate the scanning lens phased array architecture at submillimeter wavelengths with a seven-element silicon lens array. The antenna array is capable of steering a high-gain beam (>30 dBi measured) towards discrete scan angles exceeding $\pm 25^{\circ}$ at 450-650 GHz. The lens feeds, which were described in Chapter 6, are coherently excited using a novel quasi-optical transmit-array power distribution architecture. This quasi-optical system consists of a large lens antenna that distributes a single submillimeter-wave signal over seven smaller lens elements in another array with a power coupling efficiency of neary 60%. The power is then coherently coupled through seven waveguides to the scanning lens phased array. This Chapter contains the analysis of the entire quasi-optical system from the power distribution lens to the on-sky beams radiated by the array, which is validated by measurements of a prototype at 450-500 GHz.

9.1 Introduction

Future heterodyne space instruments at submillimeter wavelengths require high-gain steerable beams (>50 dBi) over a field of view of around 25° in a compact architecture. The current generation of such instruments use opto-mechanical reflectors which are bulky, slow and have high power consumption.

Alternative approaches include fully sampled phased arrays and limited-scan sparse arrays. While fully sampled phased arrays can achieve the required beam steering, such arrays at submillimeter wavelengths suffer from integration limitations and thermal constraints and can not achieve the required gain. Furthermore, fully integrated active technology is not sensitive enough for space-based astronomy and planetary science applications and the current active heterodyne technologies (i.e., Schottky-, SIS- or HEB-based detectors) are too bulky to accomodate half-wavelength sampling due to the use of waveguide split-block technology [169]. Other options, such as sparse phased arrays exploiting subarraying techniques [75], [76] or fed by Fabry-Pérot cavities [73], [74] are not able to cover the required field of view.

To overcome these problems and meet the requirements in terms of space, weight and power (SWaP) for future SmallSat and CubeSat missions, we have proposed the scanning lens phased array architecture in this thesis. In order to demonstrate a scanning lens phased array, multiple lenses must be excited coherently. However, efficient

Parts of this Chapter have been published in **[C5]** and **[J7]**.

power distribution at submillimeter wavelengths is challenging. For example, power distribution (PD) using waveguides results in high losses that scale with the number of receivers. Phase gratings have also been used to generate 8 beams at 1.4 THz [170]. However, the bandwidth of such gratings decreases with the grating order, or, equivalently, the number of beams.

In this chapter, we propose a novel quasi-optical transmit array configuration to coherently distribute the power from a single submillimeter-wave source to each element in the scanning lens phased array. The transmit array geometry is schematically shown in Fig. 9.1a. Quasi-optical power distribution is achieved with a large elliptical lens fed by the multi-mode leaky-wave feed described in Chapter 6, which generates an aperture field that is nearly a plane wave. This field is then coupled to the transmit array which consists of a (bottom) static lens array connected to straight waveguides. The power is efficiently distributed (40-60%) into these waveguides with negligible relative phase shift ($< 6^\circ$) over a bandwidth of more than 35%. The waveguides coherently feed the (top) scanning lens phased array that is able to scan beams to discrete angles corresponding to the grating lobes of the array factor.

In particular, we analyze and demonstrate a very sparse scanning lens phased array consisting of seven silicon lenses, each with a diameter of around 9 wavelengths, in a hexagonal arrangement. We perform the analysis of the entire quasi-optical system, from the feed of the PD lens to on-sky patterns, using a cascaded method of antennas-in-reception. We have built and measured a prototype that operates at 450-650 GHz to validate the analysis methodology, proposed PD architecture and scanning lens phased array.

9.2 Transmit Array Efficiency Analysis Methodology

The overall geometry of the transmit array and power-distributing lens is shown in Fig. 9.1a. The bottom lens array is static while the top lens array can be mechanically actuated, for example by using a piezo-electric motor [86], but are otherwise identical and were described in Chapter 6.

The geometrical parameters of the power distribution lens (subscript PD) are shown in Fig. 9.1b. The feed design is the multi-mode leaky-wave stratification in Chapter 6. The diameter of the lens is equal to the diameter of the lens arrays above it, D_{PD} = 15.4 mm. The truncation angle of this lens, θ_{PD}, is optimized as described in the next sections.

The geometrical parameters of the lens elements (subscript e) in the transmit lens array are shown in Fig. 9.1c. The entire structure has mirror symmetry around the indicated plane. The transmit array consists of seven such elements in a hexagonal arrangement, each with a diameter of D_e = 5.13 mm and a truncation angle of $\theta_e = 17.5^\circ$. Each element has the stratification of Chapter 6 for efficient illumination of

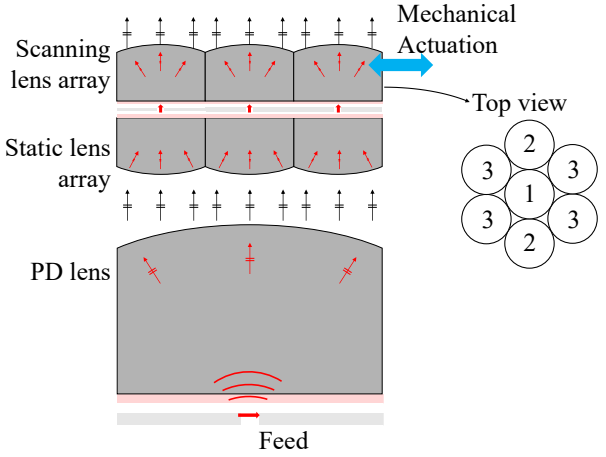

(a)

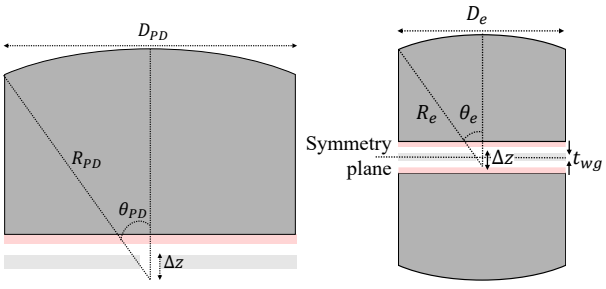

(b) (c)

Parameter	Value
D_{PD}	15.4 mm
θ_{PD}	18.5° (optimized)
R_{PD}	24.3 mm
Δz	-1.2 mm
D_e	5.14 mm
θ_e	17.25°
R_e	8.67 mm
a	362 μm
t_{wg}	300 μm

(d)

Fig. 9.1: (a) Schematic overview of the transmit lens array architecture including power-distribution lens. The geometrical parameters of the power-distribution lens and transmit array are shown in (b) and (c), respectively. The geometrical parameters of the 500 GHz transmit array are given in the table in (d).

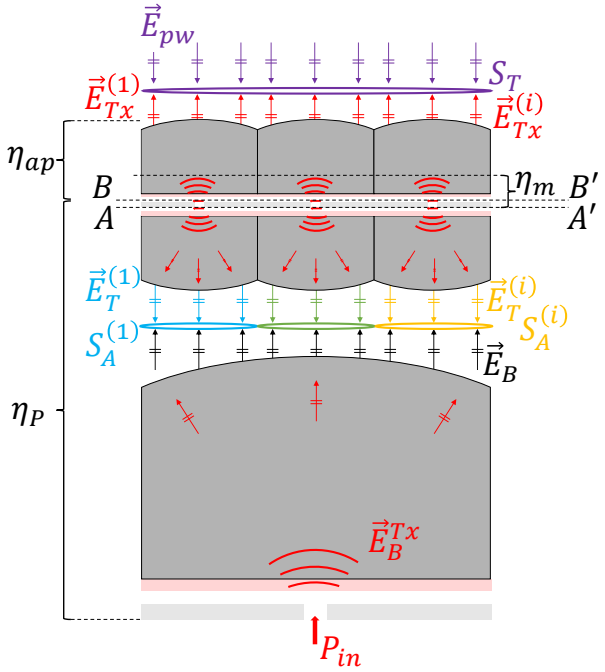

Fig. 9.2: The transmit array of Fig. 9.1a annotated to provide details on the the fields and the locations of the reaction integrals.

the lens. The top and bottom lenses are connected through a square waveguide in a ground plane with sides of $a = 362$ μm and thickness $t_{wg} = 300$ μm.

The efficiency of the transmit array, η_{Tx}, is defined as the aperture efficiency of the entire transmit array, taking the power-distribution lens into account. This efficiency term can then be optimized as a function of θ_{PD}.

To facilitate this analysis, it is convenient to split η_{Tx} into two contributions: the first represents the power coupling efficiency η_P (including impedance mismatch) and the second the aperture efficiency of the top array, η_{ap}:

$$\eta_{Tx} = \eta_P \eta_{ap} \tag{9.1}$$

These two terms are detailed in the next sections.

9.2.1 Power Coupling Efficiency

With reference to Fig. 9.2, the power coupling efficiency η_P represents the problem below the line AA', i.e., the power coupling efficiency from the feed, stimulated by a

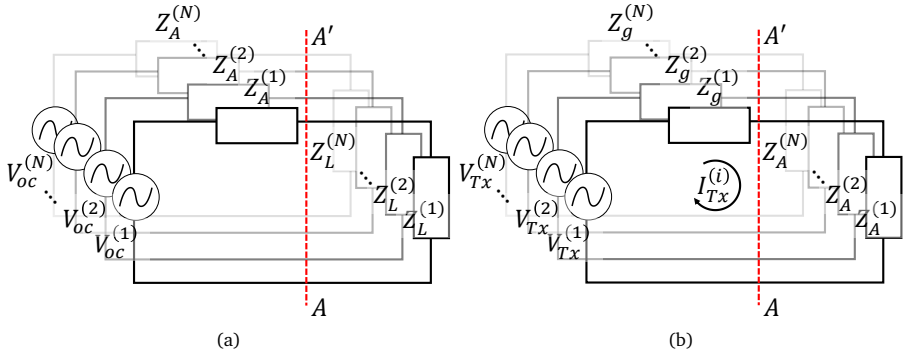

Fig. 9.3: Equivalent Thévenin circuits for the lens array in (a) reception and (b) transmission.

power P_{in}, to the sum of all powers received in the waveguides at AA', $P_{Rx}^{(i)}$:

$$\eta_P = \frac{1}{P_{in}} \sum_{i=1}^{7} P_{Rx}^{(i)} \tag{9.2}$$

To calculate $P_{Rx}^{(i)}$, we extend the methodology of lens-to-lens coupling described in Section 3.2 to lens-to-array coupling. As indicated in Fig. 9.3a, the Thévenin equivalent circuit of each receiving element in the array is considered and $P_{Rx}^{(i)}$ is the power in $Z_L^{(i)}$. Note that in general, the antenna impedances $Z_A^{(i)}$ and load impedances $Z_L^{(i)}$ can be unique, but in this case all receiving lenses are identical.

The receiving antenna impedance $Z_A^{(i)} = Z_A$ was given in Chapter 6 and is around $Z_A \approx 500\Omega$ around the central frequency. To determine $Z_L^{(i)} = Z_L$, it is apparent from Fig. 9.1c that it is equal to the impedance seen "looking up" from BB', transformed over the distance $BB' - AA'$. In other words, we can transform the impedance Z_A over the waveguide with length t_{wg} and characteristic impedance of the TE_{10} mode $\zeta_{10} = k\zeta_0/\beta$.

The receiving lens array elements are then considered in transmission. The equivalent Thévenin circuits of the transmitting antennas is given in Fig. 9.3b. Note that there are $N = 7$ circuits here, but they are all identical and therefore $I_{Tx} = I_{Tx}^{(i)}$. Referring to the methodology in Section 3.2, the received power at each lens element is then[1]:

$$P_{Rx}^{(i)} = \frac{\left| V_{oc}^{(i)} I_{Tx} \right|^2}{16 P_{Tx}} \tag{9.3}$$

[1]Note that here, in contrast to Section 3.2, we have included the effects of impedance mismatch in the received power $P_{Rx}^{(i)}$ by considering the actual Z_L in the circuits in reception, whereas we had previously included an impedance mismatch term η_m to account for the fact that $Z_L \neq Z_A^*$.

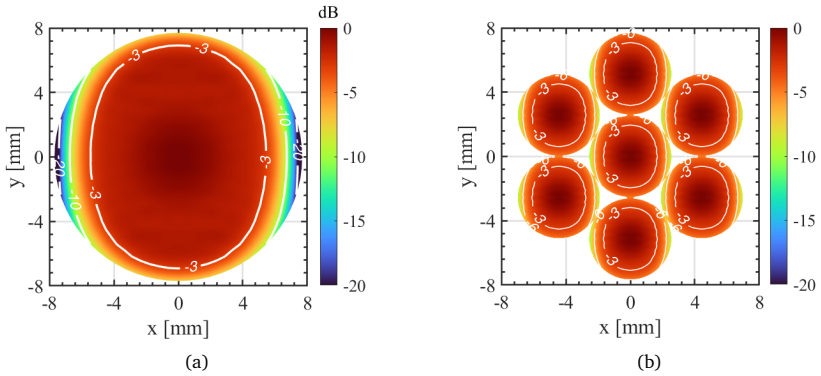

Fig. 9.4: Aperture field of (a) the large lens and (b) the bottom array.

As before, the product $V_{oc}^{(i)} I_{Tx}$ is calculated by a reaction integral of the fields transmitted by the considered antennas on the shared apertures. Note that there are now seven shared apertures, $S_A^{(i)}$, as indicated in Fig. 9.2. The field radiated by the power-distribution lens, incident on the bottom B of $S_A^{(i)}$ is $\vec{E}_B$. The field radiated by the lens elements on the top T of $S_A^{(i)}$ is $\vec{E}_T^{(i)}$. An example of the fields $\vec{E}_B$ and $\vec{E}_T$ are shown in Fig. 9.4a and Fig. 9.4b, respectively. The reaction integral between these two fields is:

$$V_{oc}^{(i)} I_{Tx} = \frac{2}{\zeta_0} \iint\limits_{S_A^{(i)}} \vec{E}_T^{(i)} \cdot \vec{E}_B \, \mathrm{d}S \tag{9.4}$$

The approach outlined above will be used to evaluate the power coupling efficiency in the next section on the optimization. However, it is also possible (if only as a sanity check) to approximate the power coupling efficiency as the product of several terms: the spillover efficiency of the large lens η_{so}^{PD}, the aperture efficiency of the small receiving lens η_{ap}^{Rx}, the impedance matching efficiency η_m at AA' and the "fill factor" η_{fill}. The fill factor, or sampling efficiency, is the proportional area of the power-distribution lens that is filled by the receiving lens array. For the seven-element hexagonal array, it was given as 78% in Section 2.3. The approximated power coupling efficiency is:

$$\eta_P \approx \eta_{so}^{PD} \cdot \eta_{ap}^{Rx} \cdot \eta_m \cdot \eta_{fill} \tag{9.5}$$

This approximation assumes that the aperture field of the large lens is uniform in amplitude and phase, which becomes increasingly inaccurate for larger θ_{PD}. However, it is still useful to have a secondary method of estimating the coupling efficiency since the transmit array is too large to simulate with full-wave solvers.

9.2.2 Top Array Efficiency

We also calculate the efficiency of the top array, η_{ap}, using the antennas-in-reception methodology. If we consider only the top lens array fed by the waveguides, the induced voltage at the terminals of the waveguides (i.e., at BB' in Fig. 9.2) can be calculated using the reaction integral over S_T between an incident plane wave, $\vec{E}_{pw}$ and the sum of the fields radiated by each of the lenses, $\vec{E}_{Tx} = \sum_{i=1}^{7} \vec{E}_{Tx}^{(i)}$. The complex weight of $\vec{E}_{Tx}^{(i)}$ is given by $V_{oc}^{(i)}$ calculated in Eq. (9.4). The reaction integral on the top side of the transmit array is:

$$(V_{oc}I)_T = \frac{2}{\zeta_0} \iint_{S_T} \vec{E}_{Tx} \cdot \vec{E}_{pw} \, \mathrm{d}S \tag{9.6}$$

and the power delivered to a matched load at the antenna terminals is

$$P_L = \frac{\left|(V_{oc}I)_T\right|^2}{16 P_{Tx}} \tag{9.7}$$

The aperture efficiency of the top array is calculated as the ratio P_L to the power incident on the lens aperture from the incident plane wave:

$$\eta_{ap} = \frac{P_L}{P_{pw}} \tag{9.8}$$

and $P_{pw} = A_A |E_{pw}|^2/(2\zeta_0)$ is the power in the plane wave incident on the lens array's area A_A.

9.3 Resulting Transmit Array Efficiency

The procedure described in Section 9.2 has been used to optimize the transmit array efficiency at 550 GHz as a function of the truncation angle (θ_{PD}) (while keeping its diameter fixed). With reference to Fig. 9.2, we have taken $\vec{E}_B$ as the aperture field of the large lens in transmission. This field is obtained by first calculating the field inside the lens using the Green's function for stratified media in the far field and then propagating this field out of the lens using geometrical optics. At the lens-air interface, the effect of a quarter-wavelength Parylene $(\varepsilon_r = 2.62)$ matching layer at 550 GHz is considered. As an example, the co-polarized component of the aperture field $\vec{E}_B$ for a truncation angle of $\theta_{PD} = 18.5^\circ$ is shown in Fig. 9.4a. The field is nearly uniform, which is due to the "top-hat" pattern of the multi-mode leaky-wave feed with a small amount of amplitude tapering towards the edges as shown in Chapter 6.

The same geometrical-optics propagation procedure is used to calculate the aperture field of the bottom array of small lenses in transmission, $\vec{E}_B$. However, since the lenses in this array are small in terms of the wavelength, we have calculated the field inside the lens over a sphere using the Green's function for stratified media in the near field.

The co-polarized component of $\vec{E}_B$ is shown in Fig. 9.4b, from which the seven lens elements can clearly be identified. The amplitude tapering at the edge of each lens is different than for the large lens due to lens being in the near field of the feed.

We have calculated the power coupling efficiency using Eq. (9.2) as a function of θ_{PD}, with the result in Fig. 9.5a. The truncation angle that provides maximum power coupling, almost 60%, is $\theta_{PD} = 18.5°$. For smaller truncation angles, most power in the power-distribution lens is lost to spill over. For larger truncation angles, the uniformity of the aperture field is too low to provide good coupling to all lenses. For very large truncation angles, $\theta_{PD} > 35°$, the power coupling efficiency increases again because all power is coupled to the central element of the transmit array. The approximation in Eq. (9.5) is in good agreement with the exact expression of Eq. (9.2) for small truncation angles, as shown by the dashed line in Fig. 9.5a. For larger truncation angles, the assumption of uniform field distribution in Eq. (9.5) no longer holds and makes the approximated formula inaccurate.

The amplitude and phase of the voltage induced on the bottom waveguide terminals, $V_{oc}^{(i)}$, for maximum η_P is shown in Fig. 9.5b. Note that due to the symmetry of the aperture fields, only three unique induced voltages are obtained (the numbering of the lenses is given in Fig. 9.1a). A maximum power difference of 2.6 dB occurs between lenses 1 and 3; the maximum phase difference is $6°$.

We have also calculated the top array efficiency as a function of θ_{PD}. The result is shown in Fig. 9.5a. The top array efficiency is more or less constant, around 76%, until the truncation angle $\theta_{PD} > 20°$. This is due to the uniformity of $\vec{E}_B$ until that angle. For larger truncation angles, the top array efficiency rapidly decreases because only the central array element is illuminated by the large lens.

The aperture efficiency of the entire transmit array, η_{Tx}, is shown in Fig. 9.5a as a function of θ_{PD}. The absolute maximum, around 42%, is achieved at $\theta_{PD} = 18.5°$. Note that this efficiency entails the entire transmit array architecture: from the power-distribution lens to the bottom array, through the waveguide and radiated into free space by the top array, including the losses due to spill-over and reflections at the various lens-air and air-lens interfaces.

Next, we have fixed $\theta_{PD} = 18.5°$ and calculated the transmit array efficiency as a function of frequency, from 450-650 GHz. The result is shown in Fig. 9.5d. The efficiency is above 30% in this entire bandwidth and above 40% between 500-575 GHz.

9.4 450-650 GHz Prototype and Measurement Setup

We have developed a 450-650 GHz transmit array prototype following the architecture in Fig. 9.1. The purpose of the prototype is twofold: First, to demonstrate coherent power distribution from the large lens to the bottom array elements and to validate

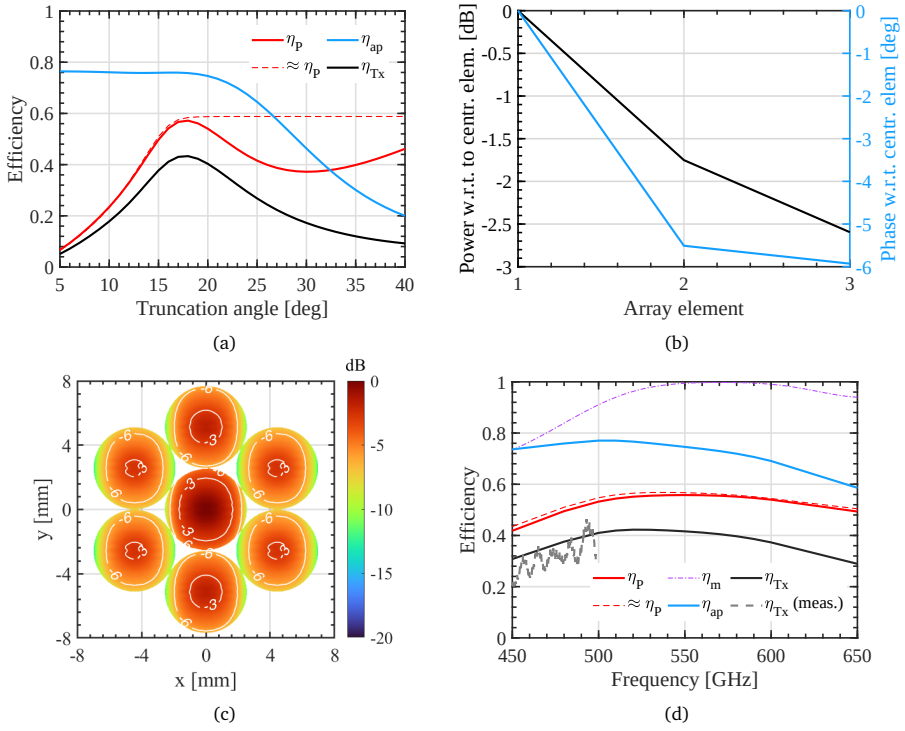

Fig. 9.5: (a) Power coupling efficiency, top array efficiency and transmit array efficiency as a function of the truncation angle of the power-distribution lens, θ_{PD}. (b) The relative power coupled to each lens element and the associated relative phase at the maximum power-coupling efficiency. (c) The resulting aperture distribution of the top array when fed with the amplitudes given in (b). All these results are shown at 550 GHz. In (d), the power coupling efficiency, top array efficiency and transmit array efficiency are shown in the frequency band 450-650 GHz. The matching efficiency is also given for reference; it is also included in the power-coupling efficiency.

the efficiency analysis and optimization in Sections 9.2 and 9.3. Second, we use the prototype to demonstrate beam steering of a very high gain beam at submillimeter waves using the scanning lens phased array architecture of Chapter 6. To realize the second goal, a piezo-electric motor is used to actuate the top lens array with respect to the feeds.

Two antennas were manufactured to demonstrate these goals: the large power-distribution lens antenna and the transmit array. The manufacturing process of both is detailed here, along with the measurement setup that was used to characterize both prototypes.

9.4.1 Prototype Power Distribution Lens and Transmit Array

The power-distribution lens antenna is a single, 15.4 mm diameter silicon elliptical lens with a truncation angle of 18.5° fed by the multi-mode leaky-wave feed developed in

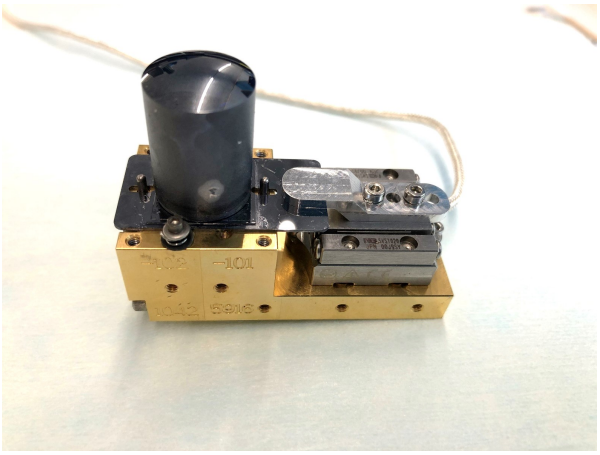

Fig. 9.6: Assembled power-distribution lens antenna prototype.

Chapter 6. The lens was fabricated and coated with a quarter-wavelength Parylene layer by Tydex. The lens is placed on top of a stack of several processed silicon wafers that contain the leaky-wave stratification as in [86] Chapter 6. Optical features on the wafers are used for alignment. The assembled wafers and lens are then placed on a gold-plated metal split-block fixture that contains a transition from the square aperture in the top to a WR-1.5 flange on the bottom. A piezo-electric motor is used to align the wafers-lens combination to the feed in the block in one axis, while the other axis is aligned with metal pins. It was estimated that the axis controlled by the piezo-actuator achieves an alignment accuracy better than 10 μm while the other axis achieved around 100 μm. While this misalignment results in a small angular tilt of the beam outside the lens, this tilt can be corrected using a 5-axis mechanical stage in the measurement setup (as will be discussed later). The assembled power-distribution lens antenna is shown in Fig. 9.6.

The transmit array prototype consists of several parts, shown in Fig. 9.7, that were manufactured with different processes. The lens arrays, which were first shown in Chapter 6, were fabricated at Veldlaser B.V. using laser ablation from a 1 mm high-resistivity silicon wafer and were subsequently coated with a quarter-wavelength Parylene anti-reflection coating at SCS Coatings. The lens arrays are pictured in Fig. 9.7a. To achieve the required extension height of the arrays, two silicon disks were turned with a height of 5.9 mm and a diameter of 19 mm. Optical alignment features were then laser-ablated from the disks, again at Veldlaser B.V. The disks are mounted on several processed wafers that contain the leaky-wave stratification. A photograph of the wafers is shown in Fig. 9.7b and the mounted silicon disks are shown in Fig. 9.7c. The top and bottom array are connected by a 300 μm thick gold-plated silicon wafer

that contains seven square waveguides which were processed using deep-reactive ion etching [138]. This wafer is shown in Fig. 9.7d. The top and bottom lens array assembly were mounted on an aluminium fixture which also houses the piezo-electric motor. The complete assembly is shown in Fig. 9.7e.

9.4.2 Antenna Measurement Setup

We used a VNA and two WR-2.2 (325-500 GHz) frequency extenders to characterize the antennas between 450-500 GHz. First, we characterize only the power-distribution lens and we subsequently mounted the transmit array after the power-distribution lens to measure the entire transmit array. The antennas are characterized over-the-air: a standard-gain horn is used to measure the gain and an open-ended waveguide was used to measure the radiation patterns. The flange (but not the opening) of the receiving waveguide is covered with a thin sheet of Eccosorb to reduce scattering and (multiple) reflections. The receiver is placed in a 3-axis CNC positioner.

The overall aperture size of the power-distribution lens and the transmit array is 15.4 mm, and the far-field distance is close to a meter at 500 GHz. To facilitate antenna measurements at a distance that fits the lab's equipment, a hyperbolic lens is used to focus the beam in a spot at 10 cm distance. This solution allows us to measure antenna gain in the focus of the hyperbolic lens and the beam patterns in a planar region surrounding the focus of the hyperbolic lens. A similar approach was taken in Chapter 8 and in [166], [167]. Photographs of the hyperbolic lens in front of the power-distribution lens and in front of the transmit array are shown in Figs. 9.8a and 9.8b.

In order to measure it, the transmit array (including hyperbolic focusing lens) is mounted on a 5-axis mechanical stage produced by Standa. This stage allows us to control the (x, y, z, θ, ϕ)-axes in steps of $1\mu\mathrm{m}/0.01^{\circ}$. Thus, precise alignment between the power-distribution lens and transmit array can be achieved. Furthermore, we can offset any slight tilt in the beam pattern of the power-distribution lens due to inaccurate alignment between its lens and feed. A photograph of the entire transmit array measurement setup is shown in Fig. 9.9.

9.5 Measured Performance

In this Section, the measured performance of both antenna prototypes is detailed. We have first independently characterized the power-distribution lens using the same measurement setup but in the absence of the transmit array. Next, this large lens was used to feed the transmit array prototype and we measured the transmit array prototype.

9.5.1 Power-distribution Lens Measurements

The measured input reflection coefficient (S_{11}) is shown in Fig. 9.10a in the WR-2.2 band showing the antenna is well matched above 420 GHz. The simulated reflection

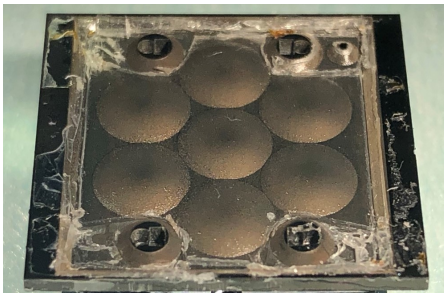

(a)

(b)

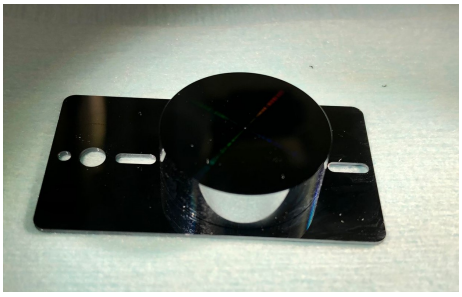

(c)

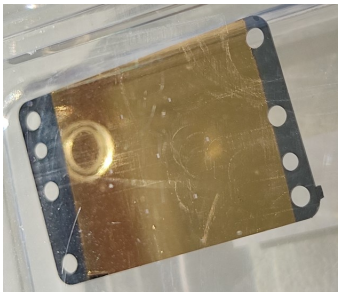

(d)

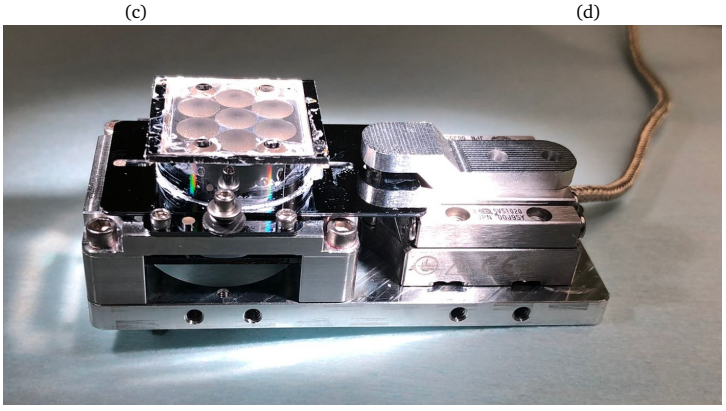

(e)

Fig. 9.7: (a) Lens array with Parylene AR coating (b) silicon wafers containing leaky-wave cavity and transformer layers (c) silicon disks assembled on the wafers (d) gold-plated silicon wafer containing seven square waveguides. The assembled transmit array prototype in shown in (e).

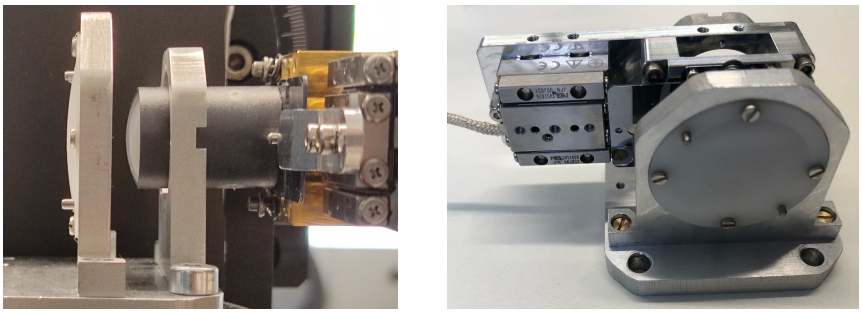

(a) (b)

Fig. 9.8: The hyperbolic lens is placed directly in front of (a) the power-distribution lens and (b) the transmit array to characterize these antennas.

coefficient was calculated using a full-wave simulation of the metal block with a finite conductivity of $\sigma = 3.5 \cdot 10^6$ S/m. This simulated result is in very good agreement with the measurement. Additionally, the gain of the antenna was measured in the spot with the standard-gain horn. The measured gain of the lens antenna is shown in Fig. 9.10b and is in very good agreement with simulations when taking into account the finite conductivity of the metal split-block and the reflection and dielectric loss of the hyperbolic lens. Especially good agreement is obtained when a time gate is applied to remove the effect of scattering in the environment and multiple reflections.

The radiation pattern of the top-hat lens was measured in the spot of the hyperbolic lens at 450-500 GHz using the open-ended waveguide. The E- and H-plane cuts of the measurement are compared to the simulations in Fig. 9.10c at 480 GHz. The measured pattern is in very good agreement with the simulated pattern, which was obtained using the antennas-in-reception methodology explained in Chapter 3. The measured 2-D radiation pattern is shown in Fig. 9.10d.

Since the measurements are in good agreement with the simulations, it is anticipated that the analysis results of Section 9.2 still hold for this prototype.

9.5.2 Transmit Array Measurements

We have measured the radiation patterns and gain of the transmit array prototype using the setup described above. The measured radiation patterns are compared to simulations in Figs. 9.11a to 9.11c at 450 GHz, 475 GHz and 500 GHz, respectively. The simulated array patterns are calculated as the multiplication of the single-element patterns (obtained by applying the antennas-in-reception formalism for a single lens) and the array factor, with the weights of the array factor being given by Fig. 9.5b. The pattern simulations are in very good agreement with the measurements with sidelobe levels of around -12 dB in the bandwidth.

The simulated directivity of the transmit array is $\eta_{ap} D_{\max}$, with $D_{\max} = 4\pi A_A / \lambda_0^2$

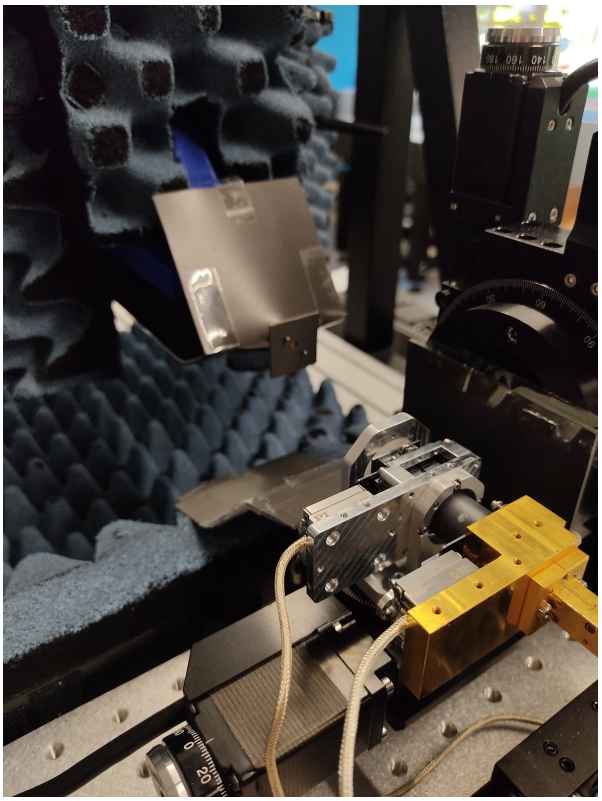

Fig. 9.9: Submillimeter-wave measurement setup for the transmit array prototype.

the maximum theoretical directivity of an aperture of area A_A. The directivity was calculated from measurements by integration of the measured radiation patterns. The simulated gain is calculated as $\eta_{Tx} D_{\max}$ and the measured gain is obtained from the measurement of the horn in the focus of the hyperbolic lens and applying Friis' equation. Some losses are calibrated out of the measurement to isolate the efficiency of the transmit array: the conduction loss in the metal split-block feeding the power-distribution lens, the dielectric loss in the Parylene matching layers covering the arrays (as analyzed in Chapter 7) and the dielectric and reflection losses due to the hyperbolic focusing lens. The simulated and measured directivity and gain are compared in Fig. 9.11d. There is a good agreement, to within $\pm$ 1 dB, between measurement and simulation indicating that the analysis methodology in Section 9.2 is accurate. For completeness, the measured η_{Tx} was calculated from the measured data and is shown in Fig. 9.5d.

Next, we used the piezo-electric motor to mechanically displace the top lens array with respect to the waveguide array. This results in beam steering of the element

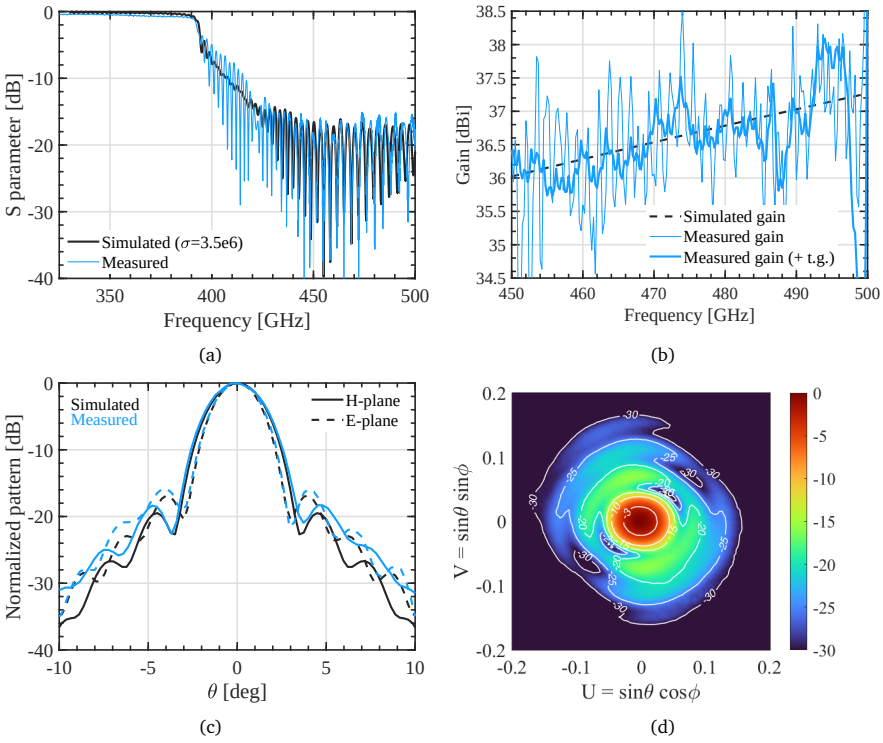

Fig. 9.10: (a) Reflection coefficient, (b) gain, (c) E- and H-plane cuts and (d) 2-D measured radiation pattern at 480 GHz of the power-distribution lens.

patterns. However, since the bottom lens array is static, the excitation through the waveguide array does not change and the lens elements of the top array are still excited in-phase. Thus, the array factor is not scanned and only a clean array pattern will emerge when the beam steering angle of the single-element pattern aligns with the grating lobes of the array factor. Since the array factor is frequency dependent, the required displacement distance that corresponds to the grating lobe angle is also frequency dependent. For example, to scan towards the third grating lobe, the measured required displacement at 450 GHz, 475 GHz and 500 GHz was 1.27 mm, 1.21 mm and 1.16 mm, respectively. The corresponding scan angles are $27.2°$, $25.5°$ and $24.6°$. The measured displacement corresponding to grating lobes 1-3 is shown in Fig. 9.12a.

The scanned patterns of the array were measured by displacing the top lens array by a distance as indicated in Fig. 9.12a and then measuring the pattern with the open-ended waveguide in the focus of the hyperbolic lens. The measured patterns for broadside and the first three grating lobes (scanning up to $25.5°$) are shown in Fig. 9.12c at 475 GHz. Due to reduced illumination efficiency, the sidelobe level of the patterns increase from -13 dB at broadside to -8 dB at the third grating lobe. How-

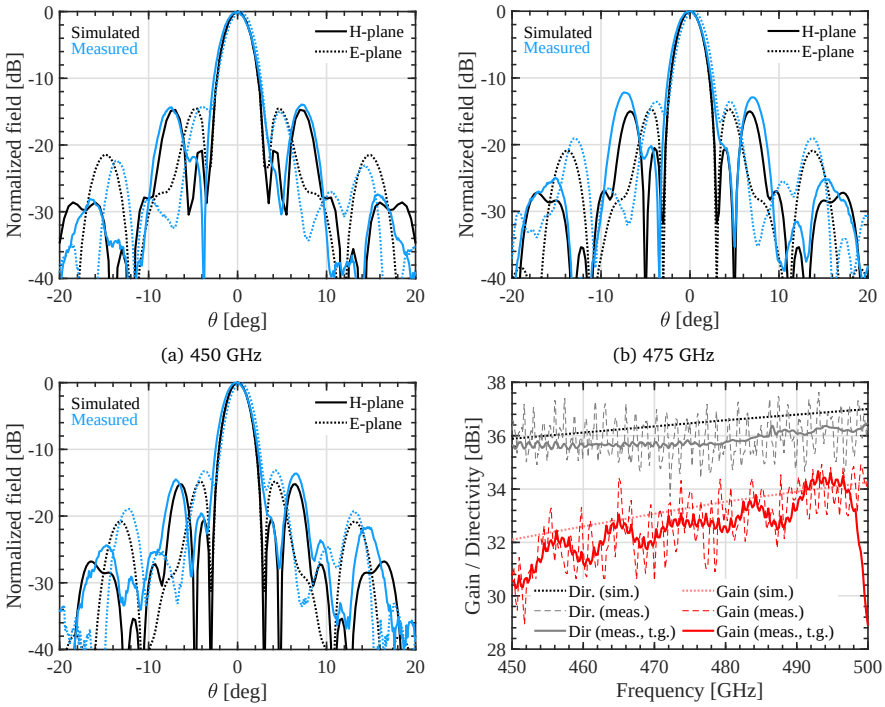

Fig. 9.11: Measured and simulated radiation patterns of the transmit array at (a) 450 GHz, (b) 475 GHz and (c) 500 GHz. (d) Measured and simulated gain and directivity in 450-500 GHz.

ever, the sidelobe level is symmetric and below -10 dB up to and including the second grating lobe (17° scanning) which is good enough for several remote sensing applications [16]. The measured radiation patterns at the third grating lobe are also shown in Fig. 9.12c at 450 GHz and 500 GHz. Symmetric sidelobe levels are achieved at these frequencies too.

The scan loss, i.e., the loss in gain relative to broadside, is shown in Fig. 9.12b. The scan loss is in line with the single-element scan loss of Chapter 6 and is around 3 dB at $25°$.

Overall, a very good agreement between measured and simulated results is achieved, demonstrating the coherent distribution of power to seven elements from a single source, the associated method of antennas in reception to calculate the efficiency and the scanning lens phased array architecture at submillimeter wavelengths.

Although the number of elements in this demonstration is relatively small, the fabrication technology can be used to scale the number of elements up by at least an order of magnitude. Additionally, we expect the same manufacturing techniques and

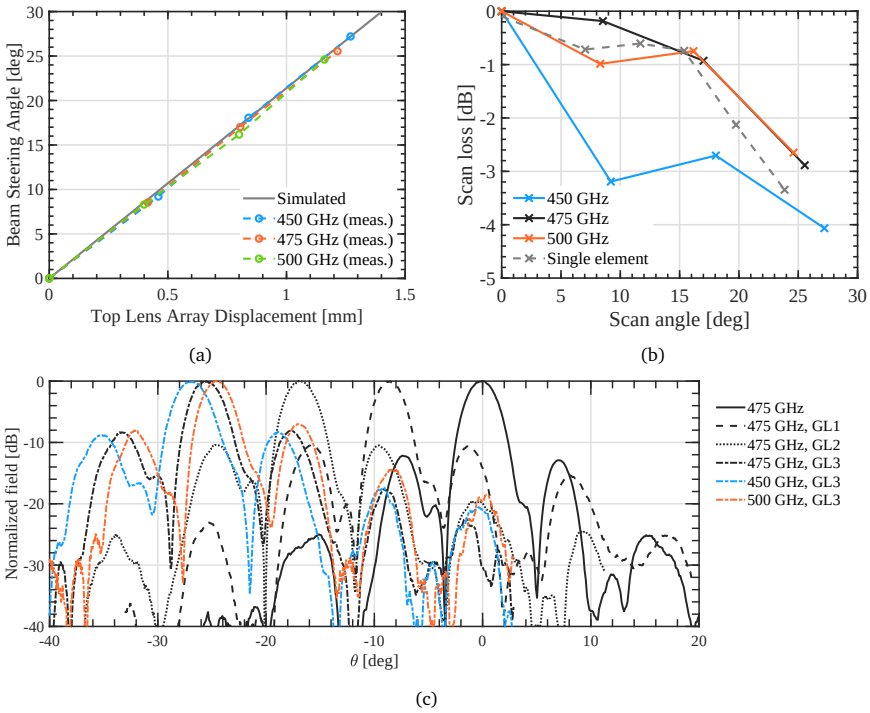

Fig. 9.12: (a) Simulated and measured scan angle of the transmit array patterns as a function of the mechanical displacement distance of the top array. (b) Measured scan loss of the transmit array. The single-element loss of Chapter 6 is shown for reference. (c) The measured radiation patterns for broadside and grating lobes 1-3.

technology to be accurate enough to create such arrays up to 2 THz. To achieve continuous beam steering, phase shifters such as those in [171] could be integrated inside the transmit array waveguides. Alternatively, the top array can serve as a focal-plane array when mixers are integrated in the waveguides. The same power distribution architecture could then be used to couple the required LO signal to the mixers with negligible phase difference and good power uniformity.

9.6 Conclusion

We have presented a novel transmit lens array architecture suitable for power distribution and high-gain beam steering at submillimeter wavelengths. The bottom half of the proposed architecture is used to achieve efficient (60%) and wide-band (35%) multi-pixel power distribution; the top half enables high-gain beam steering using a very small (around 1 mm) displacement of a lens array. We have developed a cascaded method of antennas-in-reception to analyze the full transmit array, from power-distribution lens to on-sky patterns, without full-wave simulations. High efficiency op-

eration of the transmit array is achieved with a multi-mode leaky-wave lens feed that was developed in Chapter 6 and the optimization of the power-distribution lens. A lens transmit array prototype with seven lens elements has been fabricated to operate at 450-650 GHz. Measurements of the transmit array antenna show excellent agreement with simulations in terms of patterns and gain, validating the analysis methodology that we developed.

Conclusion and Future Work

Chapter 10
Conclusion

In this thesis, we have described, analyzed, manufactured and measured a hybrid electromechanical scanning lens antenna architecture: the scanning lens phased array. The array architecture is suitable for the steering of highly directive beams at submillimeter wavelengths with a field of view of $\pm 25^{\circ}$. The hybrid phase shifting concept relies on a combination of electronic phase shifting of a sparse array with a mechanical translation of a lens array. The use of a sparse phased array significantly reduces the number of active components in the RF front-end while still enabling array-factor scanning. The translation of a lens array steers the element patterns to angles away from broadside, while simultaneously reducing the impact of grating lobes over a wide FoV. Our analysis shows that the required mechanical translation of an N-element lens array is a factor N lower than a single large lens of the same aperture dimension, which enables a mechanical implementation that is fast and low power. We further find that the lens elements in the scanning lens phased array must be fed with high aperture efficiency in order to reduce the impact of the grating lobes that arise due to the array's sparsity. Therefore, we have investigated the use of several improved resonant leaky-wave lens feeds that are suitable for low and high relative permittivity lenses. We have manufactured and demonstrated two improved leaky-wave feeds, at 180 GHz and 550 GHz. and have used them at 100 GHz in an active demonstration of the scanning lens phased array and in a transmit lens array demonstration at 550 GHz.

10.1 Analysis of (Small) Lens Antennas

We have applied an antennas-in-reception formalism to calculate the power received by the lens elements, their aperture efficiency and radiation patterns. Then, the array patterns are approximated as the multiplication of the lens element pattern and the array factor. For scan angles close to broadside, this method is shown to be accurate. For larger scan angles, the effect of multiple reflections at the lens-air interface and spill-over must be taken into account to accurately simulate the radiation pattern.

To facilitate the design of lens antennas with a small diameter, we have analyzed the near field of leaky-wave resonant antennas radiating into a semi-infinite dielectric medium. We show that the field can be locally represented as a spherical wave in a certain solid angle around broadside from the phase center far below the ground plane. The field inside this solid angle can be efficiently calculated by resorting to a non-uniform asymptotic evaluation, of the spectral Green's function along the Steepest

Descent Path (SDP), even for points very close to the LW cavity. Beyond this solid angle, given by the shadow boundary angle, a contribution due to the leaky-wave pole must also be considered to fully describe the near field. We show that the complex LW propagation constants fully define the shadow boundary angle and phase center, even for low contrast LW antennas.

To demonstrate the applicability of the proposed study, we have applied the new understanding of near-field spherical wave formation to the design and analysis of small-to-medium sized lenses. We have shown that the LW complex propagation constants can be used to define a truncated lens geometry that couples well to the leaky-wave feed and achieves a high aperture efficiency for any diameter. Moreover, we have combined the SDP calculation with the antennas in reception methodology to efficiently calculate the aperture efficiency and radiation patterns of LW lens antennas. A truncated silicon lens design with a diameter of only 4 free-space wavelengths is presented that achieves almost 80% aperture efficiency. Excellent agreement with full-wave simulations is achieved, which demonstrates the accuracy of the SDP-FO methodology. The physical insight gained in this analysis can be applied to other resonant LWAs made with different kind of stratifications, such as feeds based on frequency-selective surfaces.

10.2 High Aperture Efficiency Leaky-Wave Lens Antennas

We have demonstrated several single-element lens antenna prototypes with high aperture efficiency feeds, which are thus suitable for integration into a scanning lens phased array. To ensure applicability for a wide range of applications, we have developed both a plastic lens antenna at 180 GHz and a silicon lens antenna at 550 GHz. Both lens prototypes use novel, wideband, waveguide-based lens feeds.

The plastic lens antenna at 180 GHz is fed by a LW feed that consists of a half-wavelength air cavity and a ground plane containing annular corrugations around a circular waveguide. These corrugations, in combination with the circular waveguide, significantly reduce the impact of the spurious TM_0 mode in a wide bandwidth and all azimuthal planes. The corrugations extend the achieved bandwidth of the circular waveguide feed to lower frequencies to cover both the WR-5 and WR-6 bands, leading to a total bandwidth of 2:1 (110-220 GHz). A lens illuminated by such LW feed is shown to have cross-polarization level below -20 dB, an aperture efficiency above 80% and an S_{11} below -15 dB over the entire bandwidth. We fabricated and measured a WR-5 band antenna prototype which shows excellent agreement with the anticipated results.

To efficiently illuminate a silicon lens at 550 GHz, we proposed a multimode LW feed that is able to achieve an aperture efficiency greater than 80% over a bandwidth of 35% and a scan loss lower than 3 dB up to 25°. Compared to a standard resonant-

cavity lens feed, this LW feed includes a dielectric transformer layer between the cavity and the lens. In this way, multiple LW modes are generated which all contribute to the formation of a top-hat pattern (i.e., high aperture efficiency) while coupling to a low $f_{\#}$ lens (i.e., good scan performance). Additionally, this layer ensures impedance matching between the waveguide and the stratification without the use of a double slot iris, which simplifies the fabrication process. A prototype of an embedded lens antenna has been built at 550 GHz, integrated with a piezoelectric motor. We measured the radiation and scanning performance of the embedded pattern and combined these results with the array factor to obtain the array pattern of the phased array. We found excellent agreement between the measurement and simulated performance, validating the capability of this antenna architecture for future implementation in an active lens phased array.

To further improve the gain of silicon lenses, we have studied the performance of two different matching layers at submillimeter waves. We fabricated two otherwise identical antennas, fed by the multi-mode feed described above, which differ only in matching layer. The first matching layer is the widely-used quarter-wavelength parylene-C coating and the second a continuous impedance-transforming matching layer which was realized by periodic sub-wavelength frusta features laser-ablated directly on the lens surface. We described the laser machining process to manufacture the frusta which is suitable for shallow silicon lens arrays. We have characterized both antennas in terms of reflection coefficient, radiation patterns (directivity) and gain and compare these results to high-frequency simulations. We find that both antennas perform identically, except for the gain. The measured gain of the antenna with frusta matching layer is in very good agreement with simulations, while the parylene-C matching layer has a gain that is 1.6 dB lower. This extra loss is explained by the dielectric loss in the parylene-C. Although several other suitable low-loss materials are available to use as a matching layer, the frusta matching layer has several distinct advantages: it operates over more than an octave bandwidth and it is fabricated using the same process as the lens (array) itself.

10.3 Demonstration of Scanning Lens Phased Arrays

We have reported on the simulation, fabrication and measurement of a sparse 4x1 scanning lens phased array operating over the entire W-band (75-110 GHz) that is capable of continuous and dynamic beam steering a directive (>30 dBi) beam towards $\pm 20^{\circ}$ with low grating lobe levels. The array achieves low grating love level thanks to the use of the aforementioned high-efficiency leaky wave feed in combination with plastic lenses. The scanning lens phased array relies on a combination of mechanical and electrical phase shifting to steer the beams. To achieve the active phase shifting of the array, we developed and measured a W-band electrical phase-shifting setup that

uses IQ-mixers at low frequencies to achieve a 360° phase shift before $\times 6$ multiplication, resulting in $[0, 12\pi]$ phase control at W-band. An over-the-air calibration method was presented and implemented for such phase shifting setup. Measurements of this W-band 4×1 array prototype show excellent agreement with simulations in terms of radiation patterns, gain and scan performance, demonstrating for the first time the potential of the proposed scanning lens phased array concept.

We have also demonstrated a coherently-fed scanning lens phased array at 550 GHz using the high-efficiency multi-mode leaky-wave feed described in Chapter 6. Wideband, in-phase excitation of the lens array elements is achieved with a novel transmit lens array architecture: one large lens distributes power to an array of waveguides through a flipped array of lenses with a power coupling efficiency of 60%. The waveguides coherently feed a scanning lens phased array. The complete transmit array, from power-distribution lens to array patterns, is simulated by a cascaded method of antennas in reception. A 450-650 GHz transmit array prototype has been fabricated using silicon micromachining technology. Submillimeter-wave measurements of the array gain, patterns, and scan performance show good agreement with the simulations: a gain above 30 dBi, sidelobe levels below -12 dB and a scan loss of around 3 dB when scanning to 25°. The largest losses in the current prototype are from the parylene-C matching layers that are present on both the top and bottom lens arrays. However, this can be eliminated by using the periodic frusta matching layer that was demonstrated in Part II of this thesis. The number of elements in this demonstration (seven) can be scaled up by at least an order of magnitude with the same fabrication techniques. Additionally, the fabrication technology is precise enough to create such arrays up to 2 THz. Because the array elements are excited in-phase, the current prototype is only able to scan to discrete angles, corresponding to the grating lobes of the array factor (approximately every 5 degrees). To achieve continuous beam steering, phase shifters could be integrated inside the transmit array waveguides. Alternatively, this transmit array architecture could be used to distribute LO power to a focal-plane array when mixers are integrated in the waveguides.

Chapter 11
Future Work

From the research presented in this thesis, a multitude of interesting future research opportunities can be identified. In this Chapter, some possible future directions are described based on the broad categories of lens analysis, technology developments and application cases.

11.1 Analysis of Lenses and Lens Arrays

In Part II, we have investigated several leaky-wave feeds for silicon and plastic lens antennas. The multi-mode feed for silicon lenses, proposed in Chapter 6, achieves very high aperture efficiency in the far-field, but the near-field patterns from this feed are significantly different (and less efficient). Thus, there still exists an opportunity to investigate the applicability of similar multi-mode feeds to small silicon lenses ($D < 10\lambda_0$). For plastic lenses, we have proposed the leaky-wave feed with corrugations in the ground plane in Chapter 5. While we have demonstrated improved suppression of the TM_0 mode, especially at the lower part of the frequency band, we have not formally established a theoretical framework around this feed.

In Chapter 6, it was anticipated that the scan loss of the scanning lens phased array is dictated by the scan loss of the single element. This was demonstrated in Chapters 8 and 9, where we have used canonical elliptical lenses which are not optimized for scan performance. Therefore, an opportunity exists to improve the scan loss of lens phased arrays by investigating improved lens geometries that achieve lower scan loss or achieve an increased field-of-view for the same scan loss.

The array analysis methodology that has been used in this thesis, where the array pattern is obtained from the multiplication of the array factor and the single-element pattern obtained using the antennas-in-reception formalism, has been demonstrated to be accurate at broadside. However, for moderate scan angles, the obtained field does not accurately represent the actual array patterns. This effect is due to (multiple) reflections at the lens-air interface and spill-over into the next lens. The modeling of these effects require more research.

11.2 Technology for Lenses and Lens Arrays

A natural extension to the one-dimensional scanning lens phased arrays in this thesis is an array with two-dimensional scanning capabilities. The required 2-D piezo-electric motors are commercially available and future prototypes could incorporate them. Al-

ternatively, an architecture with two (orthogonal) 1D arrays can be investigated which may be interesting in several bi-static radar applications.

Transmit arrays with lenses, as demonstrated in Chapter 9, could also be investigated using plastic lens arrays. The wideband feed for plastic lenses with circular waveguide (with or without corrugations) is able to illuminate lenses with a very small diameter with an aperture efficiency above 85%, which is significantly better than the multi-mode feed for small-diameter silicon lenses. A hybrid plastic-silicon transmit array can also be considered. For example, the coupling to the bottom array can be maximized by using a plastic lens array while the scan performance of a silicon lens array is beneficial as the top array. Although the losses in plastic lenses increase significantly at higher frequencies, we expect that the losses in small-to-moderate diameter plastic lenses are manageable up to 300 GHz.

We have seen in Chapter 7 that the matching layer for silicon lenses, consisting of sub-wavelength frusta, achieves significantly higher transmission than a Parylene matching layer. To further improve these matching layers, especially for lenses that are not so shallow (i.e., $f_{\#} \leq 1$), a conformal patterning of the pyramids on the lens surface may be required. Further investment in the laser-ablation manufacturing process is required to create such conformal pyramids.

11.3 Applications of Scanning Lens Phased Arrays

Further research and development is required to integrate scanning lens phased arrays in several envisioned application cases. For CubeSats or SmallSats, a scientific instrument could be built around a silicon lens array at submillimeter-waves which could achieve 50 dBi of gain while remaining compact. The required amplitude and phase control could be achieved using low-frequency electronics followed by (a series of) multipliers (an approach similar to the 100 GHz lens array in Chapter 8).

For static, line-of-sight millimeter-wave communication links, such as fixed-wireless access or back-haul links, the scanning lens phased array could be a useful architecture that allows rapid and high-accuracy real-time beam alignment by scanning the beam in the order of 10° to compensate environmental effects.

Several sensing applications can be formulated for lenses with high aperture efficiency. For example, since the plastic lens with corrugations in the ground plane (Chapter 5) achieves very high lens-to-lens coupling, such a lens setup can be used for material characterization. A similar setup with two lenses facing each other, or a single mechanically scanned lens can be used for industrial non-destructive testing applications at (sub-)millimeter waves. For automotive radars, especially long-range radars, antenna gain can be increased significantly by using a small scanning lens phased array. Although the piezo-electric motors that were used in this thesis may not be quick enough for such a challenging application, fast motors ($>$200mm/s) are commercially

available.

Appendices

Appendix A
Space-wave and Leaky-wave Field Contributions

This Appendix contains derivations, starting from the electric and magnetic field representations $\vec{f}(\vec{r})$ of fields in stratified media:

$$\vec{f}(\vec{r}) = \frac{1}{4\pi^2} \int_{-\infty}^{\infty} \int_{-\infty}^{\infty} \tilde{G}^{fc}(k_x, k_y) \vec{C}(k_x, k_y) \cdot e^{-jk_x x} e^{-jk_y y} e^{-jk_z z} \, \mathrm{d}k_x \, \mathrm{d}k_y \tag{A.1}$$

in which the spectral Green's function for the field quantity $\vec{f}$ (electric or magnetic field) at observation point $\vec{r}$ due to a spectral (electric or magnetic) current $\vec{C}$ is given by $\tilde{G}^{fc}$.

A change of spectral and spatial variables is introduced:

$$\begin{aligned} k_x &= k_\rho \cos\alpha & x &= \rho \cos\phi \\ k_y &= k_\rho \sin\alpha & y &= \rho \sin\phi \end{aligned}$$

with $\rho = R \sin\theta$ and Jacobian determinant:

$$|J| = \begin{vmatrix} \frac{\partial k_x}{\partial k_\rho} & \frac{\partial k_x}{\partial k_\alpha} \\ \frac{\partial k_y}{\partial k_\rho} & \frac{\partial k_y}{\partial k_\alpha} \end{vmatrix} = k_\rho$$

The integral in Eq. (A.1) then becomes:

$$\vec{f}(\vec{r}) = \frac{1}{4\pi^2} \int_{0}^{\infty} \int_{0}^{2\pi} \tilde{G}^{fc}(k_\rho, \alpha) \vec{C}(k_\rho, \alpha) \cdot e^{-jk_\rho \rho \cos(\alpha - \phi)} e^{-jk_z z} k_\rho \, \mathrm{d}\alpha \, \mathrm{d}k_\rho \tag{A.2}$$

A.1 Integral Order Reduction

For an elementary source, the α-integral can be closed analytically into Hankel functions $H_n^{(2)}$ of the second kind of order n. For a distributed source, this procedure can be performed when the spectral current $\vec{C}$ can be assumed to be slowly-varying in α

compared to $\tilde{G}^{fc}$ and can therefore be evaluated in the α-saddle point, i.e., $\vec{C}(k_\rho, \phi)$.

In this case, Eq. (A.2) becomes:

$$\vec{f}(\vec{r}) = \frac{1}{4\pi^2} \int_0^\infty \vec{C}(k_\rho, \phi) \int_0^{2\pi} \tilde{G}^{fc}(k_\rho, \alpha) e^{-jk_\rho \rho \cos(\alpha-\phi)} \, \mathrm{d}\alpha \tag{A.3}$$

$$\cdot \, e^{-jk_z z} k_\rho \, \mathrm{d}k_\rho \tag{A.4}$$

and the integral in α is denoted as:

$$\vec{I}_\alpha^{fc} = \int_0^{2\pi} \tilde{G}^{fc}(k_\rho, \alpha) e^{-jk_\rho \rho \cos(\alpha-\phi)} \, \mathrm{d}\alpha \tag{A.5}$$

The integral $\vec{I}_\alpha^{fc}$ above can be closed analytically by using the Bessel-function identities, a proof of which is given in Appendix A.4:

$$\int_0^{2\pi} \begin{matrix} \cos(n\alpha) \\ \sin(n\alpha) \end{matrix} e^{-jk_\rho \rho \cos(\alpha-\phi)} \, \mathrm{d}\alpha = j^{-n} 2\pi \begin{matrix} \cos(n\phi) \\ \sin(n\phi) \end{matrix} J_n(k_\rho \rho) \tag{A.6}$$

where J_n is the Bessel function of the first kind and order n.

A.2 Hankel-integrals for Magnetic Current Distributions

In this Section, we consider $\vec{C} = \vec{M}$ a spectral magnetic current distribution. The dyadic spectral Green's function giving the electric field is then given by:

$$\tilde{G}^{em} = \begin{bmatrix} \tilde{G}^{em}_{xx} & \tilde{G}^{em}_{xy} \\ \tilde{G}^{em}_{yx} & \tilde{G}^{em}_{yy} \\ \tilde{G}^{em}_{zx} & \tilde{G}^{em}_{zy} \end{bmatrix} = \begin{bmatrix} \frac{(V_{\mathrm{TM}} - V_{\mathrm{TE}}) k_x k_y}{k_\rho^2} & \frac{V_{\mathrm{TM}} k_x^2 - V_{\mathrm{TE}} k_y^2}{k_\rho^2} \\ \frac{V_{\mathrm{TM}} k_x^2 + V_{\mathrm{TE}} k_y^2}{k_\rho^2} & \frac{(V_{\mathrm{TE}} - V_{\mathrm{TM}}) k_x k_y}{k_\rho^2} \\ -\zeta_d \frac{k_y}{k_d} I_{\mathrm{TM}} & \zeta_d \frac{k_x}{k_d} I_{\mathrm{TM}} \end{bmatrix}$$

$$= \begin{bmatrix} \frac{(V_{\mathrm{TM}} - V_{\mathrm{TE}}) \sin(2\alpha)}{2} & -\frac{V_{\mathrm{TE}} + V_{\mathrm{TM}} + (V_{\mathrm{TM}} - V_{\mathrm{TE}}) \cos(2\alpha)}{2} \\ \frac{V_{\mathrm{TE}} + V_{\mathrm{TM}} + (V_{\mathrm{TE}} - V_{\mathrm{TM}}) \cos(2\alpha)}{2} & \frac{(V_{\mathrm{TE}} - V_{\mathrm{TM}}) \sin(2\alpha)}{2} \\ -\zeta_d \frac{k_\rho}{k_d} I_{\mathrm{TM}} \sin(\alpha) & \zeta_d \frac{k_\rho}{k_d} I_{\mathrm{TM}} \cos(\alpha) \end{bmatrix} \tag{A.7}$$

The α-integral in Eq. (A.5) then becomes:

$$\vec{I}_{\alpha}^{em} = \begin{bmatrix} -\pi(V_{\text{TM}} - V_{\text{TE}})\sin(2\phi)J_2(k_\rho\rho) \\ \pi(V_{\text{TM}} + V_{\text{TE}})J_0(k_\rho\rho) + \pi(V_{\text{TM}} - V_{\text{TE}})\cos(2\phi)J_2(k_\rho\rho) \\ j2\pi\zeta_d\frac{k_\rho}{k_d}I_{\text{TM}}\sin(\phi)J_1(k_\rho\rho) \\ -j2\pi\zeta_d\frac{k_\rho}{k_d}I_{\text{TM}}\cos(\phi)J_1(k_\rho\rho) \\ -\pi(V_{\text{TM}} + V_{\text{TE}})J_0(k_\rho\rho) - \pi(V_{\text{TM}} - V_{\text{TE}})\cos(2\phi)J_2(k_\rho\rho) \\ \pi(V_{\text{TM}} - V_{\text{TE}})\sin(2\phi)J_2(k_\rho\rho) \end{bmatrix}$$

The integrals of Bessel functions can be expressed using Hankel functions with the help of the following identity:

$$\int_0^\infty xf(x)J_n(ax)\,\mathrm{d}x = \frac{1}{2}\int_{-\infty}^\infty xf(x)H_n^{(2)}(ax)\,\mathrm{d}x \tag{A.8}$$

The electric and magnetic fields are dependent on the polarization of $\vec{M}$. The full integral representation of the fields is given in Appendix A.2.1 for $\vec{M} = M_x\hat{x}$ and in Appendix A.2.2 for $\vec{M} = M_y\hat{y}$.

A.2.1 Magnetic current distribution along $\hat{x}$

The electric fields are given by:

$$e_\rho(\vec{r}) = \frac{\sin\phi}{8\pi}\int_{-\infty}^{\infty}\Big[V_{\text{TM}}\left(H_0^{(2)}(k_\rho\rho) - H_2^{(2)}(k_\rho\rho)\right) + V_{\text{TE}}\left(H_0^{(2)}(k_\rho\rho) + H_2^{(2)}(k_\rho\rho)\right)\Big] M_x(k_\rho,\phi)e^{-jk_z z}k_\rho\,\mathrm{d}k_\rho \tag{A.9}$$

$$e_\phi(\vec{r}) = \frac{\cos\phi}{8\pi}\int_{-\infty}^{\infty}\Big[V_{\text{TM}}\left(H_0^{(2)}(k_\rho\rho) + H_2^{(2)}(k_\rho\rho)\right) + V_{\text{TE}}\left(H_0^{(2)}(k_\rho\rho) - H_2^{(2)}(k_\rho\rho)\right)\Big] M_x(k_\rho,\phi)e^{-jk_z z}k_\rho\,\mathrm{d}k_\rho \tag{A.10}$$

$$e_z(\vec{r}) = \frac{j\zeta_d\sin\phi}{4\pi k_d}\int_{-\infty}^{\infty} I_{\text{TM}}H_1^{(2)}(k_\rho\rho)M_x(k_\rho,\phi)e^{-jk_z z}k_\rho^2\,\mathrm{d}k_\rho \tag{A.11}$$

The magnetic fields are given by:

$$h_\rho(\vec{r}) = -\frac{\cos\phi}{8\pi}\int_{-\infty}^{\infty}\Big[I_{\text{TE}}\left(H_0^{(2)}(k_\rho\rho) - H_2^{(2)}(k_\rho\rho)\right) + I_{\text{TM}}\left(H_0^{(2)}(k_\rho\rho) + H_2^{(2)}(k_\rho\rho)\right)\Big] M_x(k_\rho,\phi)e^{-jk_z z}k_\rho\,\mathrm{d}k_\rho \tag{A.12}$$

$$h_\phi(\vec{r}) = \frac{\sin\phi}{8\pi}\int_{-\infty}^{\infty}\Big[I_{\text{TE}}\left(H_0^{(2)}(k_\rho\rho) + H_2^{(2)}(k_\rho\rho)\right) + I_{\text{TM}}\left(H_0^{(2)}(k_\rho\rho) - H_2^{(2)}(k_\rho\rho)\right)\Big] M_x(k_\rho,\phi)e^{-jk_z z}k_\rho\,\mathrm{d}k_\rho \tag{A.13}$$

$$h_z(\vec{r}) = -\frac{j\cos\phi}{4\pi\zeta_d k_d}\int_{-\infty}^{\infty} V_{\text{TE}}H_1^{(2)}(k_\rho\rho)M_x(k_\rho,\phi)e^{-jk_z z}k_\rho^2\,\mathrm{d}k_\rho \tag{A.14}$$

A.2.2 Magnetic current distribution along $\hat{y}$

The electric fields are given by:

$$e_\rho(\vec{r}) = -\frac{\cos\phi}{8\pi}\int_{-\infty}^{\infty}\Big[V_{\text{TM}}\left(H_0^{(2)}(k_\rho\rho) - H_2^{(2)}(k_\rho\rho)\right) + V_{\text{TE}}\left(H_0^{(2)}(k_\rho\rho) + H_2^{(2)}(k_\rho\rho)\right)\Big] M_y(k_\rho,\phi)e^{-jk_z z}k_\rho\,\mathrm{d}k_\rho \tag{A.15}$$

$$e_\phi(\vec{r}) = \frac{\sin\phi}{8\pi}\int_{-\infty}^{\infty}\Big[V_{\text{TM}}\left(H_0^{(2)}(k_\rho\rho) + H_2^{(2)}(k_\rho\rho)\right) + V_{\text{TE}}\left(H_0^{(2)}(k_\rho\rho) - H_2^{(2)}(k_\rho\rho)\right)\Big] M_y(k_\rho,\phi)e^{-jk_z z}k_\rho\,\mathrm{d}k_\rho \tag{A.16}$$

$$e_z(\vec{r}) = -\frac{j\zeta_d\cos\phi}{4\pi k_d}\int_{-\infty}^{\infty} I_{\text{TM}}H_1^{(2)}(k_\rho\rho)M_y(k_\rho,\phi)e^{-jk_z z}k_\rho^2\,\mathrm{d}k_\rho \tag{A.17}$$

The magnetic fields are given by:

$$h_\rho(\vec{r}) = -\frac{\sin\phi}{8\pi}\int_{-\infty}^{\infty}\Big[I_{\text{TE}}\left(H_0^{(2)}(k_\rho\rho) - H_2^{(2)}(k_\rho\rho)\right) + I_{\text{TM}}\left(H_0^{(2)}(k_\rho\rho) + H_2^{(2)}(k_\rho\rho)\right)\Big] M_y(k_\rho,\phi)e^{-jk_z z}k_\rho\,\mathrm{d}k_\rho \tag{A.18}$$

$$h_\phi(\vec{r}) = -\frac{\cos\phi}{8\pi}\int_{-\infty}^{\infty}\Big[I_{\text{TE}}\left(H_0^{(2)}(k_\rho\rho) + H_2^{(2)}(k_\rho\rho)\right) + I_{\text{TM}}\left(H_0^{(2)}(k_\rho\rho) - H_2^{(2)}(k_\rho\rho)\right)\Big] M_y(k_\rho,\phi)e^{-jk_z z}k_\rho\,\mathrm{d}k_\rho \tag{A.19}$$

$$h_z(\vec{r}) = -\frac{j\sin\phi}{4\pi\zeta_d k_d}\int_{-\infty}^{\infty} V_{\text{TE}}H_1^{(2)}(k_\rho\rho)M_y(k_\rho,\phi)e^{-jk_z z}k_\rho^2\,\mathrm{d}k_\rho \tag{A.20}$$

A.3 Leaky-Wave Modal Field

When the Hankel-integrals in Appendix A.2 are evaluated over the path of steepest descent, as described in Chapter 4, the SDP crosses a leaky-wave pole at $\theta = \theta_{SB}$. To obtain the total field at $\theta > \theta_{SB}$, the residue contribution of this pole must be added to the integrals of Appendices A.2.1 and A.2.2. Explicit formulas for these residues are given below.

A.3.1 Modal field for magnetic current distribution along $\hat{x}$

The electric modal fields are given by:

$$e_\rho(\vec{r}) = \frac{j\sin\phi}{4}k_{\rho i}\Big[\mathrm{Res}\left(V_{\text{TM}}(k_{\rho i},z)\right)\left(H_0^{(2)}(k_{\rho i}\rho)-H_2^{(2)}(k_{\rho i}\rho)\right)+ \mathrm{Res}\left(V_{\text{TE}}(k_{\rho i},z)\right)\left(H_0^{(2)}(k_{\rho i}\rho)+H_2^{(2)}(k_{\rho i}\rho)\right)\Big]M_x(k_{\rho i},\phi) \tag{A.21}$$

$$e_\phi(\vec{r}) = \frac{j\cos\phi}{4}k_{\rho i}\Big[\mathrm{Res}\left(V_{\text{TM}}(k_{\rho i},z)\right)\left(H_0^{(2)}(k_{\rho i}\rho)+H_2^{(2)}(k_{\rho i}\rho)\right)+ \mathrm{Res}\left(V_{\text{TE}}(k_{\rho i},z)\right)\left(H_0^{(2)}(k_{\rho i}\rho)-H_2^{(2)}(k_{\rho i}\rho)\right)\Big]M_x(k_{\rho i},\phi) \tag{A.22}$$

$$e_z(\vec{r}) = \frac{-\zeta_d\sin\phi}{2k_d}k_{\rho i}^2\mathrm{Res}\left(I_{\text{TM}}(k_{\rho i},z)\right)H_1^{(2)}(k_{\rho i}\rho)M_x(k_{\rho i},\phi) \tag{A.23}$$

The magnetic modal fields are given by:

$$h_\rho(\vec{r}) = \frac{-j\cos\phi}{4}k_{\rho i}\Big[\mathrm{Res}\left(I_{\text{TM}}(k_{\rho i},z)\right)\left(H_0^{(2)}(k_{\rho i}\rho)+H_2^{(2)}(k_{\rho i}\rho)\right)+ \mathrm{Res}\left(I_{\text{TE}}(k_{\rho i},z)\right)\left(H_0^{(2)}(k_{\rho i}\rho)-H_2^{(2)}(k_{\rho i}\rho)\right)\Big]M_x(k_{\rho i},\phi) \tag{A.24}$$

$$h_\phi(\vec{r}) = \frac{j\sin\phi}{4}k_{\rho i}\Big[\mathrm{Res}\left(I_{\text{TM}}(k_{\rho i},z)\right)\left(H_0^{(2)}(k_{\rho i}\rho)-H_2^{(2)}(k_{\rho i}\rho)\right)+ \mathrm{Res}\left(I_{\text{TE}}(k_{\rho i},z)\right)\left(H_0^{(2)}(k_{\rho i}\rho)+H_2^{(2)}(k_{\rho i}\rho)\right)\Big]M_x(k_{\rho i},\phi) \tag{A.25}$$

$$h_z(\vec{r}) = \frac{\cos\phi}{2\zeta_d k_d}k_{\rho i}^2\mathrm{Res}\left(V_{\text{TE}}(k_{\rho i},z)\right)H_1^{(2)}(k_{\rho i}\rho)M_x(k_{\rho i},\phi) \tag{A.26}$$

A.3.2 Modal field for magnetic current distribution along $\hat{y}$

The electric modal fields are given by:

$$e_\rho(\vec{r}) = \frac{-j\cos\phi}{4}k_{\rho i}\Big[\mathrm{Res}\left(V_{\text{TM}}(k_{\rho i},z)\right)\left(H_0^{(2)}(k_{\rho i}\rho)-H_2^{(2)}(k_{\rho i}\rho)\right)+ \mathrm{Res}\left(V_{\text{TE}}(k_{\rho i},z)\right)\left(H_0^{(2)}(k_{\rho i}\rho)+H_2^{(2)}(k_{\rho i}\rho)\right)\Big]M_y(k_{\rho i},\phi) \tag{A.27}$$

$$e_\phi(\vec{r}) = \frac{j\sin\phi}{4}k_{\rho i}\Big[\mathrm{Res}\left(V_{\text{TM}}(k_{\rho i},z)\right)\left(H_0^{(2)}(k_{\rho i}\rho)+H_2^{(2)}(k_{\rho i}\rho)\right)+ \mathrm{Res}\left(V_{\text{TE}}(k_{\rho i},z)\right)\left(H_0^{(2)}(k_{\rho i}\rho)-H_2^{(2)}(k_{\rho i}\rho)\right)\Big]M_y(k_{\rho i},\phi) \tag{A.28}$$

$$e_z(\vec{r}) = \frac{\zeta_d\cos\phi}{2k_d}k_{\rho i}^2\mathrm{Res}\left(I_{\text{TM}}(k_{\rho i},z)\right)H_1^{(2)}(k_{\rho i}\rho)M_y(k_{\rho i},\phi) \tag{A.29}$$

The magnetic modal fields are given by:

$$h_\rho(\vec{r}) = \frac{-j\sin\phi}{4}k_{\rho i}\Big[\mathrm{Res}\left(I_{\text{TM}}(k_{\rho i},z)\right)\left(H_0^{(2)}(k_{\rho i}\rho)+H_2^{(2)}(k_{\rho i}\rho)\right)+ \mathrm{Res}\left(I_{\text{TE}}(k_{\rho i},z)\right)\left(H_0^{(2)}(k_{\rho i}\rho)-H_2^{(2)}(k_{\rho i}\rho)\right)\Big]M_y(k_{\rho i},\phi) \tag{A.30}$$

$$h_\phi(\vec{r}) = \frac{-j\cos\phi}{4}k_{\rho i}\Big[\mathrm{Res}\left(I_{\text{TM}}(k_{\rho i},z)\right)\left(H_0^{(2)}(k_{\rho i}\rho)-H_2^{(2)}(k_{\rho i}\rho)\right)+ \mathrm{Res}\left(I_{\text{TE}}(k_{\rho i},z)\right)\left(H_0^{(2)}(k_{\rho i}\rho)+H_2^{(2)}(k_{\rho i}\rho)\right)\Big]M_y(k_{\rho i},\phi) \tag{A.31}$$

$$h_z(\vec{r}) = \frac{\sin\phi}{2\zeta_d k_d}k_{\rho i}^2\mathrm{Res}\left(V_{\text{TE}}(k_{\rho i},z)\right)H_1^{(2)}(k_{\rho i}\rho)M_y(k_{\rho i},\phi) \tag{A.32}$$

A.4 Proof of Bessel-function-generating integrals

The following proof was derived with the help of Roderick Tapia Barroso and is similar to the steps in [172, p. 193]. This result is not new, for example it was used in [173, p. 132], but the author could not find a proof of this form in the literature.

We are looking to prove that:

$$\int_0^{2\pi} \begin{matrix}\cos(n\alpha)\\ \sin(n\alpha)\end{matrix} e^{\pm jk_\rho \rho \cos(\alpha-\phi)}\,\mathrm{d}\alpha = j^{\pm n} 2\pi \begin{matrix}\cos(n\phi)\\ \sin(n\phi)\end{matrix} J_n(k_\rho\rho) \tag{A.33}$$

where J_n is the Bessel function of the first kind and order n.

First, we establish that:

$$e^{\pm jk_\rho \rho \cos(\alpha-\phi)} = J_0(k_\rho\rho) + 2\sum_{m=1}^{\infty} (\pm j)^m J_m(k_\rho\rho)\cos(m(\alpha-\phi)) \tag{A.34}$$

which can be derived by using Euler's formula and the following identities from [174, p. 22]:

$$\cos(k_\rho\rho\cos(\alpha-\phi)) = J_0(k_\rho\rho) + 2\sum_{m=1}^{\infty}(-1)^m J_{2m}(k_\rho\rho)\cos(2m(\alpha-\phi))$$
$$\sin(k_\rho\rho\cos(\alpha-\phi)) = -2j\sum_{m=1}^{\infty}(-1)^m J_{2m+1}(k_\rho\rho)\cos((2m+1)(\alpha-\phi))$$

Next, we substitute Eq. (A.34) into the left hand side of Eq. (A.33):

$$\begin{aligned}\int_0^{2\pi} \begin{matrix}\cos(n\alpha)\\ \sin(n\alpha)\end{matrix} e^{\pm jk_\rho \rho \cos(\alpha-\phi)}\,\mathrm{d}\alpha &= J_0(k_\rho\rho)\int_0^{2\pi}\begin{matrix}\cos(n\alpha)\\ \sin(n\alpha)\end{matrix}\mathrm{d}\alpha \\ &\quad + 2\sum_{m=1}^{\infty}(\pm j)^m J_m(k_\rho\rho)\int_0^{2\pi}\begin{matrix}\cos(n\alpha)\\ \sin(n\alpha)\end{matrix}\cos(m(\alpha-\phi))\,\mathrm{d}\alpha\end{aligned} \tag{A.35}$$

Since the first integral on the right hand side of Eq. (A.35) is equal to zero for integer n, this term disappears. The second integral on the right hand side of Eq. (A.35) is only non-zero when $m = n$ (easily demonstrated by writing the (co)sine product as a (co)sine sum). The remaining terms of this integral are:

$$\frac{1}{2}\int_0^{2\pi}\begin{matrix}\cos(n\phi)\\ \sin(n\phi)\end{matrix}\mathrm{d}\alpha = \pi\begin{matrix}\cos(n\phi)\\ \sin(n\phi)\end{matrix} \tag{A.36}$$

By substituting this result back into Eq. (A.35) with $m = n$, we arrive at Eq. (A.33) that we set out to prove.

Appendix B
Closed-Form Spectral Magnetic Current Distributions

The time it takes to evaluate the integrals in Appendices A.2.1 and A.2.2 can be dramatically reduced if a closed-form expression of the spectral (magnetic) current distribution $\vec{M}$ is known. For several canonical current distribution, such as rectangular waveguides, closed-form expressions are available in text books [175]–[177]. For the double-slot iris, the spatial current distribution was given in [20, Appendix D] but the spectral current has been calculated numerically.

In this Appendix, a semi-closed-form expression[1] for the spectral currents of a double-slot iris in a semi-infinite ground plane are derived in Appendix B.1. For completeness, the closed-form expressions of the spectral magnetic current associated with rectangular and circular waveguides in semi-infinite ground planes are given in Appendices B.2 and B.3.

B.1 Double-slot Iris

A waveguide along $\hat{z}$ with its electric field oriented along $\hat{x}$ illuminates a double-slot iris. The iris slots are spaced ρ_i apart along $\hat{x}$ and have width w_i. Each iris subtends an angle α_i seen from the origin, see Fig. B.1. An approximate expression for the electric and magnetic fields in the slots is given as [20]:

$$\begin{aligned}\vec{e} &= \frac{1}{\rho}\cos\left(\frac{\pi}{2\alpha_i}\phi\right)\mathrm{rect}(\phi, 2\alpha_i)\mathrm{rect}(\rho-\rho_i/2, w_i)\hat{x} \\ &\quad + \frac{1}{\rho}\cos\left(\frac{\pi}{2\alpha_i}\phi\right)\mathrm{rect}(\phi+\pi, 2\alpha_i)\mathrm{rect}(\rho-\rho_i/2, w_i)\hat{x} \qquad \text{(B.1)} \\ \vec{h} &= \frac{1}{\zeta_0}\hat{z}\times\vec{e} \\ &= \frac{1}{\rho\zeta_0}\cos\left(\frac{\pi}{2\alpha_i}\phi\right)\mathrm{rect}(\phi, 2\alpha_i)\mathrm{rect}(\rho-\rho_i/2, w_i)\hat{y} \\ &\quad + \frac{1}{\rho\zeta_0}\cos\left(\frac{\pi}{2\alpha_i}\phi\right)\mathrm{rect}(\phi+\pi, 2\alpha_i)\mathrm{rect}(\rho-\rho_i/2, w_i)\hat{y} \qquad \text{(B.2)}\end{aligned}$$

After applying the equivalence theorem, the impressed currents that describe the

[1] The ρ-integral is closed analytically, while the ϕ-integral remains to be solved numerically.

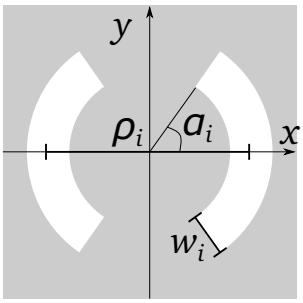

Fig. B.1: Geometry of the double-slot iris.

radiation in the half-space $z > 0$ are, in slot 1 ($s1$) and slot 2 ($s2$):

$$m_{s1}(\rho,\phi) = \frac{1}{\rho}\cos(\frac{\pi}{2\alpha_i}\phi)\mathrm{rect}(\phi, 2\alpha_i)\mathrm{rect}(\rho-\rho_i/2, w) \tag{B.3}$$

$$m_{s2}(\rho,\phi) = \frac{1}{\rho}\cos(\frac{\pi}{2\alpha_i}\phi)\mathrm{rect}(\phi+\pi, 2\alpha_i)\mathrm{rect}(\rho-\rho_i/2, w) \tag{B.4}$$

such that the total current is $\vec{m} = m_{s1}\hat{y} + m_{s2}\hat{y}$.

B.1.1 Spectrum of the Iris Currents

We now consider the spatial Fourier transform of the currents in Eq. (B.3). The spectral currents can thus be written as:

$$\vec{M}(k_x,k_y) = \int_{-\infty}^{\infty}\int_{-\infty}^{\infty} \vec{m}(x,y)e^{jk_x x}e^{jk_y y}\,\mathrm{d}x\,\mathrm{d}y \tag{B.5}$$

Which we can transform to spatial coordinates (ρ,ϕ) and spectral coordinates (k_ρ,α) in the usual way:

$$\vec{M}(k_\rho,\alpha) = \int_0^{2\pi}\int_0^{\infty} \vec{m}(\rho,\phi)e^{jk_\rho\rho\cos(\alpha-\phi)}\rho\,\mathrm{d}\rho\,\mathrm{d}\phi \tag{B.6}$$

By substituting the currents from Eq. (B.3) into this double integral, we obtain:

$$\begin{aligned} M_y(k_\rho,\alpha) &= \int_{-\alpha_i}^{\alpha_i} \cos\left(\frac{\pi}{2\alpha_i}\phi\right) \int_{(\rho_i-w_i)/2}^{(\rho_i+w_i)/2} e^{jk_\rho\rho\cos(\alpha-\phi)}\,\mathrm{d}\rho\,\mathrm{d}\phi \\ &+ \int_{-\alpha_i}^{\alpha_i} \cos\left(\frac{\pi}{2\alpha_i}\phi\right) \int_{(\rho_i-w_i)/2}^{(\rho_i+w_i)/2} e^{-jk_\rho\rho\cos(\alpha-\phi)}\,\mathrm{d}\rho\,\mathrm{d}\phi \\ &= \int_{-\alpha_i}^{\alpha_i} 2\cos\left(\frac{\pi}{2\alpha_i}\phi\right) \int_{(\rho_i-w_i)/2}^{(\rho_i+w_i)/2} \cos\left(k_\rho\rho\cos(\alpha-\phi)\right)\mathrm{d}\rho\,\mathrm{d}\phi \end{aligned} \tag{B.7}$$

The ρ-integrals can closed analytically:

$$\begin{aligned} &\int_{\rho_i/2-w_i/2}^{\rho_i/2+w_i/2} \cos(k_\rho\rho\cos(\alpha-\phi))\,\mathrm{d}\rho \\ &= \frac{\sin\left(k_\rho\frac{\rho_i+w_i}{2}\cos(\alpha-\phi)\right) - \sin\left(k_\rho\frac{\rho_i-w_i}{2}\cos(\alpha-\phi)\right)}{k_\rho\cos(\alpha-\phi)} \\ &= \frac{2}{k_\rho}\sec(\alpha-\phi)\cos\left(\frac{k_\rho\rho_i}{2}\cos(\alpha-\phi)\right)\sin\left(\frac{k_\rho w_i}{2}\cos(\alpha-\phi)\right) \end{aligned}$$

The double integral in Eq. (B.6) is thus reduced to a single integral:

$$\begin{aligned} M_y(k_\rho,\alpha) = \frac{2}{k_\rho}\int_{-\alpha_i}^{\alpha_i} &\cos\left(\frac{\pi}{2\alpha_i}\phi\right)\sec(\alpha-\phi) \\ &\cdot\cos\left(\frac{k_\rho\rho_i}{2}\cos(\alpha-\phi)\right)\sin\left(\frac{k_\rho w_i}{2}\cos(\alpha-\phi)\right)\mathrm{d}\phi \end{aligned} \tag{B.8}$$

B.2 Rectangular waveguide

For a rectangular waveguide with TE_{10}-mode distribution along $\vec{y}$ with dimensions $a \times b$ (a along $\hat{x}$, b along $\hat{y}$), the electric field can be written as [176, Table 12.1]:

$$e_y = E_0 \cos\left(\frac{\pi}{a}x\right) \operatorname{rect}(x, a) \operatorname{rect}(y, b) \tag{B.9}$$

The equivalent spatial magnetic current distribution is given by:

$$m_x = 2E_0 \cos\left(\frac{\pi}{a}x\right) \operatorname{rect}(x, a) \operatorname{rect}(y, b) \tag{B.10}$$

The spectrum of this magnetic current is:

$$\begin{aligned}
\vec{M}(k_x, k_y) &= \int_{-\infty}^{\infty}\int_{-\infty}^{\infty} \vec{m}(x, y) e^{jk_x x} e^{jk_y y}\,\mathrm{d}x\,\mathrm{d}y \\
&= \hat{x} \int_{-b/2}^{b/2} e^{jk_y y}\,\mathrm{d}y \int_{-a/2}^{a/2} \cos\left(\frac{\pi}{a}x\right) e^{jk_x x}\,\mathrm{d}x \\
&= \frac{ab\pi}{2\left(\pi^2 - \frac{k_x^2}{a^2}\right)} \cos\left(\frac{k_x a}{2}\right) \operatorname{sinc}\left(\frac{k_y b}{2}\right) \hat{x}
\end{aligned} \tag{B.11}$$

B.3 Circular waveguide

To calculate the spectral magnetic currents from a circular waveguide with a radius of ρ_0, supporting only the TE_{11} modal distribution, the method in [178, p. 337] provides a starting point[2]. Along with the Bessel-generating identities of Eq. (A.6), the following identities are also required:

$$J_0(k_c\rho) = \frac{1}{k_c\rho}J_1(k_c\rho) + J_1'(k_c\rho) \tag{B.12}$$

$$J_2(k_c\rho) = \frac{1}{k_c\rho}J_1(k_c\rho) - J_1'(k_c\rho) \tag{B.13}$$

$$\int xJ_n(ax)J_n(bx)\,\mathrm{d}x = \frac{x\left[bJ_{n-1}(bx)J_n(ax) - aJ_{n-1}(ax)J_nbx\right]}{a^2-b^2} \tag{B.14}$$

in which the notation J_1' indicates the derivative of the argument should be taken and Eq. (B.14) is known as Lommel's (first) integral [179, p. 10].

The electric field at the aperture $z = 0$ of the ground plane, given by the TE_{11} mode[3] is given as [136, p. 128]:

$$\vec{e}(\rho,\phi,0) = -\frac{j\omega\mu}{k_c}\left(\frac{1}{k_c\rho}\cos(\phi)J_1(k_c\rho)\hat{\rho} - J_1'(k_c\rho)\hat{\phi}\right)$$

However, it is more useful to describe the field distribution using Cartesian polarization. Using double-angle formulas for trigonometric functions and Eqs. (B.12) and (B.13), the field distribution is equivalently given by:

$$\vec{e}(\rho,\phi,0) = -\frac{j\omega\mu}{2k_c}\left(\left[J_0(k_c\rho) + \cos(2\phi)J_2(k_c\rho)\right]\hat{x} + J_2(k_c\rho)\sin(2\phi)\hat{y}\right)$$

Thus, the spatial equivalent magnetic current distribution is:

$$m_x(\rho,\phi,0) = -\frac{j\omega\mu}{k_c}J_2(k_c\rho)\sin(2\phi)$$

$$m_y(\rho,\phi,0) = \frac{j\omega\mu}{k_c}\left(J_0(k_c\rho) + J_2(k_c\rho)\cos(2\phi)\right)$$

[2]For a vacuum-filled waveguide, $\mu = \mu_r = 1$ in these equations.

[3]The waveguide also supports the same modal field when it is rotated around the z-axis, but here, without lack of generality, we assume that the field at the origin is polarized along $\hat{x}$, which is equivalent to choosing $A = 1$; $B = 0$ in [136].

The spectral magnetic current distributions are calculated as follows:

$$M_x(k_\rho,\alpha) = \frac{j\omega\mu}{k_c}\int_0^{\rho_0} J_2(k_c\rho)\rho \int_0^{2\pi} \sin(2\phi) e^{jk_\rho\rho\cos(\alpha-\phi)}\,\mathrm{d}\phi\,\mathrm{d}\rho$$
$$= \frac{j\omega\mu}{k_c}\sin(2\alpha)\int_0^{\rho_0} J_2(k_c\rho)J_2(k_\rho\rho)\rho\,\mathrm{d}\rho$$

using Eq. (A.33). The remaining integral is Lommel's formula (Eq. (B.14) with $n = 2$). Thus:

$$M_x(k_\rho,\alpha) = \frac{2\pi j\omega\mu\rho_0}{k_c(k_\rho^2\rho_0^2 - k_c^2\rho_0^2)}\sin(2\alpha)\left[k_c J_2(k_\rho\rho_0)J_1(k_c\rho_0)\right.$$
$$\left. - k_\rho J_1(k_\rho\rho_0)J_2(k_c\rho)\right] \qquad \text{(B.15)}$$

The same procedure is employed to calculate the spectral currents along $\hat{y}$:

$$M_y(k_\rho,\alpha) = \frac{j\omega\mu}{k_c}\int_0^{\rho_0} J_0(k_c\rho)\rho \int_0^{2\pi} e^{jk_\rho\rho\cos(\alpha-\phi)}\,\mathrm{d}\phi\,\mathrm{d}\rho$$
$$+ \frac{j\omega\mu}{k_c}\int_0^{\rho_0} J_2(k_c\rho)\rho \int_0^{2\pi} \cos(2\phi) e^{jk_\rho\rho\cos(\alpha-\phi)}\,\mathrm{d}\phi\,\mathrm{d}\rho$$

These ϕ-integrals are closed using Eq. (A.33):

$$M_y(k_\rho,\alpha) = \frac{j2\pi\omega\mu}{k_c}\left[\int_0^{\rho_0} J_0(k_\rho\rho)J_0(k_c\rho)\rho\,\mathrm{d}\rho - \cos(2\alpha)\int_0^{\rho_0} J_2(k_c\rho)J_2(k_\rho\rho)\rho\,\mathrm{d}\rho\right]$$

Which are again Lommer's integrals (B.14) for $n = 0$ and $n = 2$:

$$M_y(k_\rho,\alpha) = \frac{2\pi j\omega\mu\rho_0}{k_c(k_\rho^2\rho_0^2 - k_c^2\rho_0^2)}\left[k_\rho J_1(k_\rho\rho_0)J_0(k_c\rho_0) - k_c J_0(k_\rho\rho_0)J_1(k_c\rho_0)\right.$$
$$\left. + \cos(2\alpha)\left(k_\rho J_1(k_\rho\rho_0)J_2(k_c\rho_0) - k_c J_2(k_\rho\rho_0)J_1(k_c\rho_0)\right)\right] \qquad \text{(B.16)}$$

Appendix C
Submillimeter-Wave Dual-Band Lens Feed

In this Appendix, we describe the synthesis and analysis of a 4x4 focal-plane array (FPA) of dual-band (210-240 GHz and 500-580 GHz) lens antennas under a parabolic reflector. The work presented in this Appendix was performed in the framework of the COMETS project at the Jet Propulsion Laboratory [66], to enable spectroscopic mapping of comets. A dual-band submillimeter-wave lens antenna prototype is currently being fabricated and measured at the Jet Propulsion Laboratory.

Contrary to the other lens antenna designs in this thesis, the goal is not to create a phased array of lenses for which a maximization of the aperture efficiency of the lens is required. Instead, the lenses should form a focal-plane array under a reflector with the goal of achieving equal and overlapping on-sky beams in both frequency bands. However, the analysis and design methodologies presented in this Appendix, especially those regarding the leaky-wave feed, is analogous to the methods described in the main Chapters of this thesis.

C.1 Introduction

Comets provide a unique window through time, to the early days of our Solar System, as they are mostly unprocessed remnants of the cold accretion in the outer protoplanetary disk [15], [58]. Submillimeter instruments are well suited to observe them remotely, due to the presence of rotational lines of major cometary volatiles (e.g. water, CO, NH3, CH3OH) in the 210-240 GHz and 500-580 GHz bands [57], [180]. An example of such instrument is the Microwave Instrument on the Rosetta Orbiter (MIRO), which surveyed comet 67P/Churyumov-Gerasimenko in 2014-2016 [58]. It was a single pixel instrument that used a diplexer to split the radiation onto two independent receivers [180]. Although a lot of scientific discoveries were made with this instrument, it suffered from its single pixel receiver architecture, with a very narrow beam (7.5 arcmin at 560 GHz). The combination of small beam footprint in the close vicinity of 67P's nucleus (10 to a few hundred km) and relatively fast rotation period (12.1 hours) made it impossible to entirely map the nucleus and the inner coma before 67P significantly rotated. The highly irregular shape of the nucleus results in fast changes in the illumination from the Sun, even at small scales, which in turn results in an extremely asymmetric outgassing geometry and variable gas environment (both spatially and temporally).

Parts of this Chapter have been published in **[C22]** and **[C6]**.

The very restricted spatial and temporal coverage of the coma environment introduces significant uncertainties in the derivation of global and local gas production rates from the coma data. In addition, because the coma is very asymmetric and changes rapidly, the analysis of the data requires complex numerical modeling, which is computationally intensive. The integration and processing time per pixel takes several hours or days. The coma model themselves have significant uncertainties in their input parameters, necessitating multiple runs to compare with the data. The only way to improve on spatial and temporal sampling of the coma for future submillimeter instruments, thereby providing a larger sample base to better constrain the models from which gas production rates and abundances are derived, is to develop a multi-pixel architecture. Furthermore, given that the data analysis is computationally intensive and 2 frequency ranges are of interest, an architecture in which both beams aligned in the field of view with the same beamwidth to spatially cover the same area on the comae (see Fig. 1) would significantly facilitate the data analysis tasks. Moreover, a more compact and integrated instrument with lower power consumption would facilitate infusion in future space missions.

The next generation of a MIRO-type instrument will need a focal plane array to decrease the image acquisition time, and, both receivers will need to be integrated within the same FPA in order to save power, mass and volume. Several such dual-band instruments are currently being developed by NASA/JPL, such as [59], [66]. Specifically, COMETS – Comet Observation & Mapping Enhanced Terahertz Spectrometer, addresses the limitations outlined above by featuring the first broadband, all-solid-state submillimeter-wave heterodyne array spectrometer and radiometer. COMETS is currently under development at NASA Jet Propulsion Laboratory [66], and relies on advanced Schottky diode receiver technology and antenna technology to combine two bands (210-240 GHz and 500-580 GHz) into a 16-pixel single receiver channel. This allows to perform fast velocity-resolved maps of most of the key cometary volatiles.

From the antenna's point of view, this means that we need an antenna coupled to two independent waveguides into the two individual mixers covering the lower and higher frequency ranges. This avoids the losses associated with using a frequency diplexer. For example, waveguide-based diplexers, used for instance at Ka-band for satellite communications [181], are long structures that become lossy and unrealizable with metal CNC machining at submillimeter wavelengths. Other more integrated duplexing solutions, for example MMIC LNAs receivers found at millimeter-wave bands [182], [183], have unfeasibly high losses for Schottky-based receivers in the WR-1.5 frequency band.

To this end, we are developing a dual-band integrated 4×4 focal plane array (FPA) that achieves overlapped beams in the field of view with identical beamwidths at $f_L = 210 - 240$ GHz (LF) and $f_H = 500 - 580$ GHz (HF). The lens antennas build further

on the concepts introduced in [103] and [184]. A first concept was proposed in [185], where we use an FPA of fused silica lens antennas under a parabolic reflector, see Fig. 1(a). We proposed using a fused silica elliptical lens that is fed by two individual waveguide feeds offset from the center of the lens as the FPA element. A leaky-wave stratification based on a single-layer FSS is used to shape the radiation patterns into the lens, see Fig. 1(b), such that the lens illumination is equal at f_L and f_H and achieves high Gaussicity [186]. As a result, when the FPA is placed at the focus of a parabolic reflector, the beams radiated by the reflector will overlap and have equal beamwidth on-sky.

In this Appendix, we present the synthesis procedure of the leaky-wave stratification that is used to shape the radiation patterns inside the lens. The stratification consists of an air cavity, a dielectric transformer layer (comparable to the transformer layer in Chapter 6), a frequency-selective surface (FSS) and the lens material which is modeled as a semi-infinite dielectric. We show how to optimize the parameters of this stratification, i.e., the thickness and permittivity of the dielectric layers and the required FSS. We then synthesize the shape of the FSS based on these requirements. The optimization procedure finds the propagation constants of the leaky-wave modes at f_L and f_H simultaneously. Based on the stratification, we present the achieved radiation patterns inside the lens (the primary patterns), the radiation patterns outside the lens (the secondary patterns) and the on-sky beams (after the parabolic reflector, i.e., the tertiary patterns). We are developing a submillimeter-wave dual-band lens antenna prototype, and progress towards its demonstration is also reported.

C.2 Dual-Band Quasi-Optical System

The goal of this work is to design a quasi-optical system operating in the 210-240 GHz and 500-580 GHz frequency bands and provides beams in the sky with the same beamwidths and with high Gaussicity. In order to achieve these requirements, we propose to use a dual-band leaky-wave lens antenna in the focal plane of a parabolic reflector, see Fig. C.1. Equal on-sky beamwidth is achieved by efficiently illuminating the reflector at the low frequency band and under-illumination at the high frequency band. High on-sky Gaussicity is achieved by synthesizing beams to have high Gaussicity in the entire quasi-optical system, i.e., from primary patterns to tertiary patterns.

The scheme of the proposed lens antenna is shown in Fig. C.2a. A lens is fed by two waveguides that couple from the low frequency f_L and high frequency f_H receivers to the same leaky-wave stratification. Both waveguides are excited by the fundamental TE_{10} mode with the same polarization. Although the mutual coupling could be reduced when orthogonal polarization is used, the fabrication complexity of the metal split-block is significantly reduced for this prototype by using the same polarization. Therefore, the impact of the mutual coupling is also considered here. In order to match

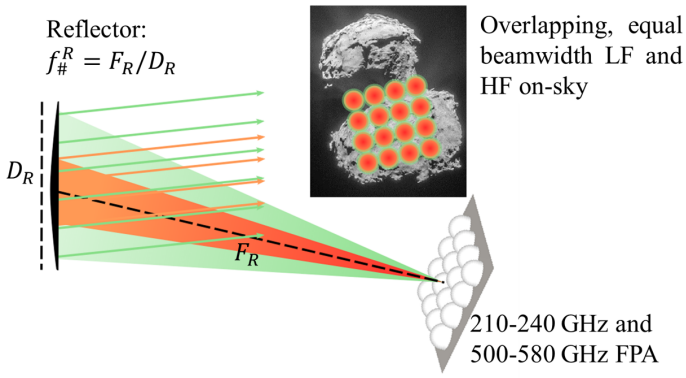

Fig. C.1

the waveguide impedance to the leaky-wave stratification, each waveguide is terminated by a double-slot iris as in [20], [103]. The feeds are offset from the center of the lens focus and will, consequently, produce a beam tilt in the secondary patterns. An elliptical lens with a low permittivity is used to minimize this beam tilt. Here, fused silica ($\varepsilon_r = 3.8$) is used because it is a low-loss material at submillimeter wavelengths.

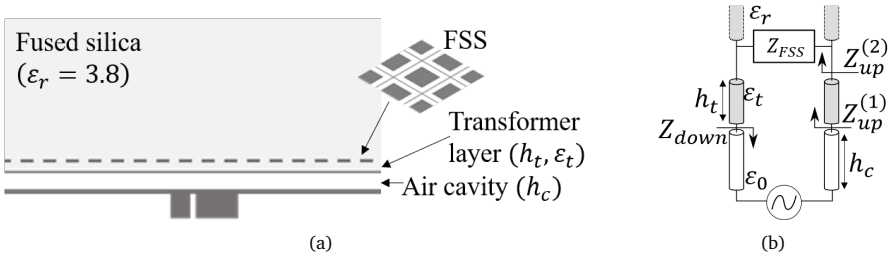

Fig. C.2: The geometry of the stratification of the dual-band lens antenna in (a) and its equivalent transverse network in (b).

In order to achieve equal beamwidth in the tertiary fields, the area of the reflector illuminated by the lens at f_L must be a factor $(f_H/f_L)^2$ larger than the reflector's area illuminated by the lens at f_H. Thus, the secondary fields should have this beamwidth ratio. Consequently, the primary field will need to have equal beamwidth for both f_L and f_H. The analysis presented in the next Section describes how we achieved equal lens illumination at f_L and f_H using a multi-mode leaky-wave feed.

C.3 Dual-Band Leaky-Wave Lens Feed Design

Half-wavelength resonant leaky-wave lens antenna feeds, consisting of a ground plane, half-wavelength air cavity and a semi-infinite medium support the propagation of

three leaky-wave (LW) modes at the central frequency: the main TM_1 / TE_1 nearly-degenerate modes and a spurious TM_0 mode [103]. These LW modes are characterized by a complex propagation constant that can be expressed as $k_\rho^{LW} = k_d[\sin(\theta_{LW}) + j\alpha_{LW}]$. Here, $\theta_{LW} = \arcsin(\beta_{LW})$ is the LW pointing angle and α_{LW} is the radial leakage rate in the cavity. The two main modes (TM_1 and TE_1) form a symmetric, nearly-Gaussian beam around broadside. The spurious TM_0 mode radiates towards larger angles and is therefore usually suppressed. The suppression of the TM_0 mode can be achieved with a double-slot iris on a thin membrane above the feeding waveguide, also ensuring impedance matching between the waveguide and the stratification [20], [103].

The bandwidth of resonant leaky-wave lens feeds is inversely proportional to the permittivity of the semi-infinite medium [20]. For example, low-permittivity plastic lenses ($\varepsilon_r = 2.5$) can achieve 40% bandwidth [20] and silicon lenses ($\varepsilon_r = 11.9$) can achieve 15% bandwidth [103]. To achieve a wider bandwidth in a silicon lens, we have developed a leaky-wave lens feed with 5 propagating leaky-wave modes in Chapter 6. However, none of these feeds are able to cover the bandwidth requirements for COMETS: f_L =210-240 GHz and f_H =500-580 GHz. The ultra-wideband leaky-wave slot antenna that uses only the frequency-independent TM_0 mode [147] is able to cover both bands in a single feed. However, the technological challenge of integrating such a slot antenna with the waveguide-based receivers at the Jet Propulsion Laboratory is considerable. Thus, to overcome the bandwidth limitation, we have investigated a dual-band leaky-wave lens feed that is waveguide-based and achieves approximately 15% bandwidth around 225 GHz and 540 GHz simultaneously.

The leaky-wave lens feed that we have investigated exploits the properties of a frequency-selective surface (FSS) to create a resonant cavity at f_L and f_H simultaneously. An earlier FSS-based dual-band antenna was developed in [184] that radiates into free-space. Here, instead, we propose the use of an FSS in a lens feed. Compared to a leaky-wave antenna radiating into free space, the bandwidth of a lens feed using the same leaky-wave poles is increased [103]. Furthermore, this approach allows us to achieve equal radiation patterns in both frequency bands.

C.3.1 Leaky-Wave Modes in Semi-Infinite Fused Silica

To obtain an optimization goal of the final (dual band) leaky-wave feed, we have first investigated the leaky-wave poles that propagate in the standard half-wavelength cavity with a fused silica lens material. Such a leaky-wave feed, using a double-slot iris to suppress the spurious TM_0 mode achieves normalized TM_1 / TE_1 LW modes that are nearly equal and are given by $k_\rho^{FS}/k_d \approx 0.21 - j0.22$ at the central frequency. In this case, the central frequency is f_c=385 GHz, which lies exactly between the desired f_L and f_H. The radiation patterns of this feed into fused silica are shown at f_C in Fig. C.3. This antenna could achieve up to 40% bandwidth [20], i.e., from 300-460

GHz.

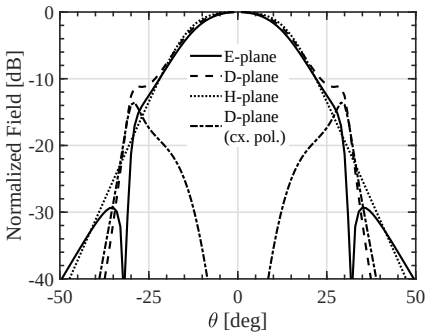

Fig. C.3: Primary radiation pattern of a leaky-wave antenna consisting of a stratification with a half-wavelength resonant cavity into semi-infinite fused silica.

In the next Section, we investigate the possibility of achieving the same normalized leaky-wave poles, k_ρ^{FS}/k_d, at $f_L \approx 0.6f_c$ (225 GHz) and $f_H \approx 1.4f_c$ (540 GHz) simultaneously.

C.3.2 Stratification Synthesis Procedure

An overview of the stratification we have analyzed is in Fig. C.2a. The feed consists of two square waveguides (one for the low frequency band and one for the high frequency band), each terminated by a double-slot iris in a ground plane. The stratification above it consists of an air cavity with thickness h_c, a transformer layer with thickness h_t and permittivity ε_t an FSS and the semi-infinite fused silica. The transverse equivalent network is shown in Fig. C.2b. We model the FSS using a homogenized surface impedance which is represented by Z_{FSS}. As will be described here, we optimize the values of these parameters to obtain the desired leaky-wave poles at f_L and f_H.

The leaky-wave modes that propagate in the cavity are the solutions k_ρ^{LW} of the TM or TE dispersion equation:

$$D^{\text{TM/TE}}(k_\rho^{LW}) = Z_{\text{up}}^{(1)}(k_\rho^{LW}, Z_{\text{FSS}}, h_t, \varepsilon_t) + Z_{\text{down}}(k_\rho^{LW}, h_c) = 0 \qquad \text{(C.1)}$$

The impedances $Z_{\text{up}}^{(1)}$ and $Z_{\text{down}} = jZ_0 \tan(k_{z0}h_c)$ are the impedances "looking up" and "looking down" into the transverse equivalent network of Fig. C.2b. To calculate $Z_{\text{up}}^{(1)}$, the impedance $Z_{\text{up}}^{(2)} = Z_d Z_{\text{FSS}}/(Z_d + Z_{\text{FSS}})$ is transformed, using the usual impedance-transform equation, over the transformer layer with Z_t and thickness h_t. Note, however, that Z_{FSS} is frequency dependent.

We are interested in finding the parameters h_c, h_t, ε_t and Z_{FSS}^{LF}, Z_{FSS}^{HF} which ensure that $k_\rho^{LW}/k_d \approx 0.21 - j0.22$ is a solution to Eq. (C.1) at f_L and f_H simultaneously. Since there are many independent parameters that can be varied, we have limited

the solution space as follows: First, the height of the cavity h_c was limited between $0.3 \leq h_c/\lambda_c \leq 0.6$, where λ_c is the free-space wavelength at f_c = 385 GHz. This cavity size is close to the size of the standard resonant cavity. Second, the permittivity of the transformer was limited to $2 \leq \varepsilon_t \leq 11.9$. These permittivity values can be synthesized by regular cylindrical perforations in a silicon slab, similar to the transformer layer in Chapter 6. Third, several simplifying assumptions are made concerning Z_{FSS}: it is i) reactive only, i.e., $Z_{\text{FSS}} = 0 + jX_{\text{FSS}}$; ii) equal for TE and TM incidence; and iii) independent of the angle of incidence. Finally, the height of the transformer layer h_t was kept as small as possible, which will help to minimize the number of undesired propagating leaky-wave modes. Concretely, this last constraint means that when multiple values of h_t solve Eq. (C.1) while the other parameters are kept constant, the lowest value of h_t is selected.

The optimization procedure is as follows:

1. Values for the height of the cavity (h_c) and the permittivity of the transformer layer (ε_t) are chosen within the given limits.
2. For a range of transformer layer heights, we find the corresponding Z_{FSS} that solve Eq. (C.1) at low and high frequency with resulting leaky-wave poles at $k_\rho^{LF/HF} = k_{\rho,LW}^{FS}$.
3. We choose the solution of Eq. (C.1) such that
   (a) $\text{Re}\{Z_{\text{FSS}}\} = 0$ and
   (b) h_t is minimal.

To clarify the procedure, we apply the procedure to a specific case. Then, in the next section, we present the generalized results of the procedure and select the optimized design.

1. The height of the cavity is selected as $h_c = 0.5\lambda_C$ and the permittivity of the transformer is chosen as $\varepsilon_t = 7$.
2. The corresponding R_{FSS} and X_{FSS} that solve Eq. (C.1) at low and high frequency for TE and TM polarization with the desired leaky-wave poles are shown as a function of the transformer layer heights h_t in Figs. C.4a and C.4b, respectively. To validate that the parameters of the stratification and FSS result in the desired LW poles in Eq. (C.1), the real and imaginary parts of the resulting LW poles are plotted in Figs. C.4c and C.4d, respectively. Indeed, all LW poles are close to $0.21 - j0.22$.
   (a) The purely reactive solution, $R_{\text{FSS}} = 0$, is found graphically from Fig. C.4a around $h_t/\lambda_t \approx 0.26$. The required X_{FSS} is then found at $h_t/\lambda_t \approx 0.26$ in Fig. C.4b. Because the ideal Z_{FSS} differs for TE and TM incidence, we average the solutions. In this case, $X_{\text{FSS}}^{LF} \approx 81\Omega$ and $X_{\text{FSS}}^{HF} \approx -134\Omega$.
   (b) In this specific case, there is no other h_t that satisfies our criteria and the procedure is stopped with all parameters being found.

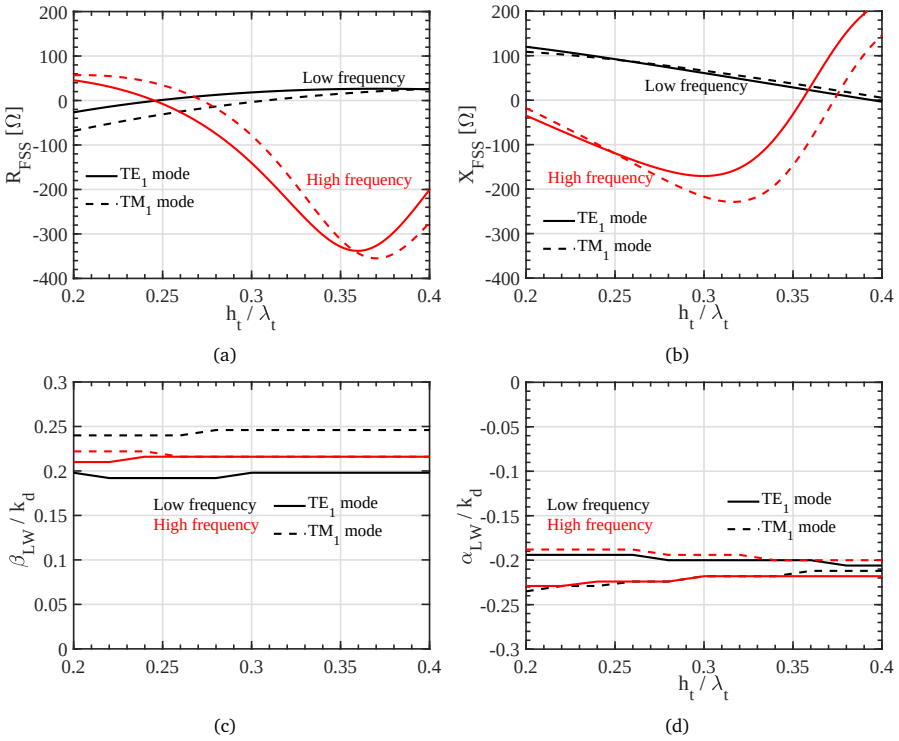

Fig. C.4: The required FSS impedance (a) R_{FSS} and (b) X_{FSS} that solve Eq. (C.1) and the resulting real and imaginary parts of k_ρ^{LW} in (c) and (d), respectively.

We note that the above procedure and constraints limit our search space and the procedure does not guarantee that a combination of stratification parameters and FSS reactances can be found in which the desired TE / TM leaky-wave modes propagate. However, in practice we did find solutions for every $\varepsilon_t \geq 3$.

C.3.3 Stratification Synthesis: Generalized Results

Next, more general results from the optimization procedure are obtained. The resulting LW modes are presented as a function of the permittivity of the transformer layer ε_t. Although we have investigated several values of the cavity height, we limit the presentation here to $h_c = 0.4\lambda_c$. For smaller values of h_c, no suitable solutions were found that satisfy all our constraints. For larger cavity sizes, more undesired LW modes propagate, which negatively affects the quality of the radiation patterns. This problem is especially manifest in the high frequency band where the cavity is electrically much larger than in the low frequency band.

In Fig. C.5, we show the real and imaginary parts of the obtained LW poles as a function of the relative permittivity of the transformer layer at the low (Figs. C.5a

and C.5b) and high frequency (Figs. C.5c and C.5d) band. Note that for each value of ε_t, the required FSS impedance and transformer thickness h_t is different but they are the result of the optimization procedure in the previous section. From Fig. C.5, it is apparent that a solution to the dispersion equation can be found that results in LW modes that are very close to the desired k_ρ^{FS} at both the low frequency and the high frequency simultaneously when $\varepsilon_t \geq 3$. These modes are indicated in black.

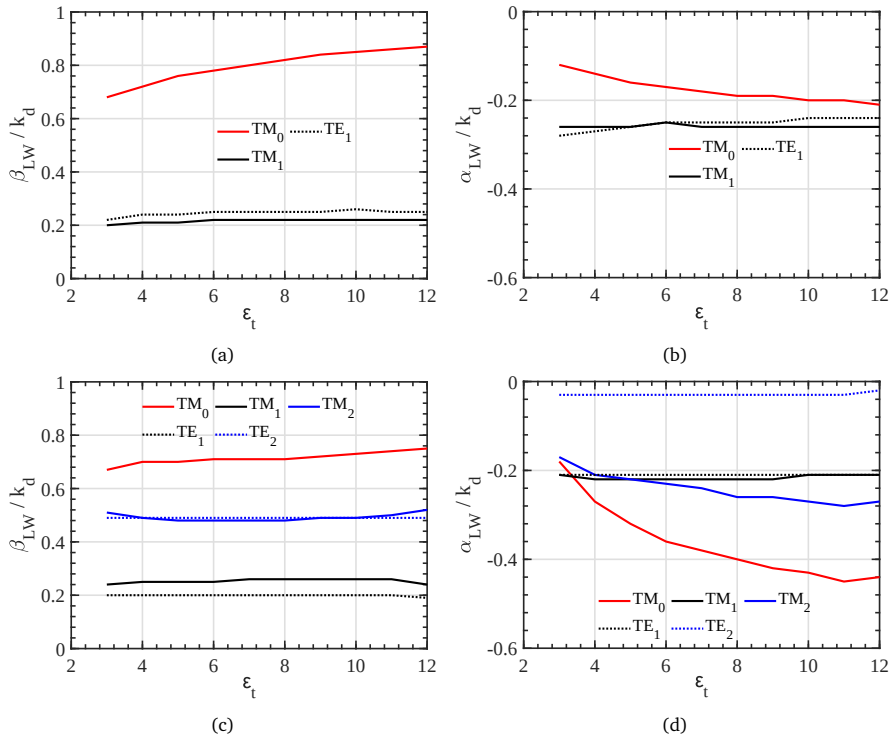

Fig. C.5: Real and imaginary parts of all propagating leaky-wave modes: For the low-frequency band in (a) and (b) and for the high-frequency band in (c) and (d).

From Fig. C.5, it is also apparent that these targeted LW modes are not the only LW modes that propagate. For the low frequency, a spurious TM_0 mode propagates which must be suppressed using the double-slot iris. At the high frequency band, more than three modes propagate (the two extra modes are the TM_2 and TE_2 mode). This is due to the combined height of the cavity and transformer layer, $h_c + h_t$.

C.3.4 Selection and Synthesis of the Optimized Stratification

During the analysis of the results of the previous section, we found a trade-off in the value of ε_t: For high ε_t, the attenuation constant of the TM_2 and TE_2 modes is large, which will reduce their impact on the radiation patterns and increase the quality of

the patterns. However, a large ε_t will also reduce the bandwidth around f_L and f_H in which the desired LW modes propagate. Therefore, a compromise must be made. We have found that $\varepsilon_t = 5$ minimizes the influence of the spurious modes while still covering the desired bandwidths. The rest of the parameters follow from the optimization procedure in the previous section: $h_t = 0.29\lambda_t = 101\mu m$, $X_{FSS}^{LF} = j100\Omega$ and $X_{FSS}^{HF} = -j350\Omega$.

The bandwidth of the stratification was analyzed by calculating the main LW modes that propagate in the optimized stratification as a function of frequency in both bands. We show the real and imaginary part of the normalized LW poles in Figs. C.6a and C.6b, respectively. The x-axis of this figure represents both the low and high frequency bandwidth that we are targeting, i.e., f/f_L for the low frequency and f/f_H for the high frequency band. The leaky-wave poles are not very dispersive in either band. Furthermore, the poles are close to the LW modes that propagate in the standard single-band resonant LW lens feed with a fused silica lens which are shown for reference.

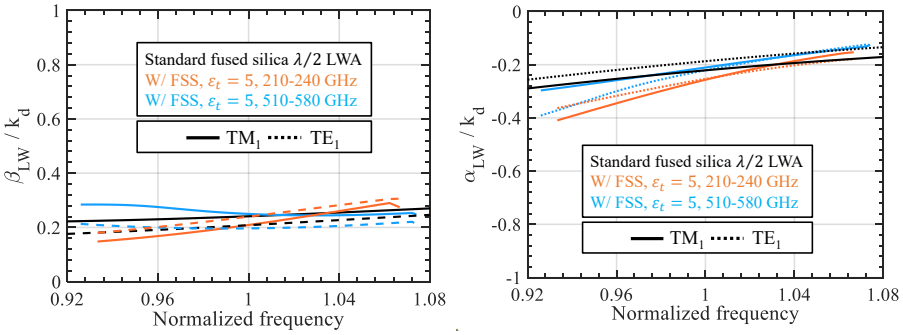

Fig. C.6: Propagating leaky-wave modes as a function of frequency in the low and high frequency band with a comparison to the modes that propagate in the standard $\lambda/2$ antenna.

Next, the required FSS and transformer layer were synthesized in real materials. For the FSS, a periodic structure consisting of loops in a ground plane with a period of around $\lambda_c/2$ was chosen, since it behaves as a capacitance at low frequencies and as an inductance at high frequencies. The dimensions of the FSS are indicated in Fig. C.7a. The desired permittivity of the transformer layer, $\varepsilon_t = 5$, was synthesized according to the method in [140] which was also applied in Chapter 6: a silicon ($\varepsilon_r = 11.9$) slab was perforated in a triangular lattice with period $d = 23\mu m$ and $p = 27\mu m$, as shown in Fig. C.7a.

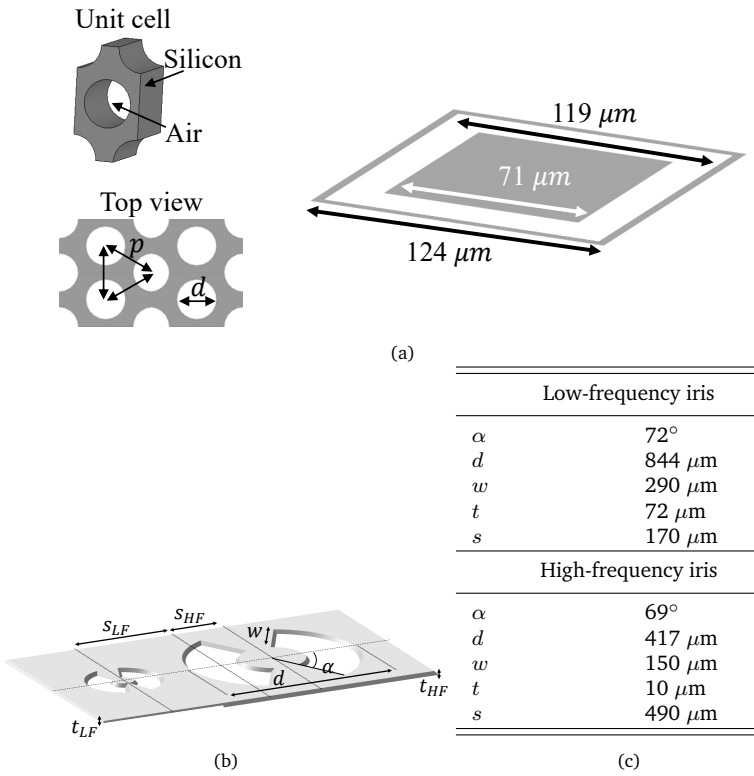

(c)

Low-frequency iris	
α	72°
d	844 μm
w	290 μm
t	72 μm
s	170 μm
High-frequency iris	
α	69°
d	417 μm
w	150 μm
t	10 μm
s	490 μm

Fig. C.7: Geometrical parameters of (a) the periodic perforations of a silicon slab and the FSS, (b) the double-slot irises and (c) tabulated dimensions of the double-slot irises.

C.4 Implementation and Performance Analysis of the Optimized Lens Feed

Impedance matching to the waveguides in both frequency bands is achieved by terminating each waveguide with a double-slot iris (see Fig. C.7b). The dimensions of these irises were chosen such that the spurious TM_0 mode is suppressed as in [20], [103]. Their thicknesses were determined by optimizing for the impedance matching bandwidth using a parametric simulation in which the FSS is modeled using a sheet impedance and the transformer layer is modeled using an isotropic slab. The optimized iris dimensions are given in Fig. C.7c. The simulated reflection coefficient with the simplified sheet impedance model is shown in Figs. C.8a and C.8b and is below -12 dB in the low frequency band and below -19 dB in the high frequency band.

The radiation patterns of the feed into the lens are initially calculated using the spectral Green's function, again assuming the FSS can be modeled as a sheet impedance and the transformer layer is an isotropic slab. The resulting patterns are shown in

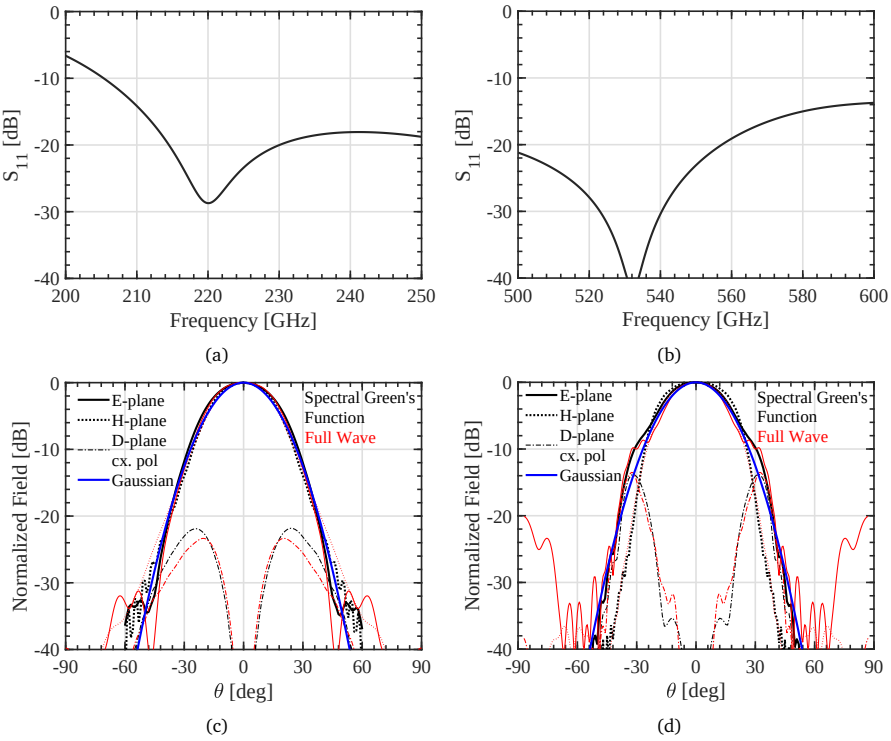

Fig. C.8: Impedance matching (S_{11}) at (a) low frequency and (b) high frequency. The resulting primary radiation patterns calculated using the spectral Green's function are shown at (c) 225 GHz and (d) 540 GHz. A comparison to full-wave simulations and the best-fitting Gaussian is also shown.

black in Figs. C.8c and C.8d at 225 and 540 GHz, respectively. Both beams have the same beamwidth, demonstrated by a very high (>93%) coupling to the same Gaussian beam superimposed in blue (the Gaussian beam is equal in both figures), confirming this aim of the dual-band design.

To validate the optimized reflection coefficient and radiation patterns, the complete feeding structure was simulated using a full-wave solver. In this validation simulation, the actual FSS structure and the perforated silicon slab, as shown in Fig. C.7a, are implemented. The full-wave radiation patterns, in red in Figs. C.8c and C.8d, are nearly in very good agreement with the spectral Green's function results, validating the design methodology. The performance of the stratification as a lens feed in the quasi-optical system is considered in the next Section.

C.5 Quasi-Optical System Performance

The radiation patterns of a 15 mm diameter lens fed by the optimized dual-band feed of the previous section, were obtained using the antennas-in-reception methodology

as discussed in Chapter 3 and [93]. Since the low- and high-frequency feeds are both slightly offset from the focus of the elliptical lens (see Fig. C.2a), a beam tilt of around 1.8 degrees at and around 4 degrees is observed at the low and high frequencies, respectively. The rotated radiation patterns (i.e., the patterns when looking in the direction of the main beam) are shown in Figs. C.9a and C.9b at low and high frequency, respectively. To show the beam tilt more clearly, the patterns are shown, uncorrected, in Fig. C.9c. In this figure, the subtended angle of the reflector is also indicated.

Next, these radiation patterns were used in GRASP to calculate the radiation patterns after a parabolic reflector with a diameter of 30 cm and $f_{\#} = 4.4$. These radiation patterns are shown in Figs. C.9d and C.9e at the center of both bands. Indeed, the radiation patterns have the same beamwidth in the two bands and overlap on the sky, which were the main goals of this investigation.

The directivity and gain of these radiation patterns were calculated in both bands. The difference between the gain and the directivity of this quasi-optical system is given by the losses due to spillover and reflection in the lens and spillover in the reflector. The directivity and gain are shown in Fig. C.10a as a function of normalized frequency. The gain is nearly constant in frequency, between 54.5 dBi and 55 dBi, in both the low- and high-frequency bands. Furthermore, the losses associated with spill over and reflections in the lens are below -1 dB in the entire quasi-optical system and for both frequency bands. Finally, we evaluated the main beam efficiency, defined as the ratio of power in the main beam of the pattern after the reflector divided by the total radiated power. This efficiency is above 96% in both bands as shown in Fig. C.10b.

C.6 Lens Antenna Prototype

We are developing and measuring a dual-band submillimeter-wave lens antenna prototype at 210-240 GHz and 500-580 GHz to demonstrate the capability of this antenna. The antenna and its constituting components are shown in Fig. C.11. It consists, from bottom to top, of a copper split block with WR-4.3 and WR-1.5 waveguide flanges to connect to frequency extenders (Fig. C.11a); several gold-plated processed silicon wafers containing a rectangular-to-square waveguide transition (Fig. C.11b); a gold-plated processed silicon wafer containing the double-slot irises (Fig. C.11c); a processed silicon wafer containing the leaky-wave cavity which is partially perforated to create the transformer layer (Fig. C.11d); and a fused silica lens with a diameter of 15 mm with the FSS patterned on the bottom (Fig. C.11e). The assembled prototype is shown in Fig. C.11f.

Measurement activities of this antenna prototype are currently being carried out at the Jet Propulsion Laboratory.

C.7 Conclusion

We have reported the progress towards a dual-band leaky-wave lens antenna operating at 210-240 GHz and 500-580 GHz simultaneously. The lens antenna can be used in a focal-plane array placed in the focus of a parabolic reflector. This quasi-optical system achieves overlapping beams and constant gain on-sky in both frequency bands. Such capability is essential for the COMETS spectrometer and radiometer that is currently under development at NASA/JPL. In this Appendix, we have emphasized the analysis and synthesis of the leaky-wave stratification for this antenna, which support leaky-wave modes that are similar to a half-wavelength resonant lens feed, but operate here at two bands simultaneously. The synthesis is based on a leaky-wave analysis of a new stratification that achieves dual-band operation due to a frequency-selective surface and a dielectric transformer layer. The design methodology has been validated by full-wave simulations. We have shown the progress towards a submillimeter-wave antenna prototype that is currently being measured. Results are expected to be published in **[J8]** after completion of the measurements.

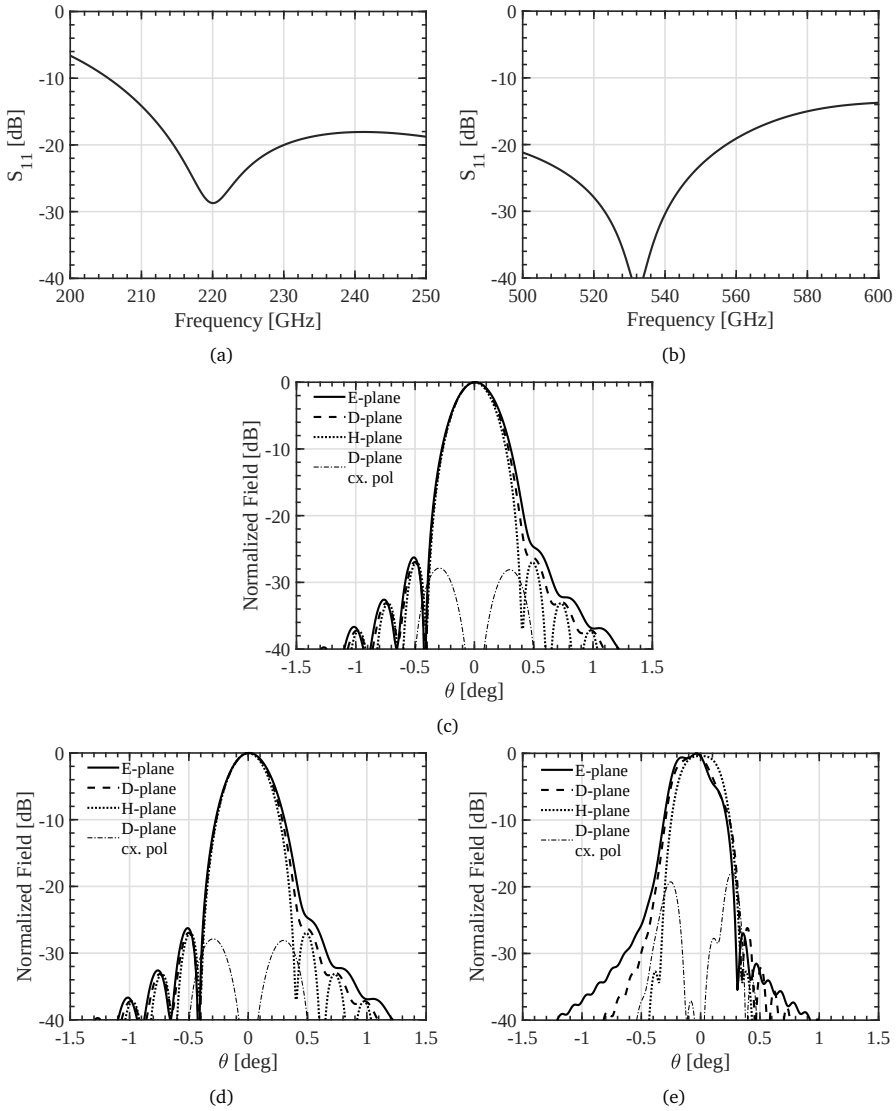

Fig. C.9: Radiation patterns of the lens looking into the main-beam direction at (a) 225 GHz and (b) 540 GHz. The beam tilt is shown in (c). Radiation patterns of the 30 cm reflector at (d) 225 GHz and (e) 540 GHz.

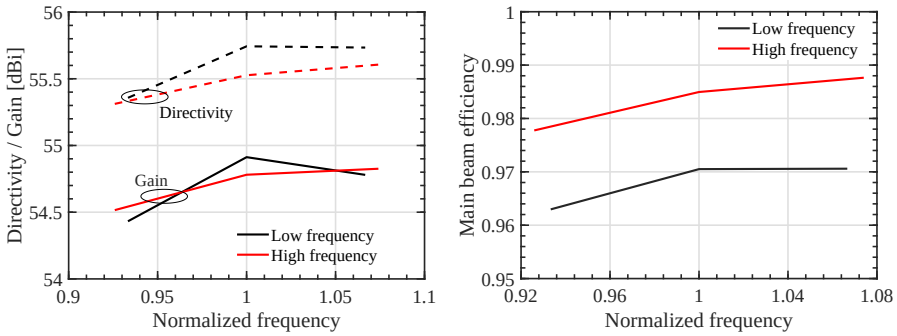

Fig. C.10: (a) Directivity and gain of the 30 cm reflector and (b) the main beam efficiency.

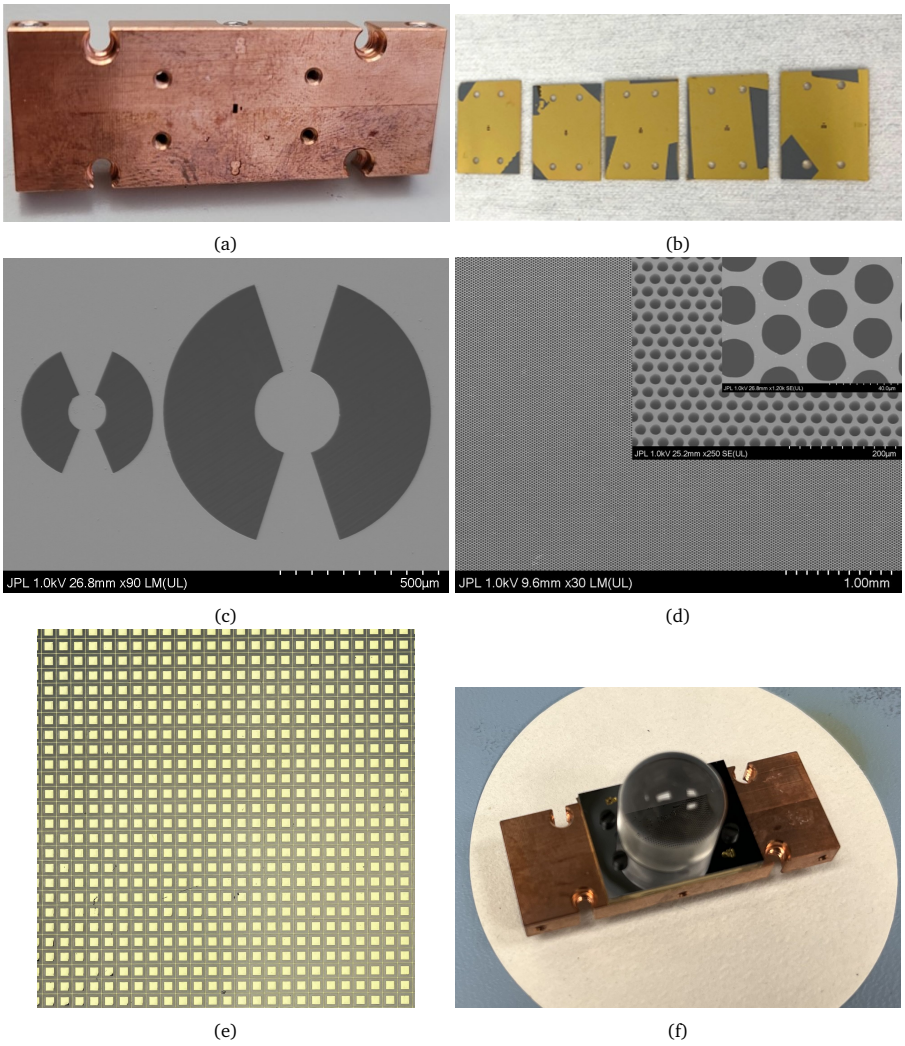

(a) (b) (c) (d) (e) (f)

Fig. C.11: Photographs of the (components of) the prototype: (a) copper waveguide split block, (b) gold-plated silcon transition wafers, (c) SEM image of the double-slot irises, (d) SEM image at various magnifications of the perforated silicon slab, (e) golden frequency-selective surface and (f) the assembled prototype showing the lens, FSS, wafers and split block.

References

[1] D. Zhao, P. Gu, J. Zhong, *et al.*, "Millimeter-Wave Integrated Phased Arrays", *IEEE Transactions on Circuits and Systems I: Regular Papers*, vol. 68, no. 10, pp. 3977–3990, Oct. 2021. DOI: 10.1109/TCSI.2021.3093093.

[2] D. Kissinger, G. Kahmen, and R. Weigel, "Millimeter-Wave and Terahertz Transceivers in SiGe BiCMOS Technologies", *IEEE Transactions on Microwave Theory and Techniques*, vol. 69, no. 10, pp. 4541–4560, Oct. 2021. DOI: 10.1109/TMTT.2021.3095235.

[3] U. R. Pfeiffer, R. Jain, J. Grzyb, *et al.*, "Current Status of Terahertz Integrated Circuits - From Components to Systems", in *2018 IEEE BiCMOS and Compound Semiconductor Integrated Circuits and Technology Symposium (BCICTS)*, Oct. 2018, pp. 1–7. DOI: 10.1109/BCICTS.2018.8551068.

[4] T. S. Rappaport, S. Sun, R. Mayzus, *et al.*, "Millimeter Wave Mobile Communications for 5G Cellular: It Will Work!", *IEEE Access*, vol. 1, pp. 335–349, 2013. DOI: 10.1109/ACCESS.2013.2260813.

[5] J. Edstam, J. Hansryd, S. Carpenter, *et al.*, "Microwave backhaul evolution – reaching beyond 100GHz", *Ericsson Technology Review*, 2017.

[6] T. S. Rappaport, Y. Xing, O. Kanhere, *et al.*, "Wireless Communications and Applications Above 100 GHz: Opportunities and Challenges for 6G and Beyond", *IEEE Access*, vol. 7, pp. 78 729–78 757, 2019. DOI: 10.1109/ACCESS.2019.2921522.

[7] M. Giordani, M. Polese, M. Mezzavilla, *et al.*, "Toward 6G Networks: Use Cases and Technologies", *IEEE Communications Magazine*, vol. 58, no. 3, pp. 55–61, Mar. 2020. DOI: 10.1109/MCOM.001.1900411.

[8] J. Hasch, E. Topak, R. Schnabel, *et al.*, "Millimeter-Wave Technology for Automotive Radar Sensors in the 77 GHz Frequency Band", *IEEE Transactions on Microwave Theory and Techniques*, vol. 60, no. 3, pp. 845–860, Mar. 2012. DOI: 10.1109/TMTT.2011.2178427.

[9] A. Eskandarian, C. Wu, and C. Sun, "Research Advances and Challenges of Autonomous and Connected Ground Vehicles", *IEEE Transactions on Intelligent Transportation Systems*, vol. 22, no. 2, pp. 683–711, Feb. 2021. DOI: 10.1109/TITS.2019.2958352.

[10] K. B. Cooper and G. Chattopadhyay, "Submillimeter-Wave Radar: Solid-State System Design and Applications", *IEEE Microwave Magazine*, vol. 15, no. 7, pp. 51–67, Nov. 2014. DOI: 10.1109/MMM.2014.2356092.

[11] P. Hillger, J. Grzyb, R. Jain, *et al.*, "Terahertz Imaging and Sensing Applications With Silicon-Based Technologies", *IEEE Transactions on Terahertz Science and Technology*, vol. 9, no. 1, pp. 1–19, Jan. 2019. DOI: 10.1109/TTHZ.2018.2884852.

[12] D. Zimdars and J. S. White, "Terahertz reflection imaging for package and personnel inspection", in *Terahertz for Military and Security Applications II*, vol. 5411, SPIE, Sep. 2004, pp. 78–83. DOI: 10.1117/12.562216.

[13] P. Siegel, "Terahertz technology in biology and medicine", *IEEE Transactions on Microwave Theory and Techniques*, vol. 52, no. 10, pp. 2438–2447, Oct. 2004. DOI: 10.1109/TMTT.2004.835916.

[14] C. E. Groppi and J. H. Kawamura, "Coherent Detector Arrays for Terahertz Astrophysics Applications", *IEEE Transactions on Terahertz Science and Technology*, vol. 1, no. 1, pp. 85–96, Sep. 2011. DOI: 10.1109/TTHZ.2011.2159555.

[15] C. Kulesa, "Terahertz Spectroscopy for Astronomy: From Comets to Cosmology", *IEEE Transactions on Terahertz Science and Technology*, vol. 1, no. 1, pp. 232–240, Sep. 2011. DOI: 10.1109/TTHZ.2011.2159648.

[16] C. Ruf, C. Swift, A. Tanner, *et al.*, "Interferometric synthetic aperture microwave radiometry for the remote sensing of the Earth", *IEEE Transactions on Geoscience and Remote Sensing*, vol. 26, no. 5, pp. 597–611, Sep. 1988. DOI: 10.1109/36.7685.

[17] D. Lamarre, J. Langen, C. C. Lin, *et al.*, "Technological Needs for European Space Agency's Microwave Limb Sounders", Darmstadt, Germany, Sep. 2000.

[18] P. Hartogh, E. Lellouch, R. Moreno, *et al.*, "Direct detection of the Enceladus water torus with Herschel", *Astronomy & Astrophysics*, vol. 532, p. L2, Aug. 2011. DOI: 10.1051/0004-6361/201117377.

[19] N. Llombart and S. O. Dabironezare, "Feasibility Study of Quasi-Optical MIMO Antennas for Radiative Near-Field Links", *IEEE Transactions on Antennas and Propagation*, vol. 70, no. 8, pp. 7073–7083, Aug. 2022. DOI: 10.1109/TAP.2022.3168724.

[20] M. Arias Campo, D. Blanco, S. Bruni, *et al.*, "On the Use of Fly's Eye Lenses with Leaky-Wave Feeds for Wideband Communications", *IEEE Transactions on Antennas and Propagation*, vol. 68, no. 4, pp. 2480–2493, Apr. 2020. DOI: 10.1109/TAP.2019.2952474.

[21] 3GPP, "New frequency range for NR (24.25-29.5 GHz)", 3rd Generation Partnership Project, Valbonne, France, Technical Report 38.815, Sep. 2021. [Online]. Available: https://www.3gpp.org/ftp/Specs/archive/38_series/38.815/.

[22] J. Pang, R. Wu, Y. Wang, *et al.*, "A 28-GHz CMOS Phased-Array Transceiver Based on LO Phase-Shifting Architecture With Gain Invariant Phase Tuning for 5G New Radio", *IEEE Journal of Solid-State Circuits*, vol. 54, no. 5, pp. 1228–1242, May 2019. DOI: 10.1109/JSSC.2019.2899734.

[23] 3GPP, "New frequency range for NR (39.5 - 43.5 GHz)", 3rd Generation Partnership Project, Valbonne, France, Technical Report 38.887, Jun. 2020. [Online]. Available: https://www.3gpp.org/ftp/Specs/archive/38_series/38.887/.

[24] Y. Wang, R. Wu, J. Pang, *et al.*, "A 39-GHz 64-Element Phased-Array Transceiver With Built-In Phase and Amplitude Calibrations for Large-Array 5G NR in 65-nm CMOS", *IEEE Journal of Solid-State Circuits*, vol. 55, no. 5, pp. 1249–1269, May 2020. DOI: 10.1109/JSSC.2020.2980509.

[25] H.-C. Park, D. Kang, S. M. Lee, *et al.*, "4.1 A 39GHz-Band CMOS 16-Channel Phased-Array Transceiver IC with a Companion Dual-Stream IF Transceiver IC for 5G NR Base-Station Applications", in *2020 IEEE International Solid- State Circuits Conference - (ISSCC)*, Feb. 2020, pp. 76–78. DOI: 10.1109/ISSCC19947.2020.9063006.

[26] U. Kodak, B. Rupakula, S. Zihir, *et al.*, "60-GHz 64- and 256-Element Dual-Polarized Dual-Beam Wafer-Scale Phased-Array Transceivers With Reticle-to-Reticle Stitching", *IEEE Transactions on Microwave Theory and Techniques*, vol. 68, no. 7, pp. 2745–2767, Jul. 2020. DOI: 10.1109/TMTT.2020.2969904.

[27] W. Shin, B.-H. Ku, O. Inac, *et al.*, "A 108–114 GHz 4x4 Wafer-Scale Phased Array Transmitter With High-Efficiency On-Chip Antennas", *IEEE Journal of Solid-State Circuits*, vol. 48, no. 9, pp. 2041–2055, Sep. 2013. DOI: 10.1109/JSSC.2013.2260097.

[28] A. Natarajan, A. Valdes-Garcia, B. Sadhu, *et al.*, "W-Band Dual-Polarization Phased-Array Transceiver Front-End in SiGe BiCMOS", *IEEE Transactions on Microwave Theory and Techniques*, vol. 63, no. 6, pp. 1989–2002, Jun. 2015. DOI: 10.1109/TMTT.2015.2422691.

[29] E. Naviasky, L. Iotti, G. LaCaille, *et al.*, "A 71-to-86-GHz 16-Element by 16-Beam Multi-User Beamforming Integrated Receiver Sub-Array for Massive MIMO", *IEEE Journal of Solid-State Circuits*, vol. 56, no. 12, pp. 3811–3826, Dec. 2021. DOI: 10.1109/JSSC.2021.3118641.

[30] S. Shahramian, M. J. Holyoak, and Y. Baeyens, "A 16-Element W-Band Phased-Array Transceiver Chipset With Flip-Chip PCB Integrated Antennas for Multi-Gigabit Wireless Data Links", *IEEE Transactions on Microwave Theory and Techniques*, vol. 66, no. 7, pp. 3389–3402, Jul. 2018. DOI: 10.1109/TMTT.2018.2822304.

[31] X. Gu, A. Valdes-Garcia, A. Natarajan, *et al.*, "W-band scalable phased arrays for imaging and communications", *IEEE Communications Magazine*, vol. 53, no. 4, pp. 196–204, Apr. 2015. DOI: 10.1109/MCOM.2015.7081095.

[32] X. Gu, D. Liu, C. Baks, *et al.*, "A compact 4-chip package with 64 embedded dual-polarization antennas for W-band phased-array transceivers", in *2014 IEEE 64th Electronic Components and Technology Conference (ECTC)*, May 2014, pp. 1272–1277. DOI: 10.1109/ECTC.2014.6897455.

[33] N. Grace, "FCC TAKES STEPS TO OPEN SPECTRUM HORIZONS FOR NEW SERVICES AND TECHNOLOGIES", *FCC News*, Mar. 2019. [Online]. Available: https://www.fcc.gov/document/fcc-opens-spectrum-horizons-new-services-technologies.

[34] X. Meng, B. Chi, Y. Liu, *et al.*, "A Fully Integrated 150-GHz Transceiver Front-End in 65-nm CMOS", *IEEE Transactions on Circuits and Systems II: Express Briefs*, vol. 66, no. 4, pp. 602–606, Apr. 2019. DOI: 10.1109/TCSII.2018.2870926.

[35] X. Tang, J. Nguyen, G. Mangraviti, *et al.*, "Design and Analysis of a 140-GHz T/R Front-End Module in 22-nm FD-SOI CMOS", *IEEE Journal of Solid-State Circuits*, pp. 1–1, 2022. DOI: 10.1109/JSSC.2021.3139359.

[36] S. Li, Z. Zhang, B. Rupakula, *et al.*, "An Eight-Element 140-GHz Wafer-Scale IF Beamforming Phased-Array Receiver With 64-QAM Operation in CMOS RF-SOI", *IEEE Journal of Solid-State Circuits*, vol. 57, no. 2, pp. 385–399, Feb. 2022. DOI: 10.1109/JSSC.2021.3102876.

[37] A. Bisognin, N. Nachabe, C. Luxey, *et al.*, "Ball Grid Array Module With Integrated Shaped Lens for 5G Backhaul/Fronthaul Communications in F-Band", *IEEE Transactions on Antennas and Propagation*, vol. 65, no. 12, pp. 6380–6394, Dec. 2017. DOI: 10.1109/TAP.2017.2755439.

[38] R. Han and E. Afshari, "A CMOS High-Power Broadband 260-GHz Radiator Array for Spectroscopy", *IEEE Journal of Solid-State Circuits*, vol. 48, no. 12, pp. 3090–3104, Dec. 2013. DOI: 10.1109/JSSC.2013.2272864.

[39] S. Kang, S. V. Thyagarajan, and A. M. Niknejad, “A 240 GHz Fully Integrated Wideband QPSK Transmitter in 65 nm CMOS”, *IEEE Journal of Solid-State Circuits*, vol. 50, no. 10, pp. 2256–2267, Oct. 2015. DOI: 10.1109/JSSC.2015.2467179.

[40] C.-H. Li, C.-L. Ko, M.-C. Kuo, *et al.*, “A 340-GHz Heterodyne Receiver Front End in 40-nm CMOS for THz Biomedical Imaging Applications”, *IEEE Transactions on Terahertz Science and Technology*, vol. 6, no. 4, pp. 625–636, Jul. 2016. DOI: 10.1109/TTHZ.2016.2566580.

[41] H. Jalili and O. Momeni, “A 0.34-THz Wideband Wide-Angle 2-D Steering Phased Array in 0.13- m SiGe BiCMOS”, *IEEE Journal of Solid-State Circuits*, vol. 54, no. 9, pp. 2449–2461, Sep. 2019. DOI: 10.1109/JSSC.2019.2925523.

[42] Y. Yang, O. D. Gurbuz, and G. M. Rebeiz, “An Eight-Element 370–410-GHz Phased-Array Transmitter in 45-nm CMOS SOI With Peak EIRP of 8–8.5 dBm”, *IEEE Transactions on Microwave Theory and Techniques*, vol. 64, no. 12, pp. 4241–4249, Dec. 2016. DOI: 10.1109/TMTT.2016.2613850.

[43] K. Guo, Y. Zhang, and P. Reynaert, “A 0.53-THz Subharmonic Injection-Locked Phased Array With 63- W Radiated Power in 40-nm CMOS”, *IEEE Journal of Solid-State Circuits*, vol. 54, no. 2, pp. 380–391, Feb. 2019. DOI: 10.1109/JSSC.2018.2877203.

[44] K. Ramasubramanian and K. Ramaiah, “Moving from Legacy 24 GHz to State-of-the-Art 77-GHz Radar”, *ATZelektronik worldwide*, vol. 13, no. 3, pp. 46–49, Jun. 2018. DOI: 10.1007/s38314-018-0029-6.

[45] S. Sun, A. P. Petropulu, and H. V. Poor, “MIMO Radar for Advanced Driver-Assistance Systems and Autonomous Driving: Advantages and Challenges”, *IEEE Signal Processing Magazine*, vol. 37, no. 4, pp. 98–117, Jul. 2020. DOI: 10.1109/MSP.2020.2978507.

[46] C. Pfeffer, R. Feger, C. Wagner, *et al.*, “FMCW MIMO Radar System for Frequency-Division Multiple TX-Beamforming”, *IEEE Transactions on Microwave Theory and Techniques*, vol. 61, no. 12, pp. 4262–4274, Dec. 2013. DOI: 10.1109/TMTT.2013.2287675.

[47] M. Steinhauer, H.-O. Ruoss, H. Irion, *et al.*, “Millimeter-Wave-Radar Sensor Based on a Transceiver Array for Automotive Applications”, *IEEE Transactions on Microwave Theory and Techniques*, vol. 56, no. 2, pp. 261–269, Feb. 2008. DOI: 10.1109/TMTT.2007.914635.

[48] S. Lutz, T. Walter, and R. Weigel, "Lens-based 77 GHZ MIMO radar for angular estimation in multitarget environments", *International Journal of Microwave and Wireless Technologies*, vol. 6, no. 3-4, pp. 397–404, Jun. 2014. DOI: 10.1017/S1759078714000506.

[49] A. Townley, P. Swirhun, D. Titz, *et al.*, "A 94-GHz 4TX–4RX Phased-Array FMCW Radar Transceiver With Antenna-in-Package", *IEEE Journal of Solid-State Circuits*, vol. 52, no. 5, pp. 1245–1259, May 2017. DOI: 10.1109/JSSC.2017.2675907.

[50] S.-Y. Jeon, S. Kim, J. Kim, *et al.*, "W-Band FMCW MIMO Radar System for High-Resolution Multimode Imaging With Time- and Frequency-Division Multiplexing", *IEEE Transactions on Geoscience and Remote Sensing*, vol. 58, no. 7, pp. 5042–5057, Jul. 2020. DOI: 10.1109/TGRS.2020.2971998.

[51] A. Visweswaran, K. Vaesen, M. Glassee, *et al.*, "A 28-nm-CMOS Based 145-GHz FMCW Radar: System, Circuits, and Characterization", *IEEE Journal of Solid-State Circuits*, vol. 56, no. 7, pp. 1975–1993, Jul. 2021. DOI: 10.1109/JSSC.2020.3041153.

[52] A. Mostajeran, A. Cathelin, and E. Afshari, "A 170-GHz Fully Integrated Single-Chip FMCW Imaging Radar with 3-D Imaging Capability", *IEEE Journal of Solid-State Circuits*, vol. 52, no. 10, pp. 2721–2734, Oct. 2017. DOI: 10.1109/JSSC.2017.2725963.

[53] A. Mostajeran, S. M. Naghavi, M. Emadi, *et al.*, "A High-Resolution 220-GHz Ultra-Wideband Fully Integrated ISAR Imaging System", *IEEE Transactions on Microwave Theory and Techniques*, vol. 67, no. 1, pp. 429–442, Jan. 2019. DOI: 10.1109/TMTT.2018.2874666.

[54] D. M. Sheen, T. E. Hall, R. H. Severtsen, *et al.*, "Standoff concealed weapon detection using a 350-GHz radar imaging system", in *Passive Millimeter-Wave Imaging Technology XIII*, vol. 7670, SPIE, Apr. 2010, pp. 57–68. DOI: 10.1117/12.852788.

[55] D. A. Robertson, D. G. Macfarlane, R. I. Hunter, *et al.*, "High resolution, wide field of view, real time 340GHz 3D imaging radar for security screening", in *Passive and Active Millimeter-Wave Imaging XX*, vol. 10189, SPIE, May 2017, pp. 83–91. DOI: 10.1117/12.2262264.

[56] F. Friederich, W. von Spiegel, M. Bauer, *et al.*, "THz Active Imaging Systems With Real-Time Capabilities", *IEEE Transactions on Terahertz Science and Technology*, vol. 1, no. 1, pp. 183–200, Sep. 2011. DOI: 10.1109/TTHZ.2011.2159559.

[57] P. D. Feldman, A. L. Cochran, and M. R. Combi, "Spectroscopic investigations of fragment species in the coma", in *Comets II*, ser. Space Science Series, Jan. 2004, ISBN: 978-0-8165-2450-1.

[58] S. Gulkis, M. Allen, C. Backus, *et al.*, "Remote sensing of a comet at millimeter and submillimeter wavelengths from an orbiting spacecraft", *Planetary and Space Science*, Highlights in Planetary Science, vol. 55, no. 9, pp. 1050–1057, Jun. 2007. DOI: 10.1016/j.pss.2006.11.011.

[59] B. Bulcha, C. M. Anderson, G. Chin, *et al.*, "Submillimeter Solar Observation Lunar Volatiles Experiment (SSOLVE) Optics and Front-end Spectrometer", in *2021 46th International Conference on Infrared, Millimeter and Terahertz Waves (IRMMW-THz)*, Aug. 2021, pp. 1–1. DOI: 10.1109/IRMMW-THz50926.2021.9566908.

[60] N. Aghanim, Y. Akrami, F. Arroja, *et al.*, "Planck 2018 results - I. Overview and the cosmological legacy of Planck", *Astronomy & Astrophysics*, vol. 641, A1, Sep. 2020. DOI: 10.1051/0004-6361/201833880.

[61] R. Cofield and P. Stek, "Design and field-of-view calibration of 114-660-GHz optics of the Earth observing system microwave limb sounder", *IEEE Transactions on Geoscience and Remote Sensing*, vol. 44, no. 5, pp. 1166–1181, May 2006. DOI: 10.1109/TGRS.2006.873234.

[62] S. Ochiai, K.-i. Kikuchi, T. Nishibori, *et al.*, "Receiver Performance of the Superconducting Submillimeter-Wave Limb-Emission Sounder (SMILES) on the International Space Station", *IEEE Transactions on Geoscience and Remote Sensing*, vol. 51, no. 7, pp. 3791–3802, Jul. 2013. DOI: 10.1109/TGRS.2012.2227758.

[63] P. H. Siegel, "THz Instruments for Space", *IEEE Transactions on Antennas and Propagation*, vol. 55, no. 11, pp. 2957–2965, Nov. 2007. DOI: 10.1109/TAP.2007.908557.

[64] J. V. Siles, K. B. Cooper, C. Lee, *et al.*, "A New Generation of Room-Temperature Frequency-Multiplied Sources With up to 10× Higher Output Power in the 160-GHz–1.6-THz Range", *IEEE Transactions on Terahertz Science and Technology*, vol. 8, no. 6, pp. 596–604, Nov. 2018. DOI: 10.1109/TTHZ.2018.2876620.

[65] D. Jayasankar, V. Drakinskiy, M. Myremark, *et al.*, "Design and development of 3.5 THz Schottky-based fundamental mixer", in *2020 50th European Microwave Conference (EuMC)*, Jan. 2021, pp. 595–598. DOI: 10.23919/EuMC48046.2021.9338204.

[66] J. Siles, J. Kawamura, M. Alonso-Del-Pino, *et al.*, "COMETS – Comets observation & Mapping enhanced THz spectrometer at 210-580 GHz: Objectives and development status", English, 2019, p. 203.

[67] R. Staehle, D. Blaney, H. Hemmati, *et al.*, "Interplanetary CubeSats: Opening the Solar System to a Broad Community at Lower Cost", *Journal of Small Satellites*, vol. 2, no. 1, pp. 161–186, Jul. 2013. [Online]. Available: https://jossonline.com/Papers1441.html.

[68] T. Reck, B. Drouin, A. Tang, *et al.*, "Submillimeter-Wave Spectrometer for Small Satellites", Washington, DC, Nov. 2016.

[69] A. Tang, M. A. D. Pino, Y. Kim, *et al.*, "Sub-Orbital Flight Demonstration of a 183/540–600 GHz Hybrid CMOS-InP and CMOS-Schottky-MEMS Limb-Sounder", *IEEE Journal of Microwaves*, vol. 1, no. 2, pp. 560–573, Apr. 2021. DOI: 10.1109/JMW.2021.3060622.

[70] J. V. Siles, R. Lin, P. Bruneau, *et al.*, "An ultra-compact 16-pixel local oscillator at 1.9 THz", in *2016 41st International Conference on Infrared, Millimeter, and Terahertz waves (IRMMW-THz)*, Sep. 2016, pp. 1–2. DOI: 10.1109/IRMMW-THz.2016.7758727.

[71] I. Mehdi, J. Siles, C. Lee, *et al.*, "Compact submillimeter-wave multi-pixel local oscillator sources", in *2015 40th International Conference on Infrared, Millimeter, and Terahertz waves (IRMMW-THz)*, Aug. 2015, pp. 1–2. DOI: 10.1109/IRMMW-THz.2015.7327567.

[72] R. Mailloux, L. Zahn, and A. Martinez, "Grating lobe control in limited scan arrays", *IEEE Transactions on Antennas and Propagation*, vol. 27, no. 1, pp. 79–85, Jan. 1979. DOI: 10.1109/TAP.1979.1142034.

[73] D. Blanco, N. Llombart, and E. Rajo-Iglesias, "On the Use of Leaky Wave Phased Arrays for the Reduction of the Grating Lobe Level", *IEEE Transactions on Antennas and Propagation*, vol. 62, no. 4, pp. 1789–1795, Apr. 2014. DOI: 10.1109/TAP.2013.2272573.

[74] F. Scattone, M. Ettorre, R. Sauleau, *et al.*, "A flat-topped leaky-wave source for phased arrays with reduced scan losses", in *The 8th European Conference on Antennas and Propagation (EuCAP 2014)*, Apr. 2014, pp. 1220–1224. DOI: 10.1109/EuCAP.2014.6901995.

[75] B. Avser, J. Pierro, and G. M. Rebeiz, "Random Feeding Networks for Reducing the Number of Phase Shifters in Limited-Scan Arrays", *IEEE Transactions on Antennas and Propagation*, vol. 64, no. 11, pp. 4648–4658, Nov. 2016. DOI: 10.1109/TAP.2016.2600861.

[76] D. Petrolati, P. Angeletti, and G. Toso, "A Lossless Beam-Forming Network for Linear Arrays Based on Overlapped Sub-Arrays", *IEEE Transactions on Antennas and Propagation*, vol. 62, no. 4, pp. 1769–1778, Apr. 2014. DOI: 10.1109/TAP.2013.2282189.

[77] R. Beresford, A. Chippendale, D. Ferris, *et al.*, "Eyes on the Sky: A Refracting Concentrator Approach to the SKA", *SKA Engineering and Management Team*, Jul. 2002. [Online]. Available: https://www.skatelescope.org/uploaded/61284_22_memo_Hall.pdf.

[78] J. James, C. Hall, and G. Andrasic, "Microstrip elements and arrays with spherical dielectric overlays", *IEE Proceedings H Microwaves, Antennas and Propagation*, vol. 133, no. 6, p. 474, 1986. DOI: 10.1049/ip-h-2.1986.0081.

[79] J. Poirier, G. Morin, Y. Antar, *et al.*, "Millimetre-wave limited-scan array using small lenses", in *IEEE Antennas and Propagation Society International Symposium. 2001 Digest. Held in conjunction with: USNC/URSI National Radio Science Meeting (Cat. No.01CH37229)*, vol. 2, Jul. 2001, 823–826 vol.2. DOI: 10.1109/APS.2001.959850.

[80] I. V. Minin and O. V. Minin, *Basic principles of Fresnel antenna arrays* (Lecture notes electrical engineering). Berlin: Springer, 2008, vol. 19, ISBN: 978-3-540-79558-2.

[81] M. Zimmerman, I. Timofeev, and K. E. Linehan, "Lensed antennas for use in cellular and other communications systems", pat. US10483650B1, Nov. 2019.

[82] S. Matitsine, L. Matytsine, and A. DeMarco, "Lens arrays configurations for improved signal performance", pat. US10923828B2, Feb. 2021.

[83] C. P. Scarborough, J. P. Turpin, D. F. Difonzo, *et al.*, "Lens antenna system", pat. EP3376595B1, Nov. 2021.

[84] G. Mumcu, M. Kacar, and J. Mendoza, "Mm-Wave Beam Steering Antenna With Reduced Hardware Complexity Using Lens Antenna Subarrays", *IEEE Antennas and Wireless Propagation Letters*, vol. 17, no. 9, pp. 1603–1607, Sep. 2018. DOI: 10.1109/LAWP.2018.2857441.

[85] S. Bosma, M. Alonso-delPino, C. Jung-Kubiak, *et al.*, "Scanning Lens Phased Array for Submillimeter Wavelengths", in *2019 44th International Conference on Infrared, Millimeter, and Terahertz Waves (IRMMW-THz)*, Sep. 2019, pp. 1–2. DOI: 10.1109/IRMMW-THz.2019.8874477.

[86] M. Alonso-delPino, C. Jung-Kubiak, T. Reck, *et al.*, "Beam Scanning of Silicon Lens Antennas Using Integrated Piezomotors at Submillimeter Wavelengths", *IEEE Transactions on Terahertz Science and Technology*, vol. 9, no. 1, pp. 47–54, Jan. 2019. DOI: 10.1109/TTHZ.2018.2881930.

[87] R. J. Mailloux, *Phased array antenna handbook* (Antennas and Electromagnetics Analysis Library), 3rd ed. Norwood, MA: Artech House, 2018, ISBN: 978-1-63081-029-0.

[88] E. Sharp, "A triangular arrangement of planar-array elements that reduces the number needed", *IRE Transactions on Antennas and Propagation*, vol. 9, no. 2, pp. 126–129, Mar. 1961. DOI: 10.1109/TAP.1961.1144967.

[89] Y. Lo and S. Lee, "Affine transformation and its application to antenna arrays", *IEEE Transactions on Antennas and Propagation*, vol. 13, no. 6, pp. 890–896, Nov. 1965. DOI: 10.1109/TAP.1965.1138541.

[90] A. Love, "The uniform hexagonal array", in *1978 Antennas and Propagation Society International Symposium*, vol. 16, Mar. 1978, pp. 450–454. DOI: 10.1109/APS.1978.1148002.

[91] J. A. Grzesik, "Hexagonal Array Factor in Closed Form", *Journal of Electromagnetic Waves and Applications*, vol. 20, no. 10, pp. 1311–1323, Jan. 2006. DOI: 10.1163/156939306779276839.

[92] E. Specht, *The best known packings of equal circles in a circle*, Sep. 2021. [Online]. Available: http://hydra.nat.uni-magdeburg.de/packing/cci/cci.html.

[93] M. Arias Campo, "On the Design of Fly's Eye Lenses at Sub-THz Frequencies for Wideband Communications", Ph.D. dissertation, Delft University of Technology, Delft, 2021. [Online]. Available: https://repository.tudelft.nl/islandora/object/uuid%3Aa9bb41e0-3d2a-4028-a218-bd85f2053545.

[94] H. Zhang, S. Bosma, A. Neto, *et al.*, "A Dual-Polarized 27-dBi Scanning Lens Phased Array Antenna for 5G Point-to-Point Communications", *IEEE Transactions on Antennas and Propagation*, vol. 69, no. 9, pp. 5640–5652, 2021. DOI: 10.1109/TAP.2021.3069494.

[95] M. Arias Campo, K. Holc, R. Weber, *et al.*, "H-band Quartz-Silicon Leaky-Wave Lens with Air-Bridge Interconnect to GaAs Front-End", *IEEE Transactions on Terahertz Science and Technology*, vol. 11, no. 3, pp. 297–309, Jan. 2021. DOI: 10.1109/TTHZ.2021.3049640.

[96] H. Zhang, S. O. Dabironezare, G. Carluccio, *et al.*, "A Fourier Optics Tool to Derive the Plane Wave Spectrum of Quasi-Optical Systems [EM Programmer's Notebook]", *IEEE Antennas and Propagation Magazine*, vol. 63, no. 1, pp. 103–116, Feb. 2021. DOI: 10.1109/MAP.2020.3027233.

[97] D. Jackson and A. Oliner, "A leaky-wave analysis of the high-gain printed antenna configuration", *IEEE Transactions on Antennas and Propagation*, vol. 36, no. 7, pp. 905–910, Jul. 1988. DOI: 10.1109/8.7194.

[98] G. V. Trentini, "Partially reflecting sheet arrays", *IRE Transactions on Antennas and Propagation*, vol. 4, no. 4, pp. 666–671, Oct. 1956. DOI: 10.1109/TAP.1956.1144455.

[99] N. Guerin, S. Enoch, G. Tayeb, *et al.*, "A metallic Fabry-Perot directive antenna", *IEEE Transactions on Antennas and Propagation*, vol. 54, no. 1, pp. 220–224, Jan. 2006. DOI: 10.1109/TAP.2005.861578.

[100] A. Hosseini, F. Capolino, and F. De Flaviis, "Gain Enhancement of a V-Band Antenna Using a Fabry-Pérot Cavity With a Self-Sustained All-Metal Cap With FSS", *IEEE Transactions on Antennas and Propagation*, vol. 63, no. 3, pp. 909–921, Mar. 2015. DOI: 10.1109/TAP.2014.2386358.

[101] H. Attia, M. L. Abdelghani, and T. A. Denidni, "Wideband and High-Gain Millimeter-Wave Antenna Based on FSS Fabry–Perot Cavity", *IEEE Transactions on Antennas and Propagation*, vol. 65, no. 10, pp. 5589–5594, Oct. 2017. DOI: 10.1109/TAP.2017.2742550.

[102] Q.-Y. Guo and H. Wong, "155 GHz Dual-Polarized Fabry–Perot Cavity Antenna Using LTCC-Based Feeding Source and Phase-Shifting Surface", *IEEE Transactions on Antennas and Propagation*, vol. 69, no. 4, pp. 2347–2352, Apr. 2021. DOI: 10.1109/TAP.2020.3019528.

[103] N. Llombart, G. Chattopadhyay, A. Skalare, *et al.*, "Novel Terahertz Antenna Based on a Silicon Lens Fed by a Leaky Wave Enhanced Waveguide", *IEEE Transactions on Antennas and Propagation*, vol. 59, no. 6, pp. 2160–2168, Jun. 2011. DOI: 10.1109/TAP.2011.2143663.

[104] R. Gardelli, M. Albani, and F. Capolino, "Array thinning by using antennas in a Fabry–Perot cavity for gain enhancement", *IEEE Transactions on Antennas and Propagation*, vol. 54, no. 7, pp. 1979–1990, Jul. 2006. DOI: 10.1109/TAP.2006.877172.

[105] A. Neto, N. Llombart, G. Gerini, *et al.*, "EBG Enhanced Feeds for the Improvement of the Aperture Efficiency of Reflector Antennas", *IEEE Transactions on Antennas and Propagation*, vol. 55, no. 8, pp. 2185–2193, Aug. 2007. DOI: 10.1109/TAP.2007.901854.

[106] S. A. Muhammad, R. Sauleau, and H. Legay, "Small-Size Shielded Metallic Stacked Fabry–Perot Cavity Antennas With Large Bandwidth for Space Applications", *IEEE Transactions on Antennas and Propagation*, vol. 60, no. 2, pp. 792–802, Feb. 2012. DOI: 10.1109/TAP.2011.2173133.

[107] A. Lalbakhsh, M. U. Afzal, K. P. Esselle, *et al.*, "Wideband Near-Field Correction of a Fabry–Perot Resonator Antenna", *IEEE Transactions on Antennas and Propagation*, vol. 67, no. 3, pp. 1975–1980, Mar. 2019. DOI: 10.1109/TAP.2019.2891230.

[108] L. Zhou, X. Duan, Z. Luo, *et al.*, "High Directivity Fabry-Perot Antenna with a Nonuniform Partially Reflective Surface and a Phase Correcting Structure", *IEEE Transactions on Antennas and Propagation*, pp. 7601–7606, 2020. DOI: 10.1109/TAP.2020.2982514.

[109] A. Lalbakhsh, M. U. Afzal, K. P. Esselle, *et al.*, "Low-Cost Nonuniform Metallic Lattice for Rectifying Aperture Near-Field of Electromagnetic Bandgap Resonator Antennas", *IEEE Transactions on Antennas and Propagation*, vol. 68, no. 5, pp. 3328–3335, May 2020. DOI: 10.1109/TAP.2020.2969888.

[110] T. N. Kaifas, D. G. Babas, G. Toso, *et al.*, "Multibeam antennas for global satellite coverage: theory and design", *IET Microwaves, Antennas & Propagation*, vol. 10, no. 14, pp. 1475–1484, Nov. 2016. DOI: 10.1049/iet-map.2015.0811.

[111] M. Alonso-delPino, S. Bosma, C. Jung-Kubiak, *et al.*, "Wideband Multimode Leaky-Wave Feed for Scanning Lens-Phased Array at Submillimeter Wavelengths", *IEEE Transactions on Terahertz Science and Technology*, vol. 11, no. 2, pp. 205–217, Mar. 2021. DOI: 10.1109/TTHZ.2020.3038033.

[112] R. Maximidis, D. Caratelli, G. Toso, *et al.*, "High-Gain Planar Array of Reactively Loaded Antennas for Limited Scan Range Applications", *Electronics*, vol. 9, no. 9, p. 1376, Aug. 2020. DOI: 10.3390/electronics9091376.

[113] F. Scattone, M. Ettorre, B. Fuchs, *et al.*, "Synthesis Procedure for Thinned Leaky-Wave-Based Arrays With Reduced Number of Elements", *IEEE Transactions on Antennas and Propagation*, vol. 64, no. 2, pp. 582–590, Feb. 2016. DOI: 10.1109/TAP.2015.2509008.

[114] D. Blanco, E. Rajo-Iglesias, A. M. Benito, *et al.*, "Leaky-Wave Thinned Phased Array in PCB Technology for Telecommunication Applications", *IEEE Transactions on Antennas and Propagation*, vol. 64, no. 10, pp. 4288–4296, Oct. 2016. DOI: 10.1109/TAP.2016.2597642.

[115] G. Lovat, P. Burghignoli, and D. Jackson, "Fundamental properties and optimization of broadside radiation from uniform leaky-wave antennas", *IEEE Transactions on Antennas and Propagation*, vol. 54, no. 5, pp. 1442–1452, May 2006. DOI: 10.1109/TAP.2006.874350.

[116] M Alonso-DelPino, C Lee, C Jung-Kubiak, *et al.*, "Design Guidelines for a Terahertz Silicon Micro-Lens Antenna", *IEEE Antennas and Wireless Propagation Letters*, vol. 12, p. 4, 2013.

[117] L. B. Felsen and N. Marcuvitz, *Radiation and scattering of waves* (IEEE Press series on electromagnetic waves). Piscataway, NJ: IEEE Press, 1994, ISBN: 978-0-7803-1088-9.

[118] S. Maci and A. Neto, "Green's function of an infinite slot printed between two homogeneous dielectrics-Part II: uniform asymptotic solution", *IEEE Transactions on Antennas and Propagation*, vol. 52, no. 3, pp. 666–676, Mar. 2004. DOI: 10.1109/TAP.2004.825500.

[119] A. Polemi and S. Maci, "On the Polarization Properties of a Dielectric Leaky Wave Antenna", *IEEE Antennas and Wireless Propagation Letters*, vol. 5, pp. 306–310, 2006. DOI: 10.1109/LAWP.2006.878889.

[120] P. Burghignoli, G. Lovat, F. Capolino, *et al.*, "Modal Propagation and Excitation on a Wire-Medium Slab", *IEEE Transactions on Microwave Theory and Techniques*, vol. 56, no. 5, pp. 1112–1124, May 2008. DOI: 10.1109/TMTT.2008.921657.

[121] G. Lovat, R. Araneo, and S. Celozzi, "Dipole Excitation of Periodic Metallic Structures", *IEEE Transactions on Antennas and Propagation*, vol. 59, no. 6, pp. 2178–2187, Jun. 2011. DOI: 10.1109/TAP.2011.2143660.

[122] F. Liang, G. W. Hanson, A. B. Yakovlev, *et al.*, "Dyadic Green's Functions for Dipole Excitation of Homogenized Metasurfaces", *IEEE Transactions on Antennas and Propagation*, vol. 64, no. 1, pp. 167–178, Jan. 2016. DOI: 10.1109/TAP.2015.2501430.

[123] P. Burghignoli, "A Leaky-Wave Analysis of the Phase Center in Fabry-Pérot Cavity Antennas", *IEEE Transactions on Antennas and Propagation*, vol. 60, no. 5, pp. 2226–2233, May 2012. DOI: 10.1109/TAP.2012.2189734.

[124] K. A. Michalski and J. R. Mosig, "Multilayered media Green's functions in integral equation formulations", *IEEE Transactions on Antennas and Propagation*, vol. 45, no. 3, pp. 508–519, Mar. 1997. DOI: 10.1109/8.558666.

[125] M. A. Hickey, Meide Qiu, and G. V. Eleftheriades, "A reduced surface-wave twin arc-slot antenna for millimeter-wave applications", *IEEE Microwave and Wireless Components Letters*, vol. 11, no. 11, pp. 459–461, Nov. 2001. DOI: 10.1109/7260.966041.

[126] N. Llombart, A. Neto, G. Gerini, *et al.*, "Impact of Mutual Coupling in Leaky Wave Enhanced Imaging Arrays", *IEEE Transactions on Antennas and Propagation*, vol. 56, no. 4, pp. 1201–1206, Apr. 2008. DOI: 10.1109/TAP.2008.919223.

[127] *CST Studio Suite*. [Online]. Available: https://www.3ds.com/products-services/simulia/products/cst-studio-suite/ (visited on 01/01/2021).

[128] A. Neto and N. Llombart, "Wideband Localization of the Dominant Leaky Wave Poles in Dielectric Covered Antennas", *IEEE Antennas and Wireless Propagation Letters*, vol. 5, pp. 549–551, 2006. DOI: 10.1109/LAWP.2006.889558.

[129] P.-S. Kildal, "Artificially soft and hard surfaces in electromagnetics", *IEEE Transactions on Antennas and Propagation*, vol. 38, no. 10, pp. 1537–1544, Oct. 1990. DOI: 10.1109/8.59765.

[130] P.-S. Kildal, E. Alfonso, A. Valero-Nogueira, *et al.*, "Local Metamaterial-Based Waveguides in Gaps Between Parallel Metal Plates", *IEEE Antennas and Wireless Propagation Letters*, vol. 8, pp. 84–87, 2009. DOI: 10.1109/LAWP.2008.2011147.

[131] N. Llombart, A. Neto, G. Gerini, *et al.*, "Planar circularly symmetric EBG structures for reducing surface waves in printed antennas", *IEEE Transactions on Antennas and Propagation*, vol. 53, no. 10, pp. 3210–3218, Oct. 2005. DOI: 10.1109/TAP.2005.856365.

[132] B. Thomas, "Design of corrugated conical horns", *IEEE Transactions on Antennas and Propagation*, vol. 26, no. 2, pp. 367–372, Mar. 1978. DOI: 10.1109/TAP.1978.1141842.

[133] M. Beruete, I. Campillo, J. S. Dolado, *et al.*, "Very low-profile "Bull's Eye" feeder antenna", *IEEE Antennas and Wireless Propagation Letters*, vol. 4, pp. 365–368, 2005. DOI: 10.1109/LAWP.2005.851104.

[134] A. Sutinjo and M. Okoniewski, "A Simple Leaky-Wave Analysis of 1-D Grooved Metal Structure for Enhanced Microwave Radiation", *IEEE Transactions on Antennas and Propagation*, vol. 60, no. 6, pp. 2719–2726, Jun. 2012. DOI: 10.1109/TAP.2012.2194655.

[135] S. Bosma, A. Neto, and N. Llombart, "On the Near-Field Spherical Wave Formation in Resonant Leaky-Wave Antennas: Application to Small Lens Design", *IEEE Transactions on Antennas and Propagation*, vol. 70, no. 2, pp. 801–812, Feb. 2022. DOI: 10.1109/TAP.2021.3137238.

[136] D. M. Pozar, *Microwave engineering*, 4th ed. Hoboken, NJ: Wiley, 2012, ISBN: 978-0-470-63155-3.

[137] H. Zhang, S. O. Dabironezare, G. Carluccio, *et al.*, "A GO/FO Tool for Analyzing Quasi-Optical Systems in Reception", in *2019 44th International Conference on Infrared, Millimeter, and Terahertz Waves (IRMMW-THz)*, Paris, France: IEEE, Sep. 2019, pp. 1–2. DOI: 10.1109/IRMMW-THz.2019.8873950.

[138] C. Jung-Kubiak, T. J. Reck, J. V. Siles, *et al.*, "A Multistep DRIE Process for Complex Terahertz Waveguide Components", *IEEE Transactions on Terahertz Science and Technology*, vol. 6, no. 5, pp. 690–695, Sep. 2016. DOI: 10.1109/TTHZ.2016.2593793.

[139] M. Alonso-delPino, T. Reck, C. Jung-Kubiak, *et al.*, "Development of Silicon Micromachined Microlens Antennas at 1.9 THz", *IEEE Transactions on Terahertz Science and Technology*, vol. 7, no. 2, pp. 191–198, Mar. 2017. DOI: 10.1109/TTHZ.2017.2655340.

[140] M. Mrnka and Z. Raida, "An Effective Permittivity Tensor of Cylindrically Perforated Dielectrics", *IEEE Antennas and Wireless Propagation Letters*, vol. 17, no. 1, pp. 66–69, Jan. 2018. DOI: 10.1109/LAWP.2017.2774448.

[141] D. Filipovic, S. Gearhart, and G. Rebeiz, "Double-slot antennas on extended hemispherical and elliptical silicon dielectric lenses", *IEEE Transactions on Microwave Theory and Techniques*, vol. 41, no. 10, pp. 1738–1749, Oct. 1993. DOI: 10.1109/22.247919.

[142] N. T. Nguyen, R. Sauleau, and C. J. Martinez Perez, "Very Broadband Extended Hemispherical Lenses: Role of Matching Layers for Bandwidth Enlargement", *IEEE Transactions on Antennas and Propagation*, vol. 57, no. 7, pp. 1907–1913, Jul. 2009. DOI: 10.1109/TAP.2009.2021884.

[143] A. Neto, L. Borselli, S. Maci, *et al.*, "Input impedance of integrated elliptical lens antennas", *IEE Proceedings - Microwaves, Antennas and Propagation*, vol. 146, no. 3, pp. 181–186, Jun. 1999. DOI: 10.1049/ip-map:19990336.

[144] A. Gatesman, J. Waldman, M. Ji, *et al.*, "An anti-reflection coating for silicon optics at terahertz frequencies", *IEEE Microwave and Guided Wave Letters*, vol. 10, no. 7, pp. 264–266, Jul. 2000. DOI: 10.1109/75.856983.

[145] S. Sahin, N. K. Nahar, and K. Sertel, "Thin-Film SUEX as an Antireflection Coating for mmW and THz Applications", *IEEE Transactions on Terahertz Science and Technology*, vol. 9, no. 4, pp. 417–421, Jul. 2019. DOI: 10.1109/TTHZ.2019.2915672.

[146] J. Lau, J. Fowler, T. Marriage, *et al.*, "Millimeter-wave antireflection coating for cryogenic silicon lenses", *Applied Optics*, vol. 45, no. 16, pp. 3746–3751, Jun. 2006. DOI: 10.1364/AO.45.003746.

[147] A. Neto, "UWB, Non Dispersive Radiation From the Planarly Fed Leaky Lens Antenna— Part 1: Theory and Design", *IEEE Transactions on Antennas and Propagation*, vol. 58, no. 7, pp. 2238–2247, Jul. 2010. DOI: 10.1109/TAP.2010.2048879.

[148] T. Hasebe, T. Hayashi, H. Takakura, *et al.*, "Development of Multi-Layer Anti-Reflection Structures for Millimeter-Wave Silicon Optics Using Deep Reactive Ion Etching Process", *Journal of Low Temperature Physics*, vol. 199, no. 1, pp. 339–347, Apr. 2020. DOI: 10.1007/s10909-019-02286-4.

[149] F. Defrance, C. Jung-Kubiak, J. Sayers, *et al.*, "16:1 bandwidth two-layer antireflection structure for silicon matched to the 190–310 GHz atmospheric window", *Applied Optics*, vol. 57, no. 18, p. 5196, Jun. 2018. DOI: 10.1364/AO.57.005196.

[150] J. D. Wheeler, B. Koopman, P. Gallardo, *et al.*, "Antireflection coatings for submillimeter silicon lenses", Montréal, Quebec, Canada, Jul. 2014, 91532Z. DOI: 10.1117/12.2057011.

[151] R. Datta, C. D. Munson, M. D. Niemack, *et al.*, "Large-aperture wide-bandwidth antireflection-coated silicon lenses for millimeter wavelengths", *Applied Optics*, vol. 52, no. 36, pp. 8747–8758, Dec. 2013. DOI: 10.1364/AO.52.008747.

[152] P. Yagoubov, T. Mroczkowski, V. Belitsky, *et al.*, "Wideband 67-116 GHz receiver development for ALMA Band 2", *Astronomy & Astrophysics*, vol. 634, A46, Feb. 2020. DOI: 10.1051/0004-6361/201936777.

[153] J. E. Golec, J. J. McMahon, A. M. Ali, *et al.*, "Design and Fabrication of Metamaterial Anti-Reflection Coatings for the Simons Observatory", in *Advances in Optical and Mechanical Technologies for Telescopes and Instrumentation IV*, Dec. 2020, p. 199. DOI: 10.1117/12.2561720.

[154] T. Nitta, Y. Sekimoto, T. Hasebe, *et al.*, "Design, Fabrication and Measurement of Pyramid-Type Antireflective Structures on Columnar Crystal Silicon Lens for Millimeter-Wave Astronomy", *Journal of Low Temperature Physics*, vol. 193, no. 5, pp. 976–983, Dec. 2018. DOI: 10.1007/s10909-018-2047-4.

[155] K. Young, Q. Wen, S. Hanany, *et al.*, "Broadband millimeter-wave anti-reflection coatings on silicon using pyramidal sub-wavelength structures", *Journal of Applied Physics*, vol. 121, no. 21, p. 213 103, Jun. 2017. DOI: 10.1063/1.4984892.

[156] R. Takaku, Q. Wen, S. Cray, *et al.*, "Large diameter millimeter-wave low-pass filter made of alumina with laser ablated anti-reflection coating", *Optics Express*, vol. 29, no. 25, p. 41 745, Dec. 2021. DOI: 10.1364/OE.444848.

[157] O. Yurduseven, "Wideband Integrated Lens Antennas for Terahertz Deep Space Investigation", Ph.D. dissertation, Delft University of Technology, Delft, 2016. [Online]. Available: https://repository.tudelft.nl/islandora/object/uuid%3Af30b8bca-173f-4a13-b545-e18e137c9fc6 (visited on 10/22/2021).

[158] A. Gonzalez, "Probe Characterization in Terahertz Near-Field Beam Measurement Systems", *IEEE Transactions on Terahertz Science and Technology*, vol. 6, no. 6, pp. 824–831, Nov. 2016. DOI: 10.1109/TTHZ.2016.2607522.

[159] H.-W Hübers, J Schubert, A Krabbe, *et al.*, "Parylene anti-reflection coating of a quasi-optical hot-electron-bolometric mixer at terahertz frequencies", *Infrared Physics & Technology*, vol. 42, no. 1, pp. 41–47, Feb. 2001. DOI: 10.1016/S1350-4495(00)00057-8.

[160] P. Irwin, P. Ade, S. Calcutt, *et al.*, "Investigation of dielectric spaced resonant mesh filter designs for PMIRR", *Infrared Physics*, vol. 34, no. 6, pp. 549–563, Dec. 1993. DOI: 10.1016/0020-0891(93)90111-J.

[161] S. C. Systems, "Parylene Properties", Tech. Rep., 2007. [Online]. Available: https://www.physics.rutgers.edu/~podzorov/parylene%20properties.pdf (visited on 04/03/2022).

[162] W. Lee, J.-O. Plouchart, C. Ozdag, *et al.*, "Fully Integrated 94-GHz Dual-Polarized TX and RX Phased Array Chipset in SiGe BiCMOS Operating up to 105 °C", *IEEE Journal of Solid-State Circuits*, vol. 53, no. 9, pp. 2512–2531, Sep. 2018. DOI: 10.1109/JSSC.2018.2856254.

[163] R. Xu and Z. N. Chen, "A Compact Beamsteering Metasurface Lens Array Antenna With Low-Cost Phased Array", *IEEE Transactions on Antennas and Propagation*, vol. 69, no. 4, pp. 1992–2002, Apr. 2021. DOI: 10.1109/TAP.2020.3026905.

[164] A. Visweswaran, C. de Martino, E. Sirignano, *et al.*, "An IQ-steering technique for amplitude and phase control of mm-wave signals", in *2015 86th ARFTG Microwave Measurement Conference*, Dec. 2015, pp. 1–4. DOI: 10.1109/ARFTG.2015.7381471.

[165] S. Bosma, N. van Rooijen, M. Alonso-delPino, *et al.*, "A Wideband Leaky-Wave Lens Antenna With Annular Corrugations in the Ground Plane", *IEEE Antennas and Wireless Propagation Letters*, vol. 21, no. 8, pp. 1649–1653, Aug. 2022. DOI: 10.1109/LAWP.2022.3176884.

[166] S. van Berkel, E. S. Malotaux, C. De Martino, *et al.*, "Wideband Double Leaky Slot Lens Antennas in CMOS Technology at Submillimeter Wavelengths", *IEEE Transactions on Terahertz Science and Technology*, vol. 10, no. 5, pp. 540–553, Sep. 2020. DOI: 10.1109/TTHZ.2020.3006750.

[167] E. Gandini, A. Tamminen, A. Luukanen, *et al.*, "Wide Field of View Inversely Magnified Dual-Lens for Near-Field Submillimeter Wavelength Imagers", *IEEE Transactions on Antennas and Propagation*, vol. 66, no. 2, pp. 541–549, Feb. 2018. DOI: 10.1109/TAP.2017.2778016.

[168] J. W. Lamb, "Miscellaneous data on materials for millimetre and submillimetre optics", *International Journal of Infrared and Millimeter Waves*, vol. 17, no. 12, pp. 1997–2034, Dec. 1996. DOI: 10.1007/BF02069487.

[169] M. Alonso-del Pino, C. Jung-Kubiak, T. Reck, *et al.*, "Micromachining for Advanced Terahertz: Interconnects and Packaging Techniques at Terahertz Frequencies", *IEEE Microwave Magazine*, vol. 21, no. 1, pp. 18–34, Jan. 2020. DOI: 10.1109/MMM.2019.2945157.

[170] B. Mirzaei, J. R. G. Silva, Y. C. Luo, *et al.*, "Efficiency of multi-beam Fourier phase gratings at 1.4 THz", *Optics Express*, vol. 25, no. 6, pp. 6581–6588, Mar. 2017. DOI: 10.1364/OE.25.006581.

[171] S. Rahiminejad, M. Alonso-delPino, T. J. Reck, *et al.*, "A Low-Loss Silicon MEMS Phase Shifter Operating in the 550-GHz Band", *IEEE Transactions on Terahertz Science and Technology*, vol. 11, no. 5, pp. 477–485, Sep. 2021. DOI: 10.1109/TTHZ.2021.3085123.

[172] R. H. Clarke and J. Brown, *Diffraction theory and antennas*, 1st ed. Chichester, West Sussex, UK: Ellis Horwood Limited, Jan. 1980, ISBN: 0-85312-182-6.

[173] N. Llombart Juan, "Development of integrated printed array antennas using EBG substrates", Ph.D. dissertation, 2006. [Online]. Available: https://repository.tno.nl/islandora/object/uuid%3A99ded773-82ae-48ea-a351-0b42e6c9a386 (visited on 04/29/2021).

[174] G. Watson, *A treatise on the theory of Bessel functions*. Cambridge, UK: Cambridge University Press, 1922.

[175] E. V. Jull, *Aperture antennas and diffraction theory* (IEE electromagnetic waves series 10). Stevenage, U.K. ; New York: P. Peregrinus on behalf of the Institution of Electrical Engineers, 1981, ISBN: 978-0-906048-52-8.

[176] C. A. Balanis, *Antenna theory: analysis and design*, 3rd ed. Hoboken, NJ: John Wiley, 2005, ISBN: 978-0-471-66782-7.

[177] C. A. Balanis, *Advanced Engineering Electromagnetics*, 2nd ed. Hoboken, N.J: John Wiley & Sons, Inc, 2012, ISBN: 978-0-470-58948-9.

[178] S. Silver, *Microwave Antenna Theory and Design* (IEE Electromagnetic Waves 19). London, UK: Peter Peregrinus, Ltd., 1984, ISBN: 978-0-86341-017-8.

[179] F. Bowman, *Introduction to Bessel Functions*. New York, USA: Dover Publications, 1958, ISBN: 0-486-60462-4.

[180] S. Gulkis, M. Frerking, J. Crovisier, *et al.*, "MIRO: Microwave Instrument for Rosetta Orbiter", *Space Science Reviews*, vol. 128, no. 1-4, pp. 561–597, May 2007. DOI: 10.1007/s11214-006-9032-y.

[181] C. A. Leal-Sevillano, J. A. Ruiz-Cruz, J. R. Montejo-Garai, *et al.*, "Novel dual-band single circular polarization antenna feeding network for satellite communications", in *The 8th European Conference on Antennas and Propagation (EuCAP 2014)*, Apr. 2014, pp. 3265–3269. DOI: 10.1109/EuCAP.2014.6902525.

[182] J. R. Montejo-Garai, J. A. Ruiz-Cruz, C. A. Leal-Sevillano, *et al.*, "Modelling of dual-polarisation diplexers based on enhanced multiport turnstile junctions", *IET Microwaves, Antennas & Propagation*, vol. 7, no. 7, pp. 485–492, 2013. DOI: 10.1049/iet-map.2012.0424.

[183] P. Kangaslahti, D. Pukala, D. Hoppe, *et al.*, "Broadband millimeter wave receiver with dual polarization", in *2011 IEEE MTT-S International Microwave Symposium*, Jun. 2011, pp. 1–4. DOI: 10.1109/MWSYM.2011.5972645.

[184] N. Memeletzoglou, E. Rajo-Iglesias, and D. Blanco, "Single-Layer Dual-Band Leaky Wave Antennas Design Methodology with Directivity Control", in *2018 IEEE International Symposium on Antennas and Propagation USNC/URSI National Radio Science Meeting*, Jul. 2018, pp. 1875–1876. DOI: 10 . 1109 / APUSNCURSINRSM.2018.8608717.

[185] S. Bosma, M. Alonso-del Pino, D. Blanco, *et al.*, "Dual-Band Leaky-Wave Lens Antenna for Submillimeter-Wave Heterodyne Instruments", in *2019 44th International Conference on Infrared, Millimeter, and Terahertz Waves (IRMMW-THz)*, Sep. 2019, pp. 1–3. DOI: 10.1109/IRMMW-THz.2019.8874461.

[186] P. F. Goldsmith, *Quasioptical systems: Gaussian beam quasioptical propagation and applications* (Chapman & Hall Publishers series on microwave technology and RF). Piscataway, NJ: IEEE Press, 1998, ISBN: 978-0-7803-3439-7.

List of publications

Journal papers

[J1] M. Alonso-delPino, S. Bosma, C. Jung-Kubiak, G. Chattopadhyay, and N. Llombart, "Wideband Multimode Leaky-Wave Feed for Scanning Lens-Phased Array at Submillimeter Wavelengths," *IEEE Transactions on Terahertz Science and Technology*, vol. 11, no. 2, pp. 205–217, Mar. 2021, doi: 10.1109/TTHZ.2020.3038033.

[J2] H. Zhang, S. Bosma, A. Neto, and N. Llombart, "A Dual-Polarized 27-dBi Scanning Lens Phased Array Antenna for 5G Point-to-Point Communications," *IEEE Transactions on Antennas and Propagation*, vol. 69, no. 9, pp. 5640-5652, Sept. 2021, doi: 10.1109/TAP.2021.3069494.

[J3] S. Bosma, A. Neto, and N. Llombart, "On the Near-Field Spherical Wave Formation in Resonant Leaky Wave Antennas: Application to Small Lens Design," *IEEE Transactions on Antennas and Propagation*, vol. 70, no. 2, pp. 801-812, Feb. 2022, doi: 10.1109/TAP.2021.3137238.

[J4] S. Bosma, N. van Rooijen, M. Alonso-delPino and N. Llombart, "A Wideband Leaky-Wave Lens Antenna with Annular Corrugations in the Ground Plane", *IEEE Antennas and Wireless Propagation Letters*, vol. 21, no. 8, pp. 1649-1653, Aug. 2022, doi: 10.1109/LAWP.2022.3176884.

[J5] S. Bosma, N. van Rooijen, M. Alonso-delPino, M. Spirito and N. Llombart, "First Demonstration of Dynamic High-Gain Beam Steering with a Scanning Lens Phased Array", *IEEE Journal of Microwaves*, vol. 2, no. 3, pp. 419-428, Jul. 2022, doi: 10.1109/JMW.2022.3179953.

[J6] J. Bueno, S. Bosma, T. Bußkamp-Alda, M. Alonso-delPino and N. Llombart, "Broadband Lossless Matching Layer for Silicon Lens Arrays at 500 GHz Using Laser Ablated Structures", *IEEE Transactions on Terahertz Science and Technology*, vol. 12, no. 6, pp. 667-672, Nov. 2022, doi: 10.1109/TTHZ.2022.3202031.

[J7] M. Alonso-delPino, S. Bosma, J. Bueno, C. Jung-Kubiak, G. Chattopadhyay and N. Llombart, "Broadband Quasi-Optical Power Distribution and Beam Steering with Transmit Lens Arrays at 500 GHz", *In preparation*.

[J8] S. Bosma, M. Alonso-delPino, S.L. van Berkel, D. Blanco, C. Jung-Kubiak, G. Chattopadhyay, J.V. Siles, and N. Llombart, "Dual-Band Leaky-Wave Lens Antenna for Submillimeter-Wave Heterodyne Instruments", *In preparation*.

Conference contributions

[C1] S. Bosma, N. van Rooijen, M. Alonso-delPino, M. Spirito and N. Llombart, "W-Band Demonstration Of Dynamic, High-Gain Beam Steering With A Scanning Lens Phased Array", *2022 47th International Conference on Infrared, Millimeter, and Terahertz Waves (IRMMW-THz)*, Sept. 2022.

[C2] J. Bueno, S. Bosma, T. Busskamp-Alda, M. Alonso-delPino and N. Llombart, "Broadband Lossless Matching Layer For Lens Arrays At THz Frequencies", *2022 47th International Conference on Infrared, Millimeter, and Terahertz Waves (IRMMW-THz)*, Sept. 2022.

[C3] M. Alonso-delPino, S. Bosma, C. Jung-Kubiak, J. Bueno, G. Chattopadhyay and N. Llombart, "Demonstration Of A Broadband Quasi-Optical Power Distribution And Beam-Steering With Transmit Lens Arrays At 550 GHz", *2022 47th International Conference on Infrared, Millimeter, and Terahertz Waves (IRMMW-THz)*, Sept. 2022.

[C4] S. Bosma, N. van Rooijen, M. Alonso-delPino, M. Spirito and N. Llombart, "On the Demonstration of Dynamic Beam-Steering with a Scanning Lens Phased Array at W-band", *2022 16th European Conference on Antennas and Propagation (EUCAP 2022)*, Mar. 2022. **Nominated for the "Best Applied Technology Paper" prize.**

[C5] M. Alonso-delPino, S. Bosma, C. Jung-Kubiak, J. Bueno, G. Chattopadhyay and N. Llombart, "Transmit Lens Arrays for Broadband THz Power Distribution and Beam Steering", *2022 16th European Conference on Antennas and Propagation (EUCAP 2022)*, Mar. 2022. **Nominated for the "Best Applied Technology Paper" prize.**

[C6] S. Bosma, M. Alonso-delPino, D. Blanco, S. van Berkel, C. Jung-Kubiak, G. Chattopadhyay, J.V. Siles, and N. Llombart, "Synthesis of Dual-Band Leaky-Wave Antenna Feeds for Submillimeter-Wave Imaging", *2022 16th European Conference on Antennas and Propagation (EUCAP 2022)*, Mar. 2022.

[C7] S. Bosma, M. Alonso-delPino, C. Jung-Kubiak, G. Chattopadhyay and N. Llombart, "Multi-Mode Leaky-Wave Feed for Scanning Lens Phased Array at 550 GHz", *2021 IEEE International Symposium on Antennas and Propagation (AP-S 2021)*, Dec. 2021.

[C8] S. Bosma, M. Alonso-delPino, D. Blanco, S. van Berkel, C. Jung-Kubiak, G. Chattopadhyay, J. Siles and N. Llombart, "A Submillimeter-Wave Dual-Band Leaky-Wave Lens Antenna for Cometary Mapping", *2021 IEEE International Symposium on Antennas and Propagation (AP-S 2021)*, Dec. 2021.

[C9] S. Bosma, A. Neto and N. Llombart, "Near-Field Spherical Wave Formation in Resonant Leaky-Wave Lens Antennas", *2021 IEEE International Symposium on Antennas and Propagation (AP-S 2021)*, Dec. 2021.

[C10] S. Bosma, N. van Rooijen, M. Alonso-delPino, and N. Llombart, "High Aperture Efficiency Plastic Lens Antenna for Scanning Lens Phased Array at 180 GHz", *2021 46th International Conference on Infrared, Millimeter, and Terahertz Waves (IRMMW-THz)*, Sept. 2021.

[C11] M. Alonso-delPino, S. Bosma, C. Jung-Kubiak, G. Chattopadhyay and N. Llombart, "Broadband Power Distribution using Multi-Mode Leaky-Wave Lens Antennas at Submillimeter Wavelengths", *2021 46th International Conference on Infrared, Millimeter, and Terahertz Waves (IRMMW-THz)*, Sept. 2021.

[C12] S. Bosma, M. Alonso-delPino, C. Jung-Kubiak, G. Chattopadhyay and N. Llombart, "High Efficiency, Wideband, Multi-Mode Leaky-Wave Feed for Scanning Lens Phased Array", *2021 15th European Conference on Antennas and Propagation (EUCAP 2021)*, Mar. 2021. **Nominated for the "Best Antenna Design paper" prize.**

[C13] M. Alonso-delPino, N. van Rooijen, S. Bosma, and N. Llombart, "A Wideband Corrugated Leaky-Wave Feed with Low Cross-Pol for High Efficiency Lens Illumination", *2021 15th European Conference on Antennas and Propagation (EUCAP 2021)*, Mar. 2021.

[C14] S. Bosma, A. Neto and N. Llombart, "Near-Field Analysis of a Leaky-Wave Resonant Feed: Application to a Small Silicon Lens", *2021 15th European Conference on Antennas and Propagation (EUCAP 2021)*, Mar. 2021.

[C15] S. Bosma, M. Alonso-delPino, C. Jung-Kubiak, and N. Llombart, "550 GHz Scanning Lens Phased Array", *2020 45th International Conference on Infrared, Millimeter, and Terahertz Waves (IRMMW-THz)*, Sept. 2020.

[C16] S. Bosma, H. Zhang, A. Neto and N. Llombart, "Near-Field Analysis of Leaky-Wave Lens Array Feeds", *2020 IEEE International Symposium on Antennas and Propagation (AP-S 2020)*, Jul. 2020.

[C17] H. Zhang, S. Bosma, A. Neto, U. Imberg and N. Llombart, "On the Design of a 27-dBi Phased Array for 5G Point-to-Point Communications", *2020 14th European Conference on Antennas and Propagation (EUCAP 2020)*, Mar. 2020.

[C18] M. Alonso-delPino, S. Bosma, C. Jung-Kubiak and N. Llombart, "On the Development of a Scanning Lens Phased Array at 550 GHz", *2020 14th European Conference on Antennas and Propagation (EUCAP 2020)*, Mar. 2020.

[C19] S. Bosma, H. Zhang, A. Neto and N. Llombart, "Near-Field Beamforming in Leaky-Wave Resonant Antennas", *2020 14th European Conference on Antennas and Propagation (EUCAP 2020)*, Mar. 2020. **Nominated for the "Best Electromagnetics paper" prize.**

[C20] S. Bosma, M. Alonso-delPino, D. Blanco, C. Jung-Kubiak and N. Llombart, "Dual-Band Leaky-Wave Lens Antenna for Submillimeter-Wave Heterodyne Instruments", *2019 44th International Conference on Infrared, Millimeter, and Terahertz*

Waves (IRMMW-THz), Sept. 2019.

[C21] S. Bosma, M. Alonso-delPino, C. Jung-Kubiak, D. Blanco and N. Llombart, "Scanning Lens Phased Array for Submillimeter Wavelengths", *2019 44th International Conference on Infrared, Millimeter, and Terahertz Waves (IRMMW-THz)*, Sept. 2019.

[C22] S. Bosma, M. Alonso-delPino, D. Blanco, J. Siles, M. Choukroun and N. Llombart, "Dual-Band Leaky-Wave Lens Antenna for Submillimeter-Wave Heterodyne Instruments", *2019 13th European Conference on Antennas and Propagation (EUCAP 2019)*, Apr. 2019.

[C23] S. Bosma, M. Alonso-delPino, D. Blanco and N. Llombart, "Fly's Eye Lens Phased Array for Submillimeter Wavelengths", *2019 13th European Conference on Antennas and Propagation (EUCAP 2019)*, Apr. 2019.

[C24] M. Alonso-delPino, S. Bosma, C. Jung-Kubiak, G. Chattopadhyay and N. Llombart, "Fly's Eye Lens Phased Array for Submillimeter-Wave Space Instruments", *2019 30th International Symposium on Space Terahertz Technology (ISSTT2019)*, Apr. 2019.

Master thesis co-supervision

[T1] N. van Rooijen, "On the Development of a Lens Phased Array at 100 GHz", *MSc. Thesis*, Delft University of Technology, Jun. 2021.

[T2] D. Loncarevic, "Spectral Analysis of the Infinite Slot Leaky Wave Antenna & Leaky Wave Antenna With Multiple Slots", *MSc. Thesis*, Delft University of Technology, Jun. 2022.

Journal papers outside the scope of this thesis

[A1] A. Endo, K. Karatsu, A. Pascual Laguna *et al.*, " Wideband on-chip terahertz spectrometer based on a superconducting filterbank", *Journal of Astronomical Telescopes, Instruments and Systems*, vol. 5, no. 3, Jul. 2019.

[A2] A. Endo, K. Karatsu, Y. Tamura *et al.*, "First light demonstration of the integrated superconducting spectrometer", *Nature Astronomy*, vol. 3, pp. 989-996, Aug. 2019.

[A3] T. Takekoshi, K. Karatsu, J. Suzuki *et al.*, "DESHIMA on ASTE: On-Sky Responsivity Calibration of the Integrated Superconducting Spectrometer", *Journal of Low Temperature Physics*, vol. 199, pp. 231-239, Feb. 2020.

About the author

Sjoerd Bosma was born on October 4, 1991 in Camperdown (Sydney), Australia. He received his B.Sc. degree and M.Sc. degree (*cum laude*) in Electrical Engineering from Delft University of Technology (TU Delft), Delft, The Netherlands in 2015 and 2017, respectively. In his Master's thesis, *Quasi-optical system for the DESHIMA spectrometer*, he described the design and analysis of the warm optics that were later used in the 10-meter ASTE telescope cabin in Chile.

In September 2017, he started his Ph.D. degree in the Terahertz Sensing Group of the faculty of Electrical Engineering, Mathematics and Computer Science at the TU Delft in collaboration with NASA's Jet Propulsion Laboratory (NASA/JPL), Pasadena, California, United States of America. His research focuses on the analysis, design and demonstration of millimeter and submillimeter-wave leaky-wave lens antenna arrays. His research was supervised by Prof. dr. Nuria Llombart (TU Delft) and dr. Maria Alonso-delPino (NASA Jet Propulsion Laboratory, now at TU Delft) and funded by the European Research Council Starting Grant LAA-CC-THz (639749). During his Ph.D. research in 2018-2019, he spent five months at the Submillimeter-Wave Advanced Technology (SWAT) group at NASA/JPL, as a Visiting Student Researcher. The work for his Ph.D. thesis has resulted in eight journal publications and 24 papers in conference proceedings. Additionally, he has co-supervised the M.Sc. theses of Nick van Rooijen and Dunja Loncarevic.

Mr. Bosma was co-nominated for the *Best Electromagnetics Paper* prize at the 14th European Conference on Antennas and Propagation (EUCAP2020), the *Best Antenna Design Paper* prize at the 15th European Conference on Antennas and Propagation (EUCAP2021) and was nominated with two papers in the category *Best Applied Technology Paper* at the 16th European Conference on Antennas and Propagation (EUCAP2022).

Sjoerd Bosma is a member of the IEEE, a member of the Antennas and Propagation Society (IEEE AP-S) and a member of the European Association on Antennas and Propagation (EurAAP). He serves as a reviewer for *IEEE Transactions on Antennas and Propagation*, the *European Conference on Antennas and Propagation* and the *International Conference on Infrared, Millimeter, and Terahertz Waves*.

Acknowledgments

Although my name is the only one on the cover of this thesis, the research presented here is the result of excellent supervision, thorough guidance and fruitful collaboration with many researchers, scientists and supporting staff in Delft and abroad. Additionally, none of this would have been possible without my friends and family that have always supported me. The paragraphs below are dedicated to all those who made this thesis possible.

To prof. dr. Nuria Llombart Juan: Thank you so much for having the confidence in me to start this Ph.D. journey, nearly five years ago. You have taught me everything I know about leaky waves, (lens) antennas, quasi-optical systems and many more topics but also a lot about life. Nuria, I am so glad that you are my promotor and I was able to perform my research under your supervision! It has been an epic journey and I am quite sad it is over but I am very grateful for all the advice you have given me when the times became rough personally. I am happy to report I am not even close to exhausting your knowledge on many areas and I hope we can continue to collaborate on interesting topics, for which we have laid the groundwork in this thesis.

To dr. Maria Alonso-delPino: I am thankful for the opportunity you have given me to collaborate with you while you were at NASA. You took a chance on me, and I like to believe it turned out well. Thanks so much for giving me an awesome stay in the US. I'll never forget Christmas 2018 with your parents. You have taught me a lot about life (in the lab and outside of it) and have always been ready to help me when I needed it. Your humbleness is exemplary, second only to your research skills. Thank you for being my co-promotor!

I am indebted to prof. dr. Andrea Neto for his guidance and expertise on leaky waves in general and in our "near field" paper in particular for which I thank him. Furthermore, as the head of the Terahertz Sensing Group, you made all of this possible in the first place, for which I am immensely grateful. I would also like to express my gratitude to dr. Darwin Blanco for his supervision during the first year and a half of my Ph.D. I am grateful to Huasheng Zhang for our successful collaboration on the "5G" paper which really kickstarted the investigation into small lenses. Many thanks to dr. Macro Spirito, who has been instrumental in teaching me about RF measurements and for his contributions to the "100 GHz array" paper.

It was an immense pleasure and honor to work with dr. Juan Bueno in the lab. Juan, I am very impressed with your craftsmanship on the "Juansorber", your work on the "groovy" paper and organization in the lab. But I am even more so for your happy

spirit, relationship advice, sense of humor and friendship.

I am humbled and grateful to have received the support, guidance and access to the fabrication skills of many at NASA's Jet Propulsion Laboratory (California, USA) including dr. Goutam Chattopadhyay, dr. Cécile Jung-Kubiak, dr. José V. Siles, dr. Sven van Berkel, dr. Imran Mehdi and many others in Pasadena. Thank you for the collaboration that we started in 2017 and for welcoming me warmly into the SWAT group. Hardly any work in this thesis would have been possible without it!

The amazing laser micromachining skill of Tobias Bußkamp-Alda at Veldlaser B.V. has allowed us to prototype numerous silicon lens arrays and the "groovy" matching layer. I extend my gratitude to him for his continuous support and hard work. The material support of the Microwave Sensing, Signals and Systems (MS3) group in realizing the demonstration in Chapter 8 was much appreciated. The Dienst Electromechanische Ontwikkeling (DEMO) at TU Delft have manufactured several of our plastic lens antennas, waveguide structures and fixtures and I kindly acknowledge the support of Bert Bakker and his colleagues.

I would like to thank the people of the Terahertz Sensing Group of which I am honored to have been a part in the past seven (!) years. Many thanks to the excellent professors, researchers and staff who have contributed to making this place ~~(one of)~~ the best in the world: prof. dr. ir. Jochem Baselmans, prof. dr. Angelo Freni, dr. Daniele Cavallo, dr. Akira Endo, dr. Paolo Sberna, dr. Giorgio Carluccio, dr. Pieter de Visser and dr. Kenichi Karatsu. I would like to give a special mention to dr. Ioan (Hansi) Lager for involving me in his work on electromagnetics when I was only a Bachelor student and being instrumental to forming my own interest in it. The support of the best and nicest secretary in the world, Everdine de Vreede-Volkers, has also been invaluable to me.

I owe many thanks to the *Hot and Cool Guys* Ralph van Schelven and Arturo Fiorellini Bernardis for being my office-mates all these years but more importantly, becoming friends. It was amazing, and I am 100% sure I couldn't have finished without you guys around. I am glad we can soon change our name to the *Hot and Cool Doctors*! David Thoen, thanks for your wise lessons, amazing glühwein and camaraderie in the past years. Whether I needed a shoulder to cry on, a person to ramble at or any other support at all, I could always count on you.

Nick van Rooijen, it was amazing to supervise you as a M.Sc. student. It has taught me a lot and I hold dear memories of the time, even if the pandemic drastically changed the way we collaborated. I hope you feel the same about it! I wish you the best of luck with your further Ph.D. endeavours, in which I have full confidence.

Dunja Loncarevic, it was my immense pleasure and honor to be your (co-)supervisor mostly during the first half of your Master's thesis. You are incredibly smart, friendly and funny. I am sure you will do amazing things even (or rather, especially) without

my supervision.

To the postdocs, fellow Ph.D. students (*lotgenoten*) and M.Sc. students that are or were in the THz Sensing Group: You have made my time in the group amazing and I could not have wished for nicer people around me on a daily basis.

To my all my friends, but especially to Jori, Kyle, Ron, Michel, Joost, Erik, Jeroen, Bram, Koen, Lex, Remon and Anatoly: thanks for the encouragement and moral support that have kept me (sort of) sane during the last years. For those who enjoyed the DJ Tiësto lectures, I promise I will make it a priority and that the mixtape will be out soon!

Pap, mam en Rieuwert: Bedankt voor jullie hulp, steun en vertrouwen de afgelopen jaren. Ik heb er ontzettend veel aan gehad! Ik hoop dat dit lullige boekje het een beetje goed kan maken. Ik hou van jullie!

Mirthe, zonder jou was dit echt nóóit gelukt. Jouw tomeloze inzet voor alles waar ik “te druk” voor was en de manier waarop je mij op de rails gehouden hebt zal voor jou ook niet altijd makkelijk geweest zijn. Ik hou van jou.

Sjoerd Bosma

Rotterdam, December 2022